

COMPARING THE MAGNITUDE AND MECHANISMS OF SUBMARINE
GROUNDWATER DISCHARGE (SGD) AND ASSOCIATED NUTRIENT FLUXES IN
ESTUARIES AND COASTAL KARST SYSTEMS: THE EXAMPLES OF MOBILE BAY
(USA) AND MARO-CERRO GORDO (SPAIN)

by

DANIEL AGUSTIN MONTIEL MARTIN

NATASHA DIMOVA, COMMITTEE CHAIR

RONA DONAHOE

BEHZAD MORTAZAVI

CHRISTOPHER SMITH

GEOFFREY TICK

YONG ZHANG

A DISSERTATION

Submitted in partial fulfillment of the requirements for the
degree of Doctor of Philosophy in the Department of
Geological Sciences in the Graduate School of
The University of Alabama

TUSCALOOSA, ALABAMA

2018

Copyright Daniel Agustin Montiel Martin 2018
ALL RIGHTS RESERVED

ABSTRACT

Submarine groundwater discharge (SGD) is an important source of natural and anthropogenic nutrients and contaminants in coastal waters. Nutrient inputs from SGD can cause or exacerbate eutrophication, hypoxia, seagrass beds degradation, and harmful algal blooms (HABs), among other ecological impacts. Coastal karst systems and estuaries are among the most complex coastal areas, where the assessment of SGD and derived nutrient fluxes is particularly challenging. Their typically heterogeneous hydrogeology combined with temporal fluctuations of marine and terrestrial forcing result in large variations of SGD in both systems. In this dissertation I evaluated the magnitude and mechanisms driving SGD and its importance as a source of water and nutrients to Maro-Cerro Gordo (a coastal karst system in southern Spain) and Mobile Bay (an estuary of the northern Gulf of Mexico). In Maro-Cerro Gordo I found that SGD accounted for an important part of the water budget of the coastal karst aquifer, the only source of freshwater for nearby population and agricultural activities. Additionally, SGD served as a vector for NO_3^- fertilizers contamination to the sea, putting at risk the endangered species of the coastal ecosystem. In Mobile Bay I found that 1/4 of the nutrient budget is delivered by SGD during the dry season as NH_4^+ (56% of the total) and DON (15% of the total), mostly on the east shore, where *Jubilees* occur. I demonstrated that these SGD-derived nutrient inputs, in contrast to previous hypotheses, are originated naturally from organic matter mineralization in a peat layer found only on the east shore of the bay. In comparison, groundwater discharge in Maro-Cerro Gordo was primarily controlled by the terrestrially driven hydraulic gradient of the karst aquifer, while in Mobile Bay SGD was mainly marine-driven by sea level fluctuations (tidal pumping).

Furthermore, the extremely fast groundwater flow of the karst aquifer in Maro-Cerro Gordo always created oxic conditions, allowing the NO_3^- contamination to reach the sea. In contrast, in the shallow coastal aquifer of Mobile Bay I found that, while the main form of nitrogen in inland fresh groundwater was NO_3^- , the SGD-derived nitrogen inputs to the bay was almost entirely in the form of NH_4^+ . These large fluxes of NH_4^+ were produced by two main processes: organic matter mineralization and dissimilatory nitrate reduction to ammonium (DNRA).

DEDICATION

To my parents, to María, and to you: Lucía.

LIST OF ABBREVIATIONS AND SYMBOLS

cm	centimeter(s)
CRP	continuous resistivity profiling
CS	coastal springs
CTD	conductivity-temperature-depth sensor
d	day(s)
DO	dissolved oxygen
DOC	dissolved organic carbon
DOM	dissolved organic matter
DON	dissolved organic nitrogen
EC	electrical conductivity
ERT	electrical resistivity tomography
FSGD	fresh submarine groundwater discharge
GC	groundwater-fed creeks
GIS	geographic information system
GMWL	global meteoric water line
GS	diffuse groundwater seepage
HAB	harmful algal bloom
IUCN	International Union for Conservation of Nature
k	gas transfer velocity
LGL	local groundwater line

m	meter(s)
RaDeCC	Radium Delayed Coincidence Counter
RMS	root mean square error
RSGD	recirculated submarine groundwater discharge
SAA	Sierra Almirajara-Alberquillas
SAC	Special Area of Conservation
SCI	Site of Community Importance
SGD	submarine groundwater discharge
SPA	Special Protection Area
SPAMI	Specially Protected Area of Mediterranean Importance
SS	submarine springs
t	water residence time
T	temperature
TOC	total organic carbon
V	volume of coastal water affected by SGD
VSMOW	Vienna Standard Mean Ocean Water
WMMWL	western Mediterranean meteoric water line
y	year(s)
α	Ostwald's solubility coefficient
λ	decay constant
%	percentage
‰	per mil

ACKNOWLEDGMENTS

I would like to thank everyone that contributed to this research, directly and indirectly. Specially, I would like to thank my academic advisor Dr. Natasha Dimova for giving me the opportunity to work with her. I am very thankful for her massive help and guidance throughout the completion of this dissertation. I also want to thank my research group members Nathan Coburn, Adam Forkner, Alex Lamore, and Jackson Stewart for their extensive help in the field. I also thank the useful comments and inputs from all my dissertation committee members, Dr. Rona Donahoe, Dr. Behzad Mortazavi, Dr. Christopher Smith, Dr. Geoffrey Tick, and Dr. Yong Zhang. I am very grateful to the Department of Geological Sciences for providing me the opportunity to develop my research skills and the teaching assistantship funding I have received for four years. I am also grateful to the Geological Sciences Advisory Board and Mr. George Lindahl for the generous scholarships they gave me.

The research conducted to develop this dissertation was partially funded by the National Science Foundation, the 2016 ExxonMobil Summer Fund, the 2015 Gulf Coast Association of Geological Societies Student Research Grant, the University of Alabama Graduate School Research and Travel Support Fund, the UA Department of Geological Sciences W. Gary Hooks Fund and A.S. Johnson Travel Fund, and the Weeks Bay National Estuarine Research Reserve.

CONTENTS

ABSTRACT	ii
DEDICATION	iv
LIST OF ABBREVIATIONS AND SYMBOLS	v
ACKNOWLEDGMENTS	vii
LIST OF TABLES	xv
LIST OF FIGURES	xvii
CHAPTER 1: INTRODUCTION	1
References	6
CHAPTER 2: ASSESSING SUBMARINE GROUNDWATER DISCHARGE (SGD) AND NITRATE FLUXES IN HIGHLY HETEROGENEOUS COASTAL KARST AQUIFERS: CHALLENGES AND SOLUTIONS	11
2.1 Abstract	11
2.2 Introduction	12
2.3 Study site and hydrogeological settings	16
2.3.1 Alberquillas Aquifer Unit	17
2.3.2 Schist formation	19
2.3.3 Conglomerate, breccia, and travertine formations	19
2.4 Methods	21
2.4.1 Tracer techniques	21
2.4.1.1 ²²⁴ Ra distribution and submarine springs discharge assessment	21
2.4.1.2 Salinity anomalies and submarine spring discharge evaluation	23

2.4.1.3 ^{222}Rn surveys and groundwater seepage assessment	24
2.4.1.4 Fresh SGD assessment in diffuse seepage	27
2.4.2 Direct groundwater flow measurements	28
2.4.2.1 Flowmeter measurements of coastal springs and creeks	28
2.4.2.2 Seepage meter measurements of diffuse seepage	29
2.4.2.3 Groundwater chemistry, stable isotopic composition, and NO_3^- fluxes	29
2.5 Results	30
2.5.1 Detecting submarine spring discharge using ^{224}Ra and salinity	30
2.5.1.1 ^{224}Ra activities in seawater and groundwater.....	30
2.5.1.2 Salinity anomalies.....	33
2.5.2 Evaluating submarine spring discharge using ^{224}Ra and salinity.....	34
2.5.2.1 ^{224}Ra mass balance	34
2.5.2.2 Salinity mass balance	37
2.5.3 Assessing diffuse groundwater seepage using a ^{222}Rn mass balance and seepage meter measurements.....	37
2.5.3.1 ^{222}Rn distribution in seawater	37
2.5.3.2 Groundwater discharge assessments in the conglomerate section (Maro Cliff).....	38
2.5.3.3 Groundwater fluxes in the karst section (Cantarrijan Beach).....	42
2.5.4 Groundwater contribution from coastal springs and groundwater-fed creeks.....	44
2.5.5 Groundwater isotopic composition, water chemistry, and nitrate fluxes.....	45
2.6 Discussion	49
2.6.1 Method selection and assessment of each form of groundwater discharge to the sea.....	49
2.6.1.1 Submarine springs.....	49

2.6.1.2 Diffuse groundwater seepage through seabed sediments	53
2.6.1.3 Subaerial forms of groundwater discharge to the sea (coastal springs and groundwater-fed creeks)	54
2.6.1.4 Total groundwater discharge to Maro-Cerro Gordo coastal area	55
2.6.2 Complexity of Sierra Almirajara-Alberquillas karst aquifer hydrodynamics.....	57
2.6.3 Importance of groundwater discharge for the water budget of Sierra Almirajara-Alberquillas Aquifer and nitrate loading to Maro-Cerro Gordo coastal area	62
2.6.4 Sensitivity analysis of methods applied	64
2.6.4.1 Parameter sensitivity of ²²⁴ Ra and salinity mass balance methods for determining discharge of submarine springs.....	64
2.6.4.2 Parameter sensitivity of the ²²² Rn mass balance and seepage meters measurements in determining diffuse seepage	67
2.6.4.3 Implications for the water budget of Sierra Almirajara-Alberquillas Aquifer.....	68
2.6.5 Global applicability of the presented methodology approach	71
2.7 Conclusions.....	71
2.8 Acknowledgments.....	73
2.9 References	75
2.10 Appendix I	85
CHAPTER 3: CONSTRAINING THE IMPORTANCE OF SUBMARINE GROUNDWATER DISCHARGE (SGD) IN HYDROGEOLOGICALLY COMPLEX ESTUARIES: EXAMPLE OF MOBILE BAY, ALABAMA	87
3.1 Abstract.....	87
3.2 Introduction.....	88
3.3 Research area	91
3.3.1 Location and estuary description	91
3.3.2 Stratigraphy and hydrogeology.....	94

3.4 Methods.....	95
3.4.1 Surface water end-members characterization	95
3.4.2 Groundwater end-member characterization.....	97
3.4.3 Shallow aquifer characterization.....	98
3.4.4 SGD assessments and Mobile Bay water budget.....	99
3.5 Results.....	100
3.5.1 Water end-members	100
3.5.1.1 Surface water end-members.....	100
3.5.1.2 Groundwater end-members.....	103
3.5.2 Shallow aquifer properties	105
3.5.2.1 Continuous resistivity profiling (CRP)	105
3.5.2.2 Electrical resistivity tomography (ERT).....	106
3.5.2.3 Shallow coastal sediments characteristics	108
3.5.3 Quantification of SGD	110
3.5.3.1 SGD variability	110
3.5.3.2 Total SGD assessment	112
3.5.3.3 FSGD and RSGD assessment	116
3.6 Discussion.....	120
3.6.1 Hydrodynamics in Mobile Bay	120
3.6.2 SGD dynamics and driving forces	123
3.6.3 Spatial distribution of SGD.....	127
3.6.4 Mobile Bay water budget.....	132
3.6.5 Ecological importance of SGD	135

3.7 Conclusions.....	136
3.8 Acknowledgments.....	137
3.9 References.....	139
3.10 Appendix II.....	148
CHAPTER 4: ARE GROUNDWATER-DERIVED NUTRIENT INPUTS IMPORTANT FOR THE JUBILEE EVENTS IN MOBILE BAY, ALABAMA?.....	168
4.1 Abstract.....	168
4.2 Introduction.....	169
4.3 Study area.....	171
4.4 Methods.....	175
4.4.1 Sample collection.....	175
4.4.2 Analytical methods.....	177
4.5 Results.....	179
4.5.1 Sediment cores.....	179
4.5.2 Groundwater composition.....	182
4.5.2.1 Dissolved oxygen.....	182
4.5.2.2 Nitrate ($\text{NO}_3^- + \text{NO}_2^-$).....	182
4.5.2.3 Ammonium (NH_4^+).....	183
4.5.2.4 Dissolved organic nitrogen (DON).....	183
4.5.2.5 Phosphorous (PO_4^{3-}).....	184
4.5.2.6 N/P ratios ($\text{NO}_3^- + \text{NH}_4^+ / \text{PO}_4^{3-}$).....	184
4.5.2.7 Stable isotopes of NO_3^- ($\delta^{15}\text{N}$ and $\delta^{18}\text{O}$).....	184
4.5.2.8 Dissolved organic carbon (DOC) and dissolved organic matter (DOM) characterization.....	185

4.5.3 Surface water composition.....	187
4.5.3.1 Dissolved oxygen.....	187
4.5.3.2 Nitrate ($\text{NO}_3^- + \text{NO}_2^-$)	188
4.5.3.3 Ammonium (NH_4^+).....	188
4.5.3.4 Dissolved organic nitrogen (DON).....	188
4.5.3.5 Phosphorous (PO_4^{3-}).....	188
4.5.3.6 N/P ratios ($\text{NO}_3^- + \text{NH}_4^+ / \text{PO}_4^{3-}$)	189
4.5.3.7 Stable isotopes of NO_3^- ($\delta^{15}\text{N}$ and $\delta^{18}\text{O}$).....	189
4.5.3.8 Dissolved organic carbon (DOC) and dissolved organic matter (DOM) characterization.....	189
4.5.4 Nutrient fluxes via SGD and river discharge.....	190
4.6 Discussion.....	194
4.6.1 Evaluating nutrients loading to Mobile Bay	194
4.6.1.1 Spatial variability of SGD-derived nutrient fluxes	194
4.6.1.2 Temporal variability of nutrient fluxes	197
4.6.2 Groundwater biogeochemical transformations and N- and P-fluxes to Mobile Bay.....	201
4.6.2.1 N- and P-fluxes on the east shore of Mobile Bay	202
4.6.2.2 N- and P-fluxes on the west shore of Mobile Bay	204
4.6.3 Nutrient sources in Mobile Bay	206
4.6.3.1 Lithological evidence.....	206
4.6.3.2 Stable isotopes evidence	208
4.6.3.3 Evidence from DOM quality and organic matter characterization:.....	212
4.6.3.4 Evidence from sediment depositional ages.....	215
4.7 Ecological implications of SGD	217

4.8 Conclusions.....	221
4.9 References.....	222
4.10 Appendix III.....	229
CHAPTER 5: CONCLUSIONS	242
References.....	247

LIST OF TABLES

2.1. Summary of values for all terms used to solve the radium and salinity mass balances to assess submarine springs discharge in the karst section. Calculated total flux (F_{SGD}) using both methods are also shown	36
2.2. Parameters used in the radon mass balance to assess diffuse seepage in Maro Cliff (conglomerate section) and Cantarrijan Beach (karst section) including estimated groundwater fluxes (F_{SGD}).	41
2.3. Comparison of groundwater seepage velocities estimated via radon model and seepage meters during July of 2016 (dry period) in Maro Cliff (conglomerate section) and Cantarrijan Beach (karst section).....	44
2.4. Summary of total groundwater discharge (TGD) including all modes of discharge (CS, GC, GS, SS), and fresh groundwater discharge from the Sierra Almirajara-Alberquillas (SAA) aquifer (daily and annual). Total nitrate fluxes to coastal waters (N-TGD) is shown for the three sections (conglomerate, Schist, and Karst sections), with respect to agricultural coverage. Relative agricultural area represents the coverage normalized by the total extension of each section near the coast	48
2.5. Values of all parameters applied in the sensitivity analysis including flux ranges estimated for each methodology	66
2.6. Applicability comparison of all methods utilized to detect and quantify different modes of groundwater discharge to the sea. Flux ranges are based on maxima and minima estimations obtained in the sensitivity analysis. Daily fluxes are shown for each form of discharge and method, and annual water budget (fresh) of Sierra Almirajara-Alberquillas (SAA).....	70
3.1. Sediment properties of the three cores extracted at each study site (TS-W, TS-SE, and TS-NE) including grain size, density, porosity, organic matter content, and hydraulic conductivity of all sediment layers identified. At study site TS-W the silt layer (B) restricted groundwater flow from layer C in which I observed a SGD plume extending 80 m in the ERT images; at study site TS-SE I observed that SGD occurred from layer D through the organic layer (B) extending 70 m; whereas at study site TS-NE SGD occurred preferentially through the coarse sand (A) and through the organic layer (B) with a SGD plume extending 100 m in layer D.....	109

3.2. Radon mass balance to assess the total SGD at each study site (TS-W, TS-SE, and TS-NE) during all sampling campaigns. Seepage velocity (ω) and groundwater fluxes (SGD) obtained from seepage meters deployments during June 2016 are also shown for each study site. The average groundwater fluxes (SGD) during the dry and wet seasons is shown for each site. Additionally, the total SGD in Mobile Bay from all study sites is presented as a range including uncertainties during each sampling campaign..... 114

3.3. Summary of values for all parameters used in the radium mixing models to assess the recirculated SGD (RSGD) at each study site (TS-W, TS-SE, and TS-NE) during the dry and wet seasons. The fraction of RSGD (f_{RSGD}) with respect to the total inputs (RSGD, river, and the seawater from the Gulf of Mexico) obtained when solving the models is shown along with the respective RSGD. The total RSGD in Mobile Bay is presented as a range including uncertainties during each sampling campaign 118

3.4. End-member values used in the site- and season-specific $\delta^{18}O$ and δ^2H mixing models utilized to calculate the proportional fraction of fresh SGD (FSGD) and recirculated SGD (RSGD) from the total SGD at all three study sites (TS-W, TS-SE, and TS-NE) during the dry and wet seasons. The fraction of both FSGD and RSGD (f_{FSGD} and f_{RSGD}) are also shown for each mixing model and their average (Average f_{FSGD} and f_{RSGD}) for each study site during the dry and wet seasons. The FSGD and RSGD values shown in the table were obtained by multiplying the Average f_{FSGD} and Average f_{RSGD} components by the average total SGD (SGD) presented in Table 3.2, measured during each season at each of the three study sites. The total FSGD and RSGD in Mobile Bay are presented as a range including variations during each sampling campaign 119

3.5. Terms utilized in the $\delta^{18}O$ - δ^2H three end-member mixing model to calculate the proportional fractions of riverine, FSGD, and seawater inputs (f_{river} , f_{fsgd} , and f_{ow}) in mobile bay during the dry and wet seasons. The table includes results for water inputs in the whole bay and at each study site individually (TS-W, TS-SE, and TS-NE) 134

4.1. Characterization of the organic matter present in the peat layer (B) analyzed from sediment core TS-SE, showing C-weight percent, N-weight percent, C/N ratio, stable isotopes $\delta^{13}C$ and $\delta^{15}N$ 181

4.2. All values utilized to evaluate the river- and SGD-derived nutrient (NO_3^- , NH_4^+ , DON and PO_4^{3-}) fluxes on the western, southeastern, and northeastern shores in Mobile Bay. The table includes values of SGD fluxes at each study site (from Chapter 3) and river discharge during the dry and wet seasons, nutrient concentrations, nutrient fluxes, and the relative importance of each nutrient to the total nutrient budget of Mobile Bay considering both river- and SGD-derived inputs 191

4.3. Groundwater specific nutrient fluxes from the Inland zone of the Miocene-Pliocene Aquifer to the intertidal zone of the aquifer, fluxes from the intertidal zone to Mobile Bay as SGD, and net fluxes after groundwater flows through the intertidal zone. Values of groundwater nutrient concentrations, groundwater flow velocity at each study site during the dry and wet seasons are also included in this table..... 199

LIST OF FIGURES

<p>2.1. Study site location and geological map showing water table contour lines (from Pérez-Ramos and Andreo, 2007), groundwater flow direction, important wells and piezometers, sampling points, and terrestrial springs. Groundwater discharge to the sea (TGD) is represented in purple and is based on this study. Coastal springs are represented as CS, groundwater-fed creeks as GC, diffuse groundwater seepage as GS, and submarine springs as SS. The study area is divided in three sections: conglomerate section, schist section, and karst section. The distribution of seagrass beds are based on Bañares-España et al. (2002), and Aranda and Otero (2014)</p>	17
<p>2.2. Average monthly precipitation and sea level change during 2010, 215, and 2016. Error bars show the monthly rainfall variability during this study. In December of 2015 slight precipitation occurred only during the first week, however, abundant rainfall took place during September-November. Sea level showed minima values during January-May and maxima during August-December. Sampling campaigns were conducted during May-July (dry periods) and December (wet periods)</p>	21
<p>2.3. Interpolated ^{224}Ra activity concentrations in September of 2010 along the schist and karst sections. Two areas of high ^{224}Ra in coastal waters were identified in the schist section near groundwater-fed Miel Creek ($56 \pm 4 \text{ dpm m}^{-3}$), and the three clustered submarine springs discharging from Cantarrijan Caves ($51 \pm 4 \text{ dpm m}^{-3}$) located in the Cantarrijan area (karst section)</p>	32
<p>2.4. Salinity anomaly map showing combined results from May, July, and December of 2015. Two areas of negative salinity anomalies were found in the conglomerate (salinity anomaly = -1.2 to -1.7) and karst (salinity anomaly = -0.3 to -1.0) sections almost perfectly aligned with their delineated extent.</p>	34
<p>2.5. Radon-222 distribution map based on surveys during July and December of 2015, and July of 2016. Two radon peaks were in found in Maro Cliff (conglomerate section) and Cantarrijan Beach (karst section) with maximum concentrations of $44 \pm 3 \times 10^3 \text{ dpm m}^{-3}$ and $30 \pm 2 \times 10^3 \text{ dpm m}^{-3}$ respectively</p>	38
<p>2.6. (a) Groundwater seepage velocity averaging results from radon mass balance and seepage meters in areas of diffuse seepage (Maro Cliff and Cantarrijan Beach). Radon distribution in (b) Maro Cliff (conglomerate section) and (c) Cantarrijan Beach (karst section) where cylinder symbols represent seepage meter locations and the star radon time series stations</p>	39

2.7. Radon fluxes result of each component of the mass balance box model during all sampling campaigns in Maro Cliff (conglomerate section) and Cantarrijan Beach (karst section). The largest tracer losses occurred via mixing due to the high exposure of both areas to waves and currents. Greater difference in SGD-²²²Rn fluxes was found between wet periods (December) and dry periods (July) in Cantarrijan Beach compared to Maro Cliff..... 43

2.8. (a) Isotopic composition ($\delta^{18}\text{O}$ and $\delta^2\text{H}$) of water samples collected during all sampling campaigns. Local Groundwater Line (LGL) represents the linear trend based on all groundwater samples collected in the study area. Global Meteoric Water Line (GMWL) is based on Craig, (1961) and the Western Mediterranean Meteoric Water Line (WMMWL) on Gat and Garmi, (1970). White color represents points of discharge in conglomerate and breccia lithology, while light grey are in travertine (conglomerate section); dark grey shows points in schist (schist section); and black color show locations in karstic marble (karst section). Maro Spring and Nerja Cave well (not points of discharge to the sea) are represented with a black and white star respectively. Water samples collected at each section (conglomerate section, schist section, and karst section) are grouped in dashed squares. (b) Isotopic composition of samples collected from points of discharge from the travertine formation in the conglomerate section. The two groundwater end-members (Maro Spring and irrigation waters) are circled, while diffuse seepage in Maro Cliff is represented with squares. 46

2.9. Mixing plots of ²²⁴Ra (a) and ²²²Rn versus salinity (b) showing best fit linear and exponential mixing lines, respectively, during surface water surveys along the coastline in September of 2010, July and December of 2015..... 51

2.10. Total groundwater discharge (TGD) in the study area divided in forms of discharge (GS: groundwater diffuse seepage, CS: coastal springs, GC: groundwater-fed creeks, SS: submarine springs), showing maximum and minimum flux during wet and dry periods. 56

2.11. Groundwater ionic relationship between NO_3^- and SO_4^{2-} where groundwater samples with similar composition are grouped in dashed squares. Symbols are presented as in Fig. 8 based on the section and lithology they are located. In the conglomerate section Maro Spring, Nerja Cave, and Maro Creek show similar SO_4^{2-} concentration with low NO_3^- , while Doncellas, Barranco Maro, Huerto Romero, and Maro Beach present NO_3^- contamination. Samples from the schist section (Miel and Alberquillas) present a distinctive signal with low NO_3^- and SO_4^{2-} concentrations. Groundwater collected in Cantarrijan Beach (karst section) shows seawater influence from saltwater recirculation in beach sediments. Arrows indicate the geochemical change before irrigation and after fertilizers application (NO_3^-), where Maro cliff (diffuse seepage) shows mixing between both groups..... 60

3.1. Research area location and hydrogeological map showing the potentiometric surface of the Miocene-Pliocene Aquifer (data from the Geological Survey of Alabama), groundwater flow direction, monitoring wells for groundwater elevation, and sampled wells. The map includes the estuary bathymetry isolines in 1-m intervals (NOAA). The

research area is divided in three sections: western shore, northeastern shore, and southeastern shore. At each section, the study sites where ERT lines, sediment core sampling, piezometers installation (Pz-1 to Pz-5), radon time series, radium assessments, and seepage meter deployments were conducted are represented with a star. The locations of Fowl River (FR), Dog River (DR), Mobile River (MR), Spanish River (SR), Tensaw River (TR), Apalachee River (AR), Blakeley River (BR), Fish River (FiR), and Magnolia River (MgR) are also indicated on the map. 93

3.2. (a) Distribution map of ^{222}Rn anomaly surveys on Mobile Bay surface water. The highest ^{222}Rn positive anomalies were found along the northeastern shore ($0.8\text{-}5.0 \times 10^3 \text{ dpm m}^{-3}$) and the southeastern shore ($0.1\text{-}5.0 \times 10^3 \text{ dpm m}^{-3}$). A positive anomaly ($0.4 - 1.5 \times 10^3 \text{ dpm m}^{-3}$) of lower magnitude was also detected in the northern sector of the western shore. Along the western shore, Bon Secour Bay, and mid-bay the ^{222}Rn concentrations were always lower resulting in negative anomalies ($-4.1 - 0.0 \times 10^3 \text{ dpm m}^{-3}$). (b) Continuous resistivity profiling (CRP) surveys conducted in Mobile Bay depicting electrical resistivity at a depth of 5-7m. The highest resistivity values (12-30 Ohm-m) were found along the northeastern and southeastern shores. Higher resistivity was also measured near the delta where river fresh water inputs occur. Both panels (a and b) show the locations where *Jubilees* occur in Mobile Bay based on Loesch (1960) and May (1971) and modified from the figure created by Fehler (2008)..... 101

3.3. Apparent water ages of Mobile Bay waters during the dry (a) and wet (b) seasons based on ^{223}Ra and Ra^{224} activity ratios. The highest water residence times were found on the southeastern shore and Bon Secour Bay, while the lowest values were found near the Mobile-Tensaw Delta and in the Mid Bay area. During dry season when river discharge was lowest, the overall residence time of the bay was higher (7.0 ± 3.5 days) compared to the wet seasons (5.1 ± 2.5 days) 103

3.4 Isotopic composition ($\delta^2\text{H}$ and $\delta^{18}\text{O}$) of water samples collected in Mobile Bay (Mobile Bay), Mobile-Tensaw River System (River), seawater from the Gulf of Mexico (Seawater), fresh groundwater (Fresh GW), and brackish groundwater (Brackish GW). Surface water samples (Mobile Bay and rivers) collected during the wet season (wet) are represented in dark grey and samples collected during the dry season (dry) are shown in light grey. Fresh groundwater samples (dark blue) were collected from inland wells W-Well-1 and W-Well-2 on the western shore, wells SE-Well-1, SE-Well-2 and SE-Well-3 on the east shore, and piezometers Pz-1 and Pz-2 at all three study sites. Brackish groundwater samples (light blue) were collected from piezometers Pz-3 to Pz-3 at all three study sites. The Local Water Line (LWL) represents the linear trend based on all water samples collected in the study area and the Global Meteoric Water Line (GMWL) is based on Craig, (1961) 104

3.5. Shore-perpendicular electrical resistivity tomography (ERT) image and geologic interpretation at study site TS-W on the western shore (a), study site TS-SE on the southeastern shore (b), and study site TS-NE on the northeastern shore (c). The location and depth of piezometers (Pz-1 to Pz-5) are also shown on each panel. On the western shore I identified a 2.5-m thick silt layer at TS-W and a groundwater plume extent of 80

m (a); at study site TS-SE a 1.5 m thick organic fine sand layer with up to 36% organic matter was found above the medium sand Miocene-Pliocene Aquifer with a groundwater plume extent of 70 m (b); whereas at study site TS-NE I found that an artificially added coarse sand deposit was present at the beach area as well as the fine sand organic layer and the underlying Miocene-Pliocene Aquifer with a groundwater plume extent of 100 m (c). Dashed lines at each ERT image depict the interphase between sediment layers. The maximum water column thickness is also indicated for each study site in the right side of each panel..... 108

3.6. Temporal variation of SGD rates (cm d^{-1}) with respect to tide stage (m) in Mobile Bay, precipitation (mm), and groundwater elevation (cm) of the Miocene-Pliocene Aquifer during March 13th-18th at study site TS-W on the western shore (a), TS-NE on the northeastern shore (b), and TS-SE on the southeastern shore (c). Two rain events occurred prior (March 11th-12th) and after (March 17th-18th) the time-series measurements, which were followed by a peak in the groundwater elevation after less than 2 days. Maximum SGD rates were reached after 3-4 days in all study sites 112

3.7. The upper bar plot shows the total SGD in Mobile Bay ($\text{m}^3 \text{d}^{-1}$) showing groundwater discharge measured at all three study sites (TS-W, TS-NE and TS-SE) during the dry (light grey) and wet (dark grey) seasons. The lower panel shows a comparison between the fresh SGD (FSGD) and recirculated SGD (RSGD) components of the total SGD during dry and wet seasons 116

3.8. Three-year time-series of precipitation (mm), Mobile-Tensaw River System discharge ($\text{m}^3 \text{d}^{-1}$), salinity in Mobile Bay, groundwater elevation at the Miocene-Pliocene Aquifer (m), and average SGD rates (cm d^{-1}) on the northeastern and southeastern shores (main areas of SGD). Typically, higher rainfall during the wet season (March) coincided with maximum riverine discharge, groundwater elevation, SGD rates, and lowest salinity in Mobile Bay. During 2017 rainfall was lower during March than in June-July, attributed to the occurrence of tropical storm Cindy in Mobile Bay. As a result, I observed the opposite trends: higher river discharge, groundwater elevation, and SGD rates during July compared to March..... 146

4.1. Study area location, showing land uses (from Ellis et al., 2011), potentiometric surface of the Miocene-Pliocene Aquifer (Geological Survey of Alabama, 2018), groundwater flow direction, monitoring wells for groundwater elevation, and sampled wells. The study area is divided in three sections: western shore, northeastern shore, and southeastern shore. At each section, the study sites where sediment core collection, intertidal piezometers installation (Pz-1 to Pz-5), SGD assessments, and SGD-derived nutrient fluxes evaluations were conducted, are represented with a star. Inland wells at both western and eastern shores are represented with an open circle. FR, DR, MR, SR, TR, AR, BR, FiR, and MgR represent the location of Fowl River, Dog River, Mobile River, Spanish River, Tensaw River, Apalachee River, Blakeley River, Fish River, and Magnolia River 172

4.2. Schematic geologic cross sections showing the lithologic characteristics of the shallow coastal sediments at study site TS-W on the western shore (a), TS-SE on the southeastern shore (b), and TS-NE on the northeastern shore (c) as presented in Chapter 3. The locations of all intertidal piezometers (Pz-1 to Pz-5) and sediment cores (highlighted in dashed rectangles) are also shown on each panel. The dashed line represents the SGD plume extent on the western shore at TS-W (80 m), on the southeastern shore at TS-SE (70 m), and the northeastern shore at TS-NE (100 m) 175

4.3. Sediment cores collected at study site TS-W on the western shore, TS-SE on the southeastern shore, and TS-NE (TS-NE-I and TS-NE-II) in the northeastern shore from locations indicated in Fig. 4.2. The presence, depth, and thickness of the peat layer (B) in the eastern shore is shown in cores TS-SE and TS-NE-I..... 180

4.4 Vertical profile of stable isotopes $\delta^{13}\text{C}$ and $\delta^{15}\text{N}$ of the organic matter present in the peat layer (B) analyzed from sediment core TS-SE. Both $\delta^{13}\text{C}$ and $\delta^{15}\text{N}$ were highest ($\delta^{13}\text{C} = -24\text{-}23\text{‰}$, $\delta^{15}\text{N} = 3\text{-}4\text{‰}$) at a depth of 50-60 cm and were lowest ($\delta^{13}\text{C} = -30\text{-}28\text{‰}$, $\delta^{15}\text{N} = 0\text{-}1\text{‰}$) at 80-90 cm. 181

4.5. Groundwater dissolved oxygen (DO), NO_3^- , NH_4^+ , DON, and PO_4^{3-} concentrations, N/P molar ratio, and nitrate stable isotopes ($\delta^{15}\text{N}$ and $\delta^{18}\text{O}$) values in the inland wells and the intertidal piezometers during the dry (a) and wet (b) seasons 187

4.6. River-derived and SGD-derived nitrogen fluxes (NO_3^- , NH_4^+ , and DON) to Mobile Bay on the western, northeastern, and southeastern shores during the wet (a) and dry (b) seasons. Most of the SGD-derived nitrogen inputs to Mobile Bay occurred on the southeastern and northeastern shores, representing an average of 93% of the total SGD-N in the bay..... 194

4.7. River-derived and total SGD-derived nitrogen fluxes (NO_3^- , NH_4^+ , and DON) to Mobile Bay from all sections during the wet (a) and dry seasons (b). Ammonium and DON were the main forms of nitrogen delivered to Mobile Bay via SGD during both the dry and wet seasons, being relatively more important to the nitrogen budget of Mobile Bay during the dry season (56% and 18% of the total respectively) 198

4.8. Schematic profile showing the annual groundwater specific nutrient fluxes from the inland zone of the Miocene-Pliocene Aquifer to the intertidal zone of the aquifer, fluxes from the intertidal zone to Mobile Bay as SGD, and net fluxes after groundwater flows through the coastal sediments. The coastal sediments at the intertidal zone generated negative net fluxes of NO_3^- and positive net fluxes of NH_4^+ , DON, and PO_4^{3-} . The sketch is not drawn to scale vertically or horizontally for an easier comparison 202

4.9. Figure 4.9. Schematic illustrating the nitrogen cycle. The dissimilatory nitrate reduction to ammonium is indicated as DNRA. This figure was modified from Chen and Wang (2015) 208

4.10. Cross plot showing the nitrate stable isotopes $\delta^{15}\text{N}$ and $\delta^{18}\text{O}$ values measured in all samples, rivers (a), Mobile Bay (b), and in groundwater (c). Samples collected on the western, southeastern, and northeastern shores are represented as white, grey, and black circles respectively. Theoretical values for anthropogenic (NO_3^- and NH_4^+ fertilizers, manure and septic waste) and natural (organic nitrogen in the sediments or soil) sources of nitrate $\delta^{15}\text{N}$ and $\delta^{18}\text{O}$ signatures are shown in all panels (Amberger and Schmidt, 1987; Kendall, 1998; Kendall et al., 2007; Xue et al., 2009). The theoretical denitrification line of $\delta^{18}\text{O}:\delta^{15}\text{N}$ as 1.5:1 is shown in all panels based on Kendall et al. (2007) and Murgulet and Tick (2013)..... 210

4.11. (a) Percentage presence of components 1, 2, and 3 (C1, C2, and C3) of dissolved organic matter (DOM) measured in pore water of the peat layer (B) at piezometer SE-Pz-4.5. DOM was primarily composed of humic-like components 2 (43%) and 1 (29%), compared to the protein-like component 3 (28%). (b) Cross plot showing the relationship between $\delta^{13}\text{C}$ and C/N of the of the organic matter present in the peat layer from sediment core TS-SE (black circles). Ranges of all possible theoretical origins of organic matter (bacteria, marine and freshwater phytoplankton, marsh and terrestrial C3 plants) are represented as defined by Lamb et al. (2006) and Guerra et al. (2015). Three specific regional end-member values measured in Mobile Bay are also shown (white circles) for marsh plant species *Spartina alterniflora* (*Spartina*), *Typha* and *Schoenoplectus* undifferentiated (*Typha* and *Schoenoplectus*), and *Juncus roemarianus* (*Juncus*) as presented by Smith and Osterman (2014). These data highlight the importance of terrestrial organic matter to Mobile Bay. All samples fall in the marsh and terrestrial C3 plants value range and regional *Spartina alterniflora* and *Juncus roemarianus* end-members 215

4.12. Vertical profile of (a) ^{210}Pb and (b) ^{137}Cs analyzes conducted on sediment core TS-SE. A peak of both isotopes can be observed from a depth of 40 cm, coinciding with the beginning of the peat layer. The depth of the peat layer is highlighted in grey..... 217

4.13. Cross plot showing the nitrogen and phosphorous concentrations measured in Mobile Bay (a), rivers (b), and groundwater (c). The Redfield molar N/P ratio of 16:1 is shown in all panels for reference. The average N/P ratio in Mobile Bay waters was 16 (Redfield ratio), while in rivers and groundwater the N/P ratios were 21 ± 9 and 270 ± 130 respectively 220

CHAPTER 1: INTRODUCTION

The phenomenon of groundwater discharge on the sea floor has been documented for more than two millennia. The earliest records date back from the Roman period describing freshwater submarine springs in the Mediterranean Sea (Kohout, 1966; Moore, 2010). Historically, the exchange of groundwater and seawater at the land-sea interphase, also known as submarine groundwater discharge (SGD), was only considered as a “*scientific curiosity*” with little actual scientific and economic importance (Kohout, 1966; Burnett and Dulaiova, 2003). However, within the last three decades SGD was found to be an essential source of water and dissolved constituents such as nutrients and pollutants to coastal environments and thus, one of the major players in coastal ecosystems (Johannes, 1980; Moore, 1999; Null et al., 2012; Rodellas et al., 2014). In river-dominated coastal systems, such as estuaries, SGD has been traditionally overlooked as it often represents only a small part of the coastal water budget compared to river inputs (Moore, 1996; Burnett et al., 2006). However, the much higher nutrient concentrations in groundwater compared to rivers often result in SGD-delivered nutrient fluxes comparable to fluvial loadings (Charette et al., 2003; Santos et al., 2008; Xu et al. 2013). In turn, excess nutrient inputs derived from SGD could cause ecological perturbations such as eutrophication, hypoxia, harmful algal blooms (HABs), and seagrass beds degradation, to mention a few (Valiela et al., 1990; Hwang et al., 2005; Garcés et al., 2011; McCoy et al., 2011; Smith and Swarzenski, 2012). In contrast, in coastal karst areas where runoff is limited due to

high infiltration rates, SGD can be a significant component of both the water and nutrient budgets (e.g., Dimova et al., 2011; Tovar-Sánchez et al., 2014; Trezzi et al., 2017). Furthermore, in karst aquifers the groundwater residence time is relatively short, allowing fast transport from land to the ocean, little natural attenuation, and thus large net pollutant fluxes (Weinstein et al., 2011; Tovar-Sánchez et al., 2014; Trezzi et al., 2016).

Evaluating the magnitude of SGD, driving mechanisms, and ultimately the SGD-derived nutrient inputs to coastal waters is highly challenging in both estuaries and coastal karst areas. Hydrogeological heterogeneities and temporally variable marine and terrestrial forcing result in large high temporal and spatial variations of SGD in both systems (Stringfield and Legrand, 1971; Pinault et al., 2004; Burnett et al. 2006; Custodio, 2010; Santos et al. 2012; Russoniello et al. 2013; Uddameri et al. 2014). Estuaries are highly dynamic systems typically associated with heterogeneous coastal aquifers that allow for complex nutrient biogeochemical transformations as groundwater flows through the coastal aquifer (Dyer 1973; Krantz et al. 2004; Slomp and Van Cappellen, 2004; Russoniello et al. 2013; Michael et al. 2016). In comparison, coastal karst aquifers are lithologically characterized by a combination of fissures, fractures, conduits, and caves that serve as preferential pathways that facilitate fast groundwater flow and create point-source nutrient inputs to the sea (Worthington, 1999; Bakalowicz et al., 2005; Barberá and Andreo, 2015). The large degree of heterogeneity in combination with marine forces in these lithologically complex coastal systems, make traditional hydrogeological modeling methods unreliable (Butscher and Huggenberger, 2007; Stalker et al. 2009; Martínez-Santos and Andreu, 2010; Rapaglia et al., 2015; Young et al. 2015). Some of these challenges have been successfully addressed by using short-lived radioisotopes from the U/Th decay series. However, some limitations and challenges remain (Lee, 1977; Moore, 1996; Burnett and Dulaiova, 2003;

Johnson et al., 2008; Knee et al., 2010). Specifically, in estuaries and coastal karst systems, their complex settings further enhance the already difficult task of evaluating SGD and derived nutrient fluxes (Burnett et al. 2003).

Maro-Cerro Gordo in Southern Spain is an environmentally protected coastal area with a karstic marble coastal aquifer. The coastal karst aquifer has been overpumped to satisfy the increasing demand from intensive agriculture and tourism. SGD was never considered an important component of the water budget of the area. However, the shortage of water in the coastal area prompted water managers to consider the need to quantify the significance of SGD in the aquifer water budget (Andreo and Carrasco, 1993). Furthermore, point-source excess nutrient inputs via SGD from agriculture lands to the sea raised questions about the magnitude of SGD-derived nutrient fluxes and their impacts on the endemic and endangered biota that inhabit the coastal ecosystem.

Frequent local reports of water quality degradation often observed in Mobile Bay, Alabama was the primary motivation for studying SGD in this coastal sandy aquifer in the Northern Gulf of Mexico (Loesch, 1960). Of particular interest for this study are two major ecological disturbances that also affect the local economy of Mobile Bay. These include (1) large-scale fish and crustaceans kills locally known as *Jubilees* that occur mostly on the east shore of Mobile Bay during the summer, and (2) harmful algal blooms (HABs) often documented in areas of limited surface water inputs. Previous studies (e.g. Loesch, 1960; May, 1973; Liefer et al., 2009; McIntyre et al., 2011) have suggested that nutrient inputs delivered by SGD might control these events, but direct assessments were never performed before this study. Further large-scale implications include a direct impact on adjacent estuaries in the Gulf of Mexico (e.g. the Mississippi Bight), and the overall nutrient budget of the Coastal Gulf Region.

The overarching goal of this dissertation is to compare the magnitude and mechanisms driving SGD and its importance as a source of water and nutrients to two coastal systems with contrasting hydrogeological settings: (1) Maro-Cerro Gordo (coastal karst system) and (2) Mobile Bay (sandy coastal aquifer in an estuary of the northern Gulf of Mexico). The dissertation consists of five chapters, an introduction chapter (Chapter 1), three manuscripts intended to be peer-reviewed journal articles (Chapter 2, Chapter 3, and Chapter 4), and an overall conclusion chapter (Chapter 5).

Chapter 2, entitled “*Assessing submarine groundwater discharge (SGD) and nitrate fluxes in highly heterogeneous coastal karst aquifers: challenges and solutions*”, coauthored by Natasha Dimova, Bartolomé Andreo, Jorge Prieto, Jordi García-Orellana, and Valentí Rodellas, was published in *Journal of Hydrology*. This chapter focuses on the evaluation of the total groundwater discharge from a coastal karst aquifer to the Maro-Cerro Gordo coastal area and the associated nitrate fluxes. This study was carried out between 2015 and 2016. Coastal groundwater discharge in this area occurs in four forms: submarine springs, subaerial coastal springs, diffuse groundwater seepage, and groundwater-fed creeks. A multi-method approach was applied to assess each form of discharge using radiotracers (^{222}Rn and ^{224}Ra) and salinity mass balances, seepage meter, and flowmeter measurements. The feasibility of each method for quantifying each form of groundwater discharge were compared, and recommendations for further applications in other karst systems worldwide were given.

Chapter 3, entitled “*Constraining the importance of submarine groundwater discharge (SGD) in hydrogeologically complex estuaries: example of Mobile Bay, Alabama*”, co-authored by Natasha Dimova, Alexander Lamore, and Jackson Stewart, is currently under review in *Estuaries and Coasts*. This study presents a detailed evaluation of the spatial and temporal

variation of SGD and its contribution to the water budget of Mobile Bay during three consecutive years (2015-2017). Special emphasis was given to areas along the east shore of Mobile Bay affected by *Jubilees* and HAB events. A combination of radiotracer techniques (^{226}Ra , ^{224}Ra , ^{223}Ra , and ^{222}Rn), stable isotopes ($\delta^{18}\text{O}$ and $\delta^2\text{H}$), and seepage meters deployments was utilized to assess SGD. Additionally, a shallow aquifer hydrogeological characterization was performed using land-based (Electrical Resistivity Tomography, ERT) and marine (Continuous Resistivity Profiling, CRP) shallow geophysical surveys, and multiple sediment cores collection.

Chapter 4, entitled “*Are groundwater-derived nutrient inputs important for the Jubilee events in Mobile Bay, Alabama?*” is coauthored by Alex Lamore, Jackson Stewart, Yuehan Lu, Dini Adyasari, Joe Lambert, and Natasha Dimova. This is the first study that attempts to complete the nutrient (NO_3^- , NH_4^+ , DON and PO_4^{3-}) budgets of Mobile Bay and evaluate the significance of the SGD-derived nutrient fluxes compared to river-derived nutrient discharge to Mobile Bay. Furthermore, the main sources of nutrients and their biogeochemical transformations in the transition of groundwater through the coastal aquifer to the bay, were evaluated using a mass balance model, nitrate stable isotopes ($\delta^{15}\text{N}$ and $\delta^{18}\text{O}$), sediment organic matter stable isotopes ($\delta^{13}\text{C}$ and $\delta^{15}\text{N}$), and dissolved organic matter (DOM) composition analyses. To evaluate the ecological implications of the SGD-derived nutrient fluxes in Mobile Bay, the locations impacted by *Jubilees* and HABs were specifically examined during this investigation.

In Chapter 5, the conclusions from each chapter are summarized, specifically focusing on the main differences in magnitude and driving forces between the two studied coastal systems, the karst system of Maro-Cerro Gordo in Spain and the estuarine system of Mobile Bay, Alabama.

References

- Andreo, B. and F. Carrasco. 1993. Estudio hidrogeológico del entorno de la Cueva de Nerja. *Geología de la Cueva Nerja* 3: 163-187.
- Bakalowicz, M. 2005. Karst groundwater: a challenge for new resources. *Hydrogeology Journal* 13: 148-160.
- Barberá, J. A. and B. Andreo. 2015. Hydrogeological processes in a fluviokarstic area inferred from the analysis of natural hydrogeochemical tracers. The case study of eastern Serranía de Ronda (S Spain). *Journal of Hydrology* 523: 500-514.
- Burnett, W. C. and H. Dulaiova. 2003. Estimating the dynamics of groundwater input into the coastal zone via continuous radon-222 measurements. *Journal of Environmental Radioactivity* 69: 21-35
- Burnett, W. C., H. Bokuniewicz, M. Huettel, W. S. Moore and M. Taniguchi. 2003. Groundwater and pore water inputs to the coastal zone. *Biogeochemistry* 66: 3-33.
- Burnett, W. C., P. K. Aggarwal, A. Aureli, H. Bokuniewicz, J. E. Cable, M. A. Charette, E. Kontar, S. Krupa, K.M. Kulkarni, A. Loveless and W. S. Moore. 2006. Quantifying submarine groundwater discharge in the coastal zone via multiple methods. *Science of the Total Environment* 367: 498-543.
- Butscher, C. and P. Huggenberger. 2007. Implications for karst hydrology from 3D geological modeling using the aquifer base gradient approach. *Journal of hydrology* 342: 184-198.
- Charette, M. A., R. Splivallo, C. Herbold, M. S. Bollinger and W. S. Moore. 2003. Salt marsh submarine groundwater discharge as traced by radium isotopes. *Marine Chemistry* 84: 113-121.
- Custodio, E. 2010. Coastal aquifers of Europe: an overview. *Hydrogeology Journal* 18: 269-280.
- Dimova, N. T., W. C. Burnett and K. Speer. 2011. A natural tracer investigation of the hydrological regime of Spring Creek Springs, the largest submarine spring system in Florida. *Continental Shelf Research* 31: 731-738.
- Dyer, K. R. 1973. *Estuaries: A Physical Introduction*. John Wiley & Sons: London. 140 pp.
- Garcés, E., G. Basterretxea and A. Tovar-Sánchez. 2011. Changes in microbial communities in response to submarine groundwater input. *Marine Ecology Progress Series* 438: 47-58.
- Hwang, D. W., G. Kim, Y. W. Lee and H. S. Yang. 2005. Estimating submarine inputs of groundwater and nutrients to a coastal bay using radium isotopes. *Marine Chemistry* 96: 61-71.

- Johannes, R. E. 1980. The ecological significance of the submarine discharge of groundwater. *Marine Ecology Progress Series* 365-373.
- Johnson, A. G., C. R. Glenn, W. C. Burnett, R. N. Peterson and P. G. Lucey. 2008. Aerial infrared imaging reveals large nutrient-rich groundwater inputs to the ocean. *Geophysical Research Letters* 35: 1-6.
- Knee, K. L., J. H. Street, E. E. Grossman, A. B. Boehm and A. Paytan. 2010. Nutrient inputs to the coastal ocean from submarine groundwater discharge in a groundwater-dominated system: relation to land use (Kona coast, Hawai'i, USA). *Limnology and Oceanography* 55: 1105-1122.
- Kohout F. A. 1966. Submarine springs: A neglected phenomenon of coastal hydrology. *Hydrology* 26: 391-413.
- Krantz, D. E., F. T. Manheim, J. F. Bratton and D. J. Phelan. 2004. Hydrogeologic setting and ground water flow beneath a section of Indian River Bay, Delaware. *Groundwater* 42: 1035-1051.
- Lee, D. R. 1977. A device for measuring seepage flux in lakes and estuaries. *Limnology and Oceanography* 22: 140-147.
- Liefer, J. D., H. L. MacIntyre, L. Novoveska, W. L. Smith and C. P. Dorsey. 2009. Temporal and spatial variability in Pseudo-nitzschia spp. in Alabama coastal waters: a hot spot linked to submarine groundwater discharge? *Harmful algae* 8: 706-714.
- Loesch, H. 1960. Sporadic mass shoreward migrations of demersal fish and crustaceans in Mobile Bay, Alabama. *Ecology* 41: 292-298.
- Macintyre, H. L., A. L. Stutes, W. L. Smith, C. P. Dorsey, A. Abraham and R. W. Dickey. 2011. Environmental correlates of community composition and toxicity during a bloom of Pseudo-nitzschia spp. in the northern Gulf of Mexico. *Journal of Plankton Research* 33: 273-295.
- Martínez-Santos P. and J. M. Andreu. 2010. Lumped and distributed approaches to model natural recharge in semiarid karst aquifers. *Journal of Hydrology* 388: 389-398.
- May, E. B. 1973. Extensive oxygen depletion in Mobile Bay, Alabama. *Limnology and Oceanography* 18: 353-366.
- McCoy, C., R. Viso, R. N. Peterson, S. Libes, B. Lewis, J. Ledoux, G. Voulgaris, E. Smith and D. Sanger. 2011. Radon as an indicator of limited cross-shelf mixing of submarine groundwater discharge along an open ocean beach in the South Atlantic Bight during observed hypoxia. *Continental Shelf Research* 31: 1306-1317.

- Michael, H. A., K. C. Scott, M. Koneshloo, X. Yu, M. R. Khan and K. Li. 2016. Geologic influence on groundwater salinity drives large seawater circulation through the continental shelf. *Geophysical Research Letters* 43.
- Moore, W. S. 1996. Large groundwater inputs to coastal waters revealed by ^{226}Ra enrichments. *Nature* 380: 612-614.
- Moore, W. S. 1999. The subterranean estuary: a reaction zone of ground water and sea water. *Marine Chemistry*, 65: 111-125.
- Moore, W. S. 2010. The effect of submarine groundwater discharge on the ocean. *Annual Review of Marine Science* 2: 59-88.
- Null, K. A., N. T. Dimova, K. L. Knee, B. K. Esser, P. W. Swarzenski, M. J. Singleton, M. Stacey and A. Paytan. 2012. Submarine groundwater discharge-derived nutrient loads to San Francisco Bay: implications to future ecosystem changes. *Estuaries and Coasts* 35: 1299-1315.
- Pinault, J. L., N. Dörfliker, B. Ladouche and M. Bakalowicz. 2004. Characterizing a coastal karst aquifer using an inverse modeling approach: The saline springs of Thau, southern France. *Water Resources Research* 40: 1-17.
- Rapaglia, J., C. Grant, H. Bokuniewicz, T. Pick and J. Scholten. 2015. A GIS typology to locate sites of submarine groundwater discharge. *Journal of Environmental Radioactivity* 145: 10-18.
- Rodellas, V., J. García-Orellana, A. Tovar-Sánchez, G. Basterretxea, J. M. López-García, D. Sánchez-Quiles, E. García-Solsona and P. Masqué. 2014. Submarine groundwater discharge as a source of nutrients and trace metals in a Mediterranean bay (Palma Beach, Balearic Islands). *Marine Chemistry* 160: 56-66.
- Russoniello, C. J., C. Fernandez, J. F. Bratton, J. F. Banaszak, D. E. Krantz, A. S. Andres, L. F. Konikow and H. A. Michael. 2013. Geologic effects on groundwater salinity and discharge into an estuary. *Journal of Hydrology* 498: 1-12.
- Santos, I. R. S., W. C. Burnett, J. Chanton, B. Mwashote, I. G. Suryaputra and T. Dittmar. 2008. Nutrient biogeochemistry in a Gulf of Mexico subterranean estuary and groundwater-derived fluxes to the coastal ocean. *Limnology and Oceanography* 53: 705-718.
- Santos, I. R., B. D. Eyre and M. Huettel. 2012. The driving forces of porewater and groundwater flow in permeable coastal sediments: A review. *Estuarine, Coastal and Shelf Science* 98: 1-15.
- Slomp, C. P. and P. Van Cappellen (2004). Nutrient inputs to the coastal ocean through submarine groundwater discharge: controls and potential impact. *Journal of Hydrology* 295: 64-86.

- Smith, C. G. and P. W. Swarzenski. 2012. An investigation of submarine groundwater—borne nutrient fluxes to the west Florida shelf and recurrent harmful algal blooms. *Limnology and oceanography* 57: 471-485.
- Stalker, J. C., R. M. Price and P. K. Swart. 2009. Determining spatial and temporal inputs of freshwater, including submarine groundwater discharge, to a subtropical estuary using geochemical tracers, Biscayne Bay, South Florida. *Estuaries and Coasts* 32: 694-708.
- Stringfield, V. T. and H. E. LeGrand. 1971. Effects of karst features on circulation of water in carbonate rocks in coastal areas. *Journal of Hydrology* 14: 139-157.
- Tovar-Sánchez, A., G. Basterretxea, V. Rodellas, D. Sánchez-Quiles, J. García-Orellana, P. Masqué and E. García-Solsona. 2014. Contribution of groundwater discharge to the coastal dissolved nutrients and trace metal concentrations in Majorca Island: karstic vs detrital systems. *Environmental Science Technology* 48: 11819-11827.
- Trezzi, G., J. García-Orellana, V. Rodellas, J. Santos-Echeandia, A. Tovar-Sánchez, E. García-Solsona and P. Masqué. 2016. Submarine groundwater discharge: A significant source of dissolved trace metals to the North Western Mediterranean Sea. *Marine Chemistry* 186: 90-100.
- Trezzi, G., J. García-Orellana, V. Rodellas, P. Masqué, E. García-Solsona and P. S. Andersson, 2017. Assessing the role of submarine groundwater discharge as a source of Sr to the Mediterranean Sea. *Geochimica et Cosmochimica Acta* 200: 42-54.
- Uddameri, V., S. Singaraju and E. A. Hernandez. 2014. Temporal variability of freshwater and pore water recirculation components of submarine groundwater discharges at Baffin Bay, Texas. *Environmental Earth Sciences* 71: 2517-2533.
- Valiela, I., J. Costa, K. Foreman, J. M. Teal, B. Howes and D. Aubrey. 1990. Transport of groundwater-borne nutrients from watersheds and their effects on coastal waters. *Biogeochemistry* 10: 177-197.
- Weinstein, Y., Y. Yechieli, Y. Shalem, W. C. Burnett, P. W. Swarzenski and B. Herut. 2011. What is the role of fresh groundwater and recirculated seawater in conveying nutrients to the coastal ocean? *Environmental Science Technology* 45: 5195-5200.
- Worthington, S. R. H. 1999. A comprehensive strategy for understanding flow in carbonate aquifers. In *Karst Modeling* Palmer A. N., Palmer M. V., Sasowsky I. D., eds. 30-37. Karst Waters Institute.
- Xu, B., W. Burnett, N. Dimova, S. Diao, T. Mi, X. Jiang and Z. Yu. 2013. Hydrodynamics in the Yellow River Estuary via radium isotopes: Ecological perspectives. *Continental Shelf Research* 66: 19-28.

Young, C., J. Tamborski and H. Bokuniewicz. 2015. Embayment scale assessment of submarine groundwater discharge nutrient loading and associated land use. *Estuarine, Coastal and Shelf Science* 158: 20-30.

CHAPTER 2:

ASSESSING SUBMARINE GROUNDWATER DISCHARGE (SGD) AND NITRATE FLUXES IN HIGHLY HETEROGENEOUS COASTAL KARST AQUIFERS: CHALLENGES AND SOLUTIONS

2.1 Abstract

Groundwater discharge in coastal karst aquifers worldwide represents a substantial part of the water budget and is a main pathway for nutrient transport to the sea. Groundwater discharge to the sea manifests under different forms, making its assessment very challenging particularly in highly heterogeneous coastal systems karst systems. In this study, I present a methodology approach to identify and quantify four forms of groundwater discharge in a mixed lithology system in southern Spain (Maro-Cerro Gordo) that includes an ecologically protected coastal area comprised of karstic marble. I found that groundwater discharge to the sea occurs via: (1) groundwater-fed creeks, (2) coastal springs, (3) diffuse groundwater seepage through seabed sediments, and (4) submarine springs. I used a multi-method approach combining tracer techniques (salinity, ^{224}Ra , and ^{222}Rn) and direct measurements (seepage meters and flowmeters) to evaluate the discharge. Groundwater discharge via submarine springs was the most difficult to assess due to their depth (up to 15 m) and extensive development of the springs conduits. I determined that the total groundwater discharge over the 16 km of shoreline of the study area was at least $11 \pm 3 \times 10^3 \text{ m}^3 \text{ d}^{-1}$ for the four types of discharge assessed. Groundwater-derived nitrate (NO_3^-) fluxes to coastal waters over ~3km (or 20%) in a highly populated and farmed section of Maro-Cerro Gordo was $641 \pm 166 \text{ mol d}^{-1}$, or ~75% of the total NO_3^- loading in the study area. I demonstrate in this study that a multi-method approach must be applied to assess all

forms of SGD and derived nutrient fluxes to the sea in highly heterogeneous karst aquifer.

2.2 Introduction

Coastal karst aquifers are 46% of the Mediterranean coastline, and play a key role in regional socioeconomic, providing residents with essential water resources (Fleury et al., 2007; Bakalowicz, 2015; Arfib and Charlier, 2016; Trezzi et al., 2017). Groundwater is often the only available source as Mediterranean precipitation is scarce and sporadic, and often limited runoff due to efficient infiltration and percolation through the karst aquifers (McCormack et al., 2014).

Typically, karstified carbonate aquifers are comprised of a complex set of fractures, conduits, and cavities generating high spatial and temporal heterogeneity in groundwater flow (Worthington, 1999; Bakalowicz et al., 2005; Barberá and Andreu, 2015). This in turn results in challenging water resources management and attempts to develop water budgets and numerical models describing karst systems often fail or result in estimates with large uncertainties (Butscher and Huggenberger, 2007; Martínez -Santos and Andreu, 2010; Rapaglia et al., 2015).

When a karst system is hydraulically connected to the sea, a significant part of groundwater can flow directly to the sea in different forms (Stringfield and Legrand, 1971; Pinault et al., 2004; Custodio, 2010). Groundwater discharge to the sea can occur via submarine springs (Fleury et al., 2007; Bakalowicz et al., 2008; Dimova et al., 2011) or subaerial coastal springs near the shoreline (Aunay et al., 2003; Mejías et al., 2008; García-Solsona et al., 2010) depending on the geologic structure (Bonacci and Roje-Bonacci, 1997; Benac et al., 2003; Stamatis et al., 2011). Conduits and fractures buried under seabed sediments near the shoreline can also produce diffuse groundwater seepage (e.g. Tovar-Sánchez et al., 2014; Rodellas et al., 2012). Conversely, impervious strata can create enough hydraulic pressure for inland springs whose runoff flows to the sea as groundwater-fed creeks without experiencing infiltration (e.g.

Yobbi, 1992; Katz et al., 2009). In this work, I will use the widely accepted term submarine groundwater discharge (SGD) for the submerged forms of groundwater discharge to the sea as defined by Burnett et al. (2003) and Moore (2010).

Groundwater discharge of unconsolidated sedimentary coastal aquifers has been considered an insignificant component in water and nutrient budgets, mostly due to its relatively small (<10%) volumetric contribution compared to surface water (Burnett and Dulaiova, 2003; Moore 2010). However, in karst systems with limited runoff, SGD is a major component of the coastal aquifer water and nutrient budget. Where excess of nutrients are delivered in coastal systems, these produce ecological perturbations such as harmful algae blooms (e.g. Hallegraeff, 1993; Smith and Swarzenski, 2012), and seagrass habitat modification (e.g. Valiela et al., 1992) to mention a few.

Coastal karst SGD can have very different composition due to the wide range of groundwater residence time and complex pathways of the discharging waters (Weinstein et al., 2011; Tovar-Sánchez et al., 2014; Trezzi et al., 2016). It is therefore necessary to apply a multi-method approach to adequately identify and assess all forms of groundwater discharge when they coexist.

A number of techniques have been developed to identify and estimate groundwater discharge to coastal areas under different climatic conditions and geologic settings. For instance, naturally occurring radon and radium isotopes are effective groundwater tracers of SGD (e.g. Cable et al., 1996; García-Solsona et al., 2010; Rodellas et al., 2015; Dimova et al., 2015) as they are chemically conservative and are typically a few orders of magnitude higher concentrations in groundwater than surface waters, allowing for easy detection in receiving coastal waters (Burnett et al., 2003). Furthermore, mass balance determination of radium and radon excess in near-shore

surface quantifies the magnitude of groundwater fluxes (Cable et al., 1996; Wong et al., 2013; Tovar-Sánchez et al., 2014). Specifically, ^{222}Rn ($t_{1/2} = 3.8$ d) and ^{224}Ra ($t_{1/2} = 3.6$ d) which have relatively short half-lives, and in the time-scale range of typical coastal mixing processes can be used in combination to assess SGD (Moore, 1996; Cable et al., 1996; Burnett and Dulaiova, 2003).

Alternatively, in areas of faster groundwater flow regimes (e.g. karst and volcanic systems), salinity (e.g. Knee et al., 2010; Stieglitz et al., 2010; García -Solsona et al., 2010; Dimova et al., 2011) and thermal anomalies along the shoreline at the points of discharge are proven to be good indicators of SGD (e.g. Pluhowski, 1972; Johnson et al., 2008; Peterson et al., 2009; Mejías et al., 2012; Tamborski et al., 2015). In areas where permeable sediments are present, direct measurements of SGD using seepage meters are used in parallel with radiotracer techniques (Lee, 1977; Burnett et al., 2006; Sadat-Noori et al., 2015).

The mixed lithology Maro-Cerro Gordo coastal area is an example where identifying and quantifying all components of groundwater discharge are critical to building a comprehensive water budget that addresses adequately the existing economic and ecological demands of the adjacent coastal communities and ecosystems. Land use includes intensive agriculture with 1.3 km² of greenhouses and additional surface tropical crops, in combination with accelerating tourism in the area during the past decades. These land uses are increasingly satisfied by groundwater extractions, in this case from the Sierra Almirajara-Alberquillas Aquifer (Andreo and Carrasco, 1993), a highly fissured and karstified marble formation within the study site.

In order to assess the severity and impact of the increasing groundwater abstractions, water managers require a comprehensive water budget for the area. The current water budget based on a mass balance approach indicates total fresh water of $50 \times 10^6 \text{ m}^3 \text{ y}^{-1}$ for the Sierra

Almijara-Alberquillas Aquifer (Castillo et al., 2001). This budget was suggested to be comprised of: (1) inland springs and intermittent creeks ($32 \times 10^6 \text{ m}^3 \text{ y}^{-1}$), (2) extraction for irrigation and consumption purposes ($12 \times 10^6 \text{ m}^3 \text{ y}^{-1}$), (3) water transfer to the Neogene-Quaternary coastal formations, and the remaining part to (4) groundwater discharge to the sea ($6 \times 10^6 \text{ m}^3 \text{ y}^{-1}$). A more recent water mass balance budget using the APLIS (A = altitude, P = slope, L = lithology, I = infiltration landforms, S = soil type) method (Andreo et al., 2008) included an infiltration coefficient of 40 - 45% and confirmed that the total budget of the Sierra Almijara-Alberquillas Aquifer is $50 \times 10^6 \text{ m}^3 \text{ y}^{-1}$ for 2003 – 2005, which were notably dry years (Pérez-Ramos and Andreo, 2007). This assessment based on 2003-2005 data found a slightly higher natural drainage through springs ($38 \times 10^6 \text{ m}^3 \text{ y}^{-1}$) and extraction ($15 \times 10^6 \text{ m}^3 \text{ y}^{-1}$) compared to the estimate by Castillo et al. (2001), suggesting that groundwater discharge is negligible. However, more recently SGD was found to be significant at $1 \times 10^6 \text{ m}^3 \text{ y}^{-1}$ in Maro-Cerro Gordo using a combination of GIS-based approach, hydrometeorological methods, and preliminary ^{224}Ra evaluations (Andreo et al., 2017).

In this study, I performed a comprehensive assessment of the total groundwater discharge to the sea in the Maro-Cerro Gordo area through the application of a set of methods selective to each form of discharge. I used a combination of radiotracers (^{222}Rn and ^{224}Ra) and salinity mass balances, seepage meter measurements, and flowmeter measurements to: (1) identify point discharges to the sea; and (2) quantify the total groundwater discharge from the Sierra Almijara-Alberquillas Aquifer to adjacent coastal waters. I further (3) estimated groundwater-derived nitrate (NO_3^-) fluxes to the coastal waters of Maro-Cerro Gordo and compared these NO_3^- fluxes in an ecologically protected area (with low anthropogenic activities) to unprotected zones (with intense agriculture and overpopulation). The sampling campaigns were conducted during base

flow conditions to provide a conservative estimate of the total groundwater discharge to the sea and nitrate fluxes of the Sierra Almirajara-Alberquillas Aquifer and Maro-Cerro Gordo coastal area. Finally, (4) I compared the applicability of each method to assess the forms of groundwater discharge and made recommendations for applying this approach to other karst aquifer systems worldwide.

2.3 Study site and hydrogeological settings

The study site, Maro-Cerro Gordo, is located along the coastal fringe between Nerja and La Herradura in the easternmost section of the Malaga Province and part of the western Granada Province (southern Spain) along 16 km of shoreline (Fig. 2.1). Approximately 80% of the study area is within the environmentally protected Maro-Cerro Gordo Natural Area, which comprises 3.58 km² and 14.31 km² of terrestrial and marine surface respectively. The area is characterized by a typical Mediterranean climate with average annual precipitation of 500 mm y⁻¹ occurring almost entirely during fall and winter (Andreo and Carrasco, 1993). I have divided the area in three sections based on their predominant lithology and associated forms of discharge. From east to west these are: (1) karst section, which includes the Cerro Gordo cape from Cañuelo Beach to La Herradura; (2) schist section, confined between El Cañuelo Beach and Maro Beach; and (3) conglomerate section, which comprises the area between Maro Beach and Nerja (city) (Fig. 2.1).

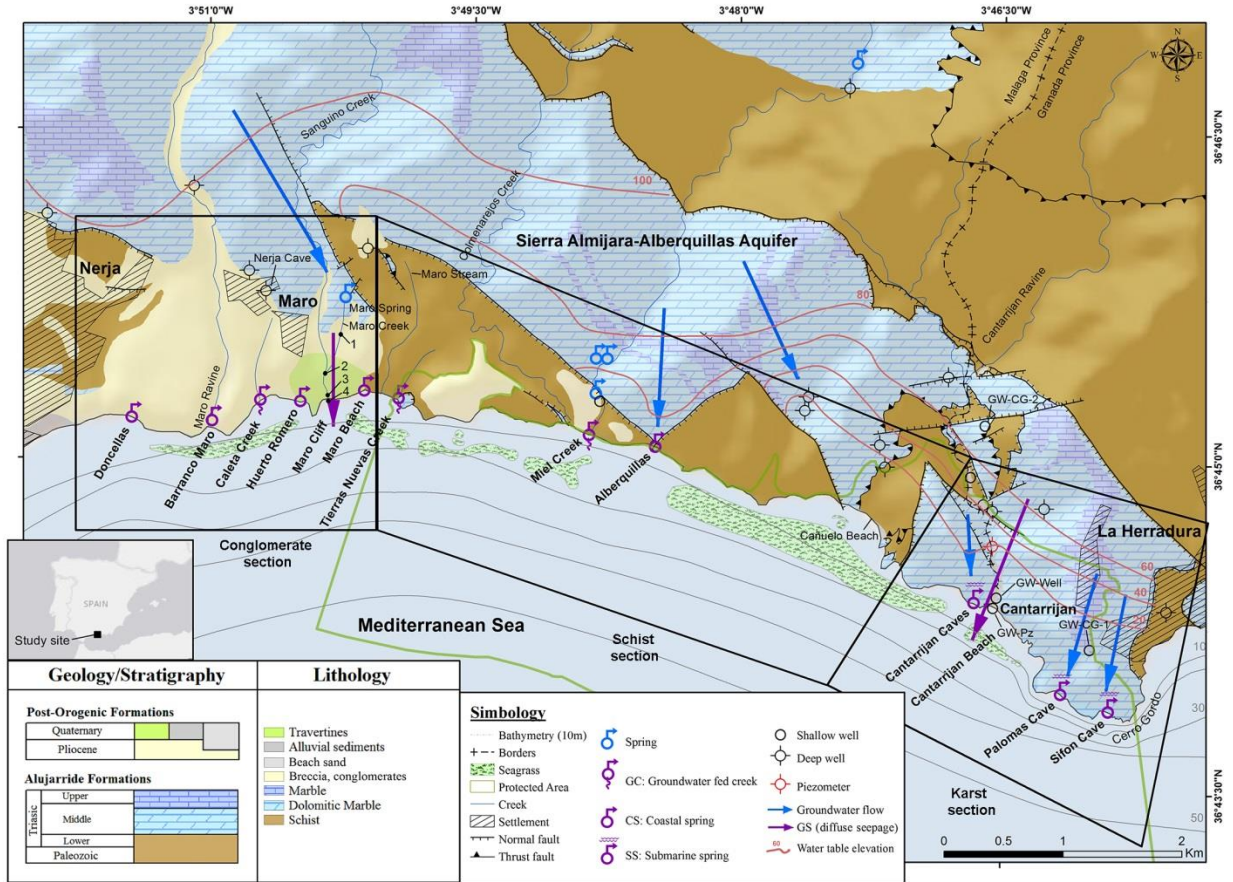


Figure 2.1. Study site location and geological map showing water table contour lines (from Pérez-Ramos and Andreo, 2007), groundwater flow direction, important wells and piezometers, sampling points, and terrestrial springs. Groundwater discharge to the sea (TGD) is represented in purple and is based on this study. Coastal springs are represented as CS, groundwater-fed creeks as GC, diffuse groundwater seepage as GS, and submarine springs as SS. The study area is divided in three sections: conglomerate section, schist section, and karst section. The distribution of seagrass beds are based on Bañares-España et al. (2002), and Aranda and Otero (2014).

2.3.1 Alberquillas Aquifer Unit

The main aquifer formation in the study area is the Alberquillas Aquifer Unit, a telogenetic karst formation that underlines the southeast sector of the Sierra Almijara Aquifer unit and is comprised of highly fissured and karstified Triassic marble (Andreo and Carrasco, 1993). The lithology varies from dolomitic to calcitic marble over the 600 m maximum thickness from basement to the surface (Andreo et al., 1993). In general, the primary porosity of

this unit is negligible and the degree of karstification is locally higher in the lower portion, with the exception of Nerja Cave, which is a $3 \times 10^5 \text{ m}^3$ cavity located 158 m above sea level and 930 m from the shoreline (Durán, 1996; Andreo et al., 1993; Jordá et al., 2011).

The Alberquillas Aquifer Unit exhibits an elongated shape towards the southeast and a total surface of 60 km^2 , and is directly in contact with the Mediterranean Sea only along the karst section (Fig. 2.1). The two aquifer units (Alberquillas and Almirajara Aquifer units) are hydraulically connected, constituting the Sierra Almirajara-Alberquillas Aquifer (142 km^2), which recharges from local precipitation (Carrasco et al., 1998). Conceptual hydrogeological models developed for the Sierra Almirajara-Alberquillas Aquifer suggest that groundwater generally flows from north to south, and SGD occurs mainly in eastern Cerro Gordo (Andreo and Carrasco 1993; Carrasco et al., 1998; Pérez-Ramos and Andreo, 2007).

The first attempt to locate SGD in Maro-Cerro Gordo was performed by Espejo et al. (1988) via airborne infrared thermal remote sensing. Two thermal anomalies were detected during this survey, one in the Maro area (conglomerate section), and one in the vicinity of Cerro Gordo and Cantarrijan (karst section); these were also confirmed by lower surface seawater salinity (Espejo et al., 1988).

A cluster of three submarine caves with active springs (Cantarrijan Caves) were identified at water depths of about 7 m near the Cantarrijan Beach (Fig. 2.1) during SCUBA diving explorations in the karst section during this study. The vents of these springs are located at the same depth and only 2 – 3 m away from each other. Thus, in my assessments the flux of these three springs was treated as a single discharge point. I identified the vents of two additional submarine springs at water depths of 12 m (Palomas Cave) and 15 m (Sifon Cave) in anchialine caves with up to 10 m of horizontal development (Fig. 2.1). These caves, together with the three

small Cantarrijan Cave springs, represent the deep SGD of Sierra Almirajara-Alberquillas Aquifer in the karst section. From SCUBA diving observations, I found that all three discharge points are related to highly-developed karstic conduits at depth. I found during this study that they were active even during droughts (Fig. 2.2), showing base flow conditions of Sierra Almirajara-Alberquillas Aquifer water budget drainage.

2.3.2 Schist formation

Alberquillas Aquifer Unit is overlaying a concordant Paleozoic schist formation along most of its extension and is tectonically in contact through a set of faults (Andreo et al., 1993). Metamorphosed during the Alpine Orogeny it presents a maximum thickness of 500 m and very low hydraulic conductivity (Andreo et al., 1993). Outcrops of the schist formation can be found almost along the entire schist section (Fig. 2.1). The schist formation serves as a hydrogeological barrier for SGD in this area (Andreo and Carrasco, 1993), and groundwater discharge to the sea in this section manifests as four small-size creeks and one coastal spring. The four creeks include: Tierras Nuevas Creek which emanates from a soil layer on the schist formation; the Colmenarejos Creek which was dry over the sampling campaigns; Miel Creek which is of particular interest as it is solely fed by permanently discharging springs located along the Sierra Almirajara-Alberquillas Aquifer in the sea (Andreo and Carrasco, 1993). The Maro Stream was observed to be produced by irrigation excess from abundant agriculture located nearby.

Lastly, the Alberquillas coastal spring, located 20 m from the shore at the Alberquillas Beach at the contact between the highly permeable Alberquillas Aquifer Unit karstic marble and impermeable schist, was found to have a perennial flow regime.

2.3.3 Conglomerate, breccia, and travertine formations

Pliocene conglomerate and breccia deposits with a maximum thickness of 60 m, form ~ 90% of the conglomerate section of the study area, representing the second most important permeable formation in the study site (Fourniguet, 1975; Andreo et al., 1993; Guerra-Merchán and Serrano, 1993). This formation is comprised of marble fragments cemented by a red matrix, showing signs of dissolution in the upper portion due to its calcite composition. Its hydraulic conductivity permits limited groundwater flow mainly due to primary porosity and the slight presence of fractures (Andreo and Carrasco, 1993). In the coastline comprised of this formation, groundwater discharge can be identified visually as two coastal springs, the Doncellas and Barranco Maro Spring and the groundwater-fed creek (Caleta Creek) which originates from a spring located near the town of Maro (Fig. 2.1). On the easternmost sector of the conglomerate section, south from the town of Maro, a 30 m thick highly porous and permeable quaternary travertine is present in direct contact with the sea at Maro Cliff to the south (Jordá, 1988). The two small coastal springs of Huerto Romero and Maro Beach are present in this formation along with the intermittent groundwater-fed creek of Maro Creek. I have observed that excess water from the Maro Spring located approximately 1 km to the north of Maro Cliff, flows as Maro Creek and discharges to the sea from the travertine cliff as a waterfall that is intermittently active depending on irrigation times. The Maro Spring is well-known and it was included in the Sierra Almirajara-Alberquillas Aquifer water budget, and it is utilized for drinking and irrigation purposes (Liñán et al., 2000). The Sanguino Creek remained dry throughout this study.

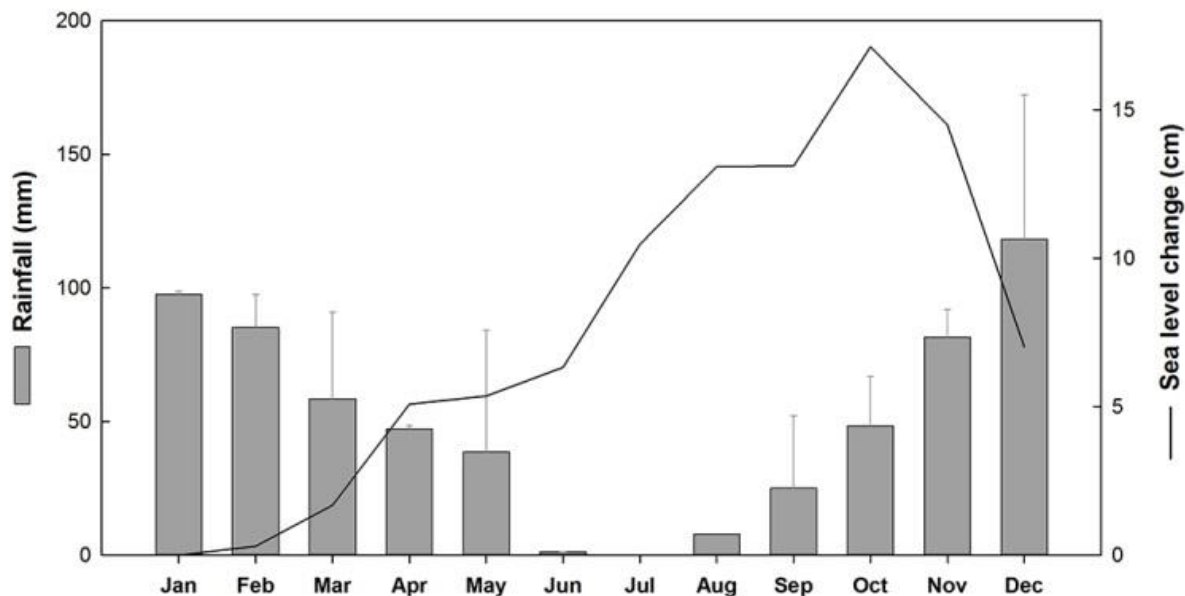


Figure 2.2. Average monthly precipitation and sea level change during 2010, 2015, and 2016. Error bars show the monthly rainfall variability during this study. In December of 2015 slight precipitation occurred only during the first week, however, abundant rainfall took place during September-November. Sea level showed lower values during January-May and higher during August-December. Sampling campaigns were conducted during May-July (dry periods) and December (wet periods).

2.4 Methods

Water fluxes to the sea from karstic submarine springs were quantified using (1) ^{224}Ra and (2) salinity mass balances, groundwater seepage was quantified using both (3) a ^{222}Rn box model mass balance and (4) seepage meter deployments in the locations where radon anomalies were observed. Subaerial groundwater discharge from coastal springs and groundwater-fed creeks was measured directly using a flowmeter (5).

2.4.1 Tracer techniques

2.4.1.1 ^{224}Ra distribution and submarine springs discharge assessment

A total of 38 discrete ^{224}Ra samples of 60 L each were collected in September of 2006 and 2010 to survey the schist and karst sections (Fig. 2.1). All seawater samples were collected at a depth of 0.3 m, with the exception of SW-7 and SW-21 that were collected at the submarine

springs at 8 m and 15 m respectively. Seawater (n = 30) and groundwater (n = 8) samples were obtained using a submersible pump, and were later passed through a PVC column filled with about 25 g of MnO₂-coated-fibers (Mn-fibers) at a flow rate of approximately 1 L min⁻¹ to allow for a quantitative absorption of ²²⁴Ra (Moore, 1976; 2008). Mn-fibers were then transferred to the lab, rinsed with Ra-free water, and partially dried (Sun and Torgersen, 1998). Activities of ²²⁴Ra were measured using a Radium Delayed Coincidence Counter (RaDeCC) system (Moore and Arnold, 1996; García-Solsona et al., 2008). The Mn-fibers were counted twice, with the first time immediately after collection to assess the total ²²⁴Ra in the water, and a second time after a month to evaluate the supported ²²⁴Ra in equilibrium with ²²⁸Th. The excess of ²²⁴Ra was used to construct a ²²⁴Ra mass balance following Charette et al. (2001), which assumes that the ²²⁴Ra excess in coastal waters is the result of groundwater inputs (Eq. 2.1). This approach was applied to assess water fluxes (F_{SGD} , m³ d⁻¹) originated from the three submarine springs present in the karst section of the study site (Fig 2.1):

$$F_{SGD} = \frac{(Ra_{sw} - Ra_{ow}) \times V + Ra_{sw} \times V \times \lambda}{Ra_{SGD}} \quad (2.1)$$

where Ra_{sw} is the ²²⁴Ra activity in coastal waters, i.e. the surface water end-member (dpm m⁻³); Ra_{ow} is the offshore ²²⁴Ra activity in open waters (dpm m⁻³); Ra_{SGD} is the activity of the groundwater end-member (dpm m⁻³); t is the coastal water residence time (d); V is the volume (m³) of coastal water affected by each submarine spring (SGD plume; and λ is the ²²⁴Ra decay constant (0.1894 d⁻¹).

Because this area is greatly exposed to prevailing west winds, large waves, and intensive mixing, I assumed that the residence time (t) of the water in this high energy coastline must be no more than one day. Thus, I used the one-day value in the mass balance model. The volume affected by SGD (V) was constrained using the surface area of the salinity anomaly created by

the spring plume and corresponding water depths, obtained from the Andalusia Council of Environment bathymetry database: <http://www.juntadeandalucia.es/medioambiente/site/rediam>. To obtain the ^{224}Ra activity (Ra_{sw}) surface water end-member representative of the whole water column, average values of water samples collected from the surface and at the depth of the spring discharge were used.

2.4.1.2 Salinity anomalies and submarine spring discharge evaluation

To identify and quantify submarine springs discharge following the 1-meter isobath parallel to the shoreline, three salinity boat surveys were performed in May, July, and December of 2015 along the entire stretch of the studied coastline. Electrical conductivity (EC) and temperature (T , °C) were measured continuously at a constant depth of 0.3 m with accuracies of $\pm 20 \mu\text{S cm}^{-1}$ and $\pm 0.1^\circ\text{C}$ by towing a conductivity-temperature-depth sensor (CTD, Solinst[®]) from boat at a speed of about 2 km h^{-1} . Seawater salinity values were obtained from EC using the conversion method 2520B (Standard Methods for the Examination of Water and Wastewater, APHA, 1999). Data were recorded in 2 min intervals concurrently with precise GPS boat positioning recorded in 30-sec intervals (Garmin Etrex[®] 20x) with an accuracy of $\pm 3 \text{ m}$. Electrical conductivity and temperature of groundwater samples were measured using a Pro2030 (YSI Inc.) handheld instrument with accuracies of $\pm 1 \mu\text{S cm}^{-1}$, and $\pm 0.3^\circ\text{C}$. Before sampling, the CTD sensor and handheld instrument (YSI) were calibrated using two conductivity solutions (Oakton[®]): $1413 \mu\text{S cm}^{-1}$ and $12,880 \mu\text{S cm}^{-1}$, measured at 25°C . Temperature correction for EC was automatically performed using linear compensations of $2\% \text{ }^\circ\text{C}^{-1}$ and $1.91\% \text{ }^\circ\text{C}^{-1}$ for the CTD sensor and the handheld instrument respectively.

To compare data points from all surveys and identify consistent spatial salinity variations (i.e. permanent groundwater fluxes) independent of seasonal fluctuations, salinity values from

each survey were normalized based on their total average. Salinity anomalies were defined as positive when salinity is higher than average and negative when it is lower than the average value.

A salinity mass balance based on the salinity anomalies generated by submarine springs inputs was constructed to determine groundwater fluxes (F_{SGD} , $m^3 d^{-1}$) in the karst section using Eq. 2.1 and following Crusius et al. (2005) and Knee et al. (2010). To calculate the fresh water fraction of the spring discharge, I used the approach described in Knee et al. (2010), which indirectly defines the groundwater salinity end-member (Sal_{SGD}) to be zero (Eq. 2.2):

$$F_{SGD} = \frac{(Sal_{ow} - Sal_{sw}) \times V}{t \cdot Sal_{ow}} \quad (2.2)$$

where, Sal_{ow} and Sal_{sw} represent salinity values of open water and coastal surface waters. As in Eq. 2.1, V is the volume of coastal water affected by SGD (m^3); and t is the coastal water residence time (d). I used the same end-member values as in the ^{224}Ra mass balance. Note that this mass balance assumes a groundwater salinity end-member (Sal_{SGD}) of zero in order to quantify only the fresh component of SGD (Knee et al., 2010).

2.4.1.3 ^{222}Rn surveys and groundwater seepage assessment

Seawater ^{222}Rn concentrations were measured in surface coastal waters (at about 0.3 m depth) in July, December of 2015, and July of 2016 along all sections using a RAD AQUA set up (Durrige Co., Inc.) as described in Dulaiova et al. (2005) and further improved by Dimova et al. (2009). To obtain radon-in-water concentrations, the measured radon-in-air was corrected using the temperature-dependent Ostwald's solubility coefficient (Macintyre et al., 1995) (Eq. 2.3):

$$\alpha = 0.105 + 0.405e^{(-0.05027 \times T)} \quad (2.3)$$

where T ($^{\circ}\text{C}$) is the water temperature, measured in 2 min intervals using a temperature data logger (HOBO[®], Onset[®] Inc.). Analytical uncertainties of ^{222}Rn in water were most of the time lower to 10%. The RAD AQUA system was run stationary for at least 20 min at the beginning of all surveys to achieve water/air and radioactive equilibrium (Dimova et al., 2009), and set up to measure in 10 min intervals while moving at boat speed of 2 km h^{-1} to allow for detection of rapid ^{222}Rn changes. These data were coupled with GPS coordinates to be mapped later.

Diffuse groundwater seepage was quantified using a ^{222}Rn mass balance (box model) as described in Burnett and Dulaiova (2003) during July of 2015 and 2016, and December of 2016. To evaluate diffuse groundwater seepage using a ^{222}Rn mass balance (Eq. 2.4), ^{222}Rn time-series (1 - 2 days long) were conducted in the Maro Cliff and Cantarrijan Beach seepage area. For this study, this mass balance was modified to account for radon inputs to the sea from a small groundwater-fed waterfall (Maro Creek) (Fig. 2.1). Radon fluxes (F_{GW}) ($\text{dpm m}^{-2} \text{ h}^{-1}$) from groundwater discharge were determined using mass balance equation where total ^{222}Rn inputs to the water column are balanced by radon:

$$F_{\text{GW}} = F_{\text{Atm}} + F_{\text{Mix}} - F_{\text{Waterfall}} - C_{\text{Ra}} - F_{\text{Diff}} \quad (2.4)$$

where F_{Atm} is the ^{222}Rn atmospheric evasion fluxes through the water/air interphase; F_{Mix} are mixing losses due to tidal variations and horizontal mixing; $F_{\text{waterfall}}$ are fluxes of ^{222}Rn into the system from a groundwater-fed waterfall present in Maro Cliff; C_{Ra} is the production of ^{222}Rn from ^{226}Ra decay within the water column; and F_{Diff} is ^{222}Rn diffusion flux from seabed sediments.

To assess the contribution of ^{222}Rn from Maro Creek the radon flux from the creek ($F_{\text{waterfall}}$) was calculated by multiplying the average creek radon concentration by the water flux which was based of flowmeter measurements and specific area of discharge. This correction was

only done during Creek flow regime. Corrections for the production of ^{222}Rn from dissolved ^{226}Ra (i.e. supported radon) in coastal waters (C_{Ra}) were done utilizing the Mn-fiber collected in September of 2006 (one sample) and in July of 2016 (two samples) in Maro Cliff and Cantarrijan Beach at the time series stations. The average concentration (September 2006 and July 2016) was applied in the ^{222}Rn mass balance. The procedure follows the technique described in details in (Charette et al., 2001). The ^{226}Ra equilibrated samples were counted via gamma spectrometry (HPGe well detector, Canberra GCW3522) using the ^{214}Pb peak at 352 keV. Atmospheric evasion of ^{222}Rn (F_{Atm}) was calculated based on the water/air interphase ^{222}Rn concentration gradient (dpm m^{-3}), ^{222}Rn Ostwald solubility coefficient, and ^{222}Rn gas transfer velocity (k , m h^{-1}). The gas transfer velocity (m h^{-1}) was calculated using Eq. 2.5 as described in Macintyre et al. (1995):

$$k(600) = 0.45 \times u_{10}^{1.6} \left(\frac{Sc}{600} \right)^{-b} \quad (2.5)$$

where u_{10} is wind velocity at 10 m above sea level (m s^{-1}) acquired from an internet web service (<http://www.wunderground.com/>), Sc is the Schmidt number, and b is a factor that ranges from $\frac{1}{2}$ ($u_{10} < 3.6 \text{ m s}^{-1}$) to $\frac{2}{3}$ ($u_{10} > 3.6 \text{ m s}^{-1}$).

During high wind conditions (July of 2015), I used Eq. 2.6 (all terms are defined in Eq. 2.5) designed in Kremer et al. (2003) for shallow waters and a wide range of wind speeds (Cockenpot et al., 2015):

$$k(600) = 1.65 \times e^{(u_{10})} \left(\frac{Sc}{600} \right)^{-b} \quad (2.6)$$

Molecular diffusion flux of ^{222}Rn from seabed sediments (F_{Diff}) was determined using the approach described in Martens et al. (1980).

After all corrections were made, negative fluxes were considered mixing losses (F_{Mix}). The pore water ^{222}Rn concentration and porosity of sediments were determined based on the

procedure reported in Corbett et al. (1998). Groundwater seepage velocity (SGD , cm d^{-1}) was then calculated (Eq. 2.7) by dividing SGD-derived ^{222}Rn fluxes by the representative groundwater ^{222}Rn concentration end-member (Rn_{SGD} , dpm m^{-3}) (Burnett and Dulaiova, 2003).

The groundwater end-member (Rn_{SGD}) was assessed in groundwater collected from a small cavity in the travertine cliff located 1 m a.s.l. in Maro Cliff, and GW-Well in Cantarrijan Beach (Fig. 2.1). Groundwater ^{222}Rn concentrations were analyzed with a RAD7 using a RAD H₂O set up in duplicate 250 mL samples.

$$SGD = \frac{F_{GW}}{Rn_{SGD}} \quad (2.7)$$

In order to calculate groundwater fluxes (F_{SGD} , $\text{m}^3 \text{d}^{-1}$), the obtained seepage velocities were multiplied by the total area through which SGD occurs using Eq. 2.8:

$$F_{SGD} = SGD \times A \quad (2.8)$$

where SGD represents seepage velocity (cm d^{-1}), and A is the seepage area (m^2). To constrain the seepage area (A) at the beach face, I conducted a high-resolution ^{222}Rn survey by manually moving a small boat at a speed of 15 m h^{-1} . For more precise results, during this survey, the RAD AQUA system was let to equilibrate for 20 min every 2 - 10 m of shoreline. The high-resolution ^{222}Rn survey data was mapped using a linear ordinary kriging interpolation method (ArcGIS 10), each concentration interval was then contoured (using the ArcGIS 10 contour spatial analyst) to obtain ^{222}Rn concentration isolines. The seepage area (A) was delineated by creating a polygon that followed the $35 \times 10^3 \text{ dpm m}^{-3}$ isoline as a threshold in Maro Cliff and $6 \times 10^3 \text{ dpm m}^{-3}$ in Cantarrijan Beach. The seepage area (m^2) was obtained by calculating the polygon geometry based on the ETRS 1989 UTM Zone 30N projected coordinate system.

2.4.1.4 Fresh SGD assessment in diffuse seepage

As defined by Taniguchi et al. (2002), diffuse groundwater seepage is comprised of two components: (1) a fresh (meteoric) groundwater component and (2) a recirculated seawater component. To calculate the fresh water component in seepage areas of the study site (e.g. in Cantarrijan Beach), I applied a salinity mixing model (Eqs. 2.9 and 2.10) as described in Taniguchi et al., (2005) and used by many others (e.g. Charette et al., 2007; Taniguchi et al., 2008; Santos et al., 2009). The approach relies on two basic equations:

$$f_{\text{FSGD}} + f_{\text{RSGD}} = 1 \quad (2.9)$$

$$\text{Sal}_{\text{FSGD}} \times f_{\text{FSGD}} + \text{Sal}_{\text{RSGD}} \times f_{\text{RSGD}} = \text{Sal}_{\text{SGD}} \times f_{\text{SGD}} \quad (2.10)$$

where f_{FSGD} and f_{RSGD} represent the fresh and recirculated fractions of SGD, and Sal_{FSGD} and Sal_{RSGD} are the salinity values measured in fresh groundwater (GW-Well) and maximum recirculated salinity (GW-Pz-4).

2.4.2 Direct groundwater flow measurements

2.4.2.1 Flowmeter measurements of coastal springs and creeks

The location of coastal springs and inland springs feeding groundwater-fed creeks were identified via field observations. The discharge from the identified coastal springs (Doncellas, Barranco Maro, Huerto Romero, Maro Beach, and Alberquillas) and groundwater-fed creeks (Caleta Creek, Tierras Nuevas Creek, and Miel Creek) entering the sea, were measured using a flowmeter (OTT C2, OTT Hydromet GmbH) with an accuracy of $\pm 10\%$. Channel widths were between 10 cm and 140 cm and depths were below 30 cm in all springs and creeks. Flow velocity measurements at the average water depths were recorded in 10 cm intervals across the stream cross section right before discharge into the sea. Water fluxes were calculated for each interval multiplying width (10 cm) and depth by flow velocity. Total water flux ($\text{m}^3 \text{d}^{-1}$) was then

calculated by adding water fluxes in all intervals. To observe differences between dry and wet periods measurements were conducted during July and December of 2016.

2.4.2.2 Seepage meter measurements of diffuse seepage

To verify ^{222}Rn -based SGD estimates, I deployed multiple seepage meters in July of 2016. Lee-type seepage meters, built following the procedure described in Lee (1977) were deployed near the ^{222}Rn time series station in areas of active groundwater seepage (Maro Cliff and Cantarrijan Beach) during July of 2016. Four seepage meters were deployed in Maro Cliff and nine in Cantarrijan Beach to obtain a representative evaluation of the seepage area. These were made of a bottomless 60 L plastic drum with an area of 0.12 m^2 with a plastic bag attached to a two-way valve (Isiorho and Meyer, 1999; Schincariol and McNeil, 2002; Rosenberry, 2008). The seepage meters were submerged and slowly inserted in the sediments leaving 2 cm of space between the sediments and the drum interior top. The seepage meter was positioned inclined in order to leave the valve side slightly higher allowing any gas to escape before plastic bag attachment; the water volume entering the plastic bag and time elapsed were then recorded (Lee, 1977). Seepage velocities (SGD , cm d^{-1}) were calculated using Eq. 2.11 modified from Lee (1977):

$$SGD = \frac{68.79 \times V}{t} \quad (2.11)$$

where V is volume of water entering the plastic bag (mL); t is the time elapsed (s), and 68.79 is a unit conversion factor specific to the 0.12 m^2 flow area to obtain seepage velocity in cm d^{-1} .

Groundwater discharge ($\text{m}^3 \text{ d}^{-1}$) was calculated using Eq. 2.8.

2.4.2.3 Groundwater chemistry, stable isotopic composition, and NO_3^- fluxes

During July and December of 2015, and in July of 2016 water stable isotopes ($\delta^2\text{H}$ and $\delta^{18}\text{O}$), NO_3^- and SO_4^{2-} were measured in all points of groundwater discharge to the sea, Maro

Spring, and a well located in the conglomerate section (Nerja Cave) (Fig. 2.1). A total of 23 samples were collected in Maro Cliff and Cantarrijan Beach (GW-Well) (n = 4), all subaerial coastal springs (Doncellas, Barranco Maro, Huerto Romero, Maro Beach, and Alberquillas, n = 14), and groundwater-fed creeks (Maro Creek and Miel Creek, n = 5) during all sampling campaigns.

Water samples were collected for analysis in 150 mL bottles and stored at 4°C until measurement, diluted to 1 mS cm⁻¹, and filtered before analysis. NO₃⁻ and SO₄²⁻ concentrations were analyzed at the CEHIUMA (Center of Hydrogeology of the University of Malaga) laboratory via ionic chromatography (Metrohm 881 Compact IC Pro) with an accuracy of ± 2%. Water stable isotopes (δ²H and δ¹⁸O) were also analyzed at the CEHIUMA using a Laser Cavity Ring-Down Spectrometer (Picarro CRDS L2120-i) with accuracies of ± 1‰ and ± 0.1‰ for δ²H and δ¹⁸O respectively. Isotopic ratios were calculated using the Vienna Standard Mean Ocean Water (VSMOW, in ‰). Nitrate fluxes ($F_{NO_3^-}$, mmol d⁻¹) to the sea were calculated by multiplying NO₃⁻ concentrations at each point of discharge during each sampling campaign by corresponding measured groundwater flux (Eq. 2.12):

$$F_{NO_3^-} = F_{SGD} \times [NO_3^-] \quad (2.12)$$

where $[NO_3^-]$ represents nitrate concentrations (mmol m⁻³), and F_{SGD} is the groundwater flux (m³ d⁻¹)

2.5 Results

2.5.1 Detecting submarine spring discharge using ²²⁴Ra and salinity

2.5.1.1 ²²⁴Ra activities in seawater and groundwater

During the ²²⁴Ra sampling campaign in September of 2010, the average ²²⁴Ra concentrations in surface waters along the study area was 17 ± 2 dpm m⁻³ (n=30) ranging from

56 ± 4 dpm m^{-3} to 8 ± 1 dpm m^{-3} (Fig. 2.3; Appendix I Table 1). In general, ^{224}Ra values along the schist and karst sections of the study area were lower compared to other Mediterranean regions (e.g. Moore, 2006; García-Solsona et al., 2010; Rodellas et al., 2014). However, two distinctive ^{224}Ra -high anomalies in coastal surface waters were identified during this survey; these were associated with water inputs with average salinity of 0.8 from the groundwater-fed Miel Creek (56 ± 4 dpm m^{-3}), and the three clustered submarine springs discharging from Cantarrijan Caves (51 ± 4 dpm m^{-3}) located in the Cantarrijan area (Fig. 2.3). Miel Creek (average salinity anomaly = 0.3), which flows through the marble formation of Alberquillas Aquifer Unit for a total length of approximately 5 km, has a perennial flow, a firm indication that it is fed by groundwater (Fig. 2.3). Indeed, a set of springs located predominantly in the southernmost section of the Creek at the marble-schist contact have been observed to maintain the constant creek flow regime all year long. The second peak of ^{224}Ra was located right above the three submarine springs (Cantarrijan Caves) near Cantarrijan Beach. Average ^{224}Ra values significantly higher (20 ± 7 dpm m^{-3}) than offshore background activity (8 ± 1 dpm m^{-3}) were detected also along the karst section from Cantarrijan to Cerro Gordo, where Alberquillas Aquifer Unit is directly in contact with the sea (Fig. 2.3).

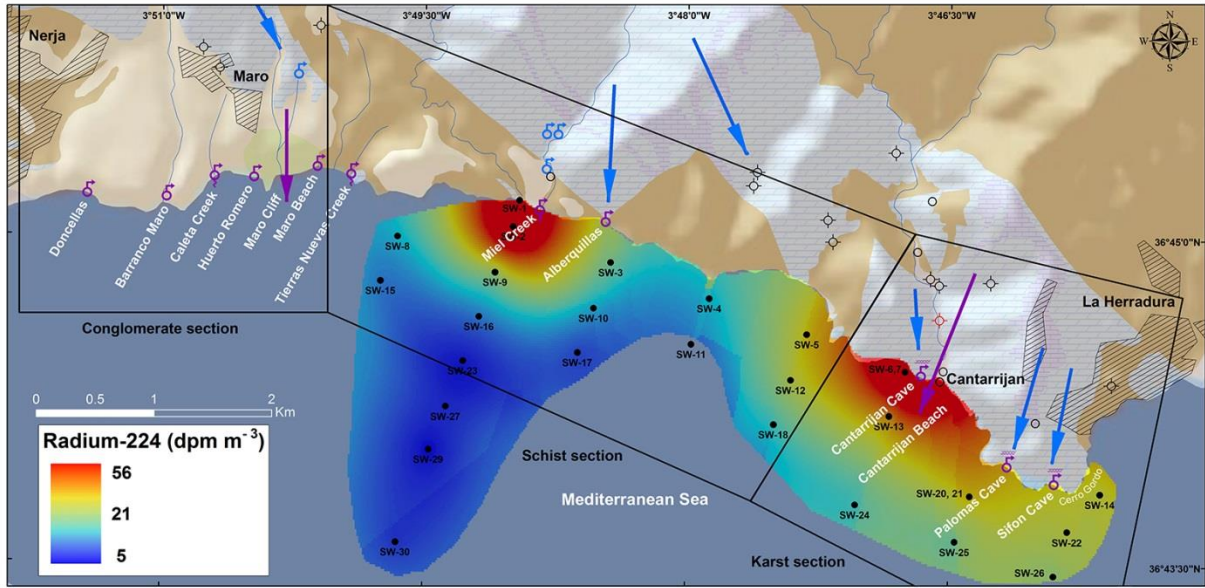


Figure 2.3. Interpolated ^{224}Ra activity concentrations in September of 2010 along the schist and karst sections. Two areas of high ^{224}Ra in coastal waters were identified in the schist section near groundwater-fed Miel Creek ($56 \pm 4 \text{ dpm m}^{-3}$), and the three clustered submarine springs discharging from Cantarrijan Caves ($51 \pm 4 \text{ dpm m}^{-3}$) located in the Cantarrijan area (karst section).

Radium-224 in groundwater in Cantarrijan Beach varied from $660 \pm 30 \text{ dpm m}^{-3}$ (salinity anomaly = 1.6) in a shallow well (GW-Well, Appendix I Table 1) to $5500 \pm 430 \text{ dpm m}^{-3}$ (salinity = 31.1) in five piezometers installed on the shore (GW-Pz-1-5, Appendix I Table 1). Activity of ^{224}Ra in groundwater collected from two wells in the karstic marble (GW-CG-1 and GW-CG-2, Appendix I Table 1) showed similar activities, $1260 \pm 90 \text{ dpm m}^{-3}$ and $1020 \pm 80 \text{ dpm m}^{-3}$ with salinities of 2.2 and 0.6 respectively. The variation of ^{224}Ra concentrations in GW-Well and Pz-1-5 can be explained by the seawater recirculation in the beach sediments. Radium concentration in fresh waters is very low due to adsorption onto particles. However, in pore water with higher ionic strength (i.e. brackish and salt water) radium desorbs due to cation exchange. This process increases dissolved ^{224}Ra concentration (Webster et al., 1995).

2.5.1.2 Salinity anomalies

The average salinity in coastal waters of the study site during continuous measurements in September of 2010 was 36.4 ± 0.2 , during May of 2015 was 36.6 ± 4.0 , in July 2015 was 37.2 ± 1.2 , and in December of 2015 was 34.5 ± 1.7 . A negative salinity anomaly of -1.2 to -1.7 was observed during all sampling campaigns in the conglomerate section in the vicinity of multiple coastal springs (Doncellas, Barranco Maro, Huerto Romero, and Maro Beach) and two groundwater-fed creeks (Caleta Creek, and Tierras Nuevas Creek) (Fig. 2.4). However, in the schist section where Alberquillas coastal spring enters the sea, salinity was generally similar to the average throughout the coastline with a value of 36.3 in September of 2010, 37.1 in May of 2015, 37.1 in July of 2015, and 34.4 in December of 2015. Similarly, small salinity variation (Fig. 2.4) associated with high ^{224}Ra (Fig. 2.3) was observed near the outlet of the groundwater-fed Miel Creek.

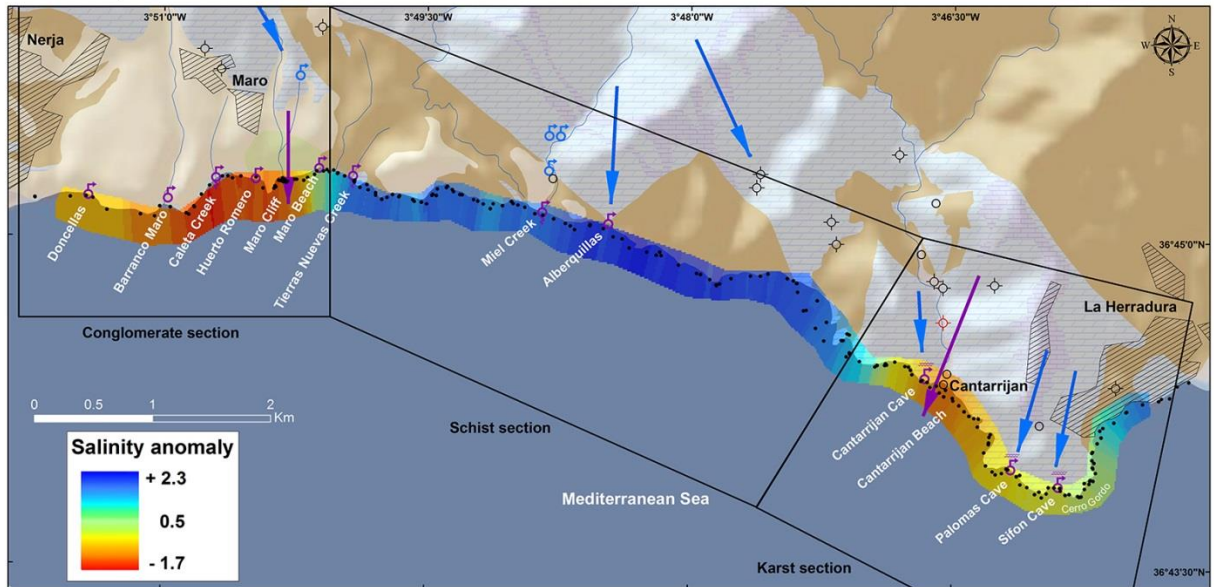


Figure 2.4. Salinity anomaly map showing combined results from May, July, and December of 2015. Two areas of negative salinity anomalies were found in the conglomerate (salinity anomaly = -1.2 to -1.7) and karst (salinity anomaly = -0.3 to -1.0) sections almost perfectly aligned with their delineated extent.

In the karst section (Fig. 2.1), where the karstic marble formation is in contact with the sea, negative salinity anomalies (-0.3 to -1.0) coincided with previously observed high ^{224}Ra concentrations in coastal waters near the Palomas and Sifon Caves submarine springs. The largest salinity anomaly (-1.0) in the karst section was found in Cantarrijan Beach, which could be related to Cantarrijan Caves springs. However, the lowest values are distributed along the beach area, slightly deviated to the East off Cantarrijan Caves, where groundwater seepage through marine sediments can, therefore, also be occurring.

2.5.2 Evaluating submarine spring discharge using ^{224}Ra and salinity

2.5.2.1 ^{224}Ra mass balance

To assess groundwater discharge in the areas of high ^{224}Ra (12 – 51 dpm m^{-3}) and negative salinity anomalies (-0.3 to -1.0), i.e. the areas of Cantarrijan Caves, Palomas Cave, and

Sifon Cave submarine springs (Figs. 2.2 and 2.3), I used a ^{224}Ra mass balance following Moore (1996) and Charette et al. (2001; Eq. 2.1). The main assumption in this approach is that the ^{224}Ra excess in the karst section is considered to be originated solely by submarine springs.

SGD through Cantarrijan Caves was quantified using the ^{224}Ra coastal water end-member measured in SW-6, SW-7, SW-13 and SW-24 ($Ra_{sw} = 25 \pm 2 \text{ dpm m}^{-3}$, $n = 4$), where SW-7 was collected at the depth of discharge (8 m). Average offshore background activity ($8 \pm 1 \text{ dpm m}^{-3}$) measured in SW-23, SW-27, SW-29, and SW-30 was used as the open water end-member (Ra_{ow}) (Appendix I Table 1). Groundwater samples collected from well GW-CG-1 (Fig.2.1), which is the closest well to the submarine springs and is representative of the marble aquifer formation, was used as the groundwater end-member ($1260 \pm 90 \text{ dpm m}^{-3}$, salinity = 2.2). Following the same approach, SGD was also evaluated in the area of Palomas Cave using SW- SW-20, SW-21, and SW-25 ($Ra_{sw} = 18 \pm 2 \text{ dpm m}^{-3}$, $n = 3$), where SW-21 was collected at 15 m depth of discharge. In Sifon Cave samples SW-14, SW-22, and SW-26 were used as the coastal water end-member. The same open water (Ra_{ow}) and groundwater (Ra_{SGD}) end-members were used: $1260 \pm 90 \text{ dpm m}^{-3}$ and $8 \pm 1 \text{ dpm m}^{-3}$ respectively (Fig. 2.3; Table 2.1).

The estimated groundwater fluxes (F_{SGD}) through Cantarrijan Caves was $4.7 \pm 0.5 \times 10^3 \text{ m}^3 \text{ d}^{-1}$, at Palomas cave was $4.3 \pm 0.5 \times 10^3 \text{ m}^3 \text{ d}^{-1}$, and for Sifon Cave was $3.7 \pm 0.4 \times 10^3 \text{ m}^3 \text{ d}^{-1}$. This represents a total flux of $12.8 \pm 1.4 \times 10^3 \text{ m}^3 \text{ d}^{-1}$ via submarine springs, where reported errors are based on analytical uncertainties of ^{224}Ra measurements.

	Radium (1) mass balance			Salinity mass balance (2)			V ($\times 10^5 \text{ m}^3$)	F _{SGD} (1) ($\times 10^3 \text{ m}^3 \text{ d}^{-1}$)	F _{SGD} (2)
	Ra _{sw}	Ra _{SGD} (dpm m ⁻³)	Ra _{ow}	Sal _{sw}	Sal _{SGD}	Sal _{ow}			
Cantarrijan	25 ± 2	1260 ± 90	8 ± 1	36.3 ± 0.1	0.0	36.5	2.67	4.7 ± 0.5	0.8 ± 0.1
Palomas	18 ± 2	1260 ± 90	8 ± 1	36.4 ± 0.1	0.0	36.5	4.04	4.3 ± 0.5	0.9 ± 0.1
Sifon	17 ± 2	1260 ± 90	8 ± 1	36.4 ± 0.1	0.0	36.5	3.72	3.7 ± 0.4	0.5 ± 0.1
Total flux								12.8 ± 1.4	2.3 ± 0.2

Table 2.1. Summary of values for all terms used to solve the radium and salinity mass balances to assess submarine springs discharge in the karst section. Calculated total flux (F_{SGD}) using both methods are also shown.

2.5.2.2 Salinity mass balance

The salinity anomaly created by the Cantarrijan, Palomas, and Sifon Caves in the karst section (Fig. 2.4, Table 2.1) allowed us to construct individual mass-balances at each location and calculate SGD independently of the ^{224}Ra approach. Considering that the salinity of groundwater discharge of these springs is the same value of the endmember used for the ^{224}Ra method (Table 2.1), and applying Eq. 2.2 I calculated a total groundwater flux of $0.8 \pm 0.1 \times 10^3 \text{ m}^3 \text{ d}^{-1}$ in Cantarrijan Caves, $0.9 \pm 0.1 \times 10^3 \text{ m}^3 \text{ d}^{-1}$ in Palomas Cave, and $0.5 \pm 0.1 \times 10^3 \text{ m}^3 \text{ d}^{-1}$ through Sifon Cave; representing a total of $2.3 \pm 0.2 \times 10^3 \text{ m}^3 \text{ d}^{-1}$.

2.5.3 Assessing diffuse groundwater seepage using a ^{222}Rn mass balance and seepage meter measurements

2.5.3.1 ^{222}Rn distribution in seawater

High ^{222}Rn concentrations were measured in two distinct areas in the Maro Cliff area (conglomerate section) and Cantarrijan Beach (karst section) with maximum concentrations of $44 \pm 3 \times 10^3 \text{ dpm m}^{-3}$ and $30 \pm 2 \times 10^3 \text{ dpm m}^{-3}$ respectively (Fig. 2.5). In general, along the conglomerate section, ^{222}Rn activities were within background levels ($1.9 \pm 0.6 \times 10^3 \text{ dpm m}^{-3}$) with the mentioned exception of a cove in the Maro Cliff area where the travertine formation is in contact with the sea. In this location, a 15-m travertine cliff ends in coarse seabed sand through which groundwater seepage was identified underlying a 1.5-m water column. In the karst section, high ^{222}Rn was detected only along the Cantarrijan Beach where a steep ravine, formed in the marble formation, ends in a big opening comprised of coarse sand, pebbles, cobbles, and even boulders suggesting flash flooding events in the ravine after significant precipitations.

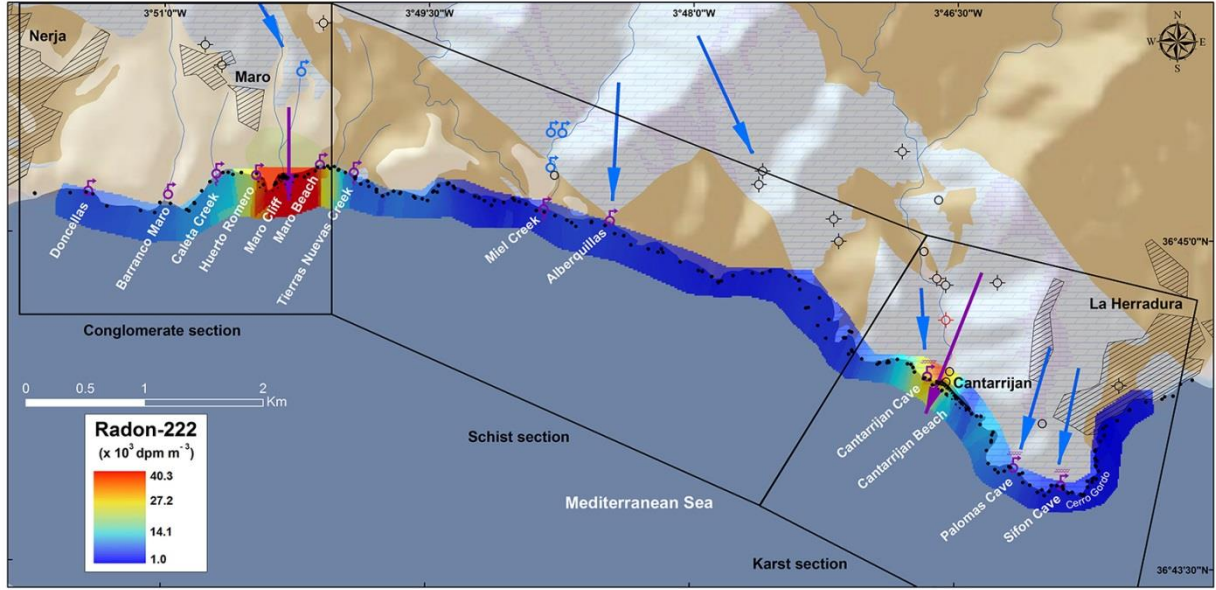


Figure 2.5. Radon-222 distribution map based on surveys during July and December of 2015, and July of 2016. Two radon peaks were found in Maro Cliff (conglomerate section) and Cantarrijan Beach (karst section) with maximum concentrations of $44 \pm 3 \times 10^3 \text{ dpm m}^{-3}$ and $30 \pm 2 \times 10^3 \text{ dpm m}^{-3}$ respectively.

2.5.3.2 Groundwater discharge assessments in the conglomerate section (Maro Cliff)

Diffuse groundwater seepage was identified in this area during all ^{222}Rn surveys (July and December of 2015, and July of 2016) suggesting the seepage is maintained by base groundwater flow (Fig. 2.6a). I calculated that ^{222}Rn contribution from the waterfall (i.e., $F_{\text{Waterfall}}$) was on average $16 \pm 6 \text{ dpm m}^{-2} \text{ d}^{-1}$ (Table 2.2). To account for the production of ^{222}Rn from ^{226}Ra dissolved in coastal waters (C_{Ra}), I used the averaged concentration ($280 \pm 50 \text{ dpm m}^{-3}$, $n = 3$) measured in September of 2006 ($306 \pm 40 \text{ dpm m}^{-3}$, $n = 1$) and July of 2016 ($260 \pm 50 \text{ dpm m}^{-3}$, $n = 2$) at the time series station (Table 2.2, Fig. 2.6b). Atmospheric evasion (F_{Atm}) was calculated using Eq 8 except in July of 2015, when wind speed was much higher (8 m s^{-1}) and I used Eq. 2.6 instead. Diffusive flux of ^{222}Rn from seabed sediments (F_{Diff}) was $619 \pm 57 \text{ dpm m}^{-2} \text{ d}^{-1}$ accounting for only 0.2 – 0.5% of total ^{222}Rn fluxes (Fig. 2.7). As one would expect in coastal

waters with little protection against wind and waves, mixing losses in this study represent the main ^{222}Rn loss in the model (Fig. 2.7).

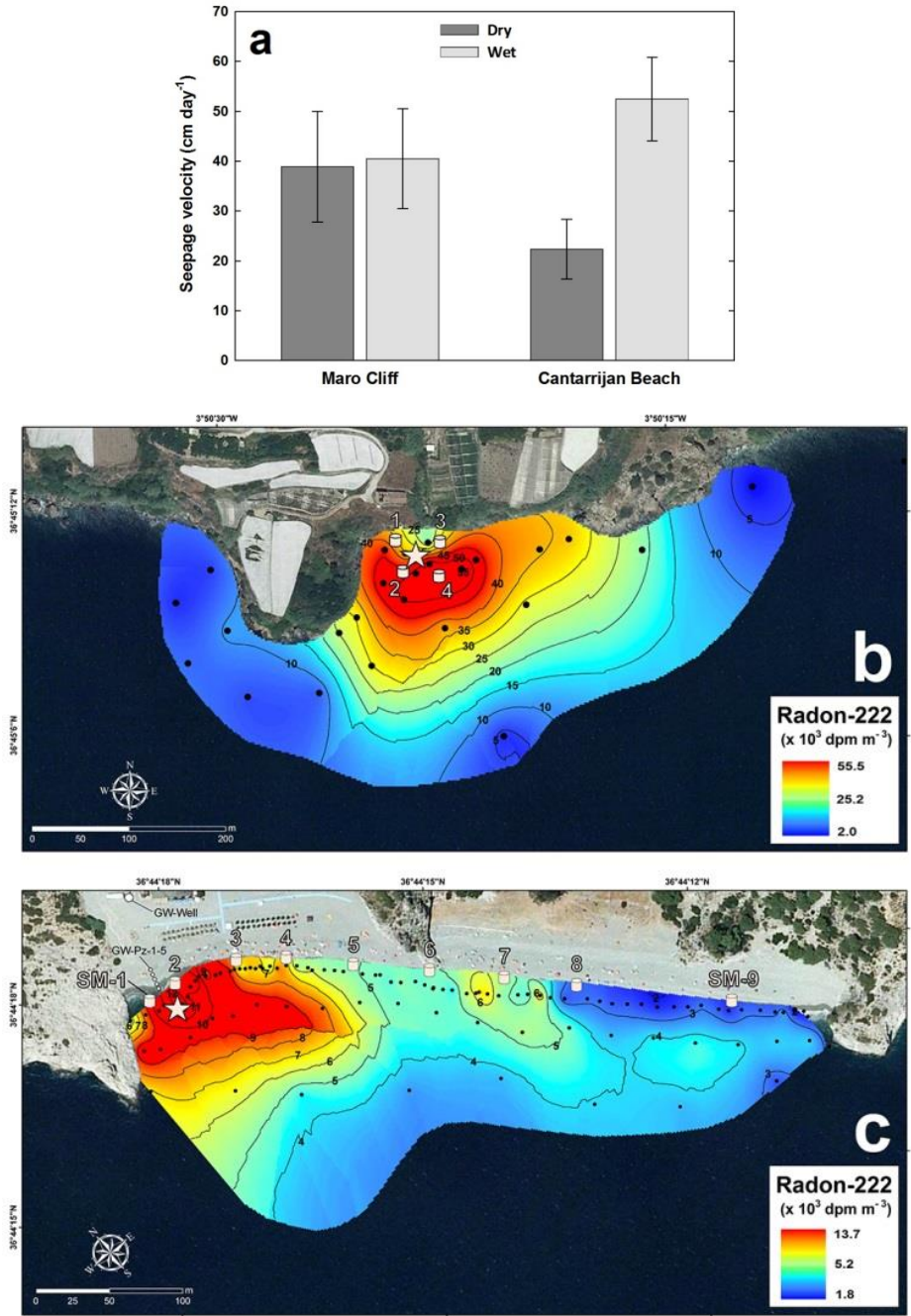


Figure 2.6. (a) Groundwater seepage velocity averaging results from radon mass balance and seepage meters in areas of diffuse seepage (Maro Cliff and Cantarrijan Beach). Radon distribution in (b) Maro Cliff (conglomerate section) and (c) Cantarrijan Beach (karst section) where cylinder symbols represent seepage meter locations and the star radon time series stations.

The ^{222}Rn concentrations in groundwater end-members (Rn_{SGD}) were $350 \pm 50 \times 10^3$ dpm m^{-3} , $440 \pm 60 \times 10^3$ dpm m^{-3} , and $320 \pm 30 \times 10^3$ dpm m^{-3} during July, December of 2015, and July of 2016 respectively, with an average value of $370 \pm 50 \times 10^3$ dpm m^{-3} . Based on these estimates (Table 2.2) and applying Eq. 2.4, I obtained average seepage velocities of 39 ± 10 cm d^{-1} ($n = 43$) in July 2015, 40 ± 11 cm d^{-1} ($n = 78$) in December of 2015, and 38 ± 10 cm d^{-1} ($n = 90$) during July of 2016. Reported SGD uncertainties are calculated based on ^{222}Rn variations from all samples collected in the area to obtain the groundwater end-members (Rn_{SGD}) (Burnett et al., 2007); which ranged from $320 \pm 30 \times 10^3$ dpm m^{-3} to $690 \pm 50 \times 10^3$ dpm m^{-3} ($n = 8$) during this study.

Utilizing Eq. 2.8 I estimated total groundwater fluxes based on the ^{222}Rn box model to be $3.0 \pm 0.8 \times 10^3$ m^3 d^{-1} during July of 2015, $3.1 \pm 0.8 \times 10^3$ m^3 d^{-1} in December of 2015, and $2.9 \pm 0.7 \times 10^3$ m^3 d^{-1} in July of 2016 (Table 2.2). Using Eq. 2.11 an average seepage velocity of 28 ± 6 cm d^{-1} (Table 2.3) was calculated. This assessment is in good agreement with the average ^{222}Rn -based value of 38 ± 10 cm d^{-1} . Using Eq. 2.8 and a seepage area of 7.7×10^3 m^2 based on the radon concentration (Fig. 2.6b), I calculated a groundwater flux of $2.1 \pm 0.4 \times 10^3$ m^3 d^{-1} in July of 2016 (Table 2.3).

		Rn_{SGD} ($\times 10^3$ dpm m^{-3})	$F_{Waterfall}$ ($\times 10^3$ dpm $m^{-2} d^{-1}$)	C_{Ra} (dpm m^{-3})	F_{Diff} (dpm $m^{-2} d^{-1}$)	F_{Mix} ($\times 10^3$ dpm $m^{-2} d^{-1}$)	F_{Atm}	Seepage Area ($\times 10^3$ m^2)	SGD ($cm d^{-1}$)	F_{SGD} ($\times 10^3$ $m^3 d^{-1}$)
Maro Cliff	Jul-15	350 ± 50	16 ± 6	280 ± 50	619 ± 57	149 ± 40	33 ± 9	7.7	39 ± 10	3.0 ± 0.8
	Dec-15	440 ± 60	21 ± 8	280 ± 50	619 ± 57	238 ± 64	11 ± 3	7.7	40 ± 11	3.1 ± 0.8
	Jul-16	320 ± 30	10 ± 5	280 ± 50	619 ± 57	160 ± 43	25 ± 7	7.7	38 ± 10	2.9 ± 0.7
Cantarrijan Beach	Jul-15	310 ± 70	N/A	170 ± 40	455 ± 51	-		4.3	-	-
	Dec-15	240 ± 60	N/A	170 ± 40	455 ± 51	84 ± 13	30 ± 5	4.3	52 ± 8	2.3 ± 0.3
	Jul-16	350 ± 40	N/A	170 ± 40	455 ± 51	115 ± 18	27 ± 4	4.3	22 ± 3	0.9 ± 0.1

Table 2.2. Parameters used in the radon mass balance to assess diffuse seepage in Maro Cliff (conglomerate section) and Cantarrijan Beach (karst section) including estimated groundwater fluxes (F_{SGD}).

2.5.3.3 Groundwater fluxes in the karst section (Cantarrijan Beach)

Multiple radon surveys in this area (July and December of 2015, and July of 2016) indicated a strong seasonality in seawater ^{222}Rn concentrations, with an average of $75 \pm 3 \times 10^3$ dpm m^{-3} in December and $11 \pm 2 \times 10^3$ dpm m^{-3} in July, suggesting higher SGD during the wet period. The average ^{226}Ra concentration (C_{Ra}) was 170 ± 40 dpm m^{-3} measured in September of 2006 (169 ± 30 dpm m^{-3} , $n = 1$) and July of 2016 (170 ± 40 dpm m^{-3} , $n = 2$) (Table 2.3). The variation of the groundwater ^{222}Rn end-member ($240 \pm 60 \times 10^3$ dpm m^{-3} to $350 \pm 40 \times 10^3$ dpm m^{-3} , $n = 6$) was used to calculate the final groundwater discharge flux uncertainties. Seepage velocities in December and July were on average 52 ± 8 cm d^{-1} ($n = 61$) and 22 ± 3 cm d^{-1} ($n = 115$) respectively (Table 2.3).

I found that groundwater seepage occurs only in the westernmost sector at the end of the Cantarrijan Ravine (Fig. 2.6c). Seepage velocities, determined from all seepage meters deployed along the beach, show that groundwater seepage ceases exactly at the location where seepage meter SM-4 was deployed (Fig. 2.6c). I used this as a criterion to define the seepage face and decided to use the ^{222}Rn contour line of $6 \pm 1 \times 10^3$ dpm m^{-3} to calculate the seepage area, and averaged SM-1-4 to determine a seepage velocity of 23 ± 7 cm d^{-1} . Using the ^{222}Rn method I found that the total diffuse groundwater seepage in the Cantarrijan Beach area ranged from $2.3 \pm 0.3 \times 10^3$ $\text{m}^3 \text{d}^{-1}$ during the wet period to $0.9 \pm 0.1 \times 10^3$ $\text{m}^3 \text{d}^{-1}$ during dry conditions; whereas seepage meter measurements resulted in $0.9 \pm 0.2 \times 10^3$ $\text{m}^3 \text{d}^{-1}$.

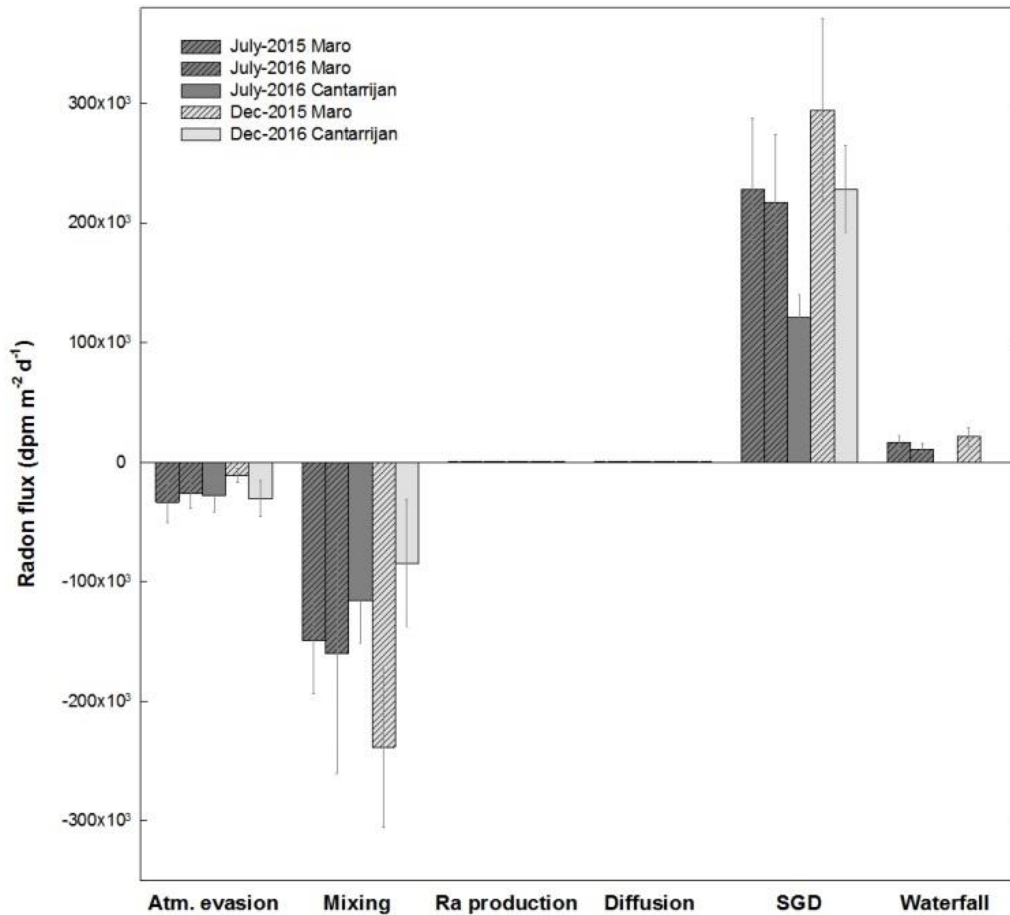


Figure 2.7. Radon fluxes result of each component of the mass balance box model during all sampling campaigns in Maro Cliff (conglomerate section) and Cantarrijan Beach (karst section). The largest tracer losses occurred via mixing due to the high exposure of both areas to waves and currents. Greater difference in SGD-²²²Rn fluxes was found between wet periods (December) and dry periods (July) in Cantarrijan Beach compared to Maro Cliff.

During all sampling campaigns, the groundwater sampled from the shallow well at Cantarrijan Beach (GW-Well, Fig.2.1) always had salinity values of 1.6 – 3.2. During September of 2010, salinities of 6.6 – 31.1 were also observed in pore water samples collected in all five piezometers installed on the beach (GW-PZ-1-5, Fig 2.1). Based on the salinity mixing model (using Eqs. 2.9 and 2.10) I calculated that the fresh fraction of SGD at this site was 48% of the total groundwater seepage. Therefore, when constructing the Sierra Almirajara-Alberquillas

Aquifer freshwater water budget for July of 2016, only $0.4 \pm 0.1 \times 10^3 \text{ m}^3 \text{ d}^{-1}$ (representative of the 48% freshwater component) should be taken into account.

	SGD seepage rate (cm d^{-1})	
	Maro Cliff	Cantarrijan Beach
Radon model	38 ± 10	22 ± 3
Seepage meters	28 ± 7	23 ± 7
SM-1	19	13
SM-2	32	32
SM-3	37	26
SM-4	25	20
SM-5		0
SM-6		1
SM-7		0
SM-8		0
SM-9		1

Table 2.3. Comparison of groundwater seepage velocities estimated via radon model and seepage meters during July of 2016 (dry period) in Maro Cliff (conglomerate section) and Cantarrijan Beach (karst section).

2.5.4 Groundwater contribution from coastal springs and groundwater-fed creeks

Groundwater discharge to the sea during dry conditions calculated using flowmeter measurements in July of 2016 from coastal spring Huerto Romero was $37 \pm 3 \text{ m}^3 \text{ d}^{-1}$, from Maro Beach was $26 \pm 2 \text{ m}^3 \text{ d}^{-1}$, from Barranco Maro was $17 \pm 1 \text{ m}^3 \text{ d}^{-1}$, from Doncellas was $460 \pm 40 \text{ m}^3 \text{ d}^{-1}$, and from Alberquillas was $1060 \pm 90 \text{ m}^3 \text{ d}^{-1}$ (Appendix I Table 2). The discharge from groundwater-fed creek Miel Creek was $1230 \pm 110 \text{ m}^3 \text{ d}^{-1}$, from Caleta Creek $160 \pm 10 \text{ m}^3 \text{ d}^{-1}$, and from Tierras Nuevas Creek was $110 \pm 10 \text{ m}^3 \text{ d}^{-1}$. The total discharge from all creeks was $3100 \pm 280 \text{ m}^3 \text{ d}^{-1}$; which represents 33% of the total groundwater discharge in the study area.

In December of 2016, during high flow conditions, discharge from coastal springs Huerto Romero was $100 \pm 9 \text{ m}^3 \text{ d}^{-1}$, from Maro Beach was $43 \pm 4 \text{ m}^3 \text{ d}^{-1}$, from Barranco Maro was $69 \pm 6 \text{ m}^3 \text{ d}^{-1}$, from Doncellas was $530 \pm 50 \text{ m}^3 \text{ d}^{-1}$, and from Alberquillas was $1590 \pm 140 \text{ m}^3 \text{ d}^{-1}$.

Discharge via groundwater-fed Miel Creek was $1820 \pm 160 \text{ m}^3 \text{ d}^{-1}$, from Caleta Creek was $220 \pm$

$20 \text{ m}^3 \text{ d}^{-1}$, and from Tierras Nuevas Creek was $190 \pm 20 \text{ m}^3 \text{ d}^{-1}$; which constitutes $4580 \pm 60 \text{ m}^3 \text{ d}^{-1}$ or 37% of the total discharge in the study area (Appendix I Table 2).

2.5.5 Groundwater isotopic composition, water chemistry, and nitrate fluxes

Isotopic values are widely scattered along a linear trend (Local Groundwater Line, LGL) with a slope of 6.06, with averages of -42‰ and -7.1‰ for $\delta^2\text{H}$ and $\delta^{18}\text{O}$ respectively (Figs. 2.8a and 2.8b). All samples fall between the Global Meteoric Water Line (GMWL; Craig, 1961) and the Western Mediterranean Meteoric Water Line (WMMWL; Gat and Garmi, 1970), samples collected in or derived from Maro Spring are situated slightly above the WMMWL. Deuterium values ranged from $-33 \pm 1\text{‰}$ to $-46 \pm 1\text{‰}$, while $\delta^{18}\text{O}$ were between $-5.6 \pm 0.1\text{‰}$ and $-7.8 \pm 0.1\text{‰}$ (Appendix I Table 2). I observed that groundwater collected from Maro Spring (conglomerate section) has the lightest isotopic signature of -46‰ and -7.7‰ for $\delta^2\text{H}$ and $\delta^{18}\text{O}$ respectively. Samples collected in the conglomerate section from coastal springs Barranco Maro, Huerto Romero, Maro Beach, and groundwater-fed Maro Creek showed values that ranged from -45 and -7.6 to -43‰ and -7.2‰ . At the point of seepage discharge in the sea, Maro Cliff showed slightly higher values of -44‰ and -7.4‰ for $\delta^2\text{H}$ and $\delta^{18}\text{O}$. Coastal springs Doncellas, Alberquillas, and groundwater-fed Miel Creek all located in the schist section, are grouped together with Nerja Cave (conglomerate section), showing average values of -33‰ and -5.5‰ for $\delta^2\text{H}$ and $\delta^{18}\text{O}$. Samples collected from GW-Well (Cantarrijan Beach), have the highest values in the study area with averages of -22‰ and -3.8‰ for $\delta^2\text{H}$ and $\delta^{18}\text{O}$.

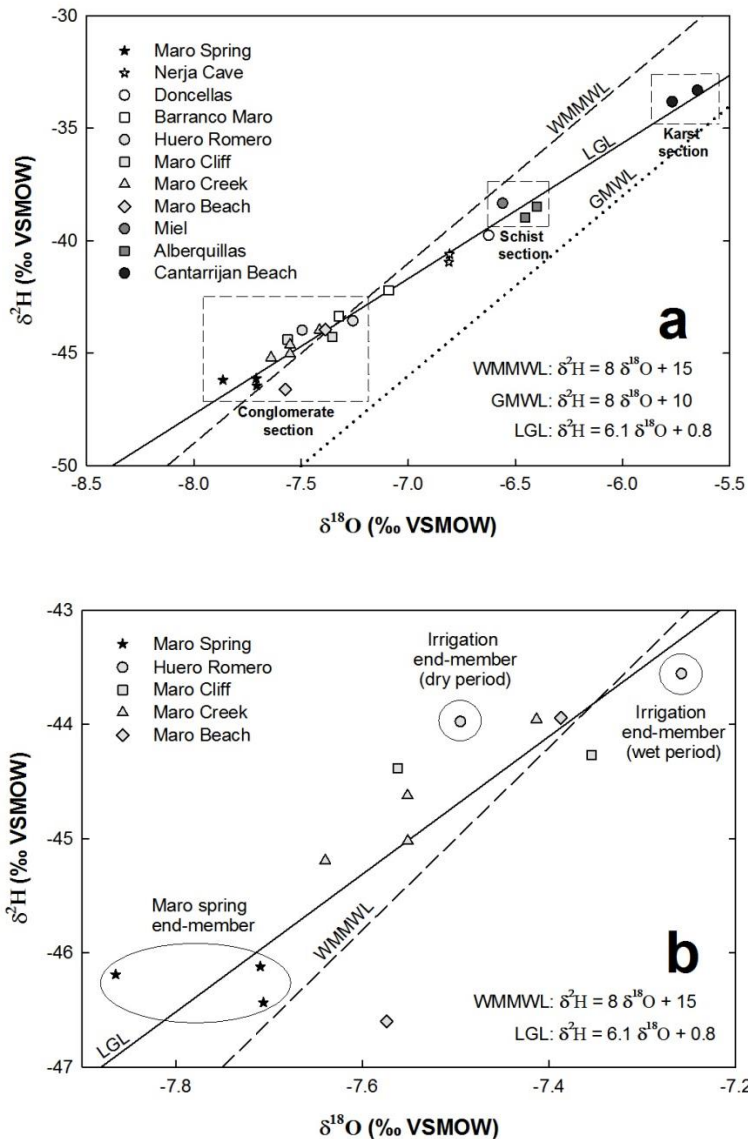


Figure 2.8. (a) Isotopic composition ($\delta^{18}\text{O}$, $\delta^2\text{H}$) of water samples collected during all sampling campaigns. Local Groundwater Line (LGL) represents the linear trend based on all groundwater samples collected in the study area. Global Meteoric Water Line (GMWL) is based on Craig, (1961) and the Western Mediterranean Meteoric Water Line (WMMWL) on Gat and Garmi, (1970). White color represents points of discharge in conglomerate and breccia lithology, while light grey are in travertine (conglomerate section); dark grey shows points in schist (schist section); and black color show locations in karstic marble (karst section). Maro Spring and Nerja Cave well (not points of discharge to the sea) are represented with a black and white star respectively. Water samples collected at each section (conglomerate section, schist section, and karst section) are grouped in dashed squares. (b) Isotopic composition of samples collected from points of discharge from the travertine formation in the conglomerate section. The two groundwater end-members (Maro Spring and irrigation waters) are circled, while diffuse seepage in Maro Cliff is represented with squares.

Groundwater sulphate (SO_4^{2-}) concentrations ranged from $500 \pm 10 \text{ mmol m}^{-3}$ in Alberquillas coastal spring to $3220 \pm 64 \text{ mmol m}^{-3}$ in Cantarrijan Beach ($n = 23$) (Appendix I Table 2). Samples collected in the conglomerate section from coastal springs Doncellas, Barranco Maro, Huerto Romero, Maro Beach; groundwater-fed Maro Creek, and diffuse seepage in Maro Cliff had similar SO_4^{2-} concentrations ranging between 1500 and 3000 mmol m^{-3} . All samples (including Maro Spring) collected from Sierra Almirajara-Alberquillas Aquifer in this area fall within a SO_4^{2-} concentration range of $1700 - 2600 \text{ mmol m}^{-3}$. Miel Creek and coastal spring Alberquillas (schist section) showed lower values ranging from 500 ± 10 to $710 \pm 14 \text{ mmol m}^{-3}$. Water collected in Cantarrijan Beach had the highest concentration in the study area, with an average of $3030 \pm 60 \text{ mmol m}^{-3}$ (Appendix I Table 2).

Nitrate (NO_3^-) concentrations were highest in coastal springs of the conglomerate section including Doncellas, Barranco Maro, Huerto Romero, and Maro Beach with an average of $446 \pm 50 \text{ mmol m}^{-3}$ ($n = 6$). Water samples that were directly derived from Maro Spring (Maro spring, Maro Creek) and did not experience infiltration (i.e. had no fertilizer added), showed NO_3^- concentration of $5 - 21 \text{ mmol m}^{-3}$. NO_3^- concentrations in diffuse groundwater seepage in Maro Cliff were consistently near $130 \pm 3 \text{ mmol m}^{-3}$ ($n = 2$). Samples collected in the schist section from groundwater-fed Miel Creek and coastal spring Alberquillas, and in the karst section from Cantarrijan Beach, showed levels of NO_3^- ranging from 55 mmol m^{-3} in Miel Creek to 168 mmol m^{-3} in Cantarrijan Beach ($n = 5$) (Appendix I Table 2).

	TGD	CS	GC	GS	SS	Fresh TGD from SAA	Annual budget SAA	Agricultural area	Relative agricultural area	N-TGD
	$(\times 10^3 \text{ m}^3 \text{ d}^{-1})$						$(\times 10^6 \text{ m}^3 \text{ y}^{-1})$	(km^2)	$(\%)$	(mol d^{-1})
Conglomerate section	3.5 – 4.0	0.5 – 0.8	0.1 – 0.2	2.9 – 3.0	0	0.1 – 0.2	0.06 – 0.08	204	95	550 - 732
Schist section	2.4 – 3.6	1.1 – 1.6	1.3 – 2.0	0	0	2.3 – 3.4	0.8 – 1.2	103	7	136 – 204
Karst section	3.0 – 4.8	0	0	0.9 – 2.3	2.1 – 2.5	2.5 – 3.6	1.0 – 1.3	0	0	18 – 53

Table 2.4. Summary of total groundwater discharge (TGD) including all modes of discharge (CS, GC, GS, SS), and fresh groundwater discharge from the Sierra Almirajara-Alberquillas (SAA) aquifer (daily and annual). Total nitrate fluxes to coastal waters (N-TGD) is shown for the three sections (conglomerate, Schist, and Karst sections), with respect to agricultural coverage. Relative agricultural area represents the coverage normalized by the total extension of each section near the coast.

Nitrate fluxes were unevenly distributed in the three sections of the study site (Table 2.4). The combination of high NO_3^- in coastal springs and high flow groundwater seepage results in NO_3^- fluxes in the conglomerate section of $550 \pm 140 \text{ mol d}^{-1}$ and $730 \pm 190 \text{ mol d}^{-1}$. During this study, NO_3^- fluxes in the schist and karst section together were $150 \pm 20 \text{ mol d}^{-1}$ during dry and $250 \pm 40 \text{ mol d}^{-1}$ during wet periods (Table 2.4).

2.6 Discussion

2.6.1 Method selection and assessment of each form of groundwater discharge to the sea

2.6.1.1 Submarine springs

Quantifying submarine springs discharge in the karst section was found to be the most difficult part of this study. None of the data collected during the three ^{222}Rn boat surveys along the coastline showed tracer anomalies in the areas of submarine spring discharge (Fig. 2.5). However, I was able to detect ^{224}Ra and salinity anomalies produced by the three submarine springs discharging from Cantarrijan, Palomas, and Sifon Caves (Fig. 2.3 and 2.4). Concentrations of ^{224}Ra were on average four times higher ($20 \pm 7 \text{ dpm m}^{-3}$, $n = 10$) compared to offshore waters ($8 \pm 1 \text{ dpm m}^{-3}$, $n = 4$) in locations where no ^{222}Rn signal was detected.

Considering that ^{224}Ra and ^{222}Rn have similar half-lives and experience similar mixing, I hypothesize that the lower ^{222}Rn concentrations in coastal waters of the karst section must be due to degassing. Similar effects on dissolved ^{222}Rn and ^{224}Ra have been observed in coastal waters by Dulaiova and Burnett (2006) and Stieglitz et al. (2010). As found in this study site, both studies showed a strong correlation between ^{222}Rn concentration and salinity or ^{222}Rn and ^{224}Ra , trends that are consistent with a ^{222}Rn deficiency due to atmospheric evasion (Stieglitz et al., 2010). Furthermore, when combining the ^{222}Rn concentration data with salinity anomalies from all boat surveys along the entire shoreline, I observe that ^{222}Rn concentrations decrease at a faster

rate than salinity when closer to the groundwater source (Fig. 2.9a, 2.9b). If wind conditions are constant during the surveys (which there were), following the 1st Fick's Law, degassing due to molecular diffusion through the water-atmosphere interphase must be enhanced when seawater ²²²Rn concentration is higher (the concentration gradient is higher). Thus, this effect is most likely created because the water column-atmosphere concentration gradient in areas close to the groundwater source is at its highest, favoring atmospheric evasion.

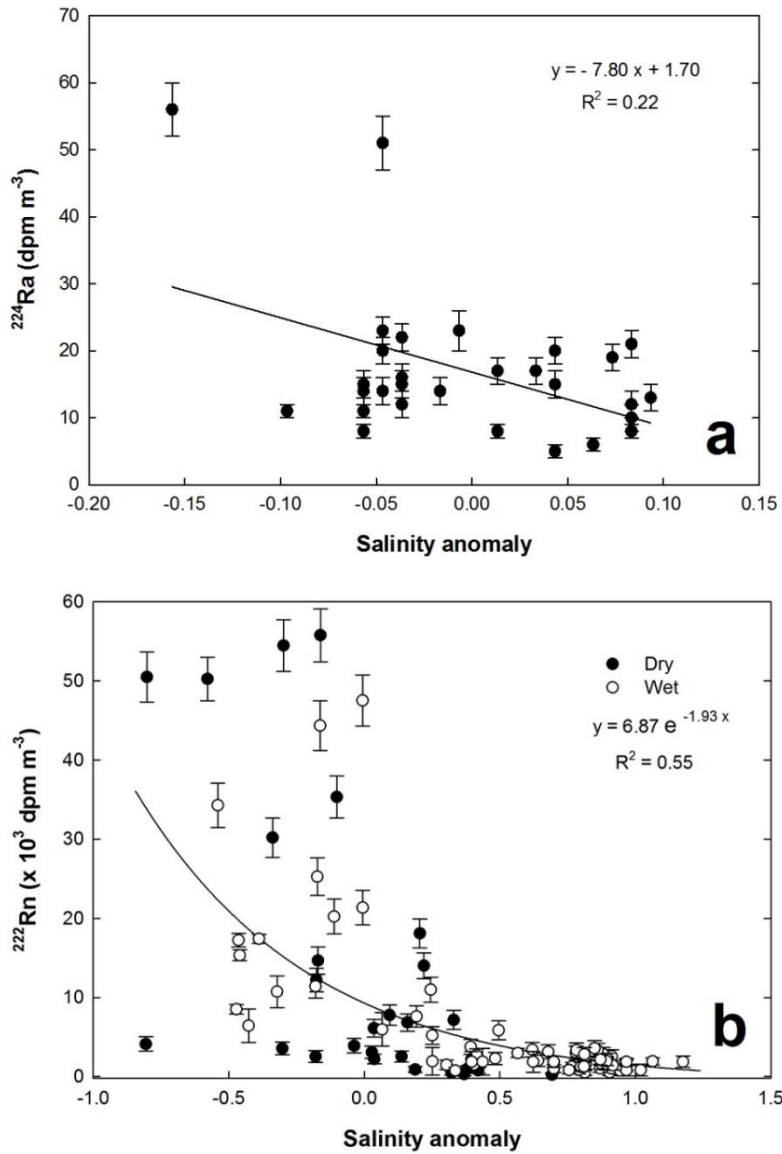


Figure 2.9. Mixing plots of ^{224}Ra (a) and ^{222}Rn versus salinity (b) showing best fit linear and exponential mixing lines, respectively, during surface water surveys along the coastline in September of 2010, July and December of 2015.

Based on these findings, I concluded that ^{224}Ra (Eq. 2.1) and salinity (Eq. 2.2) mass balances are the two methods better suited to evaluate groundwater discharge from submarine springs of the ones utilized in this study. However, I found a significant difference between the springs discharge assessments obtained using these two tracers; the flux based on the ^{224}Ra mass

balance was $12.8 \pm 1.4 \times 10^3 \text{ m}^3 \text{ d}^{-1}$, whereas using the salinity mass balance I calculated a discharge of $2.3 \pm 0.2 \times 10^3 \text{ m}^3 \text{ d}^{-1}$. I suggest that the difference could be explained by selection of the end-member in the mixing model, which has been previously described by others as a factor in correct determination of groundwater discharge (e.g. Peterson et al., 2008; Moore, 1996; Cerdà-Domènech et al., 2017). A critical component in any tracer study is the selection of a representative groundwater end-member (Ra_{SGD} and Sal_{SGD}) collected at the point of discharge.

All submarine springs described here are located in submarine caves (Cantarrijan, Palomas, and Sifon Caves) with vents parallel to the surface (i.e. horizontal geometry) at depths of 8 – 15 m below sea level. The springs discharge occurs parallel to the land surface at about 5 – 10 m landward from the caves entrance. SCUBA diving to the springs vents for representative groundwater/spring water end-member was challenging, thus the presented estimates of spring discharge are based on groundwater from the closest located well (GW-CG-1, Fig. 2.1) with a ^{224}Ra concentration of $1260 \pm 90 \text{ dpm m}^{-3}$ and salinity of 2.2 ± 0.1 .

Because springs conduits are subject to seawater intrusion, I suggest that the salinity of the discharging spring water could be higher than groundwater salinity sampled from the inland well (GW-CG-1) which I used as the groundwater end-member (Ra_{SGD} and Sal_{SGD}). While in fresh water, radium is mostly attached to particles and its dissolved concentration is very low, in brackish spring water radium would be mostly dissolved and I would have observed higher ^{224}Ra in the end-member waters (Burnett et al., 2006; Cerdà-Domènech et al., 2017). Based on the correlation between salinity and ^{224}Ra desorption, a salinity increase of 5 to the groundwater end-member (GW-CG-1) would produce an extrapolated ^{224}Ra increase of 60 dpm m^{-3} , resulting in a decrease spring flux of about 65%, which is closer to the salinity mass balance estimation. A salinity of 5 in submarine springs seems reasonable as it is similar to those found by García-

Solsona et al. (2010) in a coastal karst aquifer in eastern Spain, where annual average salinity of outflowing brackish submarine springs was 6.8. Furthermore, in well GW-CG-1 located 500 m inland from the submarine springs in the karstic marble, a salinity value of 2.2 was measured, also indicating that a value of 5 was plausible.

The salinity mass balance method estimates only the fresh water fraction of the spring discharge. In this way, the difference in discharge estimation using a ^{224}Ra and a salinity mass balance is found because the ^{224}Ra method estimates the total (brackish) discharge, while the salinity method accounts only for the fresh portion. Therefore, only the spring discharge based on the salinity model should be used in the water budget of Sierra Almirajara-Alberquillas Aquifer.

2.6.1.2 Diffuse groundwater seepage through seabed sediments

In contrast to the case of submarine spring discharge, I found that groundwater seepage through seabed sediments (Maro Cliff, conglomerate section; and Cantarrijan Beach, karst section) was most adequately detectable using ^{222}Rn as a tracer and direct measurements (i.e. seepage meters). The observed ^{222}Rn concentrations in receiving surface waters were as high as $44 \pm 3 \times 10^3 \text{ dpm m}^{-3}$ at both groundwater seepage areas, i.e. Maro Cliff and Cantarrijan Beach (Fig. 2.4).

Although, I also observed high ^{224}Ra concentrations in samples collected near Cantarrijan Beach (Fig. 2.3), these were associated with nearby discharge from the Cantarrijan Caves submarine spring (Fig. 2.3, sampling points SW-6, SW-7, and SW-13). Indeed, during one of the dry period sampling events (July of 2016), I did not detect any ^{224}Ra in coastal waters of Cantarrijan Beach giving us confidence that the previously observed signals (September 2010) were from the springs and not from the diffuse seepage. For the same reason, salinity could not be used as a tracer in either of the seepage areas (Maro Cliff and Cantarrijan Beach) because

salinity anomalies were also created mostly by nearby coastal and submarine springs respectively, overwhelming the salinity signal that is only due to diffuse seepage.

In this complex scenario, ^{222}Rn was the only groundwater tracer able to uniquely identify diffuse groundwater seepage to the sea and a ^{222}Rn mass balance was thus used to quantify groundwater seepage fluxes. Based on this mass balance in the Maro Cliff area, I calculated a discharge of $2.9 \pm 0.8 \times 10^3 \text{ m}^3 \text{ d}^{-1}$ (Table 2.2), whereas using seepage meter deployments ($n = 4$) the discharge was $2.1 \pm 0.4 \times 10^3 \text{ m}^3 \text{ d}^{-1}$. In the Cantarrijan Beach I found very similar seepage flux estimates using the ^{222}Rn approach ($0.9 \pm 0.1 \times 10^3 \text{ m}^3 \text{ d}^{-1}$) and using seepage meters ($0.8 \pm 0.2 \times 10^3 \text{ m}^3 \text{ d}^{-1}$) with a total of 9 deployments (Table 2.2). While the two methods agree very well, I recommend using the ^{222}Rn method over seepage meters. The main advantages of the ^{222}Rn technique are (1) fully automatic data collection with very little field efforts, (2) temporal and spatially integrated SGD estimates, which allow capturing small hydraulic conductivity variations over large areas of diffuse seepage (Burnett et al., 2001).

2.6.1.3 Subaerial forms of groundwater discharge to the sea (coastal springs and groundwater-fed creeks)

Coastal springs, and creeks that are primarily groundwater sustained, were only present at the conglomerate and schist sections of the study site that are comprised of conglomerate and schist, where permeabilities are lower than in the marble formation (karst section). During boat surveys ^{222}Rn activity levels in coastal waters of these two sections were always within background offshore values ($1.0 \pm 0.2 \times 10^3 \text{ dpm m}^{-3}$, Fig. 2.5) even at the points of coastal springs and groundwater-fed creeks discharge that were visually identified. I attributed the observed low ^{222}Rn concentrations to degassing and radioactive decay during groundwater transit from land to the ocean. For instance, ^{222}Rn concentration at the point of the groundwater-fed

Maro Creek origin (Maro Spring, $250 \pm 90 \text{ dpm m}^{-3}$) was significantly higher than at the point of the Creek entrance to the sea (Maro Creek 3, $16 \pm 7 \text{ dpm m}^{-3}$) (Fig. 2.1; Appendix I Table 2).

However, I was able to find groundwater signature of the Miel Creek and the Alberquillas coastal spring in coastal waters of the schist section using ^{224}Ra concentration anomalies; radium was $56 \pm 4 \text{ dpm m}^{-3}$ and $12 \pm 2 \text{ dpm m}^{-3}$ respectively at their point of entry to the sea (Fig. 2.1).

While coastal springs were easily located visually, additional field efforts were usually required to determine whether the creeks were solely fed by groundwater inputs from the karst aquifer in order to be considered (or not) in the total groundwater budget of Sierra Almirajara-Alberquillas Aquifer.

2.6.1.4 Total groundwater discharge to Maro-Cerro Gordo coastal area

Combining all groundwater fluxes to the sea in Maro-Cerro Gordo, I estimate a daily groundwater discharge that ranged between $9 \pm 2 \times 10^3 \text{ m}^3 \text{ d}^{-1}$ during dry periods and $12 \pm 3 \times 10^3 \text{ m}^3 \text{ d}^{-1}$ during wet periods, with an average of $11 \pm 3 \times 10^3 \text{ m}^3 \text{ d}^{-1}$. This combined discharge is composed of: $3.6 - 4.0 \times 10^3 \text{ m}^3 \text{ d}^{-1}$ in the conglomerate section, $2.4 - 3.6 \times 10^3 \text{ m}^3 \text{ d}^{-1}$ in the schist section, and $3.3 - 4.7 \times 10^3 \text{ m}^3 \text{ d}^{-1}$ in the karst section (Appendix I Table 2). As described above, differences in the geologic settings in each section, have defined the form of groundwater flow to the sea (Fig. 2.10, Table 2.4).

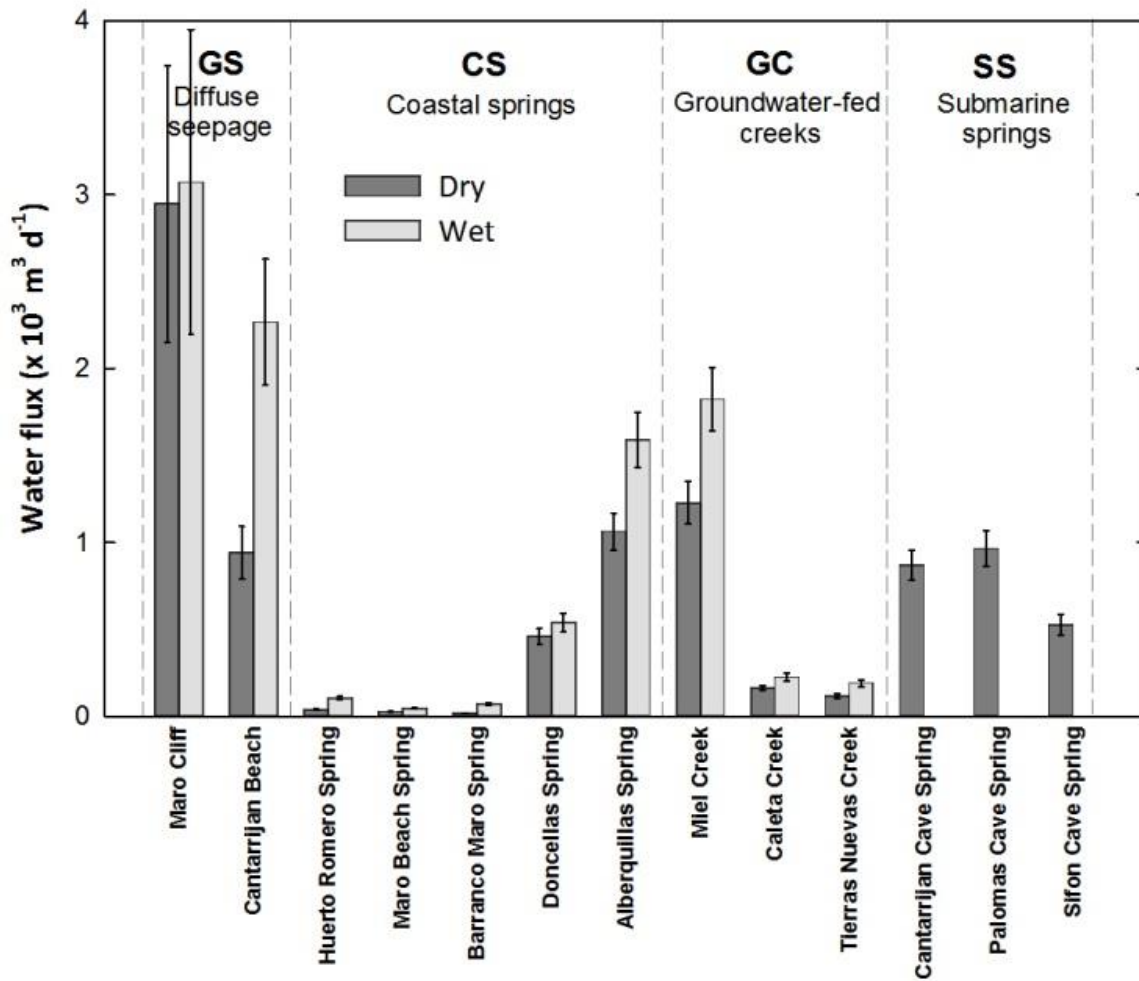


Figure 2.10. Total groundwater discharge (TGD) in the study area divided in forms of discharge (GS: groundwater diffuse seepage, CS: coastal springs, GC: groundwater-fed creeks, SS: submarine springs), showing maximum and minimum flux during wet and dry periods.

In the conglomerate section, most of the groundwater flow takes place preferentially through the travertine formation as groundwater seepage and it is 25 - 31% of the total discharge in the study area, whereas small coastal springs dispersed along the section contribute to 5 – 6%, and groundwater-fed creeks for 1 – 2%. The ubiquitous presence of a schist formation in the schist section impedes direct submarine flow and groundwater discharge converges in two points: groundwater-fed Miel Creek, and Alberquillas coastal spring which account for 25 – 30%

of the total discharge. In the karst section, where Sierra Almirajara-Alberquillas Aquifer is in direct connection with the sea, SGD takes place as groundwater seepage through marine sediments in Cantarrijan Beach assessed to account for 10 - 18%. Karstic submarine springs in Cantarrijan Caves, Palomas Cave, and Sifon Cave represent 19 - 25% of the total groundwater discharge to the sea.

2.6.2 Complexity of Sierra Almirajara-Alberquillas karst aquifer hydrodynamics

The large spatial variations in the different forms of groundwater discharge in this coastal karst aquifer were also reflected in the seasonal variability of discharge during contrasting periods (Fig. 2.2). For instance, in Maro Cliff (conglomerate section, Fig. 2.1) I expected higher seepage rates in December during the wet period (Fig. 2.2). However, the discharge estimations for the dry period (July) and the wet period (December) were statistically identical: groundwater seepage in Maro Cliff during the dry period was $2.9 \pm 0.8 \times 10^3 \text{ m}^3 \text{ d}^{-1}$ and $3.0 \pm 0.8 \times 10^3 \text{ m}^3 \text{ d}^{-1}$ during the wet period.

There are two hypotheses that attempt to explain the observed lack of seasonal variation of groundwater discharge in Maro Cliff. The first hypothesis suggests that the observed steady flow is maintained by continuous infiltration of agricultural irrigation water used by the adjacent greenhouse fields. A second hypothesis, proposed by Espejo et al. (1988) and Castillo et al. (2001) suggests that the surplus of groundwater that maintains the base flow during the dry season originates from the Sierra Almirajara-Alberquillas Aquifer. The authors propose that groundwater is transferred from the Sierra Almirajara-Alberquillas Aquifer to the coast through the adjacent conglomerate unit and travertines near the small town of Maro. These two hydrogeologic units are indeed in immediate contact with the sea (Fig. 2.1). To test both hypotheses I used two common geochemical approaches.

I first differentiated between heavier isotopic ($\delta^2\text{H}$ and $\delta^{18}\text{O}$) compositions (more positive values), associated with evaporation processes or mixing with seawater (Gat, 1971). The isotopic composition of groundwater collected from Maro Spring (i.e. in the conglomerate section) showed the most negative values (-46‰, -7.7‰) on the local groundwater line (LWL) in this area (Fig. 2.8b). These values correspond to the composition of deep groundwater flow in Sierra Almirajara-Alberquillas Aquifer (Liñán et al., 2000). Groundwater seepage in Maro Cliff presents average isotopic values (-44‰ and -7.4‰) that are similar but slightly higher than Maro Spring, suggesting that water transfer from the marble formation is a plausible option.

To differentiate between irrigation water and water transferred from the Sierra Almirajara-Alberquillas Aquifer to the travertines, the water stable isotopes end-members have to be very different than the deep/spring groundwater which has a negative composition compared to more positive values of evaporated irrigation water. I know that the water used for irrigation is withdrawn by farmers from Maro Spring. However, once extracted and in contact with the atmosphere, the water isotopic composition changes to more positive isotopic values. I also found that the collected spring water utilized for irrigation is typically stored in holding tanks and used when needed. During this holding time and in the process of irrigation, the water experiences further evaporation, and as a result, it should result in even more positive isotopic signature such as the waters of the coastal spring Barranco Maro (up to -43 and -7.3). The isotopic signature of irrigation water is thus, very different from the original Maro Spring water, allowing us to define a two-end-member system where coastal spring Huerto Romero represents the most evaporated irrigation water (Fig. 2.8b). Based on a mixing model using these end-members I found that seeping groundwater at Maro Cliff is indeed composed mostly from infiltrating irrigation water. I also found that the ratio of Maro Spring water to irrigation changes

depending on the season with highest percentage (up to 82%) of irrigation water during the dry period compared to the wet period (74%).

To further confirm these findings, I utilized water quality parameters, such as sulfate (SO_4^{2-}) and nitrate (NO_3^-) concentrations, to differentiate between these two water sources. Infiltrated irrigation water should have much higher NO_3^- concentrations and constant SO_4^{2-} , whereas deep groundwater should contain natural concentrations of NO_3^- . Thus, NO_3^- content can be used as an indication of irrigation origin. The isotopic composition of Sierra Almirajera-Alberquillas Aquifer in this area fall within a narrow SO_4^{2-} concentration range (1700 – 2600 mmol m^{-3}) (Fig. 2.11), being naturally high in Maro Spring groundwater (Liñán et al., 2000). When plotting SO_4^{2-} and NO_3^- concentrations in water, all water samples derived from Maro Spring before infiltration showed low NO_3^- concentration (5 – 21 mmol m^{-3}) and naturally high levels of SO_4^{2-} (Fig. 2.11). All samples collected from coastal springs that discharge to the sea (Doncellas, Barranco Maro, Huerto Romero, and Maro Beach coastal springs), showed levels of SO_4^{2-} typical of Sierra Almirajera-Alberquillas Aquifer and high levels of NO_3^- (more than 350 mmol m^{-3}) indicating fertilizer inputs. On the other hand, samples collected at the area of seepage through seabed sediments in the Maro Cliff, showed NO_3^- concentrations (130 mmol m^{-3}) that are closer to the observed background levels of Sierra Almirajera-Alberquillas groundwater representative (5 – 21 mmol m^{-3}) than to the contaminated infiltrated water (Fig. 2.11).

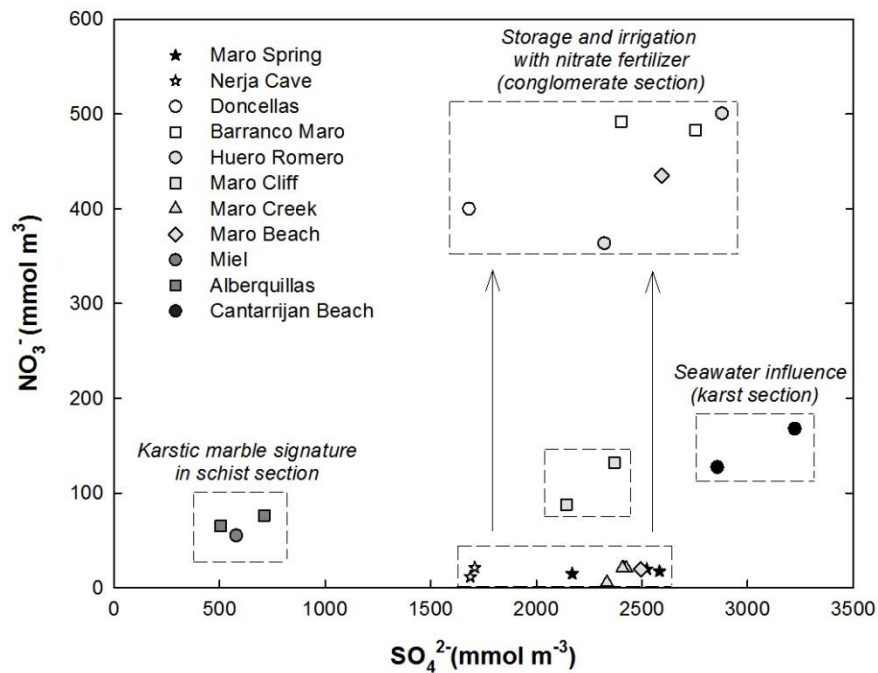


Figure 2.11. Groundwater ionic relationship between NO_3^- and SO_4^{2-} where groundwater samples with similar composition are grouped in dashed squares. Symbols are presented as in Fig. 2.8 based on the section and lithology they are located. In the conglomerate section Maro Spring, Nerja Cave, and Maro Creek show similar SO_4^{2-} concentration with low NO_3^- , while Doncellas, Barranco Maro, Huerto Romero, and Maro Beach present NO_3^- contamination. Samples from the schist section (Miel and Alberquillas) present a distinctive signal with low NO_3^- and SO_4^{2-} concentrations. Groundwater collected in Cantarrijan Beach (karst section) shows seawater influence from saltwater recirculation in beach sediments. Arrows indicate the geochemical change before irrigation and after fertilizers application (NO_3^-), where Maro cliff (diffuse seepage) shows mixing between both groups.

Therefore, I am confident that groundwater seepage to the sea observed and quantified in Maro Cliff is mostly generated as a result of infiltrated irrigation water. I found uniform groundwater flux (independently of rainfall) in this area throughout the year (Fig. 2.6a) supporting this hypothesis. Irrigation occurs constantly throughout the year, and infiltration through the highly porous travertine constitutes a constant source of water that flows towards the coast and ultimately discharges into the sea as groundwater seepage. Irrigation water from greenhouse farming is collected from the Maro Spring and thus SGD in the Maro Cliff should

not be added to the total budget of the aquifer system as it has been already accounted as groundwater from Maro Spring on land. This is a significant new finding and should be considered when compiling the total water budget of the Sierra Almirajara-Alberquillas Aquifer.

In contrast to the groundwater seepage dynamics in Maro Cliff (conglomerate section), the seepage rates in the Cantarrijan Beach (karst section) were seasonally modulated; the groundwater flux that the Cantarrijan Beach area received in the dry period was $0.9 \pm 0.1 \times 10^3 \text{ m}^3 \text{ d}^{-1}$ which was half of its wet period discharge ($2.3 \pm 0.3 \times 10^3 \text{ m}^3 \text{ d}^{-1}$). Differences in aquifer recharge and sea level variations between the dry and wet periods have control on the magnitude of SGD (Carrasco et al, 1998; Santos et al., 2009). During dry periods precipitation was absent for up to two months, decreasing the recharge from infiltrated meteoric water in Sierra Almirajara-Alberquillas Aquifer. Although during December of 2015 the area did not receive any rainfall, rain events occurred during September-November contributed to the recharge of Sierra Almirajara-Alberquillas Aquifer, deriving in higher seepage fluxes in Cantarrijan Beach (Fig. 2.2). Additionally, the mean sea level measured during 2010-2016 near the study area (Permanent Service for Mean Sea Level, <http://www.psmsl.org/data/obtaining/stations/1940.php>) showed seasonal fluctuations, with lower sea levels during January-May compared to higher levels during August-December (Fig. 2.2). The observed moderate increase of 15 cm during the dry periods has contributed to the observed higher salinity of groundwater in Cantarrijan Beach, as well as the overall lower groundwater seepage rates during the dry periods.

Based on the salinity mixing model (Eqs. 2.9 and 2.10), I calculated that the fresh fraction of SGD was 48% of the total groundwater seepage, which means that during July of 2016, only $0.4 \pm 0.1 \times 10^3 \text{ m}^3 \text{ d}^{-1}$ should be taken into account as part of the Sierra Almirajara-Alberquillas Aquifer water budget.

The salinity gradient observed from GW-Well to GW-Pz-4 is an indication that there is saltwater recirculation in the beach sediments and with the ^{222}Rn approach I have captured both the fresh and recirculated SGD (Fig. 2.6c). I did not repeat these measurements during the wet period, but I can hypothesize that this percentage was very similar based on the salinity measured in GW-Well during December of 2015 (Appendix I Table 2).

2.6.3 Importance of groundwater discharge for the water budget of Sierra Almirajara-Alberquillas Aquifer and nitrate loading to Maro-Cerro Gordo coastal area

To estimate the portion of the annual fresh groundwater discharge to the sea from Sierra Almirajara-Alberquillas Aquifer water budget, I extrapolated average daily fluxes to obtain an annual range for the wet and dry periods (Table 2.4). During this study, I found that the total groundwater discharge to the sea was $1.9 \pm 0.5 \times 10^6 \text{ m}^3 \text{ y}^{-1}$ during the dry period, and $2.6 \pm 0.8 \times 10^6 \text{ m}^3 \text{ y}^{-1}$ wet period (Table 2.4). Based on Pérez-Ramos and Andreo (2007) and Castillo et al. (2001) the total annual groundwater budget of the Sierra Almirajara-Alberquillas Aquifer is $50 \times 10^6 \text{ m}^3 \text{ y}^{-1}$, and thus the flux I estimated represents 4 - 5% of the water resources of this karst system. This is a conservative estimate and should be considered as groundwater flow at base conditions because sampling campaigns were purposely not conducted after big rain events (Fig. 2.2).

In these calculations, I do not account for groundwater seepage in Maro Cliff (conglomerate section), coastal springs Doncellas, Barranco Maro, Huerto Romero, and Maro Beach, and groundwater-fed Tierras Nuevas Creek as they are originated from irrigation water that has been already accounted as outputs from Maro Spring.

Based on the groundwater discharge to the sea, NO_3^- fluxes per unit of shore length in the conglomerate section were $205 \pm 90 \text{ mmol m}^{-1} \text{ d}^{-1}$, while the schist and karst sections together

receive between $15 \pm 3 \text{ mmol m}^{-1} \text{ d}^{-1}$ on average. When normalized by shore length, NO_3^- discharge in the conglomerate section is $3.5 \text{ mmol m}^{-2} \text{ d}^{-1}$, which compared to other anthropogenically impacted sites of coastal karst aquifers in the Mediterranean, is very similar. For example, García-Solsona et al. (2010) estimated a nitrate flux of $8.3 - 1.5 \text{ mmol m}^{-2} \text{ d}^{-1}$ in eastern Spain, and Rodellas et al. (2014) found $0.97 \text{ mmol m}^{-2} \text{ d}^{-1}$ in Majorca Island (Balearic Islands), whereas in a site in Menorca Island the flux was $18 \text{ mmol m}^{-2} \text{ d}^{-1}$ (García-Solsona et al., 2010b). It is important to note that while it only represents 20% (or 3 km) of the total shoreline length (16 km), the conglomerate section receives about 75% of the total NO_3^- delivered to Maro-Cerro Gordo coastal waters (Appendix I Table 2).

Since 1989 the Maro-Cerro Gordo Natural Area (schist and karst sections), has been protected due to the presence of endemic and endangered flora and fauna by the Council of Environment of Andalusia. The European Commission designated the area as a Special Protection Area (SPA), Specially Protected Area of Mediterranean Importance (SPAMI), Site of Community Importance (SCI), and Special Area of Conservation (SAC) (Aranda and Otero, 2014). Specifically, the conservation area hosts three species of marine phanerogams (*Zostera marina*, *Posidonia oceanica*, and *Cymodocea nodosa*), included in the IUCN Red List of Threatened Species. Seagrass provides a unique habitat for a wide range of species (Hughes et al., 2009); including the largest bivalve in the Mediterranean *Pinna nobilis* (Theodorou et al., 2015), endangered fish *Epinephelus marginatus* (Gallego et al., 2015), and marine turtle *Caretta caretta* (Tomas et al., 2001) among others. As other studies have demonstrated, nitrate surplus loading often alters the primary producers community (Rapport and Whitford, 1999), and fast growing micro and macroalgae can proliferate preventing seagrasses *Zostera marina* and *Posidonia oceanica* from having enough sunlight and space (Hauxwell et al., 2001; Deegan et

al., 2002). For example, Valiela et al. (2002) demonstrated that seagrass production could decrease up to 90% when nitrogen inputs are higher than $500 \text{ kg N ha}^{-1} \text{ y}^{-1}$. Only in the groundwater seepage area of Maro Cliff I have found that nitrogen fluxes (as nitrate) was about $2500 \text{ kg N ha}^{-1} \text{ y}^{-1}$, which is five times higher than the Valiela et al.'s assessment and should be a major concern for the ecological status of the marine system in the conglomerate section (Fig. 2.1). However, to further understand the implications of nutrients fluxes to the sea on the marine ecosystem (particularly on endemic seagrass and fauna), additional investigation in the area must be conducted.

2.6.4 Sensitivity analysis of methods applied

To further compare the applicability of methodologies utilized in the presented multi-method approach, I constructed a sensitivity analysis including each method's main assumptions.

2.6.4.1 Parameter sensitivity of ^{224}Ra and salinity mass balance methods for determining discharge of submarine springs

Three terms represent the major source of uncertainty in the ^{224}Ra and salinity mass balances I used to calculate submarine spring discharge, including (1) the residence time of the receiving coastal waters (t), (2) the volume of the SGD plume (V), and (3) the uncertainty in the determination of groundwater end-member (Ra_{SGD}) (Table 2.5).

The largest uncertainty in this model is given by the assumption of a one day residence time (t). A common technique for assessing water ages of coastal waters is based on short-lived radium isotopes, ^{223}Ra and ^{224}Ra (Moore, 2000). However, during this study I could not measure both radium isotopes and I was unable to apply this method. The karst section of Maro-Cerro Gordo displays rocky cliff areas spread across the geographically exposed to prevailing west winds coastline which reflects the influence of high energy waves. The karst aquifer has very

high secondary porosity and permeability which provides the opportunity for extensive groundwater-surface water exchange. The estimate of a one day residence time for this study is based on a comparison to similar high-energy coastal environments that are typical for the Mediterranean coastline. Under similar hydrogeological conditions in eastern Spain, using the methodology presented in Moore (2000), García-Solsona et al. (2010) assessed residence time (t) between 1.1 d and 2.7 d, whereas Tovar-Sánchez et al. (2014) found residence times of 1.7, and 1.2 days in three coves in a karst system in the eastern shore of the Majorca Island. Considering these studies and specifics of this study site, I suggest using residence times of 0.25, 0.5, 1.0, and 3.0 days in the sensitivity analysis.

To determine the volume ($V = \text{plume area} \times \text{depth}$) of the SGD plume, I used areas of salinity sea surface anomalies created by the submarine springs discharge at Maro-Cerro Gordo. Specifically, I utilized salinity anomalies of -0.3, 0.0, 0.3, and 0.6 isolines. For vertical scale I use water depths acquired from the bathymetry database of the Andalusia Council of Environment (<http://www.juntadeandalucia.es/medioambiente/site/rediam>) assuming a well-mixed water column. However, Garcia-Solsona et al. (2010) found in eastern Spain that although complete mixing in the water column could be found near the karst springs vents, the salinity anomaly measured in surface waters was limited to the 0.5 m upper most layer. Similar settings are possible in Maro-Cerro Gordo; thus, I also calculated V based on the 0.0 salinity anomaly isoline and considering a depth of 0.5 m (Table 2.5)

Method/Form of discharge	Model parameters										Final SGD estimate (x 10 ³ m ³ d ⁻¹)	Percentage difference between min and max estimate
	Residence time (days)	²²⁴ Ra gw end-member (dpm m ⁻³)	Salinity isoline	Volume SGD plume (x 10 ⁵ m ³)			²²² Rn isoline (x 10 ³ dpm m ⁻³)		Seepage area (x 10 ³ m ²)			
				Cantarrijan	Palomas	Sifon	Maro Cliff	Cantarrijan Beach	Maro Cliff	Cantarrijan Beach		
Salinity mass balance/ Submarine springs	0.25	N/A	-0.3	0.9	1.5	1.1	N/A	N/A	N/A	N/A	0.2 - 90.5	100%
	0.50	N/A	0.0	2.6	4.0	3.7	N/A	N/A	N/A	N/A		
	1.00	N/A	0.3	2.8	5.4	4.7	N/A	N/A	N/A	N/A		
	3.00	N/A	0.6	4.6	8.7	7.1	N/A	N/A	N/A	N/A		
	0.5 m water column		0.0	0.20	0.18	0.19	N/A	N/A	N/A	N/A		
²²⁴ Ra mass balance/ Submarine springs	0.25	1020 ± 80	-0.3	0.9	1.5	1.1	N/A	N/A	N/A	N/A	0.03 - 13.5	100%
	0.50		0.0	2.6	4.0	3.7	N/A	N/A	N/A	N/A		
	1.00	1260 ± 90	0.3	2.8	5.4	4.7	N/A	N/A	N/A	N/A		
	3.00		0.6	4.6	8.7	7.1	N/A	N/A	N/A	N/A		
	0.5 m water column		0.0	0.20	0.18	0.19	N/A	N/A	N/A	N/A		
²²² Rn mass balance/ Diffuse seepage	N/A	N/A	N/A	N/A	N/A	N/A	25	5	2.4	1.0	1.1 - 10.0	89%
	N/A	N/A	N/A	N/A	N/A	N/A	30	6	7.7	3.2		
	N/A	N/A	N/A	N/A	N/A	N/A	35	8	10.6	4.3		
	N/A	N/A	N/A	N/A	N/A	N/A	45	10	17.8	5.7		
Seepage meters/ Diffuse seepage	N/A	N/A	N/A	N/A	N/A	N/A	25	5	2.4	1.0	1.2 - 9.1	87%
	N/A	N/A	N/A	N/A	N/A	N/A	30	6	7.7	3.2		
	N/A	N/A	N/A	N/A	N/A	N/A	35	8	10.6	4.3		
	N/A	N/A	N/A	N/A	N/A	N/A	45	10	17.8	5.7		

Table 2.5. Values of all parameters applied in the sensitivity analysis including flux ranges estimated for each methodology.

There are only two groundwater wells in the karst section of Maro-Cerro Gordo, (GW-CG-1 and GW-CG-2). For the sensitivity analysis I used ^{224}Ra concentration in GW-CG-1 ($1260 \pm 90 \text{ dpm m}^{-3}$) and GW-CG-2 ($1020 \pm 80 \text{ dpm m}^{-3}$) as end-members, both sampled in September of 2006.

After tabulating these parameters, both the ^{224}Ra and salinity mass balance models showed the highest sensitivity to variations in the volume affected by SGD (V). I found that the total discharge from submarine springs decreases by 80% when using salinity isolines of 0.6 to 0.3 in a well-mixed water column; however, if the fresh plume is limited to the 0.5 m top layer of the water column, the decrease is up to 97%. Residence time (t) was the second most important variable affecting the variability of discharge from submarine springs, increasing by 92% when changing the residence time from 0.25 to 3.0 days (Table 2.5). The ^{224}Ra mass balance showed limited sensitivity to varying groundwater end-member values (Ra_{SGD}), when using the GW-CG-2 value instead of GW-CG-1, all estimations increased only by 20%. The maximum variation utilizing the three variables simultaneously in the ^{224}Ra mass balance was 100% with a total discharge of $0.2 - 90.5 \times 10^3 \text{ m}^3 \text{ d}^{-1}$. The salinity mass balance presented a total variation of 100% to changing t and V , with a total discharge of $0.03 - 13.5 \times 10^3 \text{ m}^3 \text{ d}^{-1}$, which represents the purely fresh discharge (Table 2.5).

2.6.4.2 Parameter sensitivity of the ^{222}Rn mass balance and seepage meters measurements in determining diffuse seepage

In the ^{222}Rn model, I considered that only the seepage area (A) could be subject to ambiguity because all terms in the model (including the groundwater end-member) have been carefully measured. To delineate the size of the seepage face I used the following ^{222}Rn concentration isolines: for the Cantarrijan Beach I used the 10, 8, 6, and 5 dpm m^{-3} , while in

Maro Cliff I used the 25, 30, 35, and 45 dpm m⁻³ (Table 2.5). For comparison reasons, were used the same seepage areas to calculate SGD when using the seepage meters approach. Using the 25 × 10³ dpm m⁻³ ²²²Rn concentration isoline in Maro Cliff produces 86% higher for both dry and wet periods, compared to seepage area based on the 45 × 10³ dpm m⁻³ isoline. The discharge ranged from 0.9 – 6.7 × 10³ m³ d⁻¹ and 0.9 – 7.5 × 10³ m³ d⁻¹ during dry and wet periods respectively. In Cantarrijan Beach I found an increase of 82%, with a discharge estimation that ranged between 0.2 – 1.2 × 10³ m³ d⁻¹ and 0.5 – 2.9 × 10³ m³ d⁻¹ during dry and wet periods. The radon method showed higher sensitivity (89%) than the seepage meter assessments (87%) (Table 2.5).

2.6.4.3 Implications for the water budget of Sierra Almijara-Alberquillas Aquifer

Using the presented ranges of fluxes of each methodology, I calculated a total groundwater discharge to the sea of 4.3 – 105.1 × 10³ m³ d⁻¹ from all forms of discharge (Table 2.6). The fresh water component of the total discharge can be obtained from the salinity mass balance in submarine springs, ²²²Rn mass balance and seepage meters for diffuse seepage in Cantarrijan Beach (47% fresh, based on the salinity mixing model), Caleta and Miel Creeks, and Alberquillas Spring (see sections 5.2 and 5.3). Applying a residence time of 0.25 d, the lowest estimated volumes affected by the SGD plume (*V*) at each submarine spring (0.2 × 10⁵ m³, 0.18 × 10⁵ m³, 0.19 × 10⁵ m³) derived from a 0.5 m water column, and the largest estimates for seepage face in Cantarrijan Beach (*A* = 1.0 × 10³ m²) for the ²²²Rn model and seepage meter methods, the minimum fresh groundwater discharge is 0.9 × 10⁶ m³ y⁻¹. Applying the assumption of a 3-days residence time, the largest *V* at each submarine spring (4.6 × 10⁵ m³, 8.7 × 10⁵ m³, 7.1 × 10⁵ m³), and the largest *A* in Cantarrijan Beach (5.7 × 10³ m²) for the ²²²Rn model and seepage meter methods, the maximum fresh groundwater discharge from Sierra Almijara-

Alberquillas Aquifer is $6.8 \times 10^6 \text{ m}^3 \text{ y}^{-1}$. A total groundwater discharge of $6.8 \times 10^6 \text{ m}^3 \text{ y}^{-1}$ seems plausible but unlikely during base flow conditions when compared to the total water budget of Sierra Almirajara-Alberquillas ($50 \times 10^6 \text{ m}^3 \text{ y}^{-1}$). However, a residence time of 1 day seems more realistic based on other studies conducted in similar areas. The application of this sensitivity analysis including all terms and applying a 1-day residence time gives a total discharge of $1.0 - 3.5 \times 10^6 \text{ m}^3 \text{ y}^{-1}$.

Mode of groundwater (GW) discharge / site name	²²⁴ Ra method		²²² Rn method		Salinity method		Seepage meter method		Flow meter method	Fresh water budget of SAA (× 10 ³ m ³ d ⁻¹)
	Obs. anomaly in seawater	Flux (×10 ³ m ³ d ⁻¹)	Obs. anomaly in seawater	Flux (×10 ³ m ³ d ⁻¹)	Obs. anomaly in seawater	Flux (×10 ³ m ³ d ⁻¹)	Obs. anomaly in seawater	Flux (×10 ³ m ³ d ⁻¹)	Flux (×10 ³ m ³ d ⁻¹)	
GW-fed creeks Caleta Tierras N. Miel	✓	N/A	×	N/A	✓	N/A	×	N/A	1.4 – 2.2	1.2 – 2.1
Coastal springs Doncellas Barranco M. Huerto R. Maro Beach Alberquillas	×	N/A	×	N/A	✓	N/A	×	N/A	1.6 – 2.4	1.1 – 1.6
Submarine springs Cantarrijan Palomas Sifon	✓	0.2 – 90.5	×	N/A	✓	0.03 – 13.5	×	N/A	N/A	0.03 – 13.5
Diffused seepage Maro Cliff Cantarrijan B.	×	N/A	✓	1.1 – 10.0	✓	N/A	✓	1.2 – 9.1	N/A	0.1 – 1.4

Table 2.6. Applicability comparison of all methods utilized to detect and quantify different modes of groundwater discharge to the sea. Flux ranges are based on maxima and minima estimations obtained in the sensitivity analysis. Daily fluxes are shown for each form of discharge and method, and annual water budget (fresh) of Sierra Almirajara-Alberquillas (SAA).

2.6.5 Global applicability of the presented methodology approach

The modes of discharge found in Maro-Cerro Gordo are commonly observed in other areas worldwide independent of climate. About half of the Mediterranean and Adriatic coastline is comprised of karst aquifers and hydrogeological settings similar to Maro-Cerro Gordo can be expected (Fleury et al., 2007, 2005; Surić et al., 2015). In most scenarios authors often point out that groundwater discharge was not quantified due to the complex settings where at least two forms of discharge occur in multiple locations (e.g. Fleury et al., 2007; Burnett et al., 2008). Similar problems are encountered in karst coastlines in the Yucatan Peninsula (Mexico), a karst platform located in the Caribbean Sea. Gonnee et al. (2014) assumed that submarine springs were representative of the total SGD in the study area, but pointed out that diffuse discharge away from springs was not measured. Null et al. (2014) assessed SGD in the eastern shore of the Yucatan Peninsula where submarine springs and diffuse seepage are present. Due to the lack of a field method to quantify groundwater seepage, they used analytical calculations to establish a first order approximation of SGD. Furthermore, SGD in volcanic systems, although geologically different than karst, have comparable dynamics due to the similar intrinsic porosity and permeability (Burnett et al., 2008; Johnson et al., 2008; Peterson et al., 2009, Dimova et al., 2012).

Common characteristics of these sites include (1) simultaneous groundwater discharge to the sea occurring in two or more forms due to highly heterogeneous geological settings, (2) high infiltration rates resulting in negligible riverine freshwater inputs, and (3) significant groundwater inputs.

2.7 Conclusions

Work presented here demonstrates that determining total groundwater discharge to the ocean from coastal karst aquifers is not trivial and it requires a very good understanding of the geology and groundwater origin to constrain an adequate water budget. Specifically, as a result of the complex geology of Maro-Cerro Gordo coastal area and highly heterogeneous Sierra Almirajara-Alberquillas coastal karst aquifer, I found that groundwater discharge manifests in four different forms: (1) groundwater-fed creeks, (2) coastal springs, (3) groundwater seepage through seabed sediments, and (4) submarine springs. These expressions of discharge are typical for karst systems and should be expected in similar geological settings elsewhere including volcanic systems, which although having different rock composition, behave hydrologically very similar. I found that only the application of a set of methods specific for each form of discharge adequately characterizes and gives a realistic evaluation of groundwater discharge to the sea and thus recommend the following approaches (Table 2.6).

Continuous ^{222}Rn measurements in coastal waters via boat surveys proved to be the most reliable method for detecting diffuse groundwater seepage through seabed sediments. The technique complements well with a ^{222}Rn mass balance model based on time-series measurements performed with the same instrumentation. I found that this method gives similar results to direct measurements carried out from Lee-type seepage meters.

The presence of submarine springs was reliably detected using continuous salinity measurements and discrete ^{224}Ra sampling. However, because negative salinity anomalies in coastal waters could be the result of discharge of other freshwater inputs (e.g. groundwater-fed creeks and coastal springs) which are likely to occur in karst systems, salinity alone is not a reliable tracer for SGD in coastal karst systems. I was able to confirm the presence of submerged springs only when combined with high concentrations of ^{224}Ra concentrations and direct

observations via SCUBA diving. Direct flowmeter measurements or applying the ^{222}Rn method would have been technically and economically challenging, given the springs depth and their lateral vent geometry.

Subaerial coastal springs and groundwater-fed creeks are easily detectable visually in the field. However, I found that tracer surveys are helpful to identify sources of springs and assessing the total discharge from both forms of subaerial groundwater discharge.

I found that the combination of hydrochemistry (SO_4^{-2} and NO_3^-) and water stable isotopes ($\delta^2\text{H}$ and $\delta^{18}\text{O}$) was ideal to decipher the origin of each point of groundwater discharge to the sea.

Nitrate fluxes, in an area where endemic and protected seagrasses *Zostera marina*, *Posidonia oceanica* are present, were found to be comparable with other coastal karst aquifers environmentally impacted by anthropogenic activities in the Mediterranean.

Based on my experience, I strongly recommend the application of the described methodology approach in coastal karst systems to assess total groundwater discharge to the sea and associated nutrients fluxes.

2.8 Acknowledgments

This research was partially funded by the University of Alabama Graduate School Research and Travel Support Fund, the UA Department of Geological Sciences W. Gary Hooks Geological Sciences Advisory Board Fund, and the A.S. Johnson Travel Fund. This work is a contribution to the Research Group RNM-308 of the Junta de Andalucía, and CGL2015-65858-R of DGICYT. V.R. acknowledges support from the European Union's Horizon 2020 research and innovation program under the Marie Skłodowska-Curie grant agreement No 748896. J.G.O would like to thank the support of the Generalitat de Catalunya to

MERS (2014 SGR – 1356). I would also want to thank José Antonio Espejel Carrión, Guillermo González Lozano, Javier López-Murcia Martin, Matías Mudarra Martínez, Diego Naranjo Roldán, Fernando Nuño López, and Juan Manuel Ruiz for their extensive help in the field.

2.9 References

- Andreo, B., F. Carrasco and C. Sanz de Galdeano. 1993. Estudio geológico del entorno de la Cueva de Nerja. *Geología de la Cueva de Nerja* 3: 25-50.
- Andreo, B. and F. Carrasco. 1993. Estudio hidrogeológico del entorno de la Cueva de Nerja. *Geología de la Cueva Nerja* 3: 163-187.
- Andreo, B., J. Vías, J. J. Durán, P. Jiménez, J. A. López-Geta and F. Carrasco. 2008. Methodology for groundwater recharge assessment in carbonate aquifers: application to pilot sites in southern Spain. *Hydrogeology Journal* 16: 911-925.
- Andreo, B., J. A. Barberá, M. Mudarra, A. I. Marín, J. García-Orellana, V. Rodellas and I. Pérez. 2017. A multi-method approach for groundwater resource assessment in coastal carbonate (karst) aquifers: the case study of Sierra Almirajara (southern Spain). *Hydrogeology Journal* 26: 1-16.
- American Public Health Association (APHA), American Water Works Association (AWWA), and Water Environment Federation (WEF). 1999. In *Standard Methods for the Examination of Water and Wastewater 20th Edition*, eds. Clescerl L., Greenberg A. and Eaton A. 2-48. United Book Press, Inc., Baltimore, Maryland. Part 2000.
- Aranda, Y. and M. Otero. 2014. Estudio de las figuras de protección de áreas marinas protegidas de Andalucía con fanerógamas marinas y propuestas de mejora para su gestión. Anexo VI. LIC.
- Arfib, B. and J. B. Charlier. 2016. Insights into saline intrusion and freshwater resources in coastal karstic aquifers using a lumped Rainfall–Discharge–Salinity model (the Port-Miou brackish spring, SE France). *Journal of Hydrology* 540 : 148-161.
- Aunay, B., P. le Strat, C. Duvail, N. Dörfliger and B. Ladouche. 2003. Méthode d'analyse géologique sur la karstification des Corbières orientales et influence des événements néogènes (tortonno-messiniens). *Hydrology of the Mediterranean and semiarid Regions* 278: 124-129.
- Bakalowicz, M. 2005. Karst groundwater: a challenge for new resources. *Hydrogeology Journal* 13: 148-160.
- Bakalowicz, M., M. El Hakim and A. El-Hajj. 2008. Karst groundwater resources in the countries of eastern Mediterranean: the example of Lebanon. *Environmental Geology* 54: 597-604.
- Bakalowicz, M. 2015. Karst and karst groundwater resources in the Mediterranean. *Environmental Earth Sciences* 74: 5-14.
- Bañares-España E., J.C. Báez, M.D. Casado, C. Díaz de Rada, A. Flores-Moya and J. Rey. 2002. Distribución y estado de las fanerógamas marinas en el Paraje natural Acantilados de

- Maro-Cerro gordo (Málaga-Granada). In Libro de Resúmenes, XII Simposio Ibérico del Bentos Marino, eds. García-Gómez J.C., Finlayson C. 30–31. Impresur, Algeciras.
- Barberá, J. A. and B. Andreo. 2015. Hydrogeological processes in a fluviokarstic area inferred from the analysis of natural hydrogeochemical tracers. The case study of eastern Serranía de Ronda (S Spain). *Journal of Hydrology* 523: 500-514.
- Benac, Č., J. Rubinić and N. Ožanić. 2003. The origine and evolution of coastal and submarine springs in Bakar Bay. *Acta Carsologica* 32: 157-171.
- Bonacci, O. and T. Roje-Bonacci. 1997. Sea water intrusion in coastal karst springs: example of the Blaž Spring (Croatia). *Hydrological Sciences Journal* 42: 89-100.
- Burnett, W. C., M. Taniguchi and J. Oberdorfer. 2001. Measurement and significance of the direct discharge of groundwater into the coastal zone. *Journal of Sea Research* 46: 109-116.
- Burnett, W. C. and H. Dulaiova. 2003. Estimating the dynamics of groundwater input into the coastal zone via continuous radon-222 measurements. *Journal of Environmental Radioactivity* 69: 21-35.
- Burnett, W. C., H. Bokuniewicz, M. Huettel, W. S. Moore and M. Taniguchi. 2003. Groundwater and pore water inputs to the coastal zone. *Biogeochemistry* 66: 3-33.
- Burnett, W. C., P. K. Aggarwal, A. Aureli, H. Bokuniewicz, J. E. Cable, M. A. Charette, E. Kontar, S. Krupa, K.M. Kulkarni, A. Loveless and W. S. Moore. 2006. Quantifying submarine groundwater discharge in the coastal zone via multiple methods. *Science of the Total Environment* 367: 498-543.
- Burnett, W. C., I. R. Santos, Y. Weinstein, P. W. Swarzenski and B. Herut. 2007. Remaining uncertainties in the use of Rn-222 as a quantitative tracer of submarine groundwater discharge. A New Focus on Groundwater–Seawater Interactions (Proceedings of Symposium HS1001 at IUGG2007, Perugia, July 2007. IAHS publication 312: 109.
- Burnett, W. C., R. Peterson, W. S. Moore and J. de Oliveira. 2008. Radon and radium isotopes as tracers of submarine groundwater discharge—results from the Ubatuba, Brazil SGD assessment intercomparison. *Estuarine, Coastal and Shelf Science* 76: 501-511.
- Butscher, C. and P. Huguenberger. 2007. Implications for karst hydrology from 3D geological modeling using the aquifer base gradient approach. *Journal of hydrology* 342: 184-198.
- Cable, J. E., W. C. Burnett, J. P. Chanton and G. L. Weatherly. 1996. Estimating groundwater discharge into the northeastern Gulf of Mexico using radon-222. *Earth and Planetary Science Letters* 144: 591-604.

- Carrasco, F., J. J. Durán, B. Andreo, C. Liñán and I. Vadillo. 1998. Consideraciones sobre el karst de Nerja. *Karst en Andalucía* 173-181.
- Castillo, A., J. Carmona and J. Benavente Herrera. 2001. Cuantificación de los recursos hídricos en la vertiente meridional del Parque Natural de Sierra Almirajara (Málaga). Consideraciones sobre su régimen de explotación. *Geogaceta* 29: 33-36.
- Cerdà-Domènech, M., V. Rodellas, A. Folch and J. García-Orellana. 2017. Constraining the temporal variations of Ra isotopes and Rn in the groundwater end-member: Implications for derived SGD estimates. *Science of the Total Environment* 595: 849-857.
- Charette, M. A., K. O. Buesseler and J. E. Andrews. 2001. Utility of radium isotopes for evaluating the input and transport of groundwater-derived nitrogen to a Cape Cod estuary. *Limnology and Oceanography* 46: 465-470.
- Charette, M. A. 2007. Hydrologic forcing of submarine groundwater discharge: Insight from a seasonal study of radium isotopes in a groundwater-dominated salt marsh estuary. *Limnology and Oceanography* 52: 230-239.
- Cockenpot, S., C. Claude and O. Radakovitch. 2015. Estimation of air–water gas exchange coefficient in a shallow lagoon based on ^{222}Rn mass balance. *Journal of Environmental Radioactivity* 143: 58-69.
- Corbett, D., W. Burnett, P. Cable and S. Clark. 1998. A multiple approach to the determination of radon fluxes from sediments. *Journal of Radioanalytical and Nuclear Chemistry* 236: 247-253.
- Craig, H. 1961. Isotopic variations in meteoric waters. *Science* 133: 1702-1703
- Crusius, J., D. Koopmans, J. F. Bratton, M. A. Charette, K. Kroeger, P. Henderson, L. Ryckman, K. Halloran and J. A. Colman. 2005. Submarine groundwater discharge to a small estuary estimated from radon and salinity measurements and a box model. *Biogeosciences* 2: 141-157.
- Custodio, E. 2010. Coastal aquifers of Europe: an overview. *Hydrogeology Journal* 18: 269-280.
- Deegan, L. A., A. Wright, S. G. Ayvazian, J. T. Finn, H. Golden, R. R. Merson and J. Harrison. 2002. Nitrogen loading alters seagrass ecosystem structure and support of higher trophic levels. *Aquatic Conservation: Marine and Freshwater Ecosystems* 12: 193-212.
- Dimova, N., W. C. Burnett and D. Lane-Smith. 2009. Improved automated analysis of radon (^{222}Rn) and thoron (^{220}Rn) in natural waters. *Environmental Science & Technology* 43: 8599-8603.

- Dimova, N. T., W. C. Burnett and K. Speer. 2011. A natural tracer investigation of the hydrological regime of Spring Creek Springs, the largest submarine spring system in Florida. *Continental Shelf Research* 31: 731-738.
- Dimova, N. T., P. W. Swarzenski, H. Dulaiova and C. R. Glenn. 2012. Utilizing multichannel electrical resistivity methods to examine the dynamics of the fresh water–seawater interface in two Hawaiian groundwater systems. *Journal of Geophysical Research: Oceans* 117: 1-12.
- Dimova, N. T., A. Paytan, J. D. Kessler, K. J. Sparrow, F. García-Tigueros Kodovska, A. L. Lecher, J. Murray and S. M. Tulaczyk. 2015. Current magnitude and mechanisms of groundwater discharge in the Arctic: case study from Alaska. *Environmental Science & Technology* 49: 12036-12043.
- Dulaiova, H., R. Peterson, W.C. Burnett and D. Lane-Smith. 2005. A multi-detector continuous monitor for assessment of ^{222}Rn in the coastal ocean. *Journal of Radioanalytical and Nuclear Chemistry* 263: 361-365.
- Dulaiova, H. and W. C. Burnett. 2006. Radon loss across the water-air interface (Gulf of Thailand) estimated experimentally from ^{222}Rn - ^{224}Ra . *Geophysical Research Letters* 33: 1-4.
- Durán, J. J. 1996. Los sistemas kársticos de la provincia de Málaga y su evolución. Contribución al conocimiento paleoclimático del Cuaternario en el Mediterráneo Occidental. Ph.D. Dissertation, Universidad Complutense de Madrid, 409 p.
- Espejo, J.M., M. C. Luanco and L. Linares. 1988. Inventario de surgencias de aguas de origen continental en el litoral mediterráneo del sur de España, mediante utilización de sensores térmicos aeroportados con apoyo de técnicas oceanográficas e hidrogeológicas. In *Tecnología de la Intrusión en Acuíferos Costeros*, eds. Fernández-Rubio, R., López-Geta, J. A., Ramos-González, G. 191-228. TIAC'88, IGME, Madrid.
- Fleury, P. 2005. Sources sous-marines et aquifères karstiques côtiers méditerranéens. Fonctionnement et caractérisation. PhD dissertation, Université Paris VI, 286 p.
- Fleury, P., M. Bakalowicz and G. de Marsily. 2007. Submarine springs and coastal karst aquifers: a review. *Journal of Hydrology* 339: 79-92.
- Fourniguet, J. 1975. Néotectonique et Quaternaire marin sur le littoral de la Sierra Nevada, Andalousie (Espagne). PhD dissertation, University of Orléans, 234 p.
- Gallego, M. A. B. and O. M. Reyes. 2015. La población de meros *Epinephelus marginatus* en el litoral andaluz (España). *Chronica Naturae* 5: 68-80.

- García-Solsona, E., J. García-Orellana, P. Masqué and H. Dulaiova. 2008. Uncertainties associated with ^{223}Ra and ^{224}Ra measurements in water via a Delayed Coincidence Counter (RaDeCC). *Marine Chemistry* 109: 198-219.
- García-Solsona, E., J. García-Orellana, P. Masqué, V. Rodellas, M. Mejías, B. Ballesteros and J. A. Domínguez. 2010. Groundwater and nutrient discharge through karstic coastal springs (Castelló, Spain). *Biogeosciences* 7: 2625-2638.
- García-Solsona, E., J. García-Orellana, P. Masqué, E. Garcés, O. Radakovitch, A. Mayer, S. Estradé and G. Basterretxea. 2010. An assessment of karstic submarine groundwater and associated nutrient discharge to a Mediterranean coastal area (Balearic Islands, Spain) using radium isotopes. *Biogeochemistry* 97: 211-229.
- Gat, J.R. and I. Garmi. 1970. Evolution of the isotopic composition of atmospheric waters in the Mediterranean Sea area. *Journal of Geophysical Research* 75: 3039 – 3048.
- Gat, J. R. 1971. Comments on the stable isotope method in regional groundwater investigations. *Water Resources Research* 7: 980-993.
- Gonnea, M. E., M. A. Charette, Q. Liu, J. A. Herrera-Silveira and S. M. Morales-Ojeda. 2014. Trace element geochemistry of groundwater in a karst subterranean estuary (Yucatan Peninsula, Mexico). *Geochimica et Cosmochimica Acta* 132: 31-49.
- Guerra-Merchán, A. and F. Serrano. 1993. Análisis estratigráfico de los materiales neógeno-cuaternarios de la región de Nerja. *Geología de la Cueva de Nerja* 3: 53-90.
- Hallegraeff, G. M. 1993. A review of harmful algal blooms and their apparent global increase. *Phycologia* 32: 79-99.
- Hauxwell, J., J. Cebrián, C. Furlong and I. Valiela. 2001. Macroalgal canopies contribute to eelgrass (*Zostera marina*) decline in temperate estuarine ecosystems. *Ecology* 82: 1007-1022.
- Hughes, A. R., S. L. Williams, C. M. Duarte, K. L. Heck and M. Waycott. 2009. Associations of concern: declining seagrasses and threatened dependent species. *Frontiers in Ecology and the Environment* 7: 242-246.
- Isiorho, S. A. and J. H. Meyer. 1999. The effects of bag type and meter size on seepage meter measurements. *Ground Water* 37: 411-413.
- Johnson, A. G., C. R. Glenn, W. C. Burnett, R. N. Peterson and P. G. Lucey. 2008. Aerial infrared imaging reveals large nutrient-rich groundwater inputs to the ocean. *Geophysical Research Letters* 35: 1-6.
- Johnson, A. G. 2008. Groundwater discharge from the leeward half of the Big Island, Hawai'i. PhD dissertation, University of Hawai'i, 145 p.

- Jordá, J.F. 1988. Los travertinos del extremo oriental de la costa de Málaga. Actas del II Congreso Geológico de España, Universidad de Granada y Sociedad Geológica de España. Granada, 391-394.
- Jordá, J. F., J. E. Aura Tortosa, E. Álvarez Fernández, B. Avezuela Aristu, E. Badal, A. Maestro González and M. P. Villalba Currás. 2011. Evolución paleogeográfica, paleoclimática y paleoambiental de la costa meridional de la Península Ibérica durante el Pleistoceno superior. El caso de la Cueva de Nerja (Málaga, Andalucía, España). *Boletín de la Real Sociedad Española de Historia Natural* 105: 137-147.
- Katz, B. G., D. W. Griffin and J. H. Davis. 2009. Groundwater quality impacts from the land application of treated municipal wastewater in a large karstic spring basin: chemical and microbiological indicators. *Science of the Total Environment* 407: 2872-2886.
- Knee, K. L., J. H. Street, E. E. Grossman, A. B. Boehm and A. Paytan. 2010. Nutrient inputs to the coastal ocean from submarine groundwater discharge in a groundwater-dominated system: relation to land use (Kona coast, Hawai'i, USA). *Limnology and Oceanography* 55: 1105-1122.
- Kremer, J. N., A. Reischauer and C. D'Avanzo. 2003. Estuary-specific variation in the air-water gas exchange coefficient for oxygen. *Estuaries and Coasts* 26: 829-836.
- Lee, D. R. 1977. A device for measuring seepage flux in lakes and estuaries. *Limnology and Oceanography* 22: 140-147.
- Liñán, C., B. Andreo and F. Carrasco. 2000. Caracterización hidrodinámica e hidroquímica del manantial de Maro (Sierra Almirajara, provincia de Málaga). *Geogaceta* 27: 95-98.
- Macintyre, S., R. Wannikhof and J.P. Chanton. 1995. Trace gas exchange across the air-water interface in freshwater and coastal marine environments. In *Biogenic Trace Gases: Measuring Emissions from Soil and Water*, eds. Matson, P.A., Harriss, R.C. 52-57.
- Martens, C. S., J. V. Klump and G. W. Kipphut. 1980. Sediment-water chemical exchange in the coastal zone traced by in situ radon-222 flux measurements. *Science* 208: 285-288.
- Martínez-Santos P. and J. M. Andreu. 2010. Lumped and distributed approaches to model natural recharge in semiarid karst aquifers. *Journal of Hydrology* 388: 389-398.
- McCormack, T., L. W. Gill, O. Naughton and P. M. Johnston. 2014. Quantification of submarine/intertidal groundwater discharge and nutrient loading from a lowland karst catchment. *Journal of Hydrology* 519: 2318-2330.
- Mejías, M., J. García-Orellana, J. L. Plata, M. Marina, E. García-Solsona, B. Ballesteros, P. Masqué, J. López and C. Fernández-Arrojo. 2008. Methodology of hydrogeological characterization of deep carbonate aquifers as potential reservoirs of groundwater. Case

- of study: the Jurassic aquifer of El Maestrazgo (Castellón, Spain). *Environmental Geology* 54: 521-536.
- Mejías, M., B. J. Ballesteros, C. Antón-Pacheco, J. A. Domínguez, J. García-Orellana, E. García-Solsona and P. Masqué. 2012. Methodological study of submarine groundwater discharge from a karstic aquifer in the Western Mediterranean Sea. *Journal of Hydrology* 464: 27-40.
- Moore, W. S. 1976. Sampling ^{228}Ra in the deep ocean. *Deep Sea Research and Oceanographic Abstracts* 23: 647-651.
- Moore, W. S. 1996. Large groundwater inputs to coastal waters revealed by ^{226}Ra enrichments. *Nature* 380: 612-614.
- Moore, W. S. and R. Arnold. 1996. Measurement of ^{223}Ra and ^{224}Ra in coastal waters using a delayed coincidence counter. *Journal of Geophysical Research* 101: 1321-1329.
- Moore, W. S. 2000. Determining coastal mixing rates using radium isotopes. *Continental Shelf Research* 20: 1993-2007.
- Moore, W. S. 2006. Radium isotopes as tracers of submarine groundwater discharge in Sicily. *Continental Shelf Research* 26: 852-861.
- Moore, W. S. 2008. Fifteen years experience in measuring ^{224}Ra and ^{223}Ra by delayed-coincidence counting. *Marine Chemistry* 109: 188-197.
- Moore, W. S. 2010. The effect of submarine groundwater discharge on the ocean. *Annual Review of Marine Science* 2: 59-88.
- Null, K. A., K. L. Knee, E. D. Crook, N. R. de Sieyes, M. Rebolledo-Vieyra, L. Hernández-Terrones and A. Paytan. 2014. Composition and fluxes of submarine groundwater along the Caribbean coast of the Yucatan Peninsula. *Continental Shelf Research* 77: 38-50.
- Pérez-Ramos, I. and B. Andreo. 2007. Masas de aguas subterráneas de Alberquillas y Sierra Almirajara. In Atlas hidrogeológico de la Provincia Málaga, ed. Duran, J. J. 143-148. Instituto Geológico y Minero de España, Diputación de Malaga.
- Peterson, R. N., W. C. Burnett, C. R. Glenn and A. G. Johnson. 2009. Quantification of point-source groundwater discharges to the ocean from the shoreline of the Big Island, Hawaii. *Limnology and Oceanography* 54: 890-904.
- Pinault, J. L., N. Dörfliger, B. Ladouche and M. Bakalowicz. 2004. Characterizing a coastal karst aquifer using an inverse modeling approach: The saline springs of Thau, southern France. *Water Resources Research* 40: 1-17.
- Pluhowski, E. J. 1972. Hydrologic interpretations based on infrared imagery of Long Island, New York. USGS Water-Supply paper 2009-B.

- Rapaglia, J., C. Grant, H. Bokuniewicz, T. Pick and J. Scholten. 2015. A GIS typology to locate sites of submarine groundwater discharge. *Journal of Environmental Radioactivity* 145: 10-18.
- Rapport, D. J. and W. G. Whitford. 1999. How Ecosystems Respond to Stress Common properties of arid and aquatic systems. *BioScience* 49: 193-203.
- Rodellas, V., J. García-Orellana, E. García-Solsona, P. Masqué, J. A. Domínguez, B. J. Ballesteros, M. Mejías and M. Zarroca. 2012. Quantifying groundwater discharge from different sources into a Mediterranean wetland by using ^{222}Rn and Ra isotopes. *Journal of Hydrology* 466: 11-22.
- Rodellas, V., J. García-Orellana, A. Tovar-Sánchez, G. Basterretxea, J. M. López-García, D. Sánchez-Quiles, E. García-Solsona and P. Masqué. 2014. Submarine groundwater discharge as a source of nutrients and trace metals in a Mediterranean bay (Palma Beach, Balearic Islands). *Marine Chemistry* 160: 56-66.
- Rodellas, V., J. García-Orellana, P. Masqué, M. Feldman and Y. Weinstein. 2015. Submarine groundwater discharge as a major source of nutrients to the Mediterranean Sea. *Proceedings of the National Academy of Sciences* 112: 3926-3930.
- Rosenberry, D. O. 2008. A seepage meter designed for use in flowing water. *Journal of Hydrology* 359: 118-130.
- Sadat-Noori, M., I. R. Santos, C. J. Sanders, L. M. Sanders and D. T. Maher. 2015. Groundwater discharge into an estuary using spatially distributed radon time series and radium isotopes. *Journal of Hydrology* 528: 703-719.
- Santos, I. R., W. C. Burnett, J. Chanton, N. Dimova and R. N. Peterson. 2009. Land or ocean?: Assessing the driving forces of submarine groundwater discharge at a coastal site in the Gulf of Mexico. *Journal of Geophysical Research: Oceans* 114: 1-11.
- Schincariol, R. A. and J. D. McNeil. 2002. Errors with small volume elastic seepage meter bags. *Ground Water* 40: 649-651.
- Smith, C. G. and P. W. Swarzenski. 2012. An investigation of submarine groundwater-borne nutrient fluxes to the west Florida shelf and recurrent harmful algal blooms. *Limnology and oceanography* 57: 471-485.
- Stamatis, G., G. Migiros, A. Kontari, E. Dikarou and D. Gamvroula. 2011. Application of tracer method and hydrochemical analyses regarding the investigation of the coastal karstic springs and the submarine spring (Anavalos) in Stoupa Bay (W. Mani Peninsula). In *Advances in the Research of Aquatic Environment*, eds. Lambrakis N., Stournaras G., Katsanou K. 459-467. Environmental Earth Sciences Springer, Heidelberg.

- Stieglitz, T. C., P. G. Cook and W. C. Burnett. 2010. Inferring coastal processes from regional-scale mapping of ^{222}Rn and salinity: examples from the Great Barrier Reef, Australia. *Journal of environmental radioactivity* 101: 544-552.
- Stringfield, V. T. and H. E. LeGrand. 1971. Effects of karst features on circulation of water in carbonate rocks in coastal areas. *Journal of Hydrology* 14: 139-157.
- Sun, Y. and T. Torgersen. 1998. The effects of water content and Mn-fiber surface conditions on ^{224}Ra measurement by ^{220}Rn emanation. *Marine Chemistry* 62: 299-306.
- Surić, M., R. Lončarić, N. Buzjak, S. T. Schultz, J. Šangulin, K. Maldini and D. Tomas. 2015. Influence of submarine groundwater discharge on seawater properties in Rovanjaska-Modrič karst region (Croatia). *Environmental Earth Sciences* 74: 5625-5638.
- Tamborski, J. J., A. D. Rogers, H. J. Bokuniewicz, J. K. Cochran and C. R. Young. 2015. Identification and quantification of diffuse fresh submarine groundwater discharge via airborne thermal infrared remote sensing. *Remote Sensing of Environment* 171: 202-217.
- Taniguchi, M., W. C. Burnett, J. E. Cable and J. V. Turner. 2002. Investigation of submarine groundwater discharge. *Hydrological Processes* 16: 2115-2129.
- Taniguchi, M., T. Ishitobi and K. I. Saeki. 2005. Evaluation of time-space distributions of submarine ground water discharge. *Ground Water* 43: 336-342.
- Taniguchi, M., T. Ishitobi, J. Chen, S. I. Onodera, K. Miyaoka, W. C. Burnett, R. Peterson, G. Liu and Y. Fukushima. 2008. Submarine groundwater discharge from the Yellow River delta to the Bohai Sea, China. *Journal of Geophysical Research: Oceans* 113: 1-11.
- Theodorou, J. A., R. James, I. Tzovenis and C. Hellio. 2015. The recruitment of the endangered fan mussel *Pinna nobilis* (Linnaeus, 1758) on the ropes of a Mediterranean mussel long line farm. *Journal of Shellfish Research* 34: 409-414.
- Tomas, J., F. J. Aznar and J. A. Raga. 2001. Feeding ecology of the loggerhead turtle *Caretta caretta* in the western Mediterranean. *Journal of Zoology* 255: 525-532.
- Tovar-Sánchez, A., G. Basterretxea, V. Rodellas, D. Sánchez-Quiles, J. García-Orellana, P. Masqué and E. García-Solsona. 2014. Contribution of groundwater discharge to the coastal dissolved nutrients and trace metal concentrations in Majorca Island: karstic vs detrital systems. *Environmental Science Technology* 48: 11819-11827.
- Trezzi, G., J. García-Orellana, V. Rodellas, J. Santos-Echeandia, A. Tovar-Sánchez, E. García-Solsona and P. Masqué. 2016. Submarine groundwater discharge: A significant source of dissolved trace metals to the North Western Mediterranean Sea. *Marine Chemistry* 186: 90-100.

- Trezzi, G., J. García-Orellana, V. Rodellas, P. Masqué, E. García-Solsona and P. S. Andersson, 2017. Assessing the role of submarine groundwater discharge as a source of Sr to the Mediterranean Sea. *Geochimica et Cosmochimica Acta* 200: 42-54.
- Valiela, I., K. Foreman, M. LaMontagne, D. Hersh, J. Costa, P. Peckol, B. DeMeo-Andreson, C. D'Avanzo, M. Babione, C.H. Sham and J. Brawley. 1992. Couplings of watersheds and coastal waters: sources and consequences of nutrient enrichment in Waquoit Bay, Massachusetts. *Estuaries* 15: 443-457.
- Valiela, I. and M. L. Cole. 2002. Comparative evidence that salt marshes and mangroves may protect seagrass meadows from land-derived nitrogen loads. *Ecosystems* 5: 92-102.
- Webster, I. T., G. J. Hancock and A. S. Murray. 1995. Modelling the effect of salinity on radium desorption from sediments. *Geochimica et Cosmochimica Acta* 59: 2469-2476.
- Weinstein, Y., Y. Yechieli, Y. Shalem, W. C. Burnett, P. W. Swarzenski and B. Herut. 2011. What is the role of fresh groundwater and recirculated seawater in conveying nutrients to the coastal ocean? *Environmental Science Technology* 45: 5195-5200.
- Wong, W. W., M. R. Grace, I. Cartwright, M. B. Cardenas, P. B. Zamora and P. L. Cook. 2013. Dynamics of groundwater-derived nitrate and nitrous oxide in a tidal estuary from radon mass balance modeling. *Limnology and Oceanography* 58: 1689-1706.
- Worthington, S. R. H. 1999. A comprehensive strategy for understanding flow in carbonate aquifers. In *Karst Modeling* Palmer A. N., Palmer M. V., Sasowsky I. D., eds. 30-37. Karst Waters Institute.
- Yobbi, D. K. 1992. Effects of tidal stage and ground-water levels on the discharge and water quality of springs in coastal Citrus and Hernando Counties, Florida, US Department of the Interior. US Geological Survey, 44 p.

2.10 Appendix I

Table 1. Salinity, temperature, and ^{224}Ra activity concentrations in September of 2006 and 2010 in groundwater (GW) and seawater (SW). GW-CG-1 is a well located in Cerro Gordo that constitutes the radium groundwater end-member (Ra_{SGD}) for Cantarrijan, Palomas, and Sifon Caves. GW-Pz and GW-Well are the installed piezometers and the shallow well sampled on the Cantarrijan Beach; these were used for the salinity mixing model end-member (Sal_{SGD} , Sal_{FSGD} and Sal_{RSGD}).

Sample ID	Date	Time	Coordinates		Temperature (°C)	Salinity	^{224}Ra (dpm m ⁻³)
			Latitude	Longitude			
SW-1	9/21/2010	8:15	36.7515	-3.8170	21.9	36.5	21 ± 2
SW-2	9/21/2010	8:35	36.7495	-3.8176	21.7	36.2	56 ± 4
SW-3	9/22/2010	15:40	36.7468	-3.8083	22.9	36.4	16 ± 2
SW-4	9/22/2010	17:12	36.7441	-3.7989	22.9	36.5	13 ± 2
SW-5	9/22/2010	9:45	36.7414	-3.7896	22.3	36.3	20 ± 2
SW-6	9/22/2010	9:02	36.7386	-3.7802	21.8	36.3	51 ± 4
SW-7	9/23/2010	9:25	36.7386	-3.7802	22.9	36.4	23 ± 3
SW-8	9/22/2010	16:20	36.7487	-3.8286	23.3	36.3	15 ± 2
SW-9	9/21/2010	8:50	36.7460	-3.8193	21.9	36.5	08 ± 1
SW-10	9/22/2010	15:50	36.7433	-3.8099	22.8	36.4	14 ± 2
SW-11	9/22/2010	17:02	36.7406	-3.8006	23.2	36.3	11 ± 1
SW-12	9/22/2010	11:09	36.7379	-3.7911	22.3	36.4	22 ± 2
SW-13	9/22/2010	9:17	36.7352	-3.7817	22.1	36.4	14 ± 2
SW-14	9/23/2010	9:50	36.7293	-3.7616	22.1	36.4	17 ± 2
SW-15	9/22/2010	16:25	36.7453	-3.8302	23.9	36.3	11 ± 1
SW-16	9/21/2010	9:10	36.7426	-3.8208	22.0	36.5	12 ± 2
SW-17	9/22/2010	16:05	36.7399	-3.8114	23.2	36.3	8 ± 1
SW-18	9/22/2010	0:00	36.7345	-3.7927	22.5	36.4	15 ± 2
SW-20	9/22/2010	8:10	36.7291	-3.7740	22.2	36.4	23 ± 2
SW-21	9/23/2010	10:05	36.7291	-3.7740	20.4	36.5	19 ± 2
SW-22	9/21/2010	14:34	36.7264	-3.7647	22.4	36.4	20 ± 2
SW-23	9/21/2010	9:20	36.7392	-3.8223	22.1	36.5	8 ± 1
SW-24	9/22/2010	8:34	36.7284	-3.7849	22.2	36.3	14 ± 2
SW-25	9/22/2010	8:20	36.7256	-3.7754	22.2	36.4	12 ± 2
SW-26	9/21/2010	14:56	36.7230	-3.7660	22.3	36.4	15 ± 2
SW-27	9/21/2010	9:30	36.7357	-3.8239	22.1	36.5	10 ± 2
SW-28	9/21/2010	15:07	36.7195	-3.7676	22.0	36.4	17 ± 2
SW-29	9/21/2010	9:45	36.7324	-3.8255	21.9	36.4	5 ± 1
SW-30	9/21/2010	11:50	36.7253	-3.8286	22.5	36.4	8 ± 1
GW-Well	9/21/2010	17:30	36.7383	-3.7771	21.7	1.6	660 ± 30
GW-Pz-1	9/21/2010	20:00	36.7380	-3.7776	22.1	14.9	2240 ± 190
GW-Pz-2	9/22/2010	9:00	36.7380	-3.7776	22.5	6.6	780 ± 50
GW-Pz-3	9/22/2010	10:00	36.7380	-3.7776	23.9	12.2	1290 ± 80
GW-Pz-4	9/22/2010	0:54	36.7380	-3.7776	24.8	31.1	5500 ± 430
GW-Pz-5	9/22/2010	13:45	36.7380	-3.7776	25.6	24.2	3970 ± 160
GW-CG-1	9/14/2006	14:45	36.7333	-3.7686	24.0	2.2	1260 ± 90
GW-CG-2	9/15/2006	10:00	36.7502	-3.7751	22.8	0.6	1020 ± 80

Table 2. Temperature, electrical conductivity (and salinity), ^{222}Rn , NO_3^- , SO_4^{2-} , $\delta^2\text{H}$, and $\delta^{18}\text{O}$ during July, December of 2015, and July of 2016. In all points of groundwater discharge to the sea, fluxes are also included.

Sampling campaign	Sample ID	Discharge type	Latitude	Longitude	Temp. (°C)	Cond. (Salinity) ($\mu\text{S cm}^{-1}$)	Discharge ($\text{m}^3 \text{d}^{-1}$)	^{222}Rn ($\times 10^3 \text{dpm m}^{-3}$)	NO_3^- (mmol m^{-3})	SO_4^{2-} (mmol m^{-3})	$\delta^2\text{H}$ (‰)	$\delta^{18}\text{O}$ (‰)
September 2010	Cantarrijan C.	SS	36.7381	-3.7784	-	-	840 ± 40	-	-	-	-	-
	Palomas C.		36.7311	-3.7698	-	-	960 ± 50	-	-	-	-	-
	Sifon C.		36.7296	-3.7657	-	-	510 ± 20	-	-	-	-	-
July 2015	Cantarrijan Beach	GS	36.7386	-3.7774	23.9	5560 (3.0)	-	310 ± 70	168	3220	-33	-5.7
	Maro Cliff		36.7531	-3.8397	21.3	794	3010 ± 810	350 ± 50	-	-	-	-
	Alberquillas	GC	36.7502	-3.8090	23.9	866	-	70 ± 40	76	711	-38	-6.4
	Nerja Cave Maro Spring Maro Creek 4	N/A	36.7612	-3.8447	23.0	707	N/A	50 ± 20	21	1710	-41	-6.8
			36.7608	-3.8379	19.5	731	N/A	140 ± 40	20	2520	-46	-7.7
36.7531			-3.8397	22.3	938	-	8 ± 3	-	-	-	-	
December 2015	Cantarrijan Beach	GS	36.7386	-3.7774	17.3	4359 (2.7)	2270 ± 360	240 ± 60	-	-	-	-
	Maro Cliff		36.7531	-3.8397	15.4	731	3060 ± 830	440 ± 60	132	2370	-44	-7.4
	Barranco Maro Huerto Romero Maro Beach	CS	36.7514	-3.8511	15.9	711	-	590 ± 30	483	2750	-42	-7.1
			36.7533	-3.8426	16.1	694	-	690 ± 50	501	2880	-44	-7.3
			36.7539	-3.8363	16.3	703	-	320 ± 30	20	2490	-47	-7.6
	Nerja Cave Maro Spring Maro Creek 1 Maro Creek 2 Maro Creek 3 Maro Creek 4	N/A	36.7612	-3.8447	16.4	687	N/A	57 ± 40	11	1690	-41	-6.8
			36.7608	-3.8379	17.1	698	N/A	250 ± 90	17	2580	-46	-7.7
			36.7602	-3.8374	17.9	754	N/A	-	21	2410	-45	-7.6
			36.7561	-3.8396	18.5	987	N/A	104 ± 20	21	2420	-45	-7.6
				36.7532	-3.8397	16.4	687	N/A	16 ± 7	21	2410	-45
			36.7531	-3.8397	17.2	784	-	4 ± 2	-	-	-	-
July 2016	Cantarrijan Beach	GS	36.7386	-3.7774	20.7	5040 (3.2)	930 ± 160	350 ± 40	127	2850	-34	-5.8
	Maro Cliff		36.7531	-3.8397	20.9	938	2870 ± 770	320 ± 30	88	2140	-44	-7.6
	Doncellas Barranco Maro Huerto Romero Maro Beach Alberquillas	CS	36.7517	-3.8579	20.8	854	460 ± 40	-	400	1680	-40	-6.6
			36.7514	-3.8511	20.2	1003	17 ± 1	-	492	2400	-43	-7.3
			36.7533	-3.8426	21.2	860	37 ± 3	220 ± 140	364	2320	-44	-7.5
			36.7539	-3.8363	20.3	1021	26 ± 2	440 ± 30	435	2590	-44	-7.4
			36.75023	-3.8090	24.5	612	1060 ± 90	-	65	505	-39	-6.5
	Miel Caleta Tierras Nuevas	GC	36.7508	-3.8152	20.9	545	1230 ± 110	-	55	578	-38	-6.6
			36.7535	-3.8458	21.4	871	160 ± 10	-	-	-	-	-
			36.7531	-3.8326	20.7	894	110 ± 10	-	-	-	-	-
Maro Spring Maro Creek 4	N/A	36.7608	-3.8379	19.6	746	N/A	-	15	2170	-46	-7.9	
		36.7531	-3.8397	21.6	1238	60 ± 9	6 ± 2	5	2330	-44	-7.4	
December 2016	Doncellas Barranco Maro Huerto Romero Maro Beach Alberquillas	CS	36.7517	-3.8579	17.1	764	530 ± 50	-	-	-	-	-
			36.7514	-3.8511	15.7	954	70 ± 6	-	-	-	-	-
			36.7533	-3.8426	16.4	819	100 ± 9	-	-	-	-	-
			36.7539	-3.8363	16.9	929	40 ± 4	-	-	-	-	-
			36.7502	-3.8090	21.2	489	1590 ± 140	-	-	-	-	-
	Miel		36.7508	-3.8152	16.0	513	1820 ± 160	-	-	-	-	-
	Caleta Tierras Nuevas Maro Creek 4	GC	36.7535	-3.8458	15.9	945	220 ± 20	-	-	-	-	-
36.7531			-3.8326	15.3	914	190 ± 20	-	-	-	-	-	
			36.7531	-3.8397	17.2	784	160 ± 10	-	-	-	-	

CHAPTER 3:
CONSTRAINING THE IMPORTANCE OF SUBMARINE GROUNDWATER DISCHARGE
(SGD) IN HYDROGEOLOGICALLY COMPLEX ESTUARIES: EXAMPLE OF MOBILE
BAY, ALABAMA

3.1 Abstract

I used a combination of radiotracer techniques (^{226}Ra , ^{224}Ra , ^{223}Ra , and ^{222}Rn), stable isotopes ($\delta^{18}\text{O}$ and $\delta^2\text{H}$), seepage meters, electrical resistivity, and sediment cores collection during three consecutive years (2015-2017) to evaluate the importance of submarine groundwater discharge (SGD) in Mobile Bay (Alabama); the fourth largest estuary in the USA. I found that the magnitude and dynamics of SGD in Mobile Bay, an estuarine system in the northern Gulf of Mexico, were mainly the result of shallow lithological heterogeneities created during the modern development of the bay. I found significant spatial and temporal variations of SGD in the bay. When compared to the riverine discharge, SGD only contributed between 0.2% (wet season) and 5% (dry season) of the total freshwater inputs to Mobile Bay. During the dry season; however, I found that 80% of the total SGD in Mobile Bay occurs in areas that are ecologically impacted by anoxia and massive fish deaths locally known as *Jubilees*. In these areas SGD comprised 37% of the total water inputs during the dry season, coinciding with the time of the year when *Jubilees* occur. Electrical resistivity surveys and characterization of sediment cores collected from the impacted areas revealed that SGD occurs through an organic layer, an important source of nutrients under anoxic conditions; indicating a correlation with *Jubilees*. In conclusion, while SGD might not be a significant source of fresh water in estuaries

as a whole, the lithological heterogeneity of estuaries can result in important SGD inputs and ecological perturbations in specific locations.

3.2 Introduction

Submarine groundwater discharge (SGD) is a significant source of water and dissolved constituents in coastal environments worldwide (Johannes 1980; Moore 1999; Sawyer et al. 2014). However, in river-dominated coastal areas such as estuaries, SGD is typically overlooked due to its limited volumetric contribution compared to fluvial fluxes. Nevertheless, it has been demonstrated that SGD can rival riverine inputs in some areas, specifically with respect to material loadings (Moore 1996; Burnett and Dulaiova 2006; Xu et al. 2013). Understanding the coastal hydrogeology and consequent temporal and spatial variability of SGD is crucial for constructing local water budgets, adequately managing water resources, and studying the effects of SGD on estuarine ecosystems worldwide (Burnett et al. 2003; Henderson et al. 2010; Xu et al. 2013; Befus et al. 2014).

Estuaries are geologically dynamic transition systems which geomorphology, water circulation, biogeochemistry, and ecology vary both temporally and spatially (Dyer 1973; Wolfe 1986; Roman et al. 2000; Krantz et al. 2004). Modern estuaries were formed approximately 5000 years ago when the sea level reached its present level following the shoreline transgression and leading to estuarine-basin sediment accumulation comprised of different facies (Wolfe 1986; Bianchi 2007; Rodriguez et al. 2010). These spatially diverse modern sediment deposits comprise the coastal shallow aquifers through which SGD often occurs (Krantz et al. 2004; Russoniello et al. 2013; Michael et al. 2016). Hydrogeological heterogeneities in combination with short- and long-term fluctuations of marine and terrestrial forcing, typical for coastal settings, result in high temporal and spatial variations of SGD in estuarine systems (Burnett et al.

2006; Santos et al. 2012; Russoniello et al. 2013; Uddameri et al. 2014). Due to this unique variability of SGD, large-scale numerical modeling and assumptions typically applied to terrestrial hydrogeological systems are not applicable to adequately evaluate SGD in estuaries (Stalker et al. 2009; Young et al. 2015).

The development of geochemical tracer techniques (e.g., radium and radon) during the last two decades has significantly advanced our ability to identify and quantify SGD in coastal zones worldwide (Burnett et al. 2003). However, characterizing SGD in estuaries still bears a number of limitations and difficulties. For example, because estuarine basins receive water inputs from multiple sources (e.g., fluvial, marine, and groundwater) that vary seasonally, one of the challenges of using geochemical tracers mass-balances and mixing models is related to uncertainties in the determination of representative end-members (e.g. Xu et al. 2013; Rodellas et al. 2017; Cerdà-Domènech et al. 2017). In the coastal zone, SGD is comprised of terrestrially-driven fresh groundwater (FSGD) and recirculated seawater (RSGD) controlled by marine forces (Taniguchi et al. 2005). Identifying and quantifying these two components is particularly important when constructing the fresh water budgets of coastal aquifers for water resources management efforts (Taniguchi et al. 2002; Null et al. 2012; Montiel et al. 2018). Typically, a salinity mixing model is used to address this task (Taniguchi et al. 2005; Charette 2007; Santos et al. 2009). However, in estuaries, salinity anomalies in the receiving surface waters are the result of both river and groundwater inputs. In these cases, applying a methodology approach based on multiple tracer techniques is imperative (Crusius et al. 2005; Tait et al. 2013).

Recent sensitivity analyses suggest that, in addition to the determination of the SGD end-members, the size of the seepage face bears the second largest uncertainty in radiotracers evaluations in the coastal zone (Montiel et al. 2018). For example, the direct output from the

radon mass-balance modeling approach is groundwater specific discharge or Darcian's velocity (cm d^{-1}) (Burnet and Dulaiova 2003) and converting the radon-derived specific discharge to groundwater discharge ($\text{m}^3 \text{d}^{-1}$) requires constraining the size of the SGD plume area (m^2). This is often highly challenging because of the ephemeral nature of radon-gas and its fast mixing in these dynamic coastal systems (Lambert and Burnett 2003; Stieglitz et al. 2010). Similarly, when using the radium-based mass-balance approach, determining the volume of the tidal prism into which SGD takes place is usually difficult because the fresh groundwater tends to accumulate preferentially in the top layer of the water column (Garcia-Solsona et al. 2010; Tovar-Sanchez et al. 2014; Montiel et al. 2018).

The Mobile Bay Estuary in Alabama is located in the northern Gulf of Mexico to the east of the Mississippi River Delta (Fig. 1). Although this is the fourth largest estuary in the USA, groundwater contribution and hence its importance, has never been studied before. However, previous studies have indicated that SGD might have significant effects on the coastal water quality with important economic and ecologic implications for this coastal region in the Gulf of Mexico (Stumpf et al. 1993; Bricker et al. 2008; Macintyre et al. 2011). During the summer, large-scale mortalities of fish and shellfish, locally known as *Jubilees*, have been observed in Mobile Bay for at least 150 years (Loesch 1960). Affected biota includes mainly demersal fish and crustaceans such as the blue crab, which are very valuable in this region (May 1973). These events have been attributed to water column stratification and oxygen depletion of bottom bay waters (May 1973; Turner et al. 1987). In addition to the *Jubilee* events, harmful algal blooms (HABs) have been reported in the southern area of Mobile Bay where river inputs are limited (Parsons and Dortch 2002; Liefer et al. 2009; Mcintyre et al. 2011; Su et al. 2014). Up to date the direct causes of these two phenomena remain poorly understood.

I assessed the SGD contribution to the water budget of the fourth largest estuary in the US, Mobile Bay, using a combination of radiotracer techniques (^{226}Ra , ^{224}Ra , ^{223}Ra , and ^{222}Rn), stable isotopes ($\delta^{18}\text{O}$ and $\delta^2\text{H}$), and seepage meter deployments during three consecutive years (2015-2017). To understand the preferential SGD flow paths in the heterogeneous shallow aquifer, I conducted shallow geophysical surveys using both land-based (Electrical Resistivity Tomography, ERT) and marine-borne (Continuous Resistivity Profiling, CRP) resistivity measurements, and collected multiple sediment cores from the adjacent shoreline to constrain the interpretations of these measurements.

3.3 Research area

3.3.1 Location and estuary description

Mobile Bay is a shallow (av. depth of 3.5 m) estuary with a total area of 1315 km². The bay exchanges water with the Gulf of Mexico mainly through Main Pass between Dauphin Island and Morgan Peninsula (Greene et al., 2007; Rodriguez et al., 2008) (Fig. 3.1). The climate of coastal Alabama is humid subtropical with annual precipitation of 1670 mm y⁻¹ and an average temperature of 21°C. Rainfall is highly variable throughout the year with a maximum during March and August and minimum during June and October (Ward et al., 2005).

The primary source of runoff into Mobile Bay (~ 95%) is the Mobile-Tensaw River System, which is comprised of five rivers at the Mobile-Tensaw River Delta: the Mobile, Spanish, Tensaw, Apalachee, and Blakeley Rivers. The average discharge of the system is 1500 × 10⁵ m³ d⁻¹ with a strong seasonal pattern that can differ considerably from year to year (Schroeder, 1978; Dzwonkowski et al., 2011). The peak of the river discharge occurs during March coinciding with the highest precipitation, whereas minimum discharge is from July to September (Schroeder et al., 1990; Ward et al., 2005). Discharge from the Mobile-Tensaw River

System is the primary control on the water circulation and residence time in Mobile Bay. However, the flushing rates and salinity variations within the bay are also affected by the interplay of several natural and anthropogenic factors including: prevailing westerly winds during fall/winter and easterly winds during spring/summer, the diurnal tidal cycle (average range is 0.4 m), groundwater inputs, and the presence of a ship channel (Fig. 3.1) dredged frequently to maintain a depth of 15 m (Byrnes et al., 2013; Webb and Marr, 2016; Du et al., 2018).

To facilitate this study, I formally divided the Mobile Bay coastline into three sections based on their shallow geologic make up, similarity in near-shore hydraulic gradients, and surface water tracer data measured during this study. Hereinafter I will refer to them as the (1) *western shore*, (2) *southeastern shore*, and (3) *northeastern shore* (Fig. 3.1). At each of these sections I had a study site (i.e. TS-W, TS-SE, and TS-NE) where I conducted parallel research for comparison purposes.



Figure 3.1. Research area location and hydrogeological map showing the potentiometric surface of the Miocene-Pliocene Aquifer (data from the Geological Survey of Alabama), groundwater flow direction, monitoring wells for groundwater elevation, and sampled wells. The map includes the estuary bathymetry isolines in 1-m intervals (NOAA). The research area is divided in three sections: western shore, northeastern shore, and southeastern shore. At each section, the study sites where ERT lines, sediment core sampling, piezometers installation (Pz-1 to Pz-5), radon time series, radium assessments, and seepage meter deployments were conducted are represented with a star. The locations of Fowl River (FR), Dog River (DR), Mobile River (MR), Spanish River (SR), Tensaw River (TR), Apalachee River (AR), Blakeley River (BR), Fish River (FiR), and Magnolia River (MgR) are also indicated on the map.

3.3.2 Stratigraphy and hydrogeology

The coastal geology of the eastern and western shores of Mobile Bay consists of a Miocene to Holocene sequence of sand strata interbedded by clay layers (Gillet et al., 2000). This configuration comprises the shallow lithology (up to 300 m) and the hydrogeological settings of the Mobile Bay shoreline. Previous studies suggest that groundwater discharge to Mobile Bay most likely occurs through two principal aquifer units comprised of highly heterogeneous deposits: the Watercourse and the Miocene-Pliocene Aquifers (Walter and Kidd, 1979; Gillet et al., 2000). The Watercourse Aquifer (referred as A1 in the literature) is the upper unconfined unit comprised of Pleistocene to Holocene alluvial and coastal deposits with a maximum thickness of 20 m that is present in the southern sector of both the western and eastern shores of Mobile Bay. In the western shore, the Miocene-Pliocene Aquifer is divided into two sandy aquifer units: the semi-confined Middle Sand and the confined Lower Sand units. The Middle Sand unit is comprised of Pliocene deposits and has a maximum thickness of 50 m. The Lower Sand unit with a thickness up to 100 m, is comprised of Miocene deposits. This unit is hydraulically disconnected from the Middle Sand and Mobile Bay at the shallow strata at about 50 m (Gillet et al., 2000). Along the eastern shore, similar stratigraphy is found in the Miocene-Pliocene Aquifer, where a 60-m thick semi-confined Pliocene sandy aquifer is in contact with Mobile Bay along the northeastern and southeastern shores (described in the literature as unit A2). The A2 unit is underlain by a confined Miocene aquifer (unit A3) with a maximum thickness of 300 m (Reed, 1971; Chandler et al., 1985). The semi-confined Middle Sand (in the western shore) and the A2 (in the eastern shore) units, both of Pliocene age, are most likely connected laterally, being part of the same stratigraphic formation. Similarly, the confined

Miocene Lower Sand and the A3 units are also laterally connected underneath Mobile Bay (Gillet et al., 2000; Ellis, 2013).

The regional water table indicates a positive hydraulic gradient towards Mobile Bay along the entire extension of its coastline (except along Bon Secour Bay), indicating that SGD can be ubiquitous (Geological Survey of Alabama, 2018) (Fig. 3.1).

3.4 Methods

3.4.1 Surface water end-members characterization

To characterize the Mobile Bay waters end-member, I conducted boat surveys at a constant speed of 2-4 km h⁻¹ along the shoreline and across Mobile Bay collecting continuous measurements for total ²²²Rn concentrations as well as discrete samples for radium isotopes (²²³Ra, ²²⁴Ra, and ²²⁶Ra) and stable isotopes ($\delta^{18}\text{O}$ and $\delta^2\text{H}$). I repeated these surveys five times, three times during the wet season (March of 2015, March 2016, and July 2017) and twice during the dry season (July of 2015 and March 2017). During all sampling campaigns, conductivity and temperature were measured continuously at 1 min intervals using a conductivity-temperature-depth sensor (CTD, Solinst[®]) with accuracies of $\pm 20 \mu\text{S cm}^{-1}$ and $\pm 0.1^\circ\text{C}$ in conjunction with GPS positioning (Lowrance HDS 5) with an accuracy of ± 1 m. Salinity values were calculated from CTD readings using the conversion method 2520B (APHA, 1999) with an error of ± 0.1 . Radon-222 concentrations in surface waters were measured in 10 min intervals using a RAD7 (Durrige Co., Inc.) portable radon-in-air monitor with a RAD AQUA accessory from a depth of 0.3 m. A detailed description of the survey procedure and RAD7 operation can be found elsewhere (Dulaiova et al., 2005; Dimova et al., 2009). To be able to compare all radon surveys and identify areas with temporally constant peaks of ²²²Rn concentrations, all radon values in surface waters were normalized to the mean value during each survey. Thus, data presented here

is reported also as ^{222}Rn anomalies, defined as positive or negative deviations from the mean. The surface water ^{222}Rn end-members at each study site (i.e. TS-W, TS-SE, and TS-NE) were determined by collecting time-series measurements in 30 –min intervals (0.5 and 5 days) using a RAD AQUA set up, with uncertainties (1σ) of 5-10%. (Fig. 3.1) (Burnett and Dulaiova, 2003).

Concentrations of radium isotopes in bay surface water were evaluated by collecting 120 L samples from a depth of 0.5 m. Samples were measured using a PVC column filled with 20 g (dry weight) of MnO_2 -coated-fibers (Mn-fibers) and filtered with 5 g of clean fiber at a flow rate of approximately 1 L min^{-1} to ensure quantitative radium absorption (Moore, 1976; 2008). Short-lived radium isotopes (^{224}Ra and ^{223}Ra) were measured using a RaDeCC (Radium Delayed Coincidence Counter) system according to Moore and Arnold (1996), Sun and Torgersen (1998), and Garcia-Solsona et al. (2008). The RaDeCC system was calibrated using external (UCSC and FSU) and internal Thorium-232 and Actinium-227 standards. Radium-226 concentrations and uncertainties were measured using the RaDeCC-based method described in Geibert et al. (2013).

Water stable isotopes ($\delta^{18}\text{O}$ and $\delta^2\text{H}$) in surface bay water were filtered with sterile $0.45 \mu\text{m}$ cellulose acetate filters and collected in 40mL vials and were analyzed at the UC Davis Stable Isotopes Facility using a laser spectrometer (Water Isotope Analyzer V2, Los Gatos Research, Inc.) with accuracies of $\pm 1\text{‰}$ and $\pm 0.1\text{‰}$ for $\delta^2\text{H}$ and $\delta^{18}\text{O}$ respectively. Isotopic ratios were calculated using the Vienna Standard Mean Ocean Water (VSMOW, in ‰).

To characterize the river surface water end-member, samples were collected during all sampling campaigns from the Mobile-Tensaw River Delta from Mobile, Tensaw, Apalachee, and Blakeley Rivers at their point of discharge to the bay. The seawater end-member was characterized using samples collected in Dauphin Island representative of the Gulf of Mexico waters entering the bay through Main Pass. Radium isotopes and stable isotopes in river and

seawater end-members were measured following the same procedures and methodologies as for Mobile Bay surface waters. Conductivity, salinity, and temperature were measured using a Pro2030 (YSI Inc.) handheld meter with accuracies of $\pm 1 \mu\text{S cm}^{-1}$, ± 0.1 , and $\pm 0.3^\circ\text{C}$.

3.4.2 Groundwater end-member characterization

To characterize the groundwater end-member at each study site (TS-W, TS-SE, and TS-NE), temperature, salinity, water stable isotopes ($\delta^{18}\text{O}$ and $\delta^2\text{H}$), and radioisotopes (^{222}Rn , ^{223}Ra , ^{224}Ra , and ^{226}Ra) were measured in preexisting inland wells and transects of shore-perpendicular piezometers installed at the shore during this study. The shore-perpendicular transects consisted of five piezometers (Pz-1 to Pz-5) installed at different depths with a 30-cm screened section in the bottom (Fig. 3.1). In all three study sites, piezometers Pz-1 were located 20 m inland from the mid-tidal line, Pz-2 and Pz-3 were placed 10 m away from the shoreline; piezometers Pz-4 were installed at the high tide mark, and piezometer Pz-5 were placed at the low tide mark. From land to offshore, the piezometers were screened at 4 m (Pz-1), 1.5 m (Pz-2), 1 m (Pz-3), 1 m (Pz-4, at the high tide mark), and 1 m (Pz-5, at the low tide mark) depths to include the subsurface mixing zone, i.e. the saltwater-fresh groundwater interphase. Additionally, during July of 2017, a 2 m multi-level piezometer (SE-Pz-4.5) was installed at study site TS-SE. Using this setup, I was able to recover pore water from six ports of the multipoint sampler, at 0.3 m depth intervals. Groundwater was also collected from five deeper wells (screen depth between 10 and 12 m) which were installed farther inland both in the western shore (W-Well-1, W-Well-2, W-Well -3) and the eastern shore (SE-Well-1 and SE-Well-2) of Mobile Bay (Fig. 3.1). In all cases, the radon groundwater end-member was measured with the RAD H₂O system (DurrIDGE, Inc.) using 250 mL duplicates, typically with uncertainties of 10-20%. Radium isotopes and stable isotopes in groundwater were measured following the same procedure and methodologies as described for

surface water end-members but using 20 L for radium samples. Similarly to the river end-member, groundwater conductivity, salinity, and temperature were also measured using the Pro2030 (YSI Inc.) handheld meter.

3.4.3 Shallow aquifer characterization

Five boat surveys employing streaming CRP measurements were conducted using an AGI SuperSting R8 Marine (AGI Inc.) resistivity meter connected to a 33 m floating streamer (11 electrodes with 3 m spacing) which was towed from a boat. Continuous measurements were collected in a dipole-dipole configuration, which allowed a total penetration depth (water column and depth below the sediment-water interface) of 7 m. To inspect the hydrogeological properties of the SGD-saturated shallow sediments, electrical resistivity data from the same depth (5-7 m) during all surveys were extracted and combined to create an integrated one-dimensional map. Land-based shore-perpendicular ERT measurements were conducted at each study site (TS-W, TS-SE, and TS-NE) using a 168 m cable (56 electrodes with 3 m spacing) in a dipole-dipole configuration, which resulted in a sediment penetration depth up to 35 m. To monitor changes in the size of the SGD plume area due to tidal forcing, I performed time-lapsed ERT measurements at each site during falling tide. Data from both CRP and ERT were processed and interpreted using EarthImager 2D software (AGI Inc.). The root mean square error (RMS) and L2-norm (sum of the squared weighted data errors) were used as data quality criteria for all measurements (Advanced Geosciences Inc., 2014). The detailed data processing procedures can be found in Cross et al. (2013) and Dimova et al. (2012).

During the installation of the deepest piezometers at each study site (i.e., piezometers Pz-1), I recovered individual sediment cores using a Geoprobe coring system (Model 5410, Geoprobe Systems Inc.). These three cores (from the three study sites) were brought to the lab

and sectioned in 5 cm intervals for density, porosity, and grain size analysis following the procedure described in Lambe (1951). Grain size was determined using decreasing pore size (2.36 to 0.038 mm) stacked sieves (Fisher Scientific USA standard). Sediments were classified based on the Wentworth scale (Wentworth, 1922). The hydraulic conductivity of each sediment type was estimated for the same sediment samples applying the Hazen approximation using the 10th percentile finer grain size (in mm) of the sediment as described in Hazen (1893). Organic matter content of each sample was obtained following the ASTM 2974-87 methodology via mass differential after combustion at 550°C (American Association for Testing and Materials, 1993).

3.4.4 SGD assessments and Mobile Bay water budget

To evaluate total SGD (both FSGD and RSGD), site-specific ^{222}Rn mass balances (Appendix II Eqs. 3.1, 3.2, and 3.3) were constructed during wet (March of 2015 and 2016, and July 2017) and dry seasons (July of 2015, June of 2016, and March 2017). Descriptions of the radon mass-balance modeling approach can be found elsewhere (Cable et al. 1996; Burnett and Dulaiova 2003; Burnett et al. 2008). During June of 2016 total SGD was also evaluated using Lee-type seepage meters (Lee 1977) that were deployed at all three study sites (Appendix II Eq. 3.4).

To assess the recirculated brackish SGD (RSGD) a three-end-member mixing model was used based on ^{224}Ra and ^{226}Ra activities (e.g. Hwang et al., 2005; Gu et al., 2012) measured in the three end-members, i.e. (1) Mobile-Tensaw River System, (2) seawater, and (3) RSGD, entering Mobile Bay (Appendix II Eqs. 3.5, 3.6, 3.7, 3.8, and 3.9) (Null et al., 2012; Moore, 2003; Young et al., 2008). In addition to the radium approach, I also utilized two-end-member mixing models (Appendix II Eqs. 3.10 and 3.11) based on the water stable isotopes $\delta^{18}\text{O}$ and $\delta^2\text{H}$

to evaluate the FSGD and RSGD components of the total SGD at of each study site following an approach described by Taniguchi et al. (2005).

Finally, the water budget of Mobile Bay was calculated using a three-end-member mixing model (Appendix II Eqs. 3.12, 3.13, and 3.14) based on the water stable isotopes ($\delta^{18}\text{O}$ and $\delta^2\text{H}$) (Doctor et al., 2006). Site-specific water budgets were also constructed for each location (TS-W, TS-ES, and TS-NE) using Eqs. 3.12, 3.13, and 3.14 (Appendix II). In this case, Mobile Bay waters $\delta^{18}O_{MB}$ and δ^2H_{MB} values were obtained exclusively from averaged surface water samples collected near shore (R1, R2, and R3).

3.5 Results

3.5.1 Water end-members

3.5.1.1 Surface water end-members

During the three-year study, ^{222}Rn concentrations in Mobile Bay waters (Mobile Bay end-member) were measured from boat surveys and continuous time-series. During all surveys, radon was always highest at both the northeastern and southeastern shores (study sites TS-NE and TS-SE) with positive anomalies of $0.8 - 5.0 \times 10^3 \text{ dpm m}^{-3}$ and $0.1 - 5.0 \times 10^3 \text{ dpm m}^{-3}$ respectively (Fig. 3.2a). Another persistent positive anomaly of $0.4 - 1.5 \times 10^3 \text{ dpm m}^{-3}$ was detected on the north end of the western shore. However, the ^{222}Rn concentrations in the rest of the western shore, Bon Secour Bay, and mid-bay waters were always significantly lower compared to the whole bay, resulting in negative anomalies of $-4.1 - 0.0 \times 10^3 \text{ dpm m}^{-3}$ (Fig. 3.2a). During all ^{222}Rn time-series measurements the temporal average surface water end-members were $4.7 \pm 1.3 \times 10^3 \text{ dpm m}^{-3}$ (n=353), $6.2 \pm 1.0 \times 10^3 \text{ dpm m}^{-3}$ (n=754), and $8.3 \pm 2.2 \times 10^3 \text{ dpm m}^{-3}$ (n=1191) at study sites TS-W, TS-SE, and TS-NE respectively.

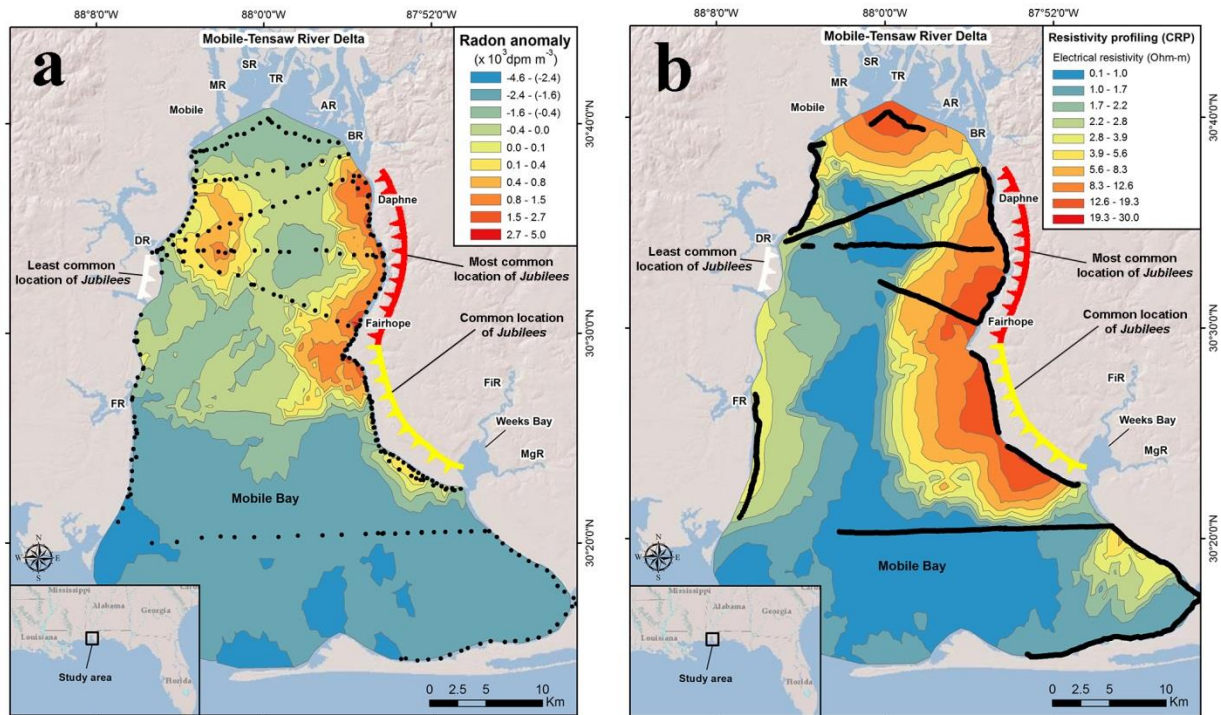


Figure 3.2. (a) Distribution map of ^{222}Rn anomaly surveys on Mobile Bay surface water. The highest ^{222}Rn positive anomalies were found along the northeastern shore ($0.8\text{--}5.0 \times 10^3 \text{ dpm m}^{-3}$) and the southeastern shore ($0.1\text{--}5.0 \times 10^3 \text{ dpm m}^{-3}$). A small positive anomaly ($0.4\text{--}1.5 \times 10^3 \text{ dpm m}^{-3}$) was also detected in the northern sector of the western shore. Along the western shore, Bon Secour Bay, and Mid-Bay the ^{222}Rn concentrations were always lower showing negative anomalies ($-4.1\text{--}0.0 \times 10^3 \text{ dpm m}^{-3}$). (b) Continuous resistivity profiling (CRP) surveys conducted in Mobile Bay showing electrical resistivity at a depth of 5-7m. The highest resistivity values (12-30 Ohm-m) were found along the northeastern and southeastern shores. Near the Mobile-Tensaw River Delta riverine freshwater inputs also result in higher resistivity. Both panels (a and b) show the locations where *Jubilees* occur in Mobile Bay based on Loesch (1960) and May (1971) and modified from the figure created by Fehler (2008).

Salinity in the bay ranged between 0.1 and 19.6 during dry seasons and 0.1 to 6.0 during wet seasons with averages of 4.2 ± 3.2 and 1.7 ± 1.8 respectively (Appendix II Fig. 1a). Water stable isotopes ($\delta^2\text{H}_{\text{MB}}$ and $\delta^{18}\text{O}_{\text{MB}}$) in bay waters were between $-11 \pm 3\text{‰}$ and $-2.2 \pm 0.8\text{‰}$ ($n=30$) during dry seasons and $-20 \pm 4\text{‰}$ and $-3.8 \pm 0.5\text{‰}$ ($n=41$) during wet seasons. Radium concentrations in Mobile Bay waters were on average $200 \pm 20 \text{ dpm m}^{-3}$ (^{226}Ra), $170 \pm 10 \text{ dpm m}^{-3}$ (^{224}Ra), $7 \pm 1 \text{ dpm m}^{-3}$ (^{223}Ra) ($n=32$) during dry seasons. During wet seasons the average

concentrations were $150 \pm 20 \text{ dpm m}^{-3}$ (^{226}Ra), $90 \pm 5 \text{ dpm m}^{-3}$ (^{224}Ra), $4 \pm 1 \text{ dpm m}^{-3}$ (^{223}Ra) (n=29) (Appendix II Table 1 and Figs. 2a and 2b). Radium concentrations in coastal bay waters from the shore-perpendicular transects R1-R3 at each study site were used as the bay surface water end-member in the mixing model (Ra_{MB}) (Appendix II Eqs. 5, 6, 7, and 8; Appendix II Table 1). The residence time (t) in Mobile Bay calculated using Eq. 3.9 (Appendix II) showed similar spatial distributions during both the dry and wet seasons, with averages of 7.0 ± 3.5 days and 5.1 ± 2.5 days, and maximum values of 8.1 and 13.9 days in the southeastern shore and Bon Secour Bay (Figs. 3.3a and 3.3b).

Salinity in the Mobile-Tensaw River System waters was always below 0.4 (i.e. fresh) during all sampling campaigns. The average water stable isotopes in the river system (δ^2H_{River} and $\delta^{18}O_{River}$) during wet seasons were $-18 \pm 3\text{‰}$ and $-3.5 \pm 0.2\text{‰}$ (n=8), and $-15 \pm 2\text{‰}$ and $-3.0 \pm 0.5\text{‰}$ (n=13) during dry seasons (Fig. 3.4). The average radium concentrations (Ra_{River}) were $150 \pm 10 \text{ dpm m}^{-3}$ (^{226}Ra), $50 \pm 3 \text{ dpm m}^{-3}$ (^{224}Ra), and $3.0 \pm 0.2 \text{ dpm m}^{-3}$ (^{223}Ra) (n=7) respectively (Appendix II Table 1).

The average salinity in the Gulf of Mexico's seawater end-member offshore of Dauphin Island was 25.8 ± 1.0 and the water stable isotopes (δ^2H_{ow} and $\delta^{18}O_{ow}$) values were 0.2 and 0.0 (n=3), both in the range of marine environments (Fig. 3.4). Radium end-members in the Gulf seawater (Ra_{ow}) were on average $40 \pm 5 \text{ dpm m}^{-3}$ (^{226}Ra), $20 \pm 3 \text{ dpm m}^{-3}$ (^{224}Ra), and 1 ± 0.2 (^{223}Ra) (n=4) during dry seasons and $50 \pm 7 \text{ dpm m}^{-3}$ (^{226}Ra), $40 \pm 6 \text{ dpm m}^{-3}$ (^{224}Ra), and 2 ± 0.5 (^{223}Ra) (n=4) during rainy seasons (Appendix II Table 1).

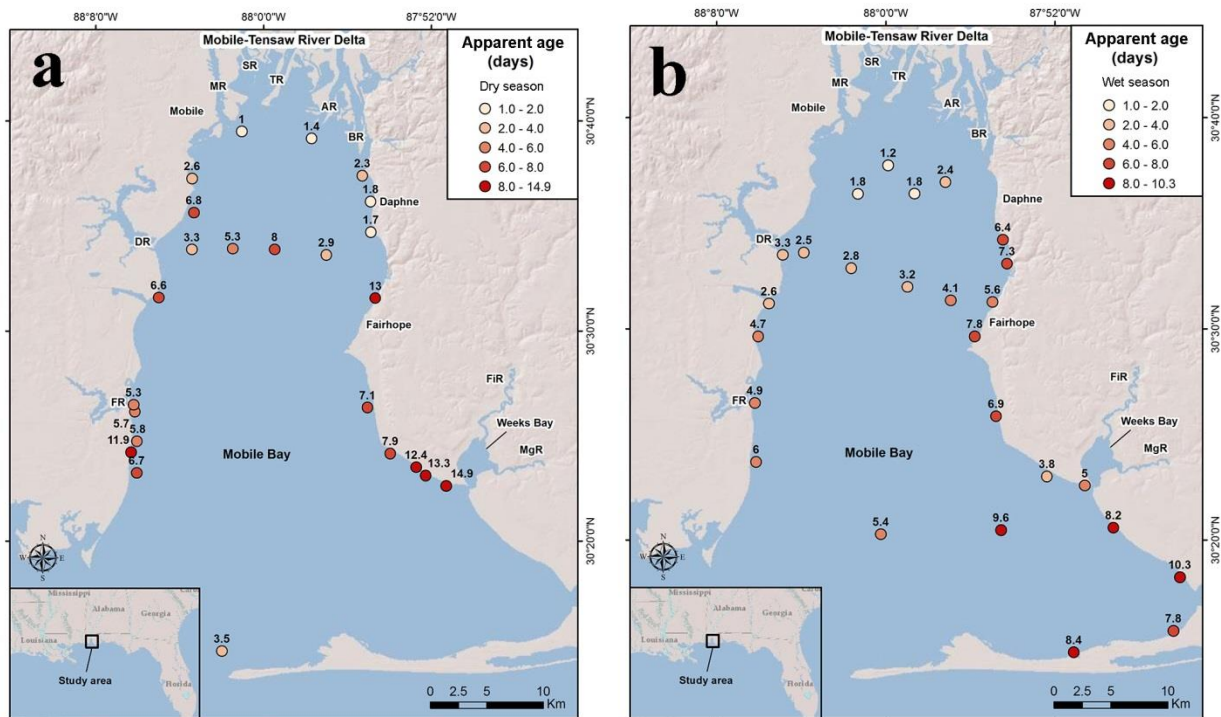


Figure 3.3. Apparent water ages of Mobile Bay waters during the dry (a) and wet (b) seasons based on ^{223}Ra and Ra^{224} activity ratios. The highest water residence times were found on the southeastern shore and Bon Secour Bay, while the lowest values were found near the Mobile-Tensaw Delta and in the Mid Bay area. During dry season when river discharge was lowest, the overall residence time of the bay was higher (7.0 ± 3.5 days) compared to the wet seasons (5.1 ± 2.5 days).

3.5.1.2 Groundwater end-members

On the western shore at study site TS-W, the ^{222}Rn groundwater end-member (Rn_{SGD}) measured in the piezometer transect installed on the beach (W-Pz-1 to W-Pz-3) was between $210 \pm 20 \times 10^3 \text{ dpm m}^{-3}$ and $440 \pm 30 \times 10^3 \text{ dpm m}^{-3}$ with an average of $320 \pm 40 \times 10^3 \text{ dpm m}^{-3}$ ($n=3$). Radium concentrations in W-Pz-5 were $6610 \pm 330 \text{ dpm m}^{-3}$ (^{226}Ra), $1130 \pm 100 \text{ dpm m}^{-3}$ (^{224}Ra), and $30 \pm 2 \text{ dpm m}^{-3}$ (^{223}Ra) ($n=1$); these values are representative of the shallow RSGD and were used as groundwater end-members in the radium mixing models (Ra_{SGD}). The average salinity of groundwater at study site TS-W ranged from 2.1 to 5.7 during wet and dry seasons respectively (Appendix II Table 1). Average water stable isotopes $\delta^2\text{H}$ and $\delta^{18}\text{O}$ values were -

9‰ and -2.1‰ (n=6) during dry seasons and -16‰ and -3.4‰ during wet seasons (n=5) (Fig. 3.4). Values and description of samples used in the mixing model applied to calculate the total SGD to Mobile Bay ($\delta^2H_{SGD}-\delta^{18}O_{SGD}$), RSGD ($\delta^2H_{RSGD}-\delta^{18}O_{RSGD}$), and FSGD ($\delta^2H_{FSGD}-\delta^{18}O_{FSGD}$) end-members can be found in Appendix II.

On the southeastern shore of Mobile Bay, at study site TS-SE, the ^{222}Rn groundwater end-member (Rn_{SGD}) was $50 \pm 10 \times 10^3 \text{ dpm m}^{-3}$ (n=6). Radium concentrations (Ra_{SGD}) were on average $520 \pm 30 \text{ dpm m}^{-3}$ (^{226}Ra), $410 \pm 30 \text{ dpm m}^{-3}$ (^{224}Ra), and $10 \pm 1 \text{ dpm m}^{-3}$ (^{223}Ra) respectively (n=2). The average salinity in groundwater at the TS-SE site ranged from 2.3 to 5.8 during wet and dry seasons respectively (Appendix II Table 1). Average $\delta^2\text{H}$ and $\delta^{18}\text{O}$ values ($\delta^2H_{SGD}-\delta^{18}O_{SGD}$) ranged between -11‰ and -2.5‰ during dry seasons and -17‰ and -3.8‰ during wet seasons (Fig. 3.4).

On the northeastern shore of Mobile Bay, at study site TS-NE, the ^{222}Rn groundwater end-member (Rn_{SGD}) was $60 \pm 20 \times 10^3 \text{ dpm m}^{-3}$ (n=8). Radium concentrations (Ra_{SGD}) were $540 \pm 50 \text{ dpm m}^{-3}$ (^{226}Ra), $480 \pm 40 \text{ dpm m}^{-3}$ (^{224}Ra), and $12 \pm 1 \text{ dpm m}^{-3}$ (^{223}Ra) respectively (n=3). The average salinity ranged from 1.0 to 2.8 during wet and dry seasons respectively (Appendix II Table 1). Average $\delta^2\text{H}$ and $\delta^{18}\text{O}$ values ($\delta^2H_{SGD}-\delta^{18}O_{SGD}$) ranged between -17‰ and -3.6‰ during dry seasons and -20‰ and -4.1‰ during wet seasons (Fig. 3.4).

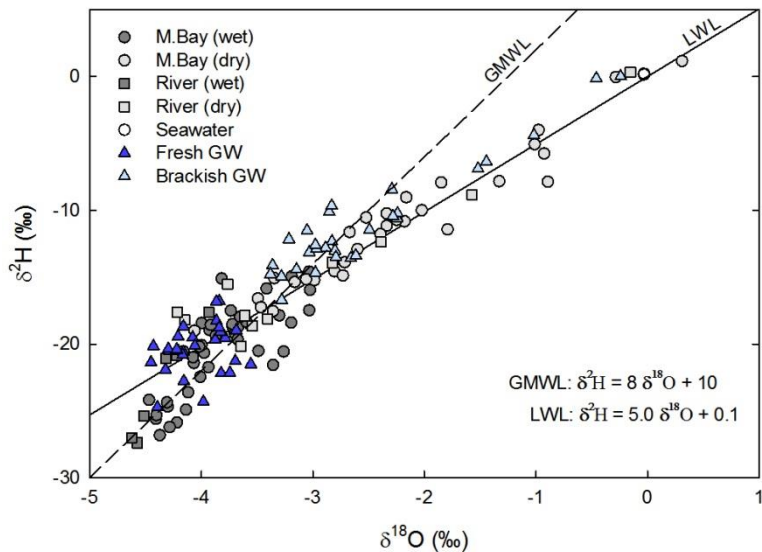


Figure 3.4 Isotopic composition ($\delta^2\text{H}$ and $\delta^{18}\text{O}$) of water samples collected in Mobile Bay (Mobile Bay), Mobile-Tensaw River System (River), seawater from the Gulf of Mexico (Seawater), fresh groundwater (Fresh GW), and brackish groundwater (Brackish GW). Surface water samples (Mobile Bay and rivers) collected during the wet season (wet) are represented in dark grey and samples collected during the dry season (dry) are shown in light grey. Fresh groundwater samples (dark blue) were collected from inland wells W-Well-1 and W-Well-2 on the western shore, wells SE-Well-1, SE-Well-2 and SE-Well-3 on the east shore, and piezometers Pz-1 and Pz-2 at all three study sites. Brackish groundwater samples (light blue) were collected from piezometers Pz-3 to Pz-3 at all three study sites. The Local Water Line (LWL) represents the linear trend based on all water samples collected in the study area and the Global Meteoric Water Line (GMWL) is based on Craig, (1961).

3.5.2 Shallow aquifer properties

3.5.2.1 Continuous resistivity profiling (CRP)

Continuous resistivity profiling (CRP) boat surveys revealed resistivity values for SGD-saturated shallow bay sediments (5-7m depth) between 12 Ohm-m and 30 Ohm-m along the southeastern and northeastern shores, with maximum values of 890 Ohm-m and 40 Ohm-m near study areas TS-NE and TS-SE respectively. Similar resistivity values were measured near the river delta, with maximum values up to 30 Ohm-m. Along the western shore resistivity values were significantly lower, between 3 and 6 Ohm-m, with a maximum of 10 Ohm-m near study

site TS-W (Fig. 3.2b). CRP transects conducted in the interior of Mobile Bay revealed resistivity values consistently lower too, between <1 Ohm-m and 3 Ohm-m (Fig. 3.2b).

3.5.2.2 Electrical resistivity tomography (ERT)

To determine the size of the SGD plume area and characterize the shallow aquifer, land-based electrical resistivity tomography (ERT) was conducted at all three study sites. In all cases, the cable was placed perpendicular to the shore (i.e. parallel to the five-piezometer transect) with about two-thirds of the cable submerged under water. To eliminate lithological interferences in the interpretation of the seepage area dimensions, in all study sites I ran time-lapsed ERT measurements (total of three measurements per site) at a fixed location during falling tide. On the western shore (study site TS-W) I identified three distinctive sediment strata (Fig. 3.5a). From top to bottom these are: (A) a shallow layer with average resistivity 10 Ohm-m found to be present throughout the 2D line; (B) a medium layer with resistivity values of 1 – 3 Ohm-m present from Pz-1 into the bay, and (C) a bottom layer that extends vertically to the full penetration depth with resistivity values between 8 Ohm-m and 35 Ohm-m. During falling tide, resistivity values of this bottom layer changed significantly, an indication that it was saturated with either fresher (groundwater) or brackish (seawater) pore water depending on the tide stage. The size of this anomaly was largest during the lowest tidal stage. In this case I found that the fresher-SGD plume extended about 80 m into the Bay (Fig. 3.5a and Appendix II Fig. 3a).

The ERT measurements conducted in the southeastern and northeastern shore (study sites TS-SE and TS-EN) indicated similar offshore stratigraphy with a sequence of horizontal sediment layers following the same pattern. At study site TS-SE, (A) a shallow sediment layer is present on the surface up to ~60 m from the shore with an electrical resistivity of about 10 Ohm-m. Underlying this shallow layer (B) I identified a sediment deposit with resistivity values of 1 –

3 Ohm-m. Up to the total depth of penetration I found a thick sediment layer (C-D) with resistivity values that varied from 10 Ohm-m to 100 Ohm-m. During time-lapsed ERT measurements, this deeper layer (C-D) experienced a significant increase in resistivity and size, indicating the presence of a groundwater plume that extended up to 70 m offshore during the lowest tide stage (Fig. 3.5b and Appendix II Fig. 3b). At study site TS-NE I found a similar stratigraphy as at study site TS-SE. However, at the land side of the groundwater-seawater mixing zone I identified a high resistivity layer (E) of > 100 Ohm-m, which was not present in study site TS-SE. These high resistivity values were associated with coarse beach sand that extend about 20 m into the bay where it was in contact with sediment layers A, B, C and D, following the same sequence as in TS-SE. During falling tide, I observed that the size of the SGD plume (observed in the coarse sand layer E and layer D) expanded in size and it was largest during the lowest stage of the tide cycle, reaching 100 m offshore (Fig. 3.5c and Appendix II Fig. 3c). I used the plume dimensions measured during the lowest tide stage at the three study sites to calculate the SGD seepage face.

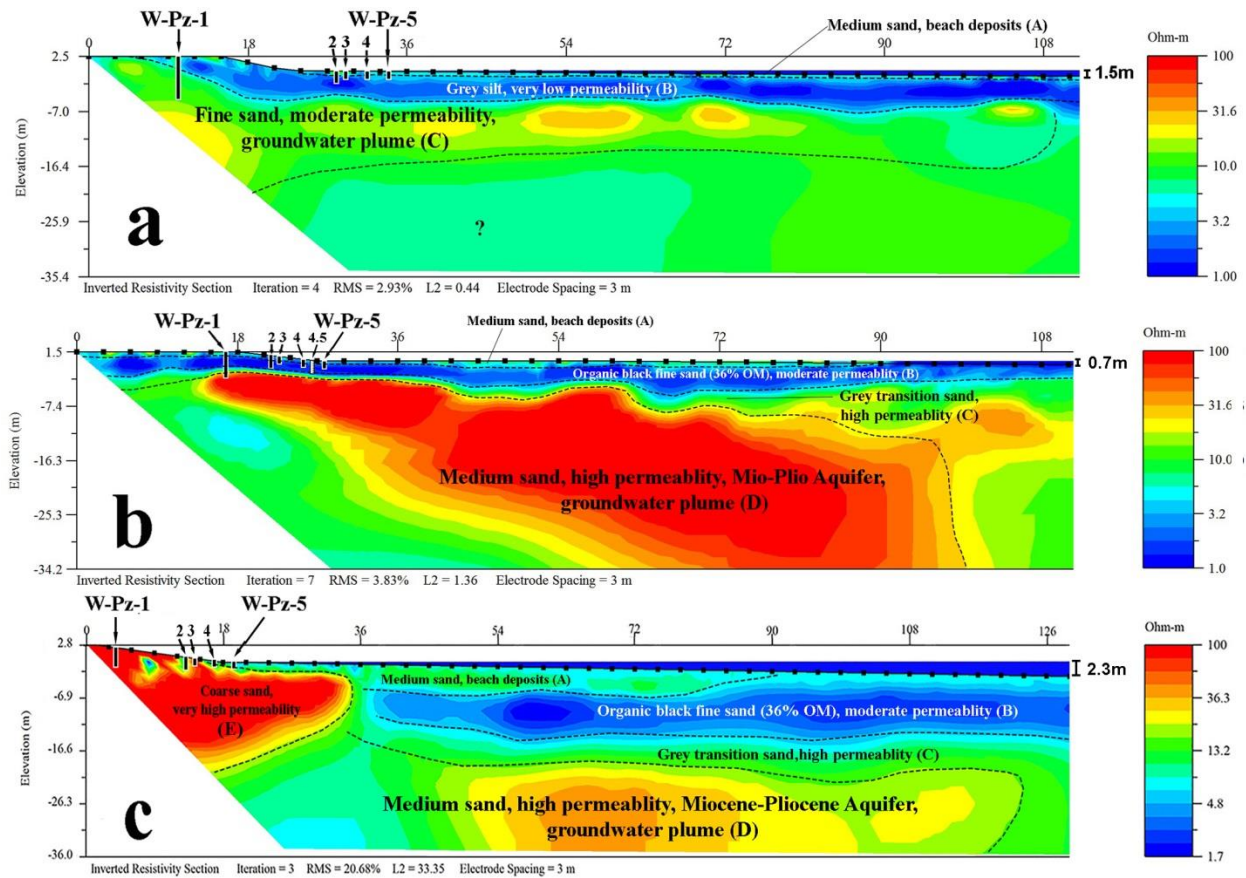


Figure 3.5. Shore-perpendicular electrical resistivity tomography (ERT) image and geologic interpretation at study site TS-W on the western shore (a), study site TS-SE on the southeastern shore (b), and study site TS-NE on the northeastern shore (c). The location and depth of piezometers (Pz-1 to Pz-5) are also shown on each panel. On the western shore I identified a 2.5-m thick silt layer at TS-W and a groundwater plume extent of 80 m (a); at study site TS-SE a 1.5 m thick organic fine sand layer with up to 36% organic matter was found above the medium sand Miocene-Pliocene Aquifer with a groundwater plume extent of 70 m (b); whereas at study site TS-NE I found that an artificially added coarse sand deposit was present at the beach area as well as the fine sand organic layer and the underlying Miocene-Pliocene Aquifer with a groundwater plume extent of 100 m (c). Dashed lines at each ERT image depict the interphase between sediment layers. The maximum water column thickness is also indicated for each study site in the right side of each panel.

3.5.2.3 Shallow coastal sediments characteristics

To constrain the geologic interpretation from the ERT measurements at each study site, I collected a total of three sediment cores (one per study site) at the intertidal zone and performed sediment analyses (Appendix II Figs. 3a, 3b, and 3c). Grain size analyses, density, porosity,

organic matter content, and hydraulic conductivity of all sediment layers can be found in Table 3.1.

Core ID	Layer	Predominant grain size	Grain density (g cm ⁻³)	Porosity	Organic matter content (%)	Hydraulic conductivity (m d ⁻¹)
TS-W	A	Medium sand (70%)	1.44	0.32	2	10.5
	B	Coarse silt (68%)	2.39	0.50	12	4.1
	C	Fine sand (58%)	1.68	0.42	5	7.9
TS-SE	A	Medium sand (75%)	1.54	0.27	3	11.5
	B	Fine sand (80%)	1.30	0.46	36	8.2
	C	Medium sand (65%)	1.28	0.38	7	16.9
	D	Medium sand (78%)	1.19	0.23	2	22.1
TS-NE	E	Coarse sand (75%)	2.24	0.36	1	58.4

Table 3.1. Sediment properties of the three cores extracted at each study site (TS-W, TS-SE, and TS-NE) including grain size, density, porosity, organic matter content, and hydraulic conductivity of all sediment layers identified. At study site TS-W the silt layer (B) restricted groundwater flow from layer C in which I observed a SGD plume extending 80 m in the ERT images; at study site TS-SE I observed that SGD occurred from layer D through the organic layer (B) extending 70 m; whereas at study site TS-NE SGD occurred preferentially through the coarse sand (A) and through the organic layer (B) with a SGD plume extending 100 m in layer D.

The sediment core from study site TS-W was 4 m long, allowing us to capture the vertical lithological structures of the beach slope (Appendix II Fig. 3a). Consistently with the ERT images, sediment analyses revealed a 3-layer structure with: layer (A) up to 0.8 m comprised of medium to coarse sand with a hydraulic conductivity of 10.5 m d⁻¹, layer (B) between 0.8 m and 3.5-m was identified as grey coarse silt to very fine sand deposit with 11% of organic matter and a hydraulic conductivity of 4.1 m d⁻¹, and layer (C) at depth between 3.5 m and 4 m was mostly olive-grey medium to fine sand with a hydraulic conductivity of 7.9 m d⁻¹

(Fig. 3.5a). Based on the stratigraphic data reported in Gillet et al. (2000), layer C most likely corresponds with the Middle Sand formation within the Miocene-Pliocene Aquifer.

The sediment core collected at study site TS-SE was 3 m long and I was able to identify four distinct layers (Appendix II Fig. 3b). From top to bottom these are: (A) a 0.5-m white quartzitic medium to coarse sand with a hydraulic conductivity of 11.5 m d^{-1} , (B) a 1.5-m organic black fine sand containing root fragments and a total organic matter content of 36% with a hydraulic conductivity of 8.2 m d^{-1} , (C) a transitional 0.3-m grey medium to fine sand with 7% organic matter and a hydraulic conductivity of 16.9 m d^{-1} , and layer (D) identified as a clear grey medium sand from 2.3m to 3m depth with a hydraulic conductivity of 22.1 m d^{-1} (Fig. 3.5b). Based on the hydrogeological studies developed in Chandler et al. (1985) and Ellis (2013), layer D probably corresponds to Aquifer A2 in the Miocene-Pliocene Aquifer. Based on the ERT measurements and sediment cores collected 100 m off the shore at TS-NE in July 2018, this this sequence of sediment layers is also present in the northeastern shore. However, the sediment core collected on the shore of site TS-NE was 3.5 m long and showed no vertical structure (Appendix II Fig. 3c); the entire core consisted of coarse sand (E), typical for anthropogenically developed beach areas. The hydraulic conductivity of this layer was the highest of all sediment layers identified during this study with 58.4 m d^{-1} (Fig. 3.5c).

3.5.3 Quantification of SGD

3.5.3.1 SGD variability

To evaluate the driving forces that control SGD and its temporal variability in Mobile Bay, during March 13th-18th of 2016, I conducted a 5-day long hourly continuous SGD rates measurements at all three study sites. During these time-series deployments, I was able to capture the response of the system to two torrential rain events between March 11th and March

18th. During March 11th (rain event 1) the area received ~100 mm of rain and in March 17th-18th a second rain event of 80 mm (rain event 2) took place. Groundwater elevation data from well GSA-B3 obtained from the Geological Survey of Alabama well GSA-B3 (http://www2.gsa.state.al.us/gsa/water/realtime_monitoring.html) and USGS-WB (<https://groundwaterwatch.usgs.gov/>) showed that each rain event was followed by a gradual increase in the Miocene-Pliocene Aquifer elevation (Fig. 3.6).

On the western shore, the tidal stage and SGD rates showed reverse correlation ($R^2=0.75$) during the entire time-series, with the maximum SGD always occurring during low tide (Fig. 3.6a, Appendix II Figs. 4b and 4b). SGD was negatively correlated with groundwater elevation (unit A2 or Middle Sands) of the Miocene-Pliocene Aquifer ($R^2=0.21$) (Fig. 3.6a, Appendix II Fig. 4c). On the northeastern shore, tidal stage and SGD rates were negatively correlated only during the first day of measurements ($R^2=0.77$) (Fig. 3.6b, Appendix II Fig. 5a). After the second day of measurements, I found that SGD rates were positively correlated with the groundwater elevation ($R^2=0.68$) (Fig. 3.6b, Appendix II Fig. 5b). On the southeastern shore the tidal stage was also negatively correlated with SGD throughout the measurement period ($R^2=0.38$) (Fig. 3.6c, Appendix II Fig. 6b) with the maximum correlation found after the second day of measurements ($R^2=0.69$) (Figs. 3.9c and 3.12b). A positive correlation between SGD and the groundwater elevation was found during the 5-day time-series ($R^2=0.17$) where SGD experienced a general decline as the groundwater elevation decreased (Fig. 3.6c, Appendix II Fig. 6c).

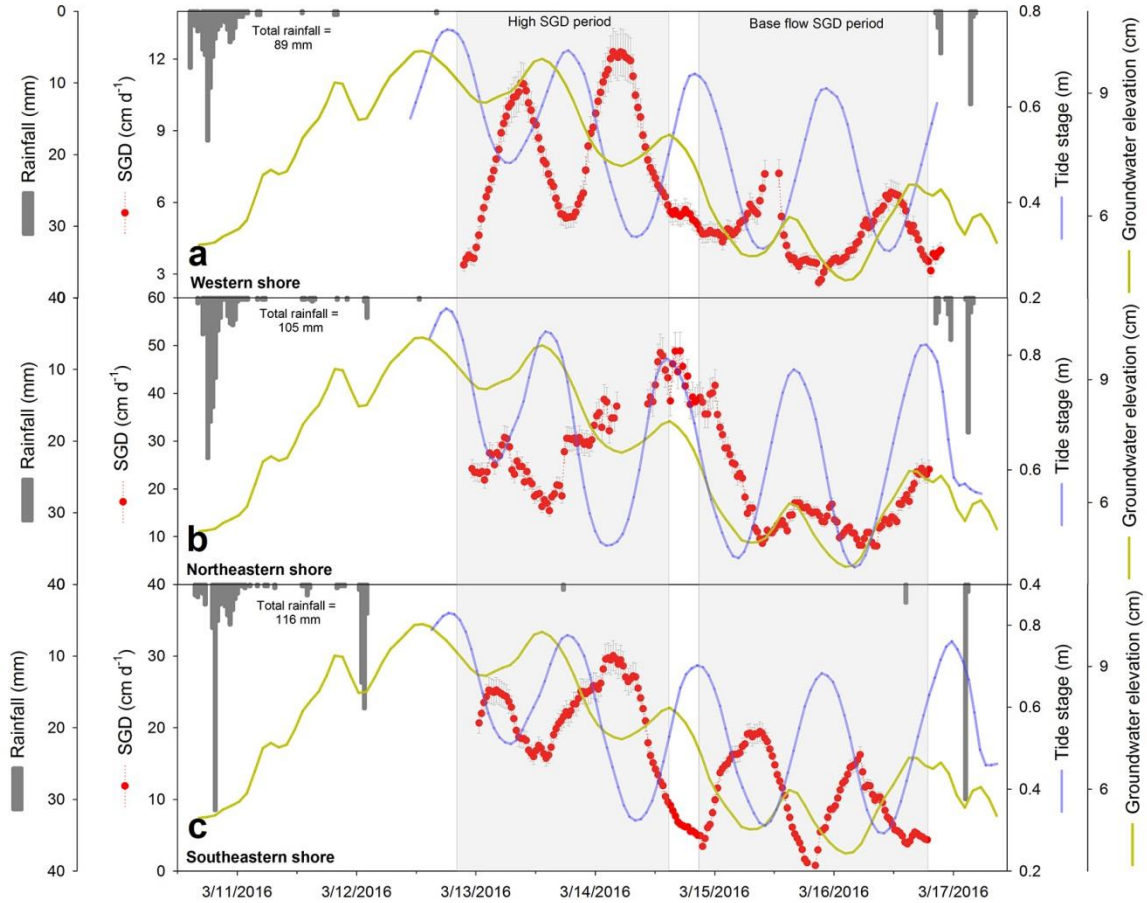


Figure 3.6. Temporal variation of SGD rates (cm d^{-1}) with respect to tide stage (m) in Mobile Bay, precipitation (mm), and groundwater elevation (cm) of the Miocene-Pliocene Aquifer during March 13th-18th at study site TS-W on the western shore (a), TS-NE on the northeastern shore (b), and TS-SE on the southeastern shore (c). Two rain events occurred prior (March 11th-12th) and after (March 17th-18th) the time-series measurements, which were followed by a peak in the groundwater elevation after less than 2 days. Maximum SGD rates were reached after 3-4 days in all study sites.

3.5.3.2 Total SGD assessments

Using the ^{222}Rn mass balance I calculated that the groundwater specific discharge (ω) on the western shore (study site TS-W) during dry seasons was on average $5 \pm 1 \text{ cm d}^{-1}$ ($n=2$), while during dry seasons the specific discharge averaged $6 \pm 2 \text{ cm d}^{-1}$ ($n=2$) (Table 3.2). Using seepage meter deployments at this site during the dry season I found an average specific discharge of $4 \pm 1 \text{ cm d}^{-1}$ ($n=24$). To obtain groundwater fluxes (SGD) applying Eq. 3.3 (Appendix II), a seepage

area (A) of $3.8 \times 10^6 \text{ m}^2$ was calculated by multiplying the SGD plume extent of 80 m based on shore-perpendicular ERT measurements during low tide (Fig. 3.5a) and a coastline length of $47.6 \times 10^3 \text{ m}$, determined by radon anomalies during boat surveys (Fig. 3.2a). Combining results from the ^{222}Rn mass balance and seepage meter measurements I calculated a total SGD flux to the western shore of Mobile Bay of $1.8 \pm 0.6 \times 10^5 \text{ m}^3 \text{ d}^{-1}$ ($n=2$) during the dry seasons, and $2.4 \pm 0.7 \times 10^5 \text{ m}^3 \text{ d}^{-1}$ ($n=2$) during and the wet seasons (Table 3.2, Fig. 3.7). All terms of the ^{222}Rn mass balance during each sampling campaign are shown in Table 3.2.

On the southeastern shore of Mobile Bay at study site TS-SE, the average groundwater specific discharge (ω) was $17 \pm 5 \text{ cm d}^{-1}$ ($n=3$) during dry seasons and $23 \pm 7 \text{ cm d}^{-1}$ ($n=3$) during wet seasons. The average specific discharge determined from the two seepage meter deployments during a dry season was $9 \pm 3 \text{ cm d}^{-1}$ ($n=24$). Using shore-perpendicular ERT measurements and radon surveys at the SE study site, a seepage area (A) of $1.5 \times 10^6 \text{ m}^2$ was calculated using the groundwater plume extent of 70 m (Fig. 3.5b) and a coastline length of $21.5 \times 10^3 \text{ m}$. Combined total SGD from the ^{222}Rn mass balance and seepage meters at TS-SE ranged between $2.3 \pm 1.0 \times 10^5 \text{ m}^3 \text{ d}^{-1}$ ($n=3$) during three dry seasons and $3.8 \pm 1.3 \times 10^5 \text{ m}^3 \text{ d}^{-1}$ ($n=3$) during three wet seasons (Table 3.2, Fig. 3.7).

Location	Season	Sampling campaign	F_{Atm}	F_{Mix}	F_{Diff}	C_{Ra}	Rn_{SGD}	A	ω	SGD	
			$(\times 10^3 \text{ dpm m}^{-2} \text{ d}^{-1})$			(dpm m^{-3})	$(\times 10^3 \text{ dpm m}^{-3})$	$(\times 10^6 \text{ m}^2)$	(cm d^{-1})	$(\times 10^5 \text{ m}^3 \text{ d}^{-1})$	
TS-W	Dry	July-15	3 ± 1	10 ± 3	0.3 ± 0.02	620 ± 60	230 ± 30	3.8	6 ± 2	2.2 ± 0.6	
		June-16	6 ± 2	11 ± 4	0.5 ± 0.04	450 ± 50	230 ± 30	3.8	4 ± 1	1.3 ± 0.4	
		June-16	Seepage meters measurements						3.8	6 ± 1	2.0 ± 0.3
									Average	1.8 ± 0.6	
	Wet	March-15	8 ± 3	43 ± 12	0.5 ± 0.03	130 ± 10	230 ± 30	3.8	6 ± 2	2.4 ± 0.7	
		March-16	17 ± 5	6 ± 2	0.4 ± 0.04	250 ± 20	230 ± 30	3.8	6 ± 2	2.4 ± 0.7	
								Average	2.4 ± 0.7		
TS-SE	Dry	July-15	6 ± 3	21 ± 8	0.6 ± 0.07	240 ± 20	50 ± 10	1.5	20 ± 6	3.0 ± 0.9	
		March-17	0.1 ± 0.01	19 ± 7	0.4 ± 0.05	190 ± 10	50 ± 10	1.5	20 ± 6	3.0 ± 1.0	
		June-16	3 ± 1	9 ± 3	0.5 ± 0.06	40 ± 3	50 ± 10	1.5	13 ± 4	2.0 ± 1.0	
		June-16	Seepage meters measurements						1.5	9 ± 3	1.4 ± 0.7
									Average	2.3 ± 1.0	
	Wet	March-15	8 ± 3	57 ± 14	0.3 ± 0.03	90 ± 5	50 ± 10	1.5	28 ± 9	4.2 ± 1.3	
March-16		32 ± 12	3 ± 1	0.4 ± 0.04	230 ± 10	50 ± 10	1.5	22 ± 7	3.3 ± 1.1		
July-17		2 ± 0.4	35 ± 10	0.5 ± 0.07	290 ± 20	50 ± 10	1.5	25 ± 8	3.8 ± 0.3		
								Average	3.8 ± 1.3		
TS-NE	Dry	June-16	2 ± 0.08	17 ± 6	0.4 ± 0.03	170 ± 20	60 ± 20	2.3	14 ± 5	3.2 ± 1.1	
		June-16	Seepage meters measurements						2.3	17 ± 4	3.9 ± 0.9
		March-17	0.5 ± 0.1	28 ± 9	0.4 ± 0.05	190 ± 10	60 ± 20	2.3	20 ± 7	4.6 ± 1.7	
									Average	3.9 ± 1.7	
	Wet	March-16	14 ± 4	8 ± 2	0.3 ± 0.03	190 ± 20	60 ± 20	2.3	24 ± 9	5.7 ± 2.0	
		July-17	9 ± 2	56 ± 19	0.5 ± 0.07	80 ± 6	60 ± 20	2.3	25 ± 9	5.8 ± 2.1	
								Average	5.7 ± 2.1		
Mobile Bay								Total	Dry	4.7-11.3	
									Wet	7.8-16.0	

Table 3.2. Radon mass balance to assess the total SGD at each study site (TS-W, TS-SE, and TS-NE) during all sampling campaigns. Seepage velocity (ω) and groundwater fluxes (SGD) obtained from seepage meters deployments during June 2016 are also shown for each study site. The average groundwater fluxes (SGD) during the dry and wet seasons is shown for each site. Additionally, the total SGD in Mobile Bay from all study sites is presented as a range including uncertainties during each sampling campaign.

At study site TS-NE on the northeastern shore of Mobile Bay, the average specific discharge (ω) was $16 \pm 6 \text{ cm d}^{-1}$ ($n=2$) during dry seasons and $24 \pm 9 \text{ cm d}^{-1}$ ($n=2$) during wet seasons. Average specific discharge was $17 \pm 4 \text{ cm d}^{-1}$ ($n=24$) using seepage meter measurements during a dry season. The groundwater plume extent (from ERT shore-perpendicular measurements) of 100 m (Fig. 3.5c) and a coastline length of $2.3 \times 10^3 \text{ m}$ (from ^{222}Rn anomalies surveys) were used to calculate a seepage area (A) of $2.3 \times 10^5 \text{ m}^2$. Average SGD derived from the ^{222}Rn mass balance and seepage meters during two dry and wet seasons was $3.9 \pm 1.7 \times 10^5 \text{ m}^3 \text{ d}^{-1}$ ($n=2$) and $5.7 \pm 2.1 \times 10^5 \text{ m}^3 \text{ d}^{-1}$ ($n=2$) respectively (Table 3.2, Fig. 3.7).

Combining the groundwater fluxes measured at all three study sites (TS-W, TS-SE, and TS-NE), I found that the total SGD (combined FSGD and RSGD) to Mobile Bay using the ^{222}Rn and seepage meter methods ranged between $8.0 \pm 3.3 \times 10^5 \text{ m}^3 \text{ d}^{-1}$ during dry seasons and $11.9 \pm 4.1 \times 10^5 \text{ m}^3 \text{ d}^{-1}$ during wet seasons (Table 3.2, Fig. 3.7).

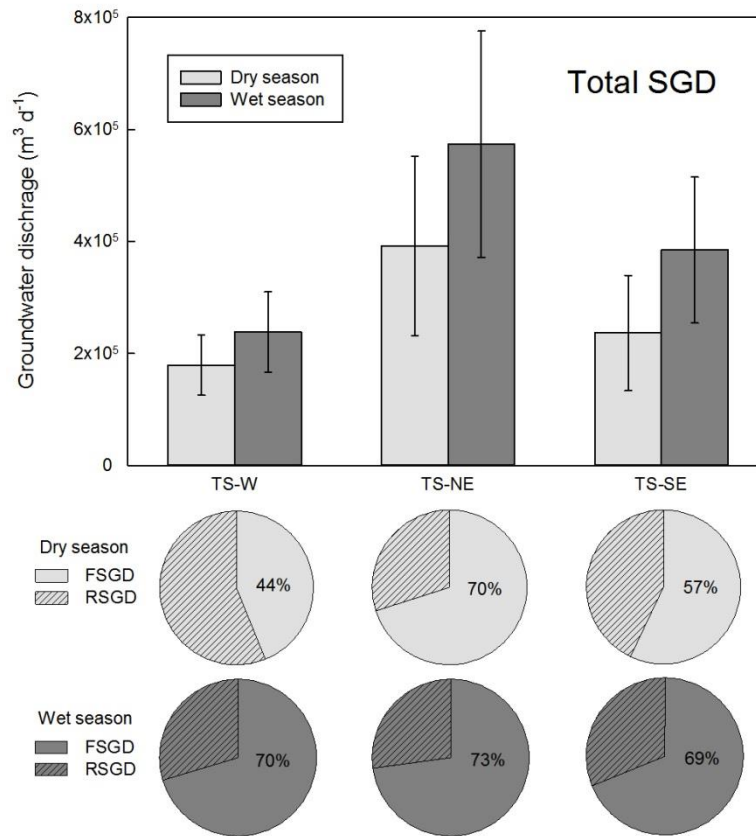


Figure 3.7. The upper bar plot shows the total SGD in Mobile Bay ($m^3 d^{-1}$) showing groundwater discharge measured at all three study sites (TS-W, TS-NE and TS-SE) during the dry (light grey) and wet (dark grey) seasons. The lower panel shows a comparison between the fresh SGD (FSGD) and recirculated SGD (RSGD) components of the total SGD during dry and wet seasons.

3.5.3.3 FSGD and RSGD individual assessments

Using the radium isotopes mixing model (Appendix II Eqs. 3.5, 3.6, and 3.7), I calculated that the average brackish recirculated SGD (RSGD) on the western shore study site (i.e. TS-W) ranged between $0.7 \pm 0.2 \times 10^5 m^3 d^{-1}$ ($n=2$) during dry seasons and $1.6 \pm 0.4 \times 10^5 m^3 d^{-1}$ ($n=2$) during wet seasons (Table 3.3). On the southeastern shore at study site TS-SE, RSGD was $1.1 \pm 0.3 \times 10^5 m^3 d^{-1}$ ($n=3$) during dry seasons and $1.7 \pm 0.4 \times 10^5 m^3 d^{-1}$ ($n=3$) during wet seasons, whereas on the northeastern shore at study site TS-NE, RSGD was $1.5 \pm 0.3 \times 10^5 m^3 d^{-1}$ ($n=2$)

during dry and $3.2 \pm 0.6 \times 10^5 \text{ m}^3 \text{ d}^{-1}$ (n=2) during wet seasons (Table 3.3). All terms used in the radium mixing model are shown in Table 3.3.

To calculate FSGD and RSGD independently of the radioisotope approaches, I also applied two site- and season-specific end-member mixing models using $\delta^{18}\text{O}$ and $\delta^2\text{H}$ (Appendix II Eqs. 3.9 and 3.10). Using this approach I found that on the western shore (TS-W) RSGD represented 56% of the total SGD during dry seasons and 30% during wet seasons (Table 3.4). In comparison, based on the radium method RSGD represented 38% and 66% during the dry and wet seasons (Table 3.3). On the southeastern shore (TS-SE), RSGD accounted for 43% (dry) to 31% (wet) and 48% (dry) to 45% (wet) using the radium approach. On the northeastern shore (TS-NE), RSGD ranged from 30% (dry) to 27% (wet), whereas the radium method yielded contributions of 38% (dry) to 56% (wet) (Table 3.3 and Table 3.4).

Based on these proportions and considering the total SGD obtained from the ^{222}Rn and seepage meter methods, FSGD in the western shore at study site TS-W was between $0.8 \pm 0.3 \times 10^5 \text{ m}^3 \text{ d}^{-1}$ during dry season and $1.7 \pm 0.5 \times 10^5 \text{ m}^3 \text{ d}^{-1}$ during the wet seasons. In the southeastern shore at study site TS-SE, FSGD ranged between $1.2 \pm 0.4 \times 10^5 \text{ m}^3 \text{ d}^{-1}$ and $2.6 \pm 0.9 \times 10^5 \text{ m}^3 \text{ d}^{-1}$; whereas at the northeastern shore study site TS-NE, FSGD was $2.7 \pm 1.1 \times 10^5 \text{ m}^3 \text{ d}^{-1}$ to $4.2 \pm 1.6 \times 10^5 \text{ m}^3 \text{ d}^{-1}$ (Table 3.4, Fig. 3.7). Combining the FSGD in all sections the total FSGD to Mobile Bay ranged between $2.8 \times 10^5 \text{ m}^3 \text{ d}^{-1}$ during the dry season and $11.5 \times 10^5 \text{ m}^3 \text{ d}^{-1}$ during the rainy season, considering all uncertainties (Table 3.4).

Location	Season	Sampling campaign	$^{226}\text{Ra}_{\text{River}}$	$^{224}\text{Ra}_{\text{River}}$	$^{226}\text{Ra}_{\text{RSGD}}$	$^{224}\text{Ra}_{\text{RSGD}}$	$^{226}\text{Ra}_{\text{ow}}$	$^{224}\text{Ra}_{\text{ow}}$	$^{226}\text{Ra}_{\text{MB}}$	$^{224}\text{Ra}_{\text{MB}}$	t	V	f_{RSGD}	RSGD	
											(d)	($\times 10^6 \text{ m}^3$)	(%)	($\times 10^5 \text{ m}^3 \text{ d}^{-1}$)	
TS-W	Dry	July-15	20 ± 2	10 ± 2	6610 ± 500	1130 ± 100	90 ± 5	20 ± 3	620 ± 30	200 ± 10	6 ± 0.3	7.6	8	1.0 ± 0.2	
		June-16	200 ± 20	70 ± 2	6610 ± 500	1130 ± 100	20 ± 2	10 ± 1	50 ± 4	100 ± 7	4 ± 0.2	7.6	3	0.5 ± 0.1	
													Average	0.7 ± 0.2	
	Wet	March-15	100 ± 7	40 ± 3	6610 ± 500	1130 ± 100	40 ± 3	40 ± 4	90 ± 5	70 ± 3	6 ± 0.4	7.6	17	2.1 ± 0.4	
		March-16	100 ± 7	40 ± 3	6610 ± 500	1130 ± 100	40 ± 3	40 ± 4	250 ± 20	90 ± 8	7 ± 0.5	7.6	10	1.1 ± 0.2	
														Average	1.6 ± 0.4
TS-SE	Dry	July-15	20 ± 2	10 ± 2	350 ± 20	340 ± 20	90 ± 5	20 ± 3	240 ± 20	100 ± 10	7 ± 0.6	3.0	23	1.0 ± 0.2	
		March-17	180 ± 10	80 ± 7	350 ± 20	340 ± 20	20 ± 2	10 ± 1	230 ± 10	220 ± 20	8 ± 0.6	3.0	35	1.3 ± 0.3	
		June-16	200 ± 20	70 ± 2	350 ± 20	340 ± 20	20 ± 2	10 ± 1	50 ± 4	60 ± 5	6 ± 0.4	3.0	18	0.9 ± 0.2	
														Average	1.1 ± 0.3
	Wet	March-15	100 ± 7	40 ± 3	700 ± 40	470 ± 30	40 ± 3	40 ± 4	90 ± 5	90 ± 5	4 ± 0.3	3.0	18	1.4 ± 0.3	
		March-16	100 ± 7	40 ± 3	700 ± 40	470 ± 30	40 ± 3	40 ± 4	230 ± 10	220 ± 20	9 ± 0.7	3.0	57	1.9 ± 0.4	
July-17		180 ± 10	80 ± 7	700 ± 40	470 ± 30	70 ± 5	50 ± 3	170 ± 10	80 ± 7	5 ± 0.4	3.0	29	1.7 ± 0.4		
													Average	1.7 ± 0.4	
TS-NE	Dry	June-16	200 ± 20	70 ± 2	540 ± 40	480 ± 30	20 ± 2	10 ± 1	170 ± 10	140 ± 10	7 ± 0.6	4.7	24	1.6 ± 0.3	
		March-17	180 ± 10	80 ± 7	540 ± 40	480 ± 30	20 ± 2	10 ± 1	60 ± 4	70 ± 5	8 ± 0.6	4.7	30	1.4 ± 0.3	
														Average	1.5 ± 0.3
	Wet	March-16	100 ± 7	40 ± 3	600 ± 40	430 ± 30	40 ± 3	40 ± 4	190 ± 20	130 ± 10	10 ± 0.9	4.7	68	3.2 ± 0.6	
		July-17	180 ± 10	80 ± 7	600 ± 40	430 ± 30	70 ± 5	50 ± 3	80 ± 6	130 ± 10	4 ± 0.3	4.7	25	3.3 ± 0.6	
														Average	3.2 ± 0.6
Mobile Bay														Dry	2.5-4.1
												Total		Wet	5.1-8.9

Table 3.3. Summary of values for all parameters used in the radium mixing models to assess the recirculated SGD (RSGD) at each study site (TS-W, TS-SE, and TS-NE) during the dry and wet seasons. The fraction of RSGD (f_{RSGD}) with respect to the total inputs (RSGD, river, and the seawater from the Gulf of Mexico) obtained when solving the models is shown along with the respective RSGD. The total RSGD in Mobile Bay is presented as a range including uncertainties during each sampling campaign.

Location	Season	$\delta^{18}\text{O}_{\text{FSGD}}$	$\delta^{18}\text{O}_{\text{RSGD}}$	$\delta^{18}\text{O}_{\text{SGD}}$	f_{FSGD}	f_{RSGD}	$\delta^2\text{H}_{\text{FSGD}}$	$\delta^2\text{H}_{\text{RSGD}}$	$\delta^2\text{H}_{\text{SGD}}$	f_{FSGD}	f_{RSGD}	Average f_{FSGD}	Average f_{RSGD}	FSGD	RSGD
		(‰ VSMOW)			(%)		(‰ VSMOW)			(%)		(%)		$(\times 10^5 \text{ m}^3 \text{ d}^{-1})$	
TS-W	Dry	-4.2	-0.5	-2.1	45	55	-20	0	-9	43	57	44 ± 6	56 ± 7	0.8 ± 0.3	1.0 ± 0.3
	Wet	-4.2	-1.5	-3.4	71	29	-20	-7	-16	70	30	70 ± 8	30 ± 3	1.7 ± 0.5	0.7 ± 0.2
TS-SE	Dry	-4.0	-0.2	-2.5	60	40	-20	0	-11	54	46	57 ± 10	43 ± 8	1.2 ± 0.4	1.0 ± 0.3
	Wet	-4.2	-2.8	-3.8	70	30	-20	-10	-17	68	32	69 ± 5	31 ± 2	2.6 ± 0.9	1.2 ± 0.4
TS-NE	Dry	-4.0	-2.2	-3.6	74	26	-20	-10	-17	67	33	70 ± 8	30 ± 4	2.7 ± 1.1	1.2 ± 0.4
	Wet	-4.2	-3.9	-4.1	66	34	-20	-18	-20	80	20	73 ± 3	27 ± 1	4.2 ± 1.6	1.5 ± 0.5
Mobile Bay												Total	Dry	2.8-6.5	2.2-4.2
													Wet	5.5-11.5	2.3-4.5

Table 3.4. End-member values used in the site- and season-specific $\delta^{18}\text{O}$ and $\delta^2\text{H}$ mixing models utilized to calculate the proportional fraction of fresh SGD (FSGD) and recirculated SGD (RSGD) from the total SGD at all three study sites (TS-W, TS-SE, and TS-NE) during the dry and wet seasons. The fraction of both FSGD and RSGD (f_{FSGD} and f_{RSGD}) are also shown for each mixing model and their average (Average f_{FSGD} and f_{RSGD}) for each study site during the dry and wet seasons. The FSGD and RSGD values shown in the table were obtained by multiplying the Average f_{FSGD} and Average f_{RSGD} components by the average total SGD (SGD) presented in Table 3.2, measured during each season at each of the three study sites. The total FSGD and RSGD in Mobile Bay are presented as a range including variations during each sampling campaign.

3.6 Discussion

3.6.1 Hydrodynamics in Mobile Bay

I found that the residence time in Mobile Bay varied seasonally and was primarily controlled by the Mobile-Tensaw River System discharge. The average water apparent age in Mobile Bay during the wet season was 5.1 days when the river flux was on average $2450 \times 10^5 \text{ m}^3 \text{ d}^{-1}$, whereas during dry seasons it was 7.0 days when the river discharge was on average $260 \times 10^5 \text{ m}^3 \text{ d}^{-1}$. These values are comparable to other river-dominated estuaries with similar river fluxes and basin morphologies (e.g., Dulaiova et al., 2006). For instance, Dulaiova and Burnett (2008) determined that the residence time in the Apalachicola Bay (Florida), a similar estuary in the Northern Gulf of Mexico, was governed by the magnitude of the Apalachicola River discharge. During high flow conditions ($878 \times 10^5 \text{ m}^3 \text{ d}^{-1}$) Dulaiova and Burnett (2008) using a similar approach estimated an average residence time of 6.9 days compared to 13.0 days during low discharge ($292 \times 10^5 \text{ m}^3 \text{ d}^{-1}$).

Based on the spatial distribution of the water apparent ages determined by this study I found that during high flow conditions, the water circulation of the river plume in Mobile Bay occurs counterclockwise. Younger ages (1.0-2.4 days) were found at the mouth of the river (as to be expected) and along the western shore of the bay (2.5-4.9 days). In contrast, older ages were detected near Main Pass (5.4-6.0 days), along the eastern shore of Mobile Bay (3.8-7.8 days), and Bon Secour Bay (7.8-10.3 days) (Fig. 3.3b). These longer residence times measured along the southeastern area of the bay are the result of the Mobile Bay's geometry and local winds (Noble et al., 1996; Park et al., 2007; Dzwonkowski et al., 2011). I suggest that Dauphin Island and the Fort Morgan Peninsula deflect part of the estuary's outflow, which is then most likely forced towards the east by the prevailing easterly winds that were present during all sampling

campaigns (<https://tidesandcurrents.noaa.gov>). This spatial distribution is in excellent agreement with estimations reported in Webb and Marr (2016) using a numerical modeling approach to determine the bay circulation. The model yielded lower residence time values (1-6 days) for the western shore and Mid-Bay area and higher residence times (8 and 14 days) on the southeastern shore and Bon Secour Bay. Furthermore, salinity distributions in Mobile Bay during this three-year study during high flow conditions confirmed this circulation pattern as well (Appendix II Fig. 1b). Low salinities (0.1-2.0) attributed to the freshwater plume of the Mobile-Tensaw River System were observed to extend from the river delta towards Main Pass along the Mid Bay area (Appendix II Fig. 1b). Consistently with the water ages, the highest salinity values within the Bay were measured in Bon Secour Bay (4.5-6.0), also indicating that the water tends to remain stagnant in this area, where evaporation leads to higher salinity values (Appendix II Fig. 1b).

However, I also observed that during the dry season (i.e. low flow conditions), the described circulation pattern was not that apparent. The water residence time increased equally along the eastern (2.3-14.9) and western (2.6-11.9 days) shores; with a gradual increase across the bay from the river delta to the south (Fig. 3.3a). I observed relatively long residence times in the Mid Bay area (2.9-8.0 days), indicating that the river plume moved preferentially near the shores (Fig. 3.3a). The salinity distribution measured during the dry season also supports this pattern, with relatively higher values in the Mid Bay area (6.0-10.0) and gradual increase along the eastern (1.0-12.0) and western shores (1.5-17.0) (Appendix II Fig. 1a). These findings based on radiotracer field data were also confirmed by Du et al. (2018), who also found that during the wet season the river plume flows preferentially along the western shore and Mid Bay area of Mobile Bay, whereas Bon Secour Bay and the southeastern shore remain unaffected by the flushing effect of the river discharge. During the dry season Du et al. (2018) also observed that

the flow direction diverts towards the western and eastern shores from the river delta towards Main Pass. Furthermore, using a modeling approach Du et al. (2018) found significantly higher residence times in Bon Secour Bay and the southeastern section during both wet and dry seasons (12-48 days), also indicating the water tendency to remain stagnant in this area.

Based on these bay water circulation patterns and using the water residence times estimated in this study I also calculated the average water flushing rate (km d^{-1}) in Mobile Bay, Alabama. Flushing rate is an extremely important ecological parameter for estuarine ecosystems. Most often the flushing rates are applied to study the transport dynamics of dissolved contaminants and suspended particles in the bay. Specifically for Mobile Bay, understanding the transport time scales of terrestrial material in the estuary and their export to the Gulf of Mexico is essential to further study the impact on the estuarine and marine ecosystems on the Gulf system (Moore and Krest, 2004; Peterson et al., 2008). As in other similar studies (e.g. Moore, 2000; Dulaiova et al., 2006), I define this term as the time that the river water inputs take to flow across the 46-km transect from the river delta to Main Pass, considering the water circulation described above.

Based on the apparent water ages and following the methodology described by Moore (2000), I estimated that the flushing rate in Mobile Bay ranged from 3.3 km d^{-1} during the dry season (when the river flux was $260 \times 10^5 \text{ m}^3 \text{ d}^{-1}$) to 4.7 km d^{-1} during the wet season (when the river flux was $2450 \times 10^5 \text{ m}^3 \text{ d}^{-1}$). For comparison, through a modeling approach Du et al. (2018) estimated that the flushing times in Mobile Bay are 32.9 and 10.2 days during low ($426 \text{ m}^3 \text{ s}^{-1}$) and high river flow ($2,199 \text{ m}^3 \text{ s}^{-1}$). These flushing times over the 46-km transect of Mobile Bay correspond to flushing rates of 1.4 km d^{-1} to 4.5 km d^{-1} , in close agreement with my estimations. Similar flushing rates have been measured in other large estuaries worldwide. For instance,

Dulaiova et al. (2006) estimated that the flushing rate in the Chao Phraya Estuary (Thailand) was 2.9 km d^{-1} with a river discharge of $41 \times 10^5 \text{ m}^3 \text{ d}^{-1}$, in the Todos os Santos Bay (Brazil) Hatje et al. (2017) measured a flushing rate of 5 km d^{-1} with a river discharge of $104 \times 10^5 \text{ m}^3 \text{ d}^{-1}$, whereas Xu et al. (2013) found a flushing rate of 8.4 km d^{-1} during a river discharge of $16416 \times 10^5 \text{ m}^3 \text{ d}^{-1}$ in the Yellow River Estuary. The flushing rate variations measured in Mobile Bay ($3.3\text{-}4.7 \text{ km d}^{-1}$) during contrasting river discharge is thus, comparable to other large estuaries under different climatic conditions, showing a dependence on river flow conditions.

3.6.2 SGD dynamics and driving forces

I found that the magnitude and dynamics of SGD in Mobile Bay (Alabama) was controlled mainly by two driving forces including (i) terrestrial hydraulic gradients in the coastal aquifer and (ii) tidal pumping (Moore, 2010; Santos et al., 2012). On a large time-scale, the dominant mechanism controlling SGD was the terrestrially driven variations in the hydraulic gradient of Miocene-Pliocene Aquifer across the watershed. I found that at this scale tidal forcing did not affect SGD dynamics significantly (Fig. 3.6). The terrestrial hydraulic gradient was also responsible for the significant seasonal variations of SGD rates observed throughout the Mobile Bay coastal aquifer system (Fig. 3.7). During the wet season, I observed that high precipitation rates increased the Miocene-Pliocene Aquifer groundwater table creating higher hydraulic gradients near the coastlines of Mobile Bay, and resulting in enhanced SGD a few days later (Fig. 3.8). I found that SGD was on average 35% higher during the wet season ($11.9 \times 10^5 \text{ m}^3 \text{ d}^{-1}$) throughout the Mobile Bay coastal zone compared to the dry season ($8.0 \times 10^5 \text{ m}^3 \text{ d}^{-1}$) (Table 3.2, Fig. 3.8). However, I found that the magnitude of these longer-term terrestrially-driven seasonal variations of SGD were also site-specific. For instance, the highest (up to 40%)

SGD difference between seasons was measured on the southeastern shore compared to the 32% difference on the northeastern shore and 25% on the western shore (Table 3.2).

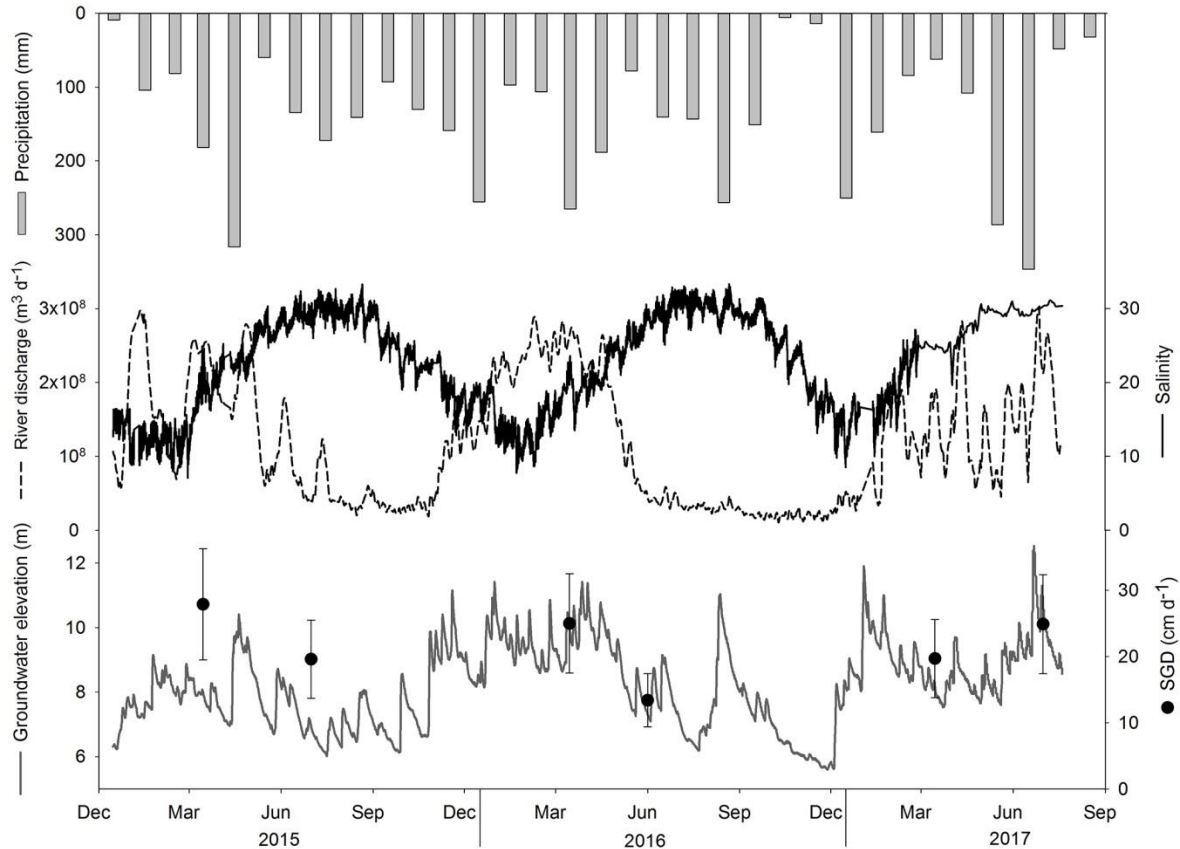


Figure 3.8. Three-year time-series of precipitation (mm), Mobile-Tensaw River System discharge ($m^3 d^{-1}$), salinity in Mobile Bay, groundwater elevation at the Miocene-Pliocene Aquifer (m), and average SGD rates ($cm d^{-1}$) on the northeastern and southeastern shores (main areas of SGD). Typically, higher rainfall during the wet season (March) coincided with maximum riverine discharge, groundwater elevation, SGD rates, and lowest salinity in Mobile Bay. During 2017 rainfall was lower during March than in June-July, attributed to the occurrence of tropical storm Cindy in Mobile Bay. As a result, I observed the opposite trends: higher river discharge, groundwater elevation, and SGD rates during July compared to March.

On a short time-scale (i.e. hours to days), SGD at each of the study sites in Mobile Bay (TS-W, TS-NE, TS-SE) was modulated by a combination of marine (tidal pumping) and terrestrial (hydraulic gradient) forces, with marine forcing prevailing during base flow conditions. An illustration of this site-specific behavior was evident throughout the continuous

five-day record conducted at each of the study sites (TS-W, TS-SE, and TS-NE) during one of the rainy seasons (Fig. 3.6). A heavy rain event (average 100 mm) two days prior to the deployment resulted in a gradual increase of the Miocene-Pliocene Aquifer level throughout the research area. The maximum groundwater elevation after the storm event coincided with the beginning of the deployments. As the local water table was gradually decreasing during the first two days of the deployment, I observed a significant decrease in the SGD rates of approximately 45% at the three sites (Fig. 3.6a, 3.6b, and 3.6c). I found that on average, it took about 2-3 days for the water table to gradually return to base flow conditions. This five-day record that included the high water table and base flow conditions provided us with the rare opportunity to examine the hydraulic response at each of the study sites. During this continuous record I distinguished two periods during this continuous record which corresponded to high and low SGD fluxes and I refer hereafter as “high SGD period” and “base flow SGD period” (Fig. 3.6).

I found that on the western shore of Mobile Bay at study site TS-W (Fig. 3.1) SGD was mainly controlled by tidal pumping (Santos et al., 2012) both during the high and base/low flow conditions (Fig. 3.6a). An evidence for this discharge mechanism is strongly supported by a good correlation ($R^2=0.75$, Appendix II Figs. 4a and 4b) between the tide stage, which was used as a proxy for tidal pumping, and SGD rates at this location. High SGD rates were always observed during low tide whereas lower discharge was found during high tide (Fig. 3.6a). However, on average, higher discharge rates (9 cm d^{-1}) were detected during the high SGD period (i.e. high water table) and lower SGD (5 cm d^{-1}) was found at the tail of the groundwater elevation decrease (i. e. towards base flow conditions). Nevertheless, the total discharge at this study site was always much lower compared to the other two study sites on the east shore (Fig. 3.7). Tidal pumping was also confirmed at the western shore of Mobile Bay by the time-lapsed ERT

measurements conducted during one of the dry seasons (July 2015) of this study. Although the tidal prism at this site is the smallest, during the shore-perpendicular ERT deployment at TS-W, I observed an overall 18% increase in the size of the SGD plume during falling tide (Appendix II Fig. 3a). Finally, I also found that these characteristics also promoted the highest seawater recirculation (RSGD) of the three sites in Mobile Bay and the maximum contrast between wet and dry seasons (30%-56%) (Fig. 3.7).

On the northeastern shore at study site TS-NE, the terrestrially-driven hydraulic gradient was the primary SGD driver during this continuous record. The correlation between the hydraulic head and SGD was significant ($R^2=0.68$, Appendix II Fig. 5b) throughout 4 days of deployment. However, tidal pumping was also an evident driving mechanism for SGD during base flow conditions (Figs. 3.6b and Appendix II Fig. 5a). This was confirmed by the time-lapsed ERT measurements conducted during the dry season (Appendix II Fig. 3c). Using these ERT images, I found that the SGD plume increased about 56% in the transition from high to low tide (Fig. 3.3c). However, I suggest that terrestrial forcing dominates the SGD dynamics over tidal pumping in the TS-NE study site. This terrestrial control of SGD was also confirmed by the mostly fresh composition of SGD (between 70-73%) during both the dry and wet seasons (Fig. 3.7).

During this continuous record, I found that SGD on the southeastern shore at study site TS-SE was controlled mostly by tidal pumping and affected by the hydraulic gradients to a lower extent. The negative correlation observed between SGD rates and the tide stage ($R^2=0.38$) measured throughout the time-series supports this finding (Appendix II Fig. 6a). Again, a much better correlation was found during the base flow SGD period when I found a correlation of $R^2=0.69$, indicating that marine forces indeed dominate the system in the southeastern shore

(Appendix II Fig. 6b). However, the SGD rates gradually decreased, following the groundwater elevation peak ($R^2=0.17$), also highlighting the lower importance of the terrestrially-driven hydraulic gradient on the SGD rates (Appendix II Fig. 6c). The time-lapsed ERT images confirmed that tidal pumping is the main factor controlling the SGD rates during base flow conditions with a SGD plume size change of 44% in the transition from high to low tide stage (Appendix II Fig. 3b). The synergic control of SGD by marine and terrestrial forces was also supported by the seasonal variation of FSGD from dry seasons (57%) to wet seasons (69%) measured in this area (Fig. 3.7).

3.6.3 Spatial distribution of SGD

I found that SGD occurs preferentially along the eastern shore of Mobile Bay throughout the year, i.e. regardless of the season. This was strongly supported by the results from two independent tracer approaches including radon anomalies in surface waters and electrical resistivity distributions (Fig. 3.2). CRP surveys revealed the highest bulk (lithology and saturating pore water) resistivity values (40-890 Ohm-m) along this side of Mobile Bay suggesting the presence of coarser sediments (sand) saturated with fresh groundwater (Fig. 3.2b). High resistivity values were also measured in the northern part of the bay near the river delta (30 Ohm-m) which were associated with the fresh water input from the Mobile-Tensaw River System. In contrast, the lower resistivity measured along the western shore and Bon Secour Bay (2.8 to 10 Ohm-m), indicated limited SGD inputs compared to the southeastern and northeastern shores (Fig. 3.2b). All ^{222}Rn surveys showed positive concentration anomalies along the eastern shore of Mobile Bay confirming the CRP indications for the presence of enhanced SGD inputs. A ^{222}Rn positive anomaly (“hot spot”) was especially pronounced ($0.1 - 5.0 \times 10^3 \text{ dpm m}^{-3}$) on the northeastern shore between the towns of Daphne and Fairhope, which is in the immediate

vicinity of study site TS-NE (Fig. 3.2b). Negative ^{222}Rn anomalies ($-4.1 - 0.0 \times 10^3 \text{ dpm m}^{-3}$), interpreted as an indication of limited discharge, were found in Bon Secour Bay and the western shore (Fig. 3.2a). A positive anomaly ($0.4 - 1.5 \times 10^3 \text{ dpm m}^{-3}$) located in the northern sector of the western shore was persistently detected during all surveys conducted during this study. I found that this ^{222}Rn “hot spot” coincides with the location of the main ship channel in Mobile Bay which is dredged to a depth of 15 m (Fig. 3.1). While I still do not have enough evidence, I speculate that such anthropogenic feature may have perforated the shallow Miocene-Pliocene Aquifer, artificially inducing SGD into the water column. Similar effects are known to exist at other locations by other studies. For example, Dimova et al. (2013) found that constructed pilings and/or artificial canals in some lakes of Florida have provided new pathways for enhanced groundwater discharge to surface waters.

The described spatial pattern of preferential groundwater discharge to Mobile Bay unveiled by the ^{222}Rn anomalies was also confirmed by the tracer-derived site-specific SGD assessments using multiple isotope approaches (^{222}Rn , ^{224}Ra , and ^{226}Ra) and seepage meters at all three study sites. Throughout the year, during both wet and dry seasons, the calculated SGD rates on the eastern shore were at least 3 times higher ($16\text{-}24 \text{ cm d}^{-1}$) than on the western shore ($5\text{-}6 \text{ cm d}^{-1}$) (Fig. 3.7, Tables 3.2 and 3.3). Although the seepage area (A) of the western shore ($3.8 \times 10^6 \text{ m}^2$) was the largest of the three shores, the groundwater fluxes obtained from the radon model and seepage meters deployments were about 40% lower ($1.8\text{-}2.4 \times 10^5 \text{ m}^3 \text{ d}^{-1}$) compared to the discharge found in the southeastern shore ($2.3\text{-}3.8 \times 10^5 \text{ m}^3 \text{ d}^{-1}$) and 50% lower compared to the northeastern shore ($3.9\text{-}5.7 \times 10^5 \text{ m}^3 \text{ d}^{-1}$). Based on this three-year study I found that most of the SGD in Mobile Bay occurs on the northeastern shore, accounting for almost 50% of the

total SGD to the bay, whereas the southeastern and northeastern shores combined represented ~80% of the total (Tables 3.2 and 3.3).

I suggest that these results can be explained by the interplay of two main hydrogeological factors: (i) hydraulic gradient variations in the coastal aquifer, mostly result of the regional topographic gradients, and (ii) inherited estuarine lithologic heterogeneities in the coastal shallow sediments that generate preferential groundwater flow paths only in certain areas.

The topographic gradients in the northeastern and southeastern shores are significantly greater than in the western shore, where the land surface is nearly flat for 10 km inland away from the shore (Danielson et al., 2013). In contrast, on the northeastern shore the topography gradient near the shore is the largest in Mobile Bay. This topography disposition determines a higher hydraulic gradient of the Watercourse and Miocene-Pliocene Aquifers in Mobile Bay (Fig. 3.1). The Geological Survey of Alabama (2018) calculated that along the western shore, the hydraulic gradient is 0.07%, along the southeastern shore is about 0.14%, while the maximum gradient in Mobile Bay is found in the northeastern shore with about 0.25% (Fig. 3.1). The higher hydraulic gradient of the coastal aquifer is also the primary control for the higher terrestrially-driven fresh SGD (FSGD) (Burnett et al., 2003; Santos et al., 2008) observed in the eastern shore (57-73%) compared to the western shore (44-70%) (Fig. 3.7). A hydraulic gradient 3.5 and 2 times higher in the southeastern and northeastern shores compared to the western shore, can partially explain the higher SGD rates in these two sections. However, I suggest that the spatial distribution of SGD is additionally controlled to a great extent by inherited estuarine lithologic heterogeneities present in Mobile Bay (Burnett et al., 2006; Holliday et al., 2007). The ERT imaging and sediment cores collected and characterized during this study at the three study sites (TS-W, TS-SE, and TS-NE) allowed us to identify the presence of preferential SGD flow

paths at the groundwater-seawater mixing zone in the Mobile Bay coastal aquifer (Figs. 3.7 and 3.8).

On the western shore, identified in this study to experience very low SGD, sediment core characterizations revealed a fine sand layer (C) at a depth of approximately 3.5 m with a hydraulic conductivity (k) of 7.9 m d^{-1} that permitted the groundwater plume to extend up to 80 m. However, above this layer I identified the presence of a 2.5-m thick silt layer (B) ($k = 4.1 \text{ m d}^{-1}$) which serves as an aquitard, restricting groundwater flow to Mobile Bay (Fig 5.a, Appendix II Fig. 3a). An independent study conducted recently near study site TS-W also supports my findings. As part of a local contaminant transport exploration Beebe and Lowery (2018) also found limited SGD in the western shore with average seepage rates of 4 cm d^{-1} compared to the average 5 cm d^{-1} found in this study. On the southeastern shore I found that a highly permeable ($k = 22.1 \text{ m d}^{-1}$) sand layer (D) (Fig. 5b, Appendix II Figs. 3b), which most likely corresponds to the Miocene-Pliocene Aquifer, allowed the groundwater plume to extend up to 70 m offshore. The deep sediment core that I recovered in this area revealed at a depth of 0.5 m an organic fine sand layer (B) ($k = 8.2 \text{ m d}^{-1}$) that facilitated SGD from the Miocene-Pliocene Aquifer (Fig. 3.5b), supporting the relatively higher SGD rates I found in this site (Table 3.2). I suggest that the highest SGD in Mobile Bay, found on the northeastern shore, was a result of the preferential groundwater flow through the coarse sand layer (up to 20 m deep) that was clearly identified by both the ERT images and the sediment core characterization. This top layer has the highest hydraulic conductivity ($k = 58.4 \text{ m d}^{-1}$) compared to all other sites. However, I found that this coarse sand layer was created artificially to build the numerous beach areas of this section of the bay. This allowed the greatest groundwater plume extension (up to 100 m offshore) and the highest SGD fluxes in Mobile Bay. The ERT images showed that within the first 20 m from the

shore, SGD occurs directly from the coarse sand into Mobile Bay while groundwater seepage in the remaining 80 m takes place through the organic fine sand layer (B) (Fig. 3.5c).

I conclude that the combination of a high hydraulic gradient (0.25%) in the coastal aquifer with the presence of highly permeable sediments ($k = 58.4 \text{ m d}^{-1}$) in the northeastern shore facilitated the observed enhanced SGD inputs on the northeastern shore of Mobile Bay ($3.9\text{-}5.7 \times 10^5 \text{ m}^3 \text{ d}^{-1}$). On the southeastern shore, the presence of the Miocene-Pliocene Aquifer in contact with an organic fine sand with moderate hydraulic conductivity ($k = 8.2 \text{ m d}^{-1}$) resulted in the second highest SGD fluxes during this study. The absence of coarse beach sand and a lower hydraulic gradient (0.14%) resulted in a slightly lower discharge ($2.3\text{-}3.8 \times 10^5 \text{ m}^3 \text{ d}^{-1}$) in comparison to the northeastern shore ($3.9\text{-}5.7 \times 10^5 \text{ m}^3 \text{ d}^{-1}$). In contrast, a low hydraulic gradient (0.07%) and the presence of a silt layer of very low hydraulic conductivity ($k = 4.1 \text{ m d}^{-1}$) in the western shore determined the lowest SGD inputs ($1.8\text{-}2.4 \times 10^5 \text{ m}^3 \text{ d}^{-1}$) and highest RSGD (30-56%) component of the research area.

The above described lithologic heterogeneities in the shallow sediments of Mobile Bay contribute significantly to the large variations in the spatial distribution of SGD. The presence of stratigraphic sequences of sediment layers with varying grain size, hydraulic conductivity, and organic matter are common in estuaries worldwide (e.g. Schwartz, 2003; Charette, 2007; Chin et al., 2010). Estuaries are highly dynamic systems where the sediment transport and deposition dynamics are affected by changing river discharge, predominant winds, tides, and anthropogenic activities (Ridgway and Shimmiel, 2002; Wilson et al., 2008; Rodriguez et al., 2010; Wang and Andutta, 2013). Additionally, most estuaries are the product of the Holocene sea level rise and subsequent river valleys inundation (Dyer, 1973; Ridgway and Shimmiel, 2002). These common characteristics typically lead to analogous lithologic heterogeneity in most estuaries,

influencing the presence and magnitude of SGD (e.g. Hwang et al., 2010; Null et al., 2012; Hatje et al., 2017).

3.6.4 Mobile Bay water budget

Based on this three-year investigation, I found that FSGD only represented a maximum of 5% of the total fresh water inputs to the bay during the dry season. During the wet season FSGD was $5.5 \times 10^5 \text{ m}^3 \text{ d}^{-1}$ to $11.5 \times 10^5 \text{ m}^3 \text{ d}^{-1}$ and the river flow was between 2300 and $2600 \times 10^5 \text{ m}^3 \text{ d}^{-1}$. Comparing these two components, SGD only represented 0.2-0.5% of the total fresh water inputs to the bay. However, during the dry season when the river discharge was between 130 and $390 \times 10^5 \text{ m}^3 \text{ d}^{-1}$ and FSGD ranged between $2.8 \times 10^5 \text{ m}^3 \text{ d}^{-1}$ and $6.5 \times 10^5 \text{ m}^3 \text{ d}^{-1}$, FSGD represented 0.7-5.0% of the fresh water inputs to the bay (Table 3.4, Fig. 3.7). These estimates of FSGD contribution to the fresh water budget of Mobile Bay are in close agreement with estimations reported in other river-dominated estuaries worldwide. For instance, Schwartz (2003) found that SGD in the Delaware Estuary accounted on average for 5% of total fresh water discharge. Kim et al. (2010) and Dulaiova et al. (2006) estimated that FSGD represented 3.4% and 4% compared to riverine discharge in the Yeongsan River Estuary (Korea) and the Gulf of Thailand respectively.

To confirm these findings, in addition to the radioisotope approach, I also used water stable isotopes ($\delta^{18}\text{O}$ and $\delta^2\text{H}$) to evaluate the relative contribution of each of the water sources to Mobile Bay including river and groundwater inputs as well as seawater entrance from Main Pass (Fig. 3.1). Based on the stable isotope mixing model (Appendix II Eqs. 3.12, 3.13, and 3.14), I found that river inputs dominated the system during the wet season with up to 89% of the total inputs to the bay, whereas seawater entrance in Mobile Bay via Main Pass was 10%. During these periods FSGD represented only 1% of the water budget (Table 3.5). Therefore, I suggest

that the importance of FSGD is higher during the dry season when river flow decreases significantly. Although the river input is still the dominant source of water to Mobile Bay (61%), the contribution of FSGD is relatively higher, accounting for up to 5% of the water budget. This agrees well with the volumetric comparison between the assessed FSGD and river flow (0.7-5.0%) based on the radioisotope approach. The lower river discharge during the dry season results in a lower flushing rate (from 4.7 km d⁻¹ during the wet season to 3.3 km d⁻¹), allowing larger amount of seawater (34%) to enter in the bay via Main Pass (Table 3.5). Furthermore, the salinity values were significantly higher near Main Pass during the dry season (Appendix II Figs. 1a and 1b), which also supports this finding.

Although these findings indicate that FSGD is not significant to the water budget of the Mobile Bay as a whole, I found that on a regional scale, SGD appears to be quite important. For instance, I found that FSGD is most important in the northeastern shore where it represented between 26% and 37% of all water inputs when compared to river (50-71%) and seawater inputs (3-14%) (Table 3.5). Proportionally, FSGD was slightly lower in the southeastern shore, where it represented 30% of the total water inputs during the dry season and 12% during the wet season. River water dominated the system in this area (59-68%), while seawater inputs did not affect this shore significantly (11-20%) due to the specific water circulation pattern in Mobile Bay (Table 3.5). With 71-75%, seawater was proportionally the largest component in the water budget of the western shore of Mobile Bay. I found that the fresh water plume from the Mobile-Tensaw River System extending to the south (Appendix II Figs. 1a and 1b) did not affect significantly the area of the southwestern shoreline (near TS-W) where river inputs represented 11-15% of the total budget. The contribution of FSGD to the budget of the western shore was the lowest of Mobile Bay, representing 10-18% of the total water inputs (Table 3.5).

Location	Season	$\delta^{18}\text{O}_{\text{River}}$	$\delta^{18}\text{O}_{\text{FSGD}}$	$\delta^{18}\text{O}_{\text{OW}}$	$\delta^{18}\text{O}_{\text{MB}}$	$\delta^2\text{H}_{\text{River}}$	$\delta^2\text{H}_{\text{FSGD}}$	$\delta^2\text{H}_{\text{OW}}$	$\delta^2\text{H}_{\text{MB}}$	f_{River}	f_{OW}	f_{SGD}
(% $\text{\textcircled{V}}$ VSMOW)												
(%)												
Mobile Bay	Dry	-3.5	-3.6	0.0	-2.3	-18	-19	0	-12	61 ± 7	34 ± 4	5 ± 0.5
	Wet	-3.4	-4.2	0.0	-3.1	-18	-20	0	-16	89 ± 6	10 ± 0.7	1 ± 0.1
TS-W	Dry	-3.0	-3.6	0.0	-1.0	-15	-20	0	-5	11 ± 3	71 ± 21	18 ± 5
	Wet	-4.4	-4.2	0.0	-4.0	-23	-20	0	-22	15 ± 1	75 ± 7	10 ± 1
TS-SE	Dry	-4.0	-3.9	0.0	-2.4	-18	-19	0	-11	59 ± 13	11 ± 2	30 ± 7
	Wet	-4.4	-4.2	0.0	-3.5	-23	-20	0	-18	68 ± 7	20 ± 2	12 ± 1
TS-NE	Dry	-3.0	-3.9	0.0	-2.9	-15	-19	0	-14	50 ± 7	14 ± 2	37 ± 5
	Wet	-4.4	-4.2	0.0	-4.2	-23	-20	0	-22	71 ± 7	3 ± 0.03	26 ± 2

Table 3.5. Site- and season-specific values utilized in the $\delta^{18}\text{O}$ - $\delta^2\text{H}$ three end-member mixing model to calculate the fractions of riverine, FSGD, and seawater inputs (f_{river} , f_{fsgd} , and f_{ow}) in mobile bay during the dry and wet seasons. The table includes results for water inputs in the whole bay and at each study site individually (TS-W, TS-SE, and TS-NE).

3.6.5 Ecological importance of SGD

During this study I found that the areas of enhanced SGD coincide very well with the locations most frequently impacted by *Jubilees* as published by Loesch (1960) and May (1973). These events have been linked to water column stratification and water anoxia near the bottom sediments, where demersal fish and crustaceans are mostly affected. *Jubilees* typically occur during easterly winds, which create a coastal upwelling effect moving the surface water away from the east shore of the bay and forcing hypoxic bottom waters to move towards the shore (May, 1973; Turner et al., 1987). Thus, I hypothesize that *Jubilee* events must be controlled by enhanced SGD inputs of anoxic and nutrient rich groundwater. Further evidence that strongly support this hypothesis was found in the analyzed lithological composition of the shallow coastal sediments through which SGD occurs. In the sediment cores that I collected at each of the two sites with highest SGD (TS-NE and TS-SE) and most frequent locations of *Jubilees*, I identified an organic fine sand layer (up to 36% organic matter content) that is only present along the southeastern and northeastern shores, extending 100 m offshore (at least). ERT images confirmed that indeed at both study sites SGD occurs through the organic sediment layer (Fig. 3.5). I suggest that the decomposition of the organic material creates anoxic conditions in flowing pore water which ultimately discharge into nearshore waters.

Furthermore, Liefer et al. (2009) and McIntyre et al. (2011) associated blooms of harmful diatoms in the southern area of Mobile Bay with nutrient inputs via SGD. Although HABs have never been studied in the eastern shore of the bay, I speculate that the ubiquitous presence of an organic sand layer combined with enhanced SGD could represent an important source of nutrients to the coastal ecosystem also triggering or supporting HAB events in the southeastern and northeastern shores, where river inputs are limited (Fig. 3.1).

3.7 Conclusions

In this study I demonstrated that hydrogeological heterogeneities in the shallow sediments controlled the occurrence and magnitude of SGD in Mobile Bay, a typical river-dominated system, which is the fourth largest estuary in the USA. I found that only the combined application of radiotracer techniques, shallow geophysics surveys, seepage meters deployments, stable isotopes analyses, and sediment cores collection allowed us to evaluate the importance of SGD in areas impacted by HABs and *Jubilees*.

Based on my results, FSGD only represented 0.2% of the total fresh water inputs in Mobile Bay during the wet season and a maximum of 5.0% during the dry season. However, I found that SGD occurred preferentially along the eastern shore of Mobile Bay, accounting for up to 80% of the total SGD in the bay and coinciding with the most frequent areas of *Jubilee* events. During the dry season, when *Jubilees* occur, I also observed that the importance of FSGD was highest in the eastern shore (30-36% of all water inputs). The relatively higher SGD contribution in the dry season, the anoxic nature of SGD, and the observed enhanced fluxes in this area might be controlling the *Jubilee* events. I hypothesize that the material decomposition in the organic sand layer identified along the eastern shore creates anoxic conditions in SGD, possibly enhancing the oxygen depletion that triggers *Jubilees*. Additionally, I speculate that the presence of this organic layer combined with the enhanced SGD rates could also represent an important source of nutrients to the coastal ecosystem, possibly triggering or supporting HAB events in the eastern shore.

The combination of a high hydraulic gradient in the coastal aquifer with the presence of highly permeable coarse sand deposits in the northeastern shore facilitated the maximum SGD inputs and FSGD portion (73%) measured in the bay. The absence of coarse beach sand and a

lower hydraulic gradient generated a slightly lower discharge in the southeastern shore compared to the northeastern shore. In contrast, a low hydraulic gradient and the presence of a silt layer with very low permeability in the western shore determined the lowest SGD and FSGD portion (44%) in Mobile Bay.

Examining the time-series measurements conducted on all three shores of Mobile Bay I observed that SGD was mainly controlled by marine-driven tidal pumping during base flow conditions. During high flow conditions, SGD was also driven by tidal pumping on the western shore and to a lower extent on the southeastern shore. However, on the northeastern shore SGD was primarily controlled by the terrestrially-driven hydraulic gradient of the coastal aquifer.

Using the water apparent age I estimated that the average water residence time of Mobile Bay was 5.1 days during the wet season (high river flow conditions) and 7.0 days during the dry season, which derived in flushing rates of 3.3 km d^{-1} and 4.7 km d^{-1} respectively. These flushing rates can be further applied in future studies to investigate the transport dynamics of dissolved contaminants and suspended particles in the bay and later mixing with seawater in the Gulf of Mexico.

The lithologic heterogeneities observed in the shallow sediments of Mobile Bay including varying grain size, hydraulic conductivity, and organic matter content are common in other estuaries. Most estuaries have a common formation history and similar lithologic and SGD settings can be expected in other large estuaries worldwide.

3.8 Acknowledgments

This research was partially funded by the National Science Foundation (NSF OIA-1632825), the 2016 ExxonMobil Summer Fund, the 2015 Gulf Coast Association of Geological Societies Student Research Grant, the University of Alabama Graduate School Research and Travel Support Fund, the UA Department of Geological Sciences W. Gary Hooks Geological

Sciences Advisory Board Fund, and the A.S. Johnson Travel Fund. I also want to thank the Mobile District US Army Corps of Engineers, Nathan Coburn, Adam Forkner, Richard Allen, and Steve Dykstra for their extensive help in the field. I am also very grateful for the massive help from the Weeks Bay National Estuarine Research Reserve by providing accommodation and technical support during all field campaigns.

3.9 References

- Advanced Geosciences, Inc. 2014. Instruction Manual for EarthImager 2D, Version 2.4.0, Resistivity and IP Inversion Software. (Available at <http://www.agiusa.com>).
- American Association for Testing and Materials. 1993. ASTM D 2974 Standard Test Methods for Moisture, Ash, and Organic Matter of Peat and Organic Soils.
- American Public Health Association (APHA), American Water Works Association (AWWA), and Water Environment Federation (WEF). 1999. In Standard Methods for the Examination of Water and Wastewater 20th Edition, eds. Clescerl L., Greenberg A. and Eaton A. 2-48. United Book Press, Inc., Baltimore, Maryland. Part 2000.
- Beebe, D. A. and B. A. Lowery. 2018. Seawater recirculation drives groundwater nutrient loading from a developed estuary shoreline with on-site wastewater treatment systems: Mobile Bay, USA. *Environmental Earth Sciences* 77: 372.
- Befus, K. M., M. B. Cardenas, D. R. Tait and D. V. Erler. 2014. Geoelectrical signals of geologic and hydrologic processes in a fringing reef lagoon setting. *Journal of hydrology*, 517: 508-520.
- Bianchi, T. S. 2007. Biogeochemistry of Estuaries, Oxford University Press, New York.
- Bricker, S. B., B. Longstaff, W. Dennison, A. Jones, K. Boicourt, C. Wicks and J. Woerner. 2008. Effects of nutrient enrichment in the nation's estuaries: a decade of change. *Harmful Algae* 8: 21-32.
- Burnett, W. C. and H. Dulaiova. 2003. Estimating the dynamics of groundwater input into the coastal zone via continuous radon-222 measurements. *Journal of Environmental Radioactivity* 69: 21-35.
- Burnett, W. C., H. Bokuniewicz, M. Huettel, W. S. Moore and M. Taniguchi. 2003. Groundwater and pore water inputs to the coastal zone. *Biogeochemistry* 66: 3-33.
- Burnett, W., P. Aggarwal, A. Aureli, H. Bokuniewicz, J. Cable, M. Charette, E. Kontar, S. Krupa, K. Kulkarni and A. Loveless. 2006. Quantifying submarine groundwater discharge in the coastal zone via multiple methods. *Science of the total Environment* 367: 498-543.
- Burnett, W. C. and H. Dulaiova. 2006. Radon as a tracer of submarine groundwater discharge into a boat basin in Donnalucata, Sicily. *Continental Shelf Research*, 26: 862-873.
- Burnett, W. C., R. Peterson, W. S. Moore and J. de Oliveira. 2008. Radon and radium isotopes as tracers of submarine groundwater discharge—results from the Ubatuba, Brazil SGD assessment intercomparison. *Estuarine, Coastal and Shelf Science* 76: 501-511.

- Byrnes, M., J. Berlinghoff and S. Griffee. 2013. Sediment Dynamics in Mobile Bay, Alabama: Development of an Operational Sediment Budget. Applied Coastal Research and Engineering Inc. Mobile Bay National Estuary Program Library, Mobile, AL. (Available at <http://www.mobilebaynep.com/library>)
- Cable, J. E., W. C. Burnett, J. P. Chanton and G. L. Weatherly. 1996. Estimating groundwater discharge into the northeastern Gulf of Mexico using radon-222. *Earth and Planetary Science Letters* 144: 591-604.
- Cerdà-Domènech, M., V. Rodellas, A. Folch and J. Garcia-Orellana. 2017. Constraining the temporal variations of Ra isotopes and Rn in the groundwater end-member: Implications for derived SGD estimates. *Science of the total environment* 595: 849-857.
- Chandler RV, J.D. Moorea and B. Gillett. 1985. Ground-water chemistry and salt-water encroachment, southern Baldwin County, Alabama. Geological Survey of Alabama Bulletin 126, 70 pp.
- Charette, M. A. 2007. Hydrologic forcing of submarine groundwater discharge: Insight from a seasonal study of radium isotopes in a groundwater-dominated salt marsh estuary. *Limnology and Oceanography* 52: 230-239.
- Chin, J. L., D. L. Woodrow, M. McGann, F. L. Wong, T. Fregoso, and B. E. Jaffe. 2010. Estuarine sedimentation, sediment character, and foraminiferal distribution in central San Francisco Bay, California. U.S. Geological Survey Open-File Report 2010-1130.
- Craig, H., 1961. Isotopic variations in meteoric waters. *Science* 133: 1702-1703.
- Cross, V. A., J. F. Bratton, K. D. Kroeger, J. Crusius, and C. R. Worley. 2013. Continuous resistivity profiling data from Great South Bay, Long Island, New York. U.S. Geological Survey Open-File Report 2011-1040.
- Crusius, J., D. Koopmans, J. F. Bratton, M. A. Charette, K. D. Kroeger, P. B. Henderson, L. Ryckman, K. Halloran and J. A. Colman. 2005. Submarine groundwater discharge to a small estuary estimated from radon and salinity measurements and a box model. *Biogeosciences* 2: 141–157.
- Danielson, J. J., J. C. Brock, D. M. Howard, D. B. Gesch, J. M. Bonisteel-Cormier and L. J. Travers. 2013. Topobathymetric model of Mobile Bay, Alabama. US Geological Survey Data Series 769.
- Dimova, N., W. C. Burnett and D. Lane-Smith. 2009. Improved automated analysis of radon (^{222}Rn) and thoron (^{220}Rn) in natural waters. *Environmental Science & Technology*, 43: 8599-8603.
- Dimova, N. T., P. W. Swarzenski, H. Dulaiova and C. R. Glenn. 2012. Utilizing multichannel electrical resistivity methods to examine the dynamics of the fresh water–seawater

- interface in two Hawaiian groundwater systems. *Journal of Geophysical Research: Oceans* 117.
- Dimova, N. T., W. C. Burnett, J. P. Chanton and J. E. Corbett. 2013. Application of radon-222 to investigate groundwater discharge into small shallow lakes. *Journal of Hydrology* 486: 112-122.
- Doctor, D. H., E. C. Alexander, M. Petrič, J. Kogovšek, J. Urbanc, S. Lojen and W. Stichler. 2006. Quantification of karst aquifer discharge components during storm events through end-member mixing analysis using natural chemistry and stable isotopes as tracers. *Hydrogeology Journal* 14: 1171-1191.
- Du, J., K. Park, J. Shen, B. Dzwonkowski, X. Yu and B. I. Yoon. 2018. Role of baroclinic processes on flushing characteristics in a highly stratified estuarine system, Mobile Bay, Alabama. *Journal of Geophysical Research: Oceans* 123.
- Dulaiova, H., R. Peterson, W.C. Burnett and D. Lane-Smith. 2005. A multi-detector continuous monitor for assessment of ^{222}Rn in the coastal ocean. *Journal of Radioanalytical and Nuclear Chemistry*, 263: 361-365.
- Dulaiova, H., W. Burnett, G. Wattayakorn and P. Sojisuorn. 2006. Are groundwater inputs into river-dominated areas important? The Chao Phraya River—Gulf of Thailand. *Limnology and Oceanography* 51: 2232-2247.
- Dulaiova, H. and W. C. Burnett. 2008. Evaluation of the flushing rates of Apalachicola Bay, Florida via natural geochemical tracers. *Marine Chemistry* 109: 395-408.
- Dyer, K. R. 1973. *Estuaries: A Physical Introduction*. John Wiley & Sons: London. 140 pp.
- Dzwonkowski, B., K. Park, H. K. Ha, W. M. Graham, F. J. Hernandez and S. P. Powers. 2011. Hydrographic variability on a coastal shelf directly influenced by estuarine outflow. *Continental Shelf Research* 31: 939-950.
- Ellis, J. 2013. Evaluation of submarine groundwater discharge and groundwater quality using a novel coupled approach: isotopic tracer techniques and numerical modeling. Master's thesis, University of Alabama, 67 pp.
- Garcia-Solsona, E., J. Garcia-Orellana, P. Masqué and H. Dulaiova. 2008. Uncertainties associated with ^{223}Ra and ^{224}Ra measurements in water via a Delayed Coincidence Counter (RaDeCC). *Marine Chemistry* 109: 198-219.
- Garcia-Solsona, E., J. Garcia-Orellana, P. Masqué, V. Rodellas, M. Mejías, B. Ballesteros and J. Domínguez. 2010. Groundwater and nutrient discharge through karstic coastal springs (Castelló, Spain). *Biogeosciences* 7: 2625-2638.

- Geibert, W., V. Rodellas, A. Annett, P. van Beek, J. Garcia-Orellana, Y. T. Hsieh and P. Masque. 2013. ^{226}Ra determination via the rate of ^{222}Rn ingrowth with the Radium Delayed Coincidence Counter (RaDeCC). *Limnology and Oceanography: Methods* 11: 594-603.
- Geological Survey of Alabama. 2018. Assessment of groundwater resources in Alabama, 2010-16. Geological Survey of Alabama Bulletin 186, 426 pp.
- Gillett, B., D. Raymond, J. Moore and B. Tew. 2000. Hydrogeology and vulnerability to contamination of major aquifers in Alabama: Area 13. Geological Survey of Alabama Circular 199A, 68 pp.
- Greene Jr, D. L., A. B. Rodriguez and J. B. Anderson. 2007. Seaward-branching coastal-plain and piedmont incised-valley systems through multiple sea-level cycles: Late Quaternary examples from Mobile Bay and Mississippi Sound, USA. *Journal of Sedimentary Research* 77: 139-158.
- Gu, H., W. S. Moore, L. Zhang, J. Du and J. Zhang. 2012. Using radium isotopes to estimate the residence time and the contribution of submarine groundwater discharge (SGD) in the Changjiang effluent plume, East China Sea. *Continental Shelf Research* 35: 95-107.
- Hatje, V., K. K. Attisano, M. F. L. de Souza, B. Mazzilli, J. de Oliveira, T. de Araújo Mora and W. C. Burnett. 2017. Applications of radon and radium isotopes to determine submarine groundwater discharge and flushing times in Todos os Santos Bay, Brazil. *Journal of environmental radioactivity* 178: 136-146.
- Hazen, A. 1893. Some physical properties of sand and gravels. Massachusetts State Board of Health. 24th Annual Report.
- Henderson, R. D., F. D. Day-Lewis, E. Abarca, C. F. Harvey, H. N. Karam, L. Liu and J. W. Lane. 2010. Marine electrical resistivity imaging of submarine groundwater discharge: sensitivity analysis and application in Waquoit Bay, Massachusetts, USA. *Hydrogeology Journal* 18: 173-185.
- Holliday, D., T. Stieglitz, P. Ridd and W. Read. 2007. Geological controls and tidal forcing of submarine groundwater discharge from a confined aquifer in a coastal sand dune system. *Journal of Geophysical Research: Oceans* 112.
- Hwang, D. W., G. Kim, Y. W. Lee and H. S. Yang. 2005. Estimating submarine inputs of groundwater and nutrients to a coastal bay using radium isotopes. *Marine Chemistry* 96: 61-71.
- Hwang, D. W., G. Kim, W. C. Lee and H. T. Oh. 2010. The role of submarine groundwater discharge (SGD) in nutrient budgets of Gamak Bay, a shellfish farming bay, in Korea. *Journal of Sea Research* 64: 224-230.

- Johannes, R. E. 1980. The ecological significance of the submarine discharge of groundwater. *Marine Ecology Progress Series* 365-373.
- Kim, J., J.-S. Kim and G. Kim. 2010. Nutrient input from submarine groundwater discharge versus intermittent river-water discharge through an artificial dam in the Yeongsan River estuary, Korea. *Ocean Science Journal* 45: 179-186.
- Krantz, D. E., F. T. Manheim, J. F. Bratton and D. J. Phelan. 2004. Hydrogeologic setting and ground water flow beneath a section of Indian River Bay, Delaware. *Groundwater* 42: 1035-1051.
- Lambe, T. W. 1951. Soil testing for engineers. John Wiley & Sons: New York. 406 pp.
- Lambert, M. J. and W. C. Burnett. 2003. Submarine groundwater discharge estimates at a Florida coastal site based on continuous radon measurements. *Biogeochemistry* 66: 55-73.
- Lee, D. R. 1977. A device for measuring seepage flux in lakes and estuaries. *Limnology and Oceanography* 22: 140-147.
- Liefer, J. D., H. L. MacIntyre, L. Novoveska, W. L. Smith and C. P. Dorsey. 2009. Temporal and spatial variability in *Pseudo-nitzschia* spp. in Alabama coastal waters: a hot spot linked to submarine groundwater discharge? *Harmful algae* 8: 706-714.
- Loesch, H. 1960. Sporadic mass shoreward migrations of demersal fish and crustaceans in Mobile Bay, Alabama. *Ecology* 41: 292-298.
- Macintyre, H. L., A. L. Stutes, W. L. Smith, C. P. Dorsey, A. Abraham and R. W. Dickey. 2011. Environmental correlates of community composition and toxicity during a bloom of *Pseudo-nitzschia* spp. in the northern Gulf of Mexico. *Journal of Plankton Research* 33: 273-295.
- May, E. B. 1973. Extensive oxygen depletion in Mobile Bay, Alabama. *Limnology and Oceanography* 18: 353-366.
- Michael, H. A., K. C. Scott, M. Koneshloo, X. Yu, M. R. Khan and K. Li. 2016. Geologic influence on groundwater salinity drives large seawater circulation through the continental shelf. *Geophysical Research Letters* 43.
- Montiel, D., N. Dimova, B. Andreo, J. Prieto, J. García-Orellana and V. Rodellas. 2018. Assessing submarine groundwater discharge (SGD) and nitrate fluxes in highly heterogeneous coastal karst aquifers: Challenges and solutions. *Journal of Hydrology* 557: 222-242.
- Moore, W. S. 1976. Sampling ^{228}Ra in the deep ocean. *Deep Sea Research and Oceanographic Abstracts* 23: 647-651.

- Moore, W. S. and R. Arnold. 1996. Measurement of ^{223}Ra and ^{224}Ra in coastal waters using a delayed coincidence counter. *Journal of Geophysical Research: Oceans* 101: 1321-1329.
- Moore, W. S. 1996. Large groundwater inputs to coastal waters revealed by ^{226}Ra enrichments. *Nature*, 380: 612-614.
- Moore, W. S. 1999. The subterranean estuary: a reaction zone of ground water and sea water. *Marine Chemistry*, 65: 111-125.
- Moore, W. S. 2000. Determining coastal mixing rates using radium isotopes. *Continental Shelf Research* 20: 1993-2007.
- Moore, W. S. 2003. Sources and fluxes of submarine groundwater discharge delineated by radium isotopes. *Biogeochemistry* 66: 75-93.
- Moore, W. S. 2008. Fifteen years experience in measuring ^{224}Ra and ^{223}Ra by delayed-coincidence counting. *Marine Chemistry* 109: 188-197.
- Moore, W. S. and J. Krest. 2004. Distribution of ^{223}Ra and ^{224}Ra in the plumes of the Mississippi and Atchafalaya Rivers and the Gulf of Mexico. *Marine Chemistry* 864: 105-119.
- Moore, W. S. 2010. The effect of submarine groundwater discharge on the ocean. *Annual review of marine science* 2: 59-88.
- Noble, M. A., W. W. Schroeder, W. J. Wiseman, H. F. Ryan and G. Gelfenbaum. 1996. Subtidal circulation patterns in a shallow, highly stratified estuary: Mobile Bay, Alabama. *Journal of Geophysical Research: Oceans* 101: 25689-25703.
- Null, K. A., N. T. Dimova, K. L. Knee, B. K. Esser, P. W. Swarzenski, M. J. Singleton, M. Stacey and A. Paytan. 2012. Submarine groundwater discharge-derived nutrient loads to San Francisco Bay: implications to future ecosystem changes. *Estuaries and Coasts* 35: 1299-1315.
- Park, K., C. K. Kim and W. W. Schroeder. 2007. Temporal variability in summertime bottom hypoxia in shallow areas of Mobile Bay, Alabama. *Estuaries and Coasts* 30: 54-65.
- Parsons, M. L. and Q. Dortch. 2002. Sedimentological evidence of an increase in Pseudo-nitzschia (Bacillariophyceae) abundance in response to coastal eutrophication. *Limnology and Oceanography* 47: 551-558.
- Peterson, R. N., W. C. Burnett, M. Taniguchi, J. Chen, I. R. Santos and T. Ishitobi. 2008. Radon and radium isotope assessment of submarine groundwater discharge in the Yellow River delta, China. *Journal of Geophysical Research: Oceans* 113.
- Reed P. C. 1971. Geologic map of Baldwin County, Alabama. Geological Survey of Alabama Special Map 94, p 55.

- Ridgway, J. and G. Shimmiel. 2002. Estuaries as repositories of historical contamination and their impact on shelf seas. *Estuarine, Coastal and Shelf Science* 55: 903-928.
- Rodellas, V., J. Garcia-Orellana, G. Trezzi, P. Masqué, T. C. Stieglitz, H. Bokuniewicz, J. K. Cochran and E. Berdalet. 2017. Using the radium quartet to quantify submarine groundwater discharge and porewater exchange. *Geochimica et Cosmochimica Acta* 196: 58-73.
- Rodriguez, A. B., D. L. Greene, J. B. Anderson and A. R. Simms. 2008. Response of Mobile Bay and eastern Mississippi Sound, Alabama, to changes in sediment accommodation and accumulation. In Response of upper Gulf Coast estuaries to Holocene climate change and sea-level rise, eds. J.B. Anderson and A.B. Rodriguez 13-29. Geological Society of America.
- Rodriguez, A. B., A. R. Simms and J. B. Anderson. 2010. Bay-head deltas across the northern Gulf of Mexico back step in response to the 8.2 ka cooling event. *Quaternary Science Reviews* 29: 3983-3993.
- Roman, C. T., N. Jaworski, F. T. Short, S. Findlay and R. S. Warren. 2000. Estuaries of the northeastern United States: habitat and land use signatures. *Estuaries* 23: 743-764.
- Russoniello, C. J., C. Fernandez, J. F. Bratton, J. F. Banaszak, D. E. Krantz, A. S. Andres, L. F. Konikow and H. A. Michael. 2013. Geologic effects on groundwater salinity and discharge into an estuary. *Journal of Hydrology* 498: 1-12.
- Santos, I. R. S., W. C. Burnett, J. Chanton, B. Mwashote, I. G. Suryaputra and T. Dittmar. 2008. Nutrient biogeochemistry in a Gulf of Mexico subterranean estuary and groundwater-derived fluxes to the coastal ocean. *Limnology and Oceanography* 53: 705-718.
- Santos, I. R., W. C. Burnett, J. Chanton, N. Dimova and R. N. Peterson. 2009. Land or ocean?: Assessing the driving forces of submarine groundwater discharge at a coastal site in the Gulf of Mexico. *Journal of Geophysical Research: Oceans* 114.
- Santos, I. R., B. D. Eyre and M. Huettel. 2012. The driving forces of porewater and groundwater flow in permeable coastal sediments: A review. *Estuarine, Coastal and Shelf Science* 98: 1-15.
- Sawyer, A. H., O. Lazareva, K. D. Kroeger, K. Crespo, C. S. Chan, T. Stieglitz and H. A. Michael. 2014. Stratigraphic controls on fluid and solute fluxes across the sediment—water interface of an estuary. *Limnology and Oceanography* 59: 997-1010.
- Schroeder, W. W. 1978. Riverine influence on estuaries: a case study. *Estuarine Interactions*: 347-364.

- Schroeder, W. W., S. P. Dinnel and W. J. Wiseman. 1990. Salinity stratification in a river-dominated estuary. *Estuaries* 13: 145-154.
- Schwartz, M. 2003. Significant groundwater input to a coastal plain estuary: assessment from excess radon. *Estuarine, Coastal and Shelf Science* 56: 31-42.
- Stalker, J. C., R. M. Price and P. K. Swart. 2009. Determining spatial and temporal inputs of freshwater, including submarine groundwater discharge, to a subtropical estuary using geochemical tracers, Biscayne Bay, South Florida. *Estuaries and Coasts* 32: 694-708.
- Stieglitz, T. C., P. G. Cook and W. C. Burnett. 2010. Inferring coastal processes from regional-scale mapping of ^{222}Rn and salinity: examples from the Great Barrier Reef, Australia. *Journal of Environmental Radioactivity* 101: 544-552.
- Stumpf, R. P., G. Gelfenbaum and J. R. Pennock. 1993. Wind and tidal forcing of a buoyant plume, Mobile Bay, Alabama. *Continental Shelf Research* 13: 1281-1301.
- Su, N., W. C. Burnett, H. L. MacIntyre, J. D. Liefer, R. N. Peterson and R. Viso. 2014. Natural radon and radium isotopes for assessing groundwater discharge into Little Lagoon, AL: Implications for harmful algal blooms. *Estuaries and Coasts* 37: 893-910.
- Sun, Y. and T. Torgersen. 1998. The effects of water content and Mn-fiber surface conditions on ^{224}Ra measurement by ^{220}Rn emanation. *Marine Chemistry* 62: 299-306.
- Tait, D. R., I. R. Santos, D. V. Erler, K. M. Befus, M. B. Cardenas and B. D. Eyre. 2013. Estimating submarine groundwater discharge in a South Pacific coral reef lagoon using different radioisotope and geophysical approaches. *Marine Chemistry* 156: 49-60.
- Taniguchi, M., W. C. Burnett, J. E. Cable and J. V. Turner. 2002. Investigation of submarine groundwater discharge. *Hydrological Processes* 16: 2115-2129.
- Taniguchi, M., T. Ishitobi and K. I. Saeki. 2005. Evaluation of time-space distributions of submarine ground water discharge. *Groundwater* 43: 336-342.
- Tovar-Sánchez, A., G. Basterretxea, V. Rodellas, D. Sánchez-Quiles, J. García-Orellana, P. Masqué, A. Jordi, J. M. López and E. Garcia-Solsona. 2014. Contribution of groundwater discharge to the coastal dissolved nutrients and trace metal concentrations in Majorca Island: karstic vs detrital systems. *Environmental Science & Technology* 48: 11819-11827.
- Turner, R., W. Schroeder and W. J. Wiseman. 1987. The role of stratification in the deoxygenation of Mobile Bay and adjacent shelf bottom waters. *Estuaries* 10: 13-19.
- Uddameri, V., S. Singaraju and E. A. Hernandez. 2014. Temporal variability of freshwater and pore water recirculation components of submarine groundwater discharges at Baffin Bay, Texas. *Environmental Earth Sciences* 71: 2517-2533.

- Walter G.R. and R. E. Kidd. 1979. Ground-water management techniques for the control of salt-water encroachment in Gulf Coast aquifers, a summary report. Geological Survey of Alabama Open-file Report, p 84.
- Wang, X. and F. Andutta. 2013. Sediment transport dynamics in ports, estuaries and other coastal environments. In Sediment Transport ed. A. Manning 3-35. InTech.
- Ward, G. M., P. M. Harris and A. K. Ward. 2005. Gulf Coast rivers of the southeastern United States. *Rivers of North America*: 125-178.
- Webb, B. M. and C. Marr. 2016. Spatial variability of hydrodynamic timescales in a broad and shallow estuary: Mobile Bay, Alabama. *Journal of Coastal Research* 32: 1374-1388.
- Wentworth, C. K. 1922. A scale of grade and class terms for clastic sediments. *The Journal of Geology* 30: 377-392.
- Wilson, A. M., M. Huettel and S. Klein. 2008. Grain size and depositional environment as predictors of permeability in coastal marine sands. *Estuarine, Coastal and Shelf Science* 80: 193-199.
- Wolfe, D. A. and B. Kjerfve. 1986. Estuarine variability: an overview. In Estuarine variability, ed. D. A. Wolfe 3-17. Academic Press.
- Xu, B., W. Burnett, N. Dimova, S. Diao, T. Mi, X. Jiang and Z. Yu. 2013. Hydrodynamics in the Yellow River Estuary via radium isotopes: Ecological perspectives. *Continental Shelf Research* 66: 19-28.
- Young, C., J. Tamborski and H. Bokuniewicz. 2015. Embayment scale assessment of submarine groundwater discharge nutrient loading and associated land use. *Estuarine, Coastal and Shelf Science* 158: 20-30.
- Young, M. B., M. E. Gonnee, D. A. Fong, W. S. Moore, J. Herrera-Silveira and A. Paytan. 2008. Characterizing sources of groundwater to a tropical coastal lagoon in a karstic area using radium isotopes and water chemistry. *Marine Chemistry* 109: 377-394.

3.10 Appendix II

Total SGD assessments

Radon model

SGD-derived ^{222}Rn fluxes (F_{SGD} , $\text{dpm m}^{-2} \text{h}^{-1}$) were determined using the following expression (Eq. 1):

$$F_{SGD} = F_{Atm} + F_{Mix} - C_{Ra} - F_{Diff} \quad (1)$$

where F_{Atm} is the atmospheric evasion fluxes of ^{222}Rn through the water/air interphase; F_{Mix} are mixing losses due to tidal variations and horizontal fluxes; C_{Ra} is the production of ^{222}Rn from ^{226}Ra decay within the water column; and F_{Diff} is the ^{222}Rn diffusion flux from seabed sediments.

Specific groundwater discharge (ω , cm d^{-1}) was calculated (Eq. 2) by dividing SGD-derived ^{222}Rn fluxes by the representative (site and season-specific) groundwater ^{222}Rn concentration end-member (Rn_{SGD} , dpm m^{-3}) (Burnett and Dulaiova, 2003):

$$\omega = \frac{F_{SGD}}{Rn_{SGD}} \quad (2)$$

To calculate groundwater fluxes (SGD , $\text{m}^3 \text{d}^{-1}$), specific discharges (ω) were multiplied by the total area (A , m^2) through which SGD occurs (Eq. 3):

$$SGD = \omega \times A \quad (3)$$

The seepage area (A) was calculated by multiplying the shoreline length affected by SGD based on ^{222}Rn and CRP boat surveys, and the offshore extend of the groundwater plume observed with ERT during low tide.

Seepage meters

The seepage meters were built using a bottomless 120 L drum with an opening on their tops where a plastic bag was attached using a two-way valve (Lee, 1977). The seepage meters were submerged and inserted in the coastal sediments near piezometers Pz-5 leaving the valve

side slightly higher allowing any gas to escape before plastic bag attachment. The water volume entering the plastic bag and time elapsed were then recorded during 12 hours at 1-hour intervals. Site-specific groundwater discharges (SGD , cm d^{-1}) were calculated using Eq. 4 modified from Lee (1977):

$$SGD = \frac{33.88 \times V}{t} \quad (4)$$

where V is the volume of water entering the plastic bag (mL); t is the time elapsed (s), and 33.88 is a unit conversion factor specific to the 0.25 m^2 flow area to obtain seepage velocity in cm d^{-1} . To calculate groundwater discharge ($\text{m}^3 \text{ d}^{-1}$) I used the same seepage areas as in the radon approach.

FSGD and RSGD assessments

Radium model

$$f_{\text{River}} + f_{\text{RSGD}} + f_{\text{OW}} = 1 \quad (5)$$

$$^{226}\text{Ra}_{\text{River}} \times f_{\text{River}} + ^{226}\text{Ra}_{\text{RSGD}} \times f_{\text{RSGD}} + ^{226}\text{Ra}_{\text{OW}} \times f_{\text{OW}} = ^{226}\text{Ra}_{\text{MB}} \times e^{-\lambda_{226} t} \quad (6)$$

$$^{224}\text{Ra}_{\text{River}} \times f_{\text{River}} + ^{224}\text{Ra}_{\text{RSGD}} \times f_{\text{RSGD}} + ^{224}\text{Ra}_{\text{OW}} \times f_{\text{OW}} = ^{224}\text{Ra}_{\text{MB}} \times e^{-\lambda_{224} t} \quad (7)$$

where f_{River} , f_{RSGD} , and f_{OW} represent the proportional fractions of river, RSGD, and open seawater entering Mobile Bay. While Ra_{River} , Ra_{RSGD} , Ra_{OW} , and Ra_{MB} are radium concentrations (dpm m^{-3}) measured in the Mobile-Tensaw River System, groundwater, seawater, and Mobile Bay. Ra_{MB} was obtained from averaged concentrations sampled in shore-perpendicular transects (R1, R2, and R3) or samples collected near the sampling stations. λ_{226} and λ_{224} are the decay constants of ^{224}Ra (0.19 d^{-1}) and ^{226}Ra ($1.18 \times 10^{-6} \text{ d}^{-1}$) and t is the bay water apparent age/residence time (d) determined using Eq. 9.

Using the fraction of RSGD (f_{RSGD}) at each location, SGD ($\text{m}^3 \text{ d}^{-1}$) was calculated using Eq. 7:

$$RSGD = \frac{f_{\text{RSGD}} \times V}{t} \quad (8)$$

The volume (V) of bay waters affected by SGD was calculated multiplying the area of seepage (A) (obtained from ^{222}Rn , CRP, and ERT surveys) by the average water column depth.

Bathymetry data were recorded with the depth sonar integrated in the built-in GPS unit used for the CRP.

The apparent age (t , days) of Mobile Bay waters was determined using the activity ratio (AR) of ^{224}Ra and ^{223}Ra in Bay waters compared to the Mobile-Tensaw River System AR applying equation 9 (Moore, 2000):

$$t = \ln \left(\frac{\left[\frac{^{224}\text{Ra}}{^{223}\text{Ra}} \right]_{\text{ini}}}{\left[\frac{^{224}\text{Ra}}{^{223}\text{Ra}} \right]_{\text{obs}}} \right) \times \frac{1}{\lambda_{224} - \lambda_{223}} \quad (9)$$

where $(^{224}\text{Ra}/^{223}\text{Ra})_{\text{ini}}$ is the initial averaged AR measured in Mobile-Tensaw River System, $(^{224}\text{Ra}/^{223}\text{Ra})_{\text{obs}}$ is the AR at any point in Mobile Bay waters, whereas λ_{224} and λ_{223} are the decay constants of ^{224}Ra (0.19 d^{-1}) and ^{223}Ra (0.06 d^{-1}). The average water residence time (t) applied in Eq. 8 at each location was calculated from the same samples utilized to obtain Ra_{MB} .

Stable isotopes model

$$f_{\text{FSGD}} + f_{\text{RSGD}} = 1 \quad (10)$$

$$\delta^2\text{H} - \delta^{18}\text{O}_{\text{FSGD}} \times f_{\text{FSGD}} + \delta^2\text{H} - \delta^{18}\text{O}_{\text{RSGD}} \times f_{\text{RSGD}} = \delta^2\text{H} - \delta^{18}\text{O}_{\text{SGD}} \times f_{\text{SGD}} \quad (11)$$

where f_{FSGD} and f_{RSGD} represent the fresh and recirculated fractions of SGD. $\delta^{18}\text{O}_{\text{FSGD}} - \delta^2\text{H}_{\text{FSGD}}$ and $\delta^{18}\text{O}_{\text{RSGD}} - \delta^2\text{H}_{\text{RSGD}}$ are the isotopic values of FSGD measured in wells (Well-1-3) and RSGD obtained from piezometers Pz-3, Pz-4, and Pz-5 at each location. The total SGD end-member was obtained from the average values of piezometers Pz-1 to Pz-5.

Water budget of Mobile Bay

$$f_{\text{River}} + f_{\text{FSGD}} + f_{\text{OW}} = 1 \quad (12)$$

$$\delta^{18}\text{O}_{\text{River}} \times f_{\text{River}} + \delta^{18}\text{O}_{\text{FSGD}} \times f_{\text{FSGD}} + \delta^{18}\text{O}_{\text{OW}} \times f_{\text{OW}} = \delta^{18}\text{O}_{\text{MB}} \quad (13)$$

$$\delta^2\text{H}_{\text{River}} \times f_{\text{River}} + \delta^2\text{H}_{\text{FSGD}} \times f_{\text{FSGD}} + \delta^2\text{H}_{\text{OW}} \times f_{\text{OW}} = \delta^2\text{H}_{\text{MB}} \quad (14)$$

where f_{River} , f_{FSGD} , and f_{OW} represent the respective fractions of riverine, FSGD, and seawater inputs. $\delta^{18}\text{O}_{\text{River}}-\delta^2\text{H}_{\text{River}}$, $\delta^{18}\text{O}_{\text{FSGD}}-\delta^2\text{H}_{\text{FSGD}}$, $\delta^{18}\text{O}_{\text{OW}}-\delta^2\text{H}_{\text{OW}}$, and $\delta^{18}\text{O}_{\text{MB}}-\delta^2\text{H}_{\text{MB}}$ are the average $\delta^{18}\text{O}$ and $\delta^2\text{H}$ values measured in the Mobile-Tensaw River System, groundwater (Well-1-3), seawater, and Mobile Bay.

Site-specific water budgets were also constructed for each location (TS-W, TS-ES, and TS-NE). In this case, Mobile Bay waters $\delta^{18}\text{O}_{\text{MB}}$ and $\delta^2\text{H}_{\text{MB}}$ values were obtained exclusively from averaged surface water samples collected near shore (R1, R2, and R3).

Table 1: Temperature, electrical conductivity, salinity, $\delta^2\text{H}$, $\delta^{18}\text{O}$, ^{222}Rn , ^{226}Ra , ^{224}Ra , ^{223}Ra , and residence time (t) measured in Mobile Bay, Mobile-Tensaw River System, groundwater wells and piezometers, and seawater from the Gulf of Mexico (in Dauphin Island) during all sampling campaigns.

Date	Sample ID	Longitude	Latitude	Temperature (°C)	Conductivity ($\mu\text{S cm}^{-1}$)	Salinity	Stable isotopes		^{222}Rn ($\times 10^3 \text{ dpm m}^{-3}$)	^{226}Ra	^{224}Ra (dpm m^{-3})	^{223}Ra	t (d)
							$\delta^2\text{H}$ (VSMOW‰)	$\delta^{18}\text{O}$ (VSMOW‰)					
March 2015	S-1	-87.84328	30.37614	22.6	10830	6.2	-9.2	-2.4	N/A	250 ± 10	170 ± 10	8 ± 0.5	5 ± 0.3
	S-2	-87.87306	30.38349	22.6	14240	8.2	-14.6	-3.0	N/A	90 ± 5	90 ± 5	3 ± 0.2	4 ± 0.2
	S-3	-87.91313	30.43098	21.4	9080	5.1	-18.8	-3.7	N/A	70 ± 4	70 ± 4	5 ± 0.3	7 ± 0.4
	S-4	-87.93006	30.49403	21.6	4830	2.6	-20.7	-4.0	N/A	90 ± 4	120 ± 9	8 ± 0.4	8 ± 0.5
	S-5	-87.90449	30.55144	22.3	2830	1.5	-21.4	-4.1	N/A	40 ± 3	40 ± 4	3 ± 0.2	7 ± 0.4
	S-6	-88.08128	30.55829	20.4	4290	2.3	-15.1	-3.8	N/A	60 ± 3	70 ± 5	3 ± 0.1	3 ± 0.2
	S-7	-88.09216	30.51984	21.7	3690	1.9	-21.7	-3.9	N/A	70 ± 4	60 ± 5	2 ± 0.1	3 ± 0.2
	S-8	-88.10060	30.49407	21.7	4560	2.4	-19.2	-3.7	N/A	90 ± 5	70 ± 3	3 ± 0.1	5 ± 0.3
	S-9	-88.10475	30.44645	22.1	4950	2.6	-20.1	-4.0	N/A	-	-	-	-
	S-10	-88.10332	30.44149	22.7	5250	2.8	-20.2	-4.0	N/A	130 ± 9	50 ± 4	3 ± 0.2	5 ± 0.3
	S-11	-88.10099	30.42176	22.3	6050	3.2	-19.0	-3.9	N/A	-	-	-	-
	S-12	-88.10169	30.40087	22.0	7750	4.1	-19.7	-3.7	N/A	-	-	-	-
	S-13	-88.10223	30.39501	21.8	7830	4.4	-18.7	-3.7	N/A	370 ± 20	80 ± 5	4 ± 0.2	6 ± 0.4
TS-SE-R3	-87.87887	30.39188	22.0	11660	6.6	-14.9	-3.2	N/A	-	-	-	-	
TS-W-R3	-88.10527	30.40376	21.3	7130	3.9	-15.8	-3.4	N/A	-	-	-	-	
MR	-88.01071	30.68467	18.8	150	0.1	-4.8	-1.1	N/A	-	-	-	-	
TR	-88.00559	30.68133	19.1	250	0.2	-4.8	-0.9	N/A	-	-	-	-	
SE-Well-1	-87.79257	30.40586	19.0	40	0.1	-18.7	-4.2	100 ± 40	-	-	-	-	
SE-Well-2	-87.88392	30.43140	18.6	50	0.1	-19.5	-3.8	60 ± 20	-	-	-	-	
July 2015	S-14	-88.10082	30.38729	30.1	29280	16.2	-4.0	-1.0	N/A	580 ± 40	90 ± 6	4 ± 0.2	7 ± 0.4
	S-15	-88.10063	30.41235	31.7	25600	13.6	-5.1	-1.0	N/A	520 ± 40	200 ± 10	7 ± 0.4	6 ± 0.4
	S-16	-88.10221	30.43576	31.3	21890	11.5	-5.8	-0.9	N/A	420 ± 30	180 ± 8	6 ± 0.3	6 ± 0.3
	S-17	-88.10332	30.44149	32.1	11570	5.7	-10.2	-2.3	N/A	370 ± 30	110 ± 9	4 ± 0.2	5 ± 0.3

	S-18	-88.08348	30.52646	31.3	20220	10.6	-11.4	-1.8	N/A	204 ± 20	170 ± 10	6 ± 0.4	7 ± 0.4
	S-19	-87.85488	30.37703	28.8	15520	8.3	-10.0	-2.0	N/A	70 ± 10	100 ± 10	3 ± 0.1	15 ± 0.9
	S-20	-87.87132	30.38527	29.0	13510	7.2	-10.8	-2.2	N/A	100 ± 10	20 ± 3	2 ± 0.1	13 ± 0.8
	S-21	-87.89934	30.40281	29.5	14410	7.6	-9.0	-2.2	N/A	130 ± 10	110 ± 9	5 ± 0.2	8 ± 0.5
	S-22	-87.91749	30.43925	30.2	12670	6.5	-7.9	-1.8	N/A	120 ± 10	70 ± 5	1 ± 0.1	7 ± 0.4
	S-23	-87.93801	30.48410	31.5	12150	6.2	-11.2	-2.3	N/A	-	-	-	-
	MR	-88.01071	30.68467	29.1	950	0.4	-13.9	-2.8	N/A	190 ± 20	120 ± 20	1 ± 0.1	N/A
	TR	-88.00559	30.68133	28.8	750	0.2	-20.2	-3.6	N/A	-	-	-	-
	AR	-87.95435	30.67318	29.5	680	0.2	-18.7	-3.5	N/A	-	-	-	-
	SE-Well-1	-87.79257	30.40586	23.6	40	0.1	-19.7	-3.9	90 ± 20	-	-	-	-
	SE-Well-2	-87.88392	30.43140	22.3	70	0.1	-20.5	-4.2	60 ± 10	-	-	-	-
March 2016	S-24	-88.10502	30.38330	22.2	5350	2.9	-19.4	-3.9	N/A	-	-	-	-
	S-25	-88.10226	30.42125	22.4	5200	2.8	-18.4	-3.6	N/A	-	-	-	-
	S-26	-88.09991	30.46609	22.5	4680	2.5	-18.5	-3.7	N/A	-	-	-	-
	S-27	-88.10152	30.49469	23.0	2900	1.5	-21.0	-4.1	N/A	-	-	-	-
	S-28	-87.87852	30.38507	21.8	3060	1.6	-18.0	-3.7	N/A	-	-	-	-
	S-29	-87.91357	30.42801	22.1	2580	1.3	-18.4	-4.0	N/A	-	-	-	-
	S-30	-87.91951	30.46050	22.2	2440	1.2	-18.6	-3.9	N/A	-	-	-	-
	TS-SE-R3	-87.87887	30.39188	23.2	4020	2.1	-17.5	-3.7	N/A	130 ± 10	220 ± 20	4 ± 0.6	7 ± 0.7
	TS-SE-R3	-87.91136	30.52604	21.0	360	0.2	-20.6	-4.2	N/A	110 ± 20	130 ± 10	3 ± 0.2	5 ± 0.8
	TS-W-R3	-88.10527	30.40376	25.2	5040	2.7	-	-	N/A	100 ± 20	90 ± 8	5 ± 0.2	6 ± 0.7
	MR	-88.01071	30.68467	16.5	230	0.1	-21.1	-4.3	N/A	-	-	-	-
	TR	-88.00559	30.68133	17.0	110	0.1	-17.6	-3.9	N/A	-	-	-	-
	AR	-87.95435	30.67318	15.3	140	0.1	-20.9	-4.2	N/A	-	-	-	-
	SE-Well-1	-87.79257	30.40586	21.8	90	0.1	-20.2	-4.4	60 ± 20	-	-	-	-
SE-Well-2	-87.88392	30.43140	21.1	60	0.1	-21.4	-4.5	24 ± 10	-	-	-	-	
W-Well-1	-88.12211	30.46031	21.2	130	0.1	-20.5	-4.3	110 ± 20	-	-	-	-	
W-Well-2	-88.12330	30.47109	21.6	140	0.1	-18.3	-3.9	90 ± 10	-	-	-	-	

	W-Well-3	-88.10803	30.48300	21.1	70	0.1	-21.9	-4.3	110 ± 20	-	-	-	-
April 2016	NE-Pz-1	-87.90843	30.53010	20.6	580	0.3	-18.2	-4.2	80 ± 20	-	-	-	-
	NE-Pz-2	-87.90854	30.53015	21.7	190	0.2	-19.8	-4.2	30 ± 6	-	-	-	-
	NE-Pz-3	-87.90855	30.53013	24.2	510	0.3	-20.4	-3.9	20 ± 7	-	-	-	-
	NE-Pz-4	-87.90860	30.53016	22.4	4270	2.3	-	-	20 ± 7	-	-	-	-
	NE-Pz-5	87.90863	30.53017	22.9	5820	3.2	-	-	10 ± 4	-	-	-	-
June 2016	SE-Pz-1a	-87.87815	30.39243	25.7	990	0.1	-13.1	-3.0	70 ± 20	-	-	-	-
	SE-Pz-1b	-87.87815	30.39243	29.0	1490	0.3	-14.1	-3.4	60 ± 20	-	-	-	-
	SE-Pz-2a	-87.87819	30.39237	23.7	1930	0.4	-12.3	-2.8	50 ± 10	-	-	-	-
	SE-Pz-2b	-87.87819	30.39237	24.7	2360	0.8	-13.6	-2.7	40 ± 10	-	-	-	-
	SE-Pz-3a	-87.87818	30.39236	24.7	7630	4.2	-13.0	-2.8	30 ± 10	-	-	-	-
	SE-Pz-3b	-87.87818	30.39236	24.8	8060	4.8	-12.8	-2.9	30 ± 9	-	-	-	-
	SE-Pz-4	-87.87823	30.39231	25.6	9540	5.3	-13.4	-2.6	40 ± 4	-	-	-	-
	SE-Pz-5	-87.87827	30.39228	23.2	9970	5.6	-12.9	-3.0	20 ± 9	350 ± 20	340 ± 20	20 ± 1	N/A
	TS-SE-R1	-87.87841	30.39241	29.6	10250	5.8	-10.5	-2.5	N/A	70 ± 6	20 ± 1	1 ± 0.1	6 ± 0.4
	TS-SE-R2	-87.87858	30.39221	27.5	10140	5.7	-19.0	-4.1	N/A	50 ± 3	40 ± 2	2 ± 0.1	13 ± 0.8
	TS-SE-R3	-87.87887	30.39188	27.9	10120	5.7	-11.6	-2.7	N/A	40 ± 3	120 ± 7	3 ± 0.2	11 ± 0.7
	W-Pz-1	-88.10646	30.40353	24.8	1540	0.7	-19.4	-4.2	210 ± 20	-	-	-	-
	W-Pz-2	-88.10632	30.40352	24.2	1680	0.8	-20.4	-4.2	440 ± 30	-	-	-	-
	W-Pz-3	-88.10632	30.40352	23.9	1910	1.0	-14.4	-3.1	310 ± 20	-	-	-	-
	W-Pz-4	-88.10629	30.40351	22.3	6380	3.8	-	-	70 ± 10	-	-	-	-
	W-Pz-5	-88.10625	30.40350	22.0	10690	6.1	-19.0	-3.7	140 ± 40	6610 ± 500	1130 ± 100	30 ± 2	N/A
	TS-W-R1	-88.10606	30.40380	27.0	20010	11.9	-	-	N/A	70 ± 5	170 ± 10	15 ± 1	14 ± 8
	TS-W-R2	-88.10573	30.40377	28.3	19890	11.8	-	-	N/A	50 ± 4	100 ± 7	9 ± 0.7	14 ± 8
	TS-W-R3	-88.10527	30.40375	29.1	20290	12.0	-	-	N/A	30 ± 2	25 ± 2	2 ± 0.1	14 ± 8
	MR	-88.01071	30.68467	23.7	160	0.1	-15.5	-3.8	N/A	70 ± 4	40 ± 2	1 ± 0.1	N/A
TR	-88.00559	30.68133	23.5	180	0.1	-18	-4.1	N/A	110 ± 6	60 ± 4	3 ± 0.2	N/A	

AR	-87.95435	30.67318	23.1	170	0.1	-17.6	-4.2	N/A	120 ± 8	10 ± 0.6	1 ± 0.1	N/A
SE-Well-1	-87.79257	30.40586	21.3	70	0.1	-19.1	-3.8	80 ± 20	-	-	-	-
SE-Well-2	-87.88392	30.43140	21.5	60	0.1	-20.6	-4.2	70 ± 20	-	-	-	-
NE-Pz-1a	-87.90843	30.53010	27.9	300	0.1	-20.2	-4.3	110 ± 20	-	-	-	-
NE-Pz-1b	-87.90843	30.53010	28.1	220	0.1	-20.4	-4.2	70 ± 20	-	-	-	-
NE-Pz-2	-87.90854	30.53015	30.2	360	0.2	-19.4	-3.9	70 ± 30	-	-	-	-
NE-Pz-3a	-87.90855	30.53013	30.7	180	0.1	-	-	40 ± 10	-	-	-	-
NE-Pz-3b	-87.90855	30.53013	27.4	140	0.1	-	-	70 ± 20	-	-	-	-
NE-Pz-4	-87.90860	30.53016	30.1	16310	9.4	-10.6	-2.2	10 ± 2	-	-	-	-
NE-Pz-5	-87.90863	30.53017	30.6	16490	9.6	-10.2	-2.2	10 ± 3	540 ± 40	480 ± 30	60 ± 5	N/A
TS-NE-R1	-87.91106	30.52579	31.0	18110	10.7	-	-	N/A	320 ± 20	190 ± 10	20 ± 1	12 ± 2
TS-NE-R3	-87.91136	30.52604	31.6	18230	10.7	-	-	N/A	160 ± 10	90 ± 8	2 ± 0.2	2 ± 0.1
TR	-88.00559	30.68133	30.1	180	0.1	-18.1	-3.4	N/A	340 ± 20	10 ± 3	2 ± 0.2	N/A
AR	-87.95435	30.67318	29.0	200	0.1	-17.9	-3.6	N/A	60 ± 5	3 ± 0.5	1 ± 0.1	N/A

December
2016

SE-Pz-1a	-87.87815	30.39243	22.7	540	0.8	-12.2	-3.2	-	-	-	-	-
SE-Pz-1b	-87.87815	30.39243	24.3	530	0.8	-	-	-	-	-	-	-
SE-Pz-2a	-87.87819	30.39237	21.0	2400	1.2	-14.6	-3.0	-	-	-	-	-
SE-Pz-2b	-87.87819	30.39237	24.6	2220	1.1	-	-	-	-	-	-	-
SE-Pz-3a	-87.87818	30.39236	21.0	11190	6.9	-10.4	-2.3	-	-	-	-	-
SE-Pz-3b	-87.87818	30.39236	21.2	14180	8.7	-	-	-	-	-	-	-
SE-Pz-4a	-87.87823	30.39231	20.8	21840	14.4	-4.4	-1.0	-	-	-	-	-
SE-Pz-4b	-87.87823	30.39231	20.7	21900	14.5	-	-	-	-	-	-	-
SE-Pz-5a	-87.87823	30.39231	19.7	26800	18.5	0.0	-0.2	-	-	-	-	-
SE-Pz-5b	-87.87827	30.39228	20.0	34580	20.0	-	-	-	-	-	-	-
TS-E-Sea	-87.87827	30.39226	17.7	36510	27.3	1.2	0.3	-	-	-	-	-
SE-Well-2	-87.88392	30.43140	20.4	90	0.0	-20.8	-4.2	-	-	-	-	-
W-Pz-1a	-88.10646	30.40353	19.8	3120	1.4	-11.4	-2.5	-	-	-	-	-
W-Pz-1b	-88.10646	30.40353	19.5	2950	1.2	-	-	-	-	-	-	-

W-Pz-2a	-88.10631	30.40352	19.2	3350	1.7	-	-	-	-	-	-	-
W-Pz-2b	-88.10631	30.40352	19.1	3780	1.9	-	-	-	-	-	-	-
W-Pz-3a	-88.10629	30.40351	18.0	6220	3.9	-14.8	-3.4	-	-	-	-	-
W-Pz-3b	-88.10629	30.40351	18.2	6250	4.0	-	-	-	-	-	-	-
W-Pz-4a	-88.10625	30.40351	17.8	18560	13.0	-	-	-	-	-	-	-
W-Pz-4b	-88.10625	30.40351	17.7	18740	13.1	-	-	-	-	-	-	-
W-Pz-5a	-88.10623	30.40351	17.2	26020	18.8	-0.1	-0.5	-	-	-	-	-
W-Pz-5b	-88.10623	30.40351	17.4	27340	20.0	-	-	-	-	-	-	-
TS-W-Sea	-88.10619	30.40350	16.5	29120	21.9	0.0	-0.3	-	-	-	-	-
MR	-88.01071	30.68467	16.5	230	0.1	0.3	-0.2	-	-	-	-	-
TR	-88.00559	30.68133	17.1	380	0.1	-8.8	-1.6	-	-	-	-	-
AR	-87.95435	30.67318	16.9	260	0.1	-12.4	-2.4	-	-	-	-	-

March
2017

S-31	-88.05538	30.59405	15.7	16040	11.7	-12.9	-2.6	N/A	220 ± 20	90 ± 5	10 ± 1	7 ± 0.4
S-32	-88.05687	30.62115	15.1	18090	13.5	-11.8	-2.4	N/A	340 ± 30	140 ± 10	10 ± 1	3 ± 0.2
S-33	-88.01750	30.65843	16.8	5470	3.6	-15.4	-3.2	N/A	100 ± 8	60 ± 4	6 ± 0.5	1 ± 0.1
S-34	-87.96182	30.65287	14.7	270	0.2	-16.6	-3.5	N/A	50 ± 4	40 ± 2	3 ± 0.3	1 ± 0.1
S-35	-88.05711	30.56466	14.1	11640	8.6	-15.2	-3.0	N/A	180 ± 10	80 ± 5	7 ± 0.5	3 ± 0.2
S-36	-88.02453	30.56527	14.6	6460	4.5	-15.2	-3.1	N/A	80 ± 6	40 ± 2	5 ± 0.4	5 ± 0.3
S-37	-87.99126	30.56479	14.5	6760	4.7	-14.6	-2.8	N/A	270 ± 20	100 ± 6	20 ± 2	8 ± 0.5
S-38	-87.95009	30.56048	14.6	5890	4.1	-10.7	-2.2	N/A	160 ± 10	80 ± 5	7 ± 0.6	3 ± 0.2
S-39	-87.95414	30.56881	14.6	5680	3.9	-14.9	-2.7	N/A	20 ± 2	10 ± 1	2 ± 0.2	8 ± 0.5
S-40	-88.02212	30.60659	16.2	5220	3.4	-17.5	-3.4	N/A	50 ± 4	20 ± 1	1 ± 0.2	8 ± 0.5
S-41	-88.05722	30.24987	18.4	12930	8.6	-7.8	-1.3	N/A	140 ± 10	80 ± 5	10 ± 1	3 ± 0.2
S-42	-88.03319	30.24594	17.8	118560	8.0	-7.9	-0.9	N/A	220 ± 20	130 ± 8	12 ± 1	2 ± 0.1
S-43	-87.91487	30.57848	18.0	7520	4.9	-13.9	-2.7	N/A	60 ± 5	70 ± 5	4 ± 0.3	2 ± 0.1
S-44	-87.91509	30.60275	17.4	3410	2.1	-15.1	-3.3	N/A	150 ± 10	240 ± 20	20 ± 2	8 ± 0.5
S-45	-87.92152	30.62343	17.3	1810	1.1	-17.2	-3.5	N/A	40 ± 2	140 ± 10	20 ± 2	-
S-46	-87.99826	30.62905	18.5	6430	3.5	-	-	N/A	150 ± 10	70 ± 5	9 ± 0.6	16 ± 1.0

S-47	-87.94899	30.52249	18.2	6350	3.4	-	-	N/A	140 ± 10	130 ± 10	7 ± 0.6	10 ± 0.6
S-48	-87.98315	30.53314	18.1	5400	3.0	-	-	N/A	190 ± 10	60 ± 4	1 ± 0.1	-
S-49	-88.02727	30.54792	18.4	5230	2.9	-	-	N/A	180 ± 10	90 ± 7	5 ± 0.3	10 ± 0.6
S-50	-88.06469	30.56019	18.8	4610	2.5	-	-	N/A	340 ± 20	110 ± 8	6 ± 0.4	9 ± 0.6
NE-Pz-1	-87.90843	30.53010	20.6	110	0.1	-20.1	-4.1	-	-	-	-	-
NE-Pz-2	-87.90854	30.53015	17.7	270	0.2	-18.8	-3.8	-	-	-	-	-
NE-Pz-3	-87.90855	30.53013	16.8	470	0.3	-16.8	-3.8	-	-	-	-	-
NE-Pz-4	-87.90860	30.53016	15.5	3290	2.1	-14.9	-3.3	-	-	-	-	-
NE-Pz-5	87.90863	30.53017	15.4	3670	2.4	-16.8	-3.9	-	-	-	-	-
SE-Pz-1	-87.87815	30.39243	18.4	1040	0.6	-11.5	-3.1	-	-	-	-	-
SE-Pz-2	-87.87819	30.39237	17.8	1590	0.6	-12.6	-3.0	-	-	-	-	-
SE-Pz-3	-87.87818	30.39236	19.1	3820	2.3	-8.4	-2.3	-	-	-	-	-
SE-Pz-4	-87.87823	30.39231	19.8	11890	7.6	-10.1	-2.9	-	-	-	-	-
SE-Pz-5	-87.87827	30.39228	14.9	17810	13.3	-6.4	-1.4	-	-	-	-	-
W-Pz-1	-88.10646	30.40353	16.9	1420	0.9	-19.8	-4.2	-	-	-	-	-
W-Pz-3	-88.10625	30.40351	15.0	4560	3.1	-13.5	-2.8	-	-	-	-	-
W-Pz-5	-88.10623	30.40351	14.8	10380	7.2	-6.9	-1.5	-	-	-	-	-
MR	-88.01071	30.68467	14.5	450	0.2	-21.0	-2.7	-	-	-	-	-
BR	-87.92734	30.66650	16.0	340	0.1	-16.7	-3.5	-	-	-	-	-

July 2017

S-51	-87.85198	30.24455	27.9	6450	3.9	-21.6	-3.4	N/A	330 ± 20	140 ± 10	7 ± 0.4	8 ± 0.5
S-52	-87.79181	30.25622	29.0	9060	4.4	-20.5	-3.5	N/A	340 ± 20	90 ± 6	4 ± 0.3	8 ± 0.5
S-53	-87.75262	30.28377	30.1	11220	5.5	-17.9	-3.3	N/A	-	-	-	-
S-54	-87.77329	30.26144	29.1	10060	4.9	-17.5	-3.0	N/A	200 ± 10	190 ± 10	10 ± 0.8	10 ± 0.6
S-55	-87.76827	30.30386	30.0	11780	5.8	-15.9	-3.0	N/A	-	-	-	-
S-56	-87.80235	30.32724	29.8	10320	5.0	-18.4	-3.2	N/A	70 ± 5	50 ± 3	1 ± 0.1	8 ± 0.5
S-57	-87.82057	30.34272	31.8	7920	3.7	-20.6	-3.3	N/A	-	-	-	-
S-58	-87.87329	30.34164	31.3	3770	1.7	-24.9	-4.1	N/A	100 ± 7	90 ± 7	2 ± 0.2	10 ± 0.6
S-59	-87.90930	30.34115	30.5	1130	0.5	-25.6	-4.4	N/A	-	-	-	-

S-60	-88.00410	30.33785	27.6	2000	0.9	-24.2	-4.5	N/A	120± 8	50 ± 3	2 ± 0.2	8 ± 0.5
S-61	-88.01090	30.59418	26.5	190	0.1	-25.9	-4.2	N/A	-	-	-	-
S-62	-87.95299	30.61587	24.6	150	0.1	-26.8	-4.4	N/A	120 ± 8	70 ± 7	1 ± 0.1	2 ± 0.1
S-63	-87.92827	30.62521	24.8	130	0.1	-26.2	-4.3	N/A	90 ± 6	80± 5	4 ± 0.3	2 ± 0.1
S-64	-87.91608	30.59560	23.3	250	0.1	-24.7	-4.3	N/A	80 ± 5	110 ± 8	4 ± 0.4	6 ± 0.4
S-65	-87.90781	30.57037	25.1	960	0.4	-24.4	-4.3	N/A	110 ± 7	110 ± 9	4 ± 0.3	6 ± 0.3
S-66	-87.99113	30.53048	29.5	250	0.1	-25.3	-4.4	N/A	-	-	-	-
TS-SE-R1	-87.87841	30.39241	28.4	4980	2.8	-	-	N/A	50 ± 3	20 ± 1	1 ± 0.1	4 ± 0.2
TS-SE-R2	-87.87858	30.39221	28.7	5010	2.9	-	-	N/A	160 ± 10	25 ± 2	2 ± 0.3	7 ± 0.4
TS-SE-R3	-87.87887	30.39188	28.3	4870	2.6	-	-	N/A	290 ± 20	190 ± 10	1 ± 0.1	-
TS-SE-Sea	-87.87827	30.39226	29.2	4660	2.4	-22.5	-4.0	N/A	-	-	-	-
TS-NE-R1	-87.91106	30.52579	29.5	4320	2.2	-	-	N/A	90 ± 6	130 ± 10	5 ± 0.4	4 ± 0.2
TS-NE-R2	-87.91120	30.52587	29.3	4720	2.5	-	-	N/A	70 ± 5	130 ± 10	6 ± 0.4	6 ± 0.4
TS-NE-R3	-87.91136	30.52604	29.7	4790	2.6	-23.6	-4.1	N/A	70 ± 5	120 ± 8	3 ± 0.3	2 ± 0.1
SE-Pz-1	-87.87815	30.39243	28.2	1660	0.4	-9.7	-2.8	-	700 ± 40	470 ± 30	10 ± 1	N/A
SE-Pz-2	-87.87819	30.39237	30.0	2400	1.1	-24.7	-4.4	-	-	-	-	-
SE-Pz-3	-87.87818	30.39236	29.4	4040	1.9	-22.2	-3.8	-	-	-	-	-
SE-Pz-4.5-a	-87.87825	30.39229	-	-	-	-22.1	-3.7	-	-	-	-	-
SE-Pz-4.5-b	-87.87825	30.39229	-	-	-	-21.5	-3.6	-	-	-	-	-
SE-Pz-4.5-c	-87.87825	30.39229	-	-	-	-21.3	-3.7	-	-	-	-	-
SE-Pz-4.5-d	-87.87825	30.39229	-	-	-	-22.8	-4.2	-	-	-	-	-
SE-Pz-4.5-e	-87.87825	30.39229	-	-	-	-24.3	-4.0	-	-	-	-	-
SE-Pz-4.5-f	-87.87825	30.39229	-	-	-	-16.7	-3.3	-	-	-	-	-
SE-Well-2	-87.88392	30.43140	25.4	120	0.1	-20.4	-4.3	-	-	-	-	-
W-Pz-1	-88.10646	30.40353	27.5	450	0.3	-17.7	-3.8	-	-	-	-	-
NE-Pz-1	-87.90843	30.53010	28.4	260	0.1	-19.5	-4.1	-	530 ± 30	540 ± 40	20 ± 2	N/A
NE-Pz-5	87.90863	30.53017	29.5	570	0.4	-20.4	-4.2	-	600 ± 40	430 ± 30	10 ± 1	N/A
MR	-88.01071	30.68467	29.0	150	0.1	-27.4	-4.6	-	180 ± 10	40 ± 5	2 ± 0.2	N/A
TR	-88.00559	30.68133	27.5	70	0.1	-27.0	-4.6	N/A	-	-	-	-

	BR	-87.92734	30.66650	29.4	140	0.1	-25.4	-4.5	N/A	-	-	-	-
October 2014	SW-DI-1	-88.07790	30.25111	30.1	38560	24.5	0.2	0.0	N/A	-	-	-	-
	SW-DI-2	-88.13789	30.25508	30.5	41910	26.8	0.2	0.0	N/A	-	-	-	-
	SW-DI-3	-88.19241	30.25037	30.2	41550	26.1	0.1	0.0	N/A	-	-	-	-

Figure 1. Spatial distribution of salinity measured in Mobile Bay showing combined values from all surveys conducted during the dry season (a) and wet season (b). During the dry season salinity was on average higher (4.2) than during wet periods (1.7). The lowest salinity values were always measured near the Mobile-Tensaw River System, whereas the highest values were measured on the western shore and Bon Secour Bay.

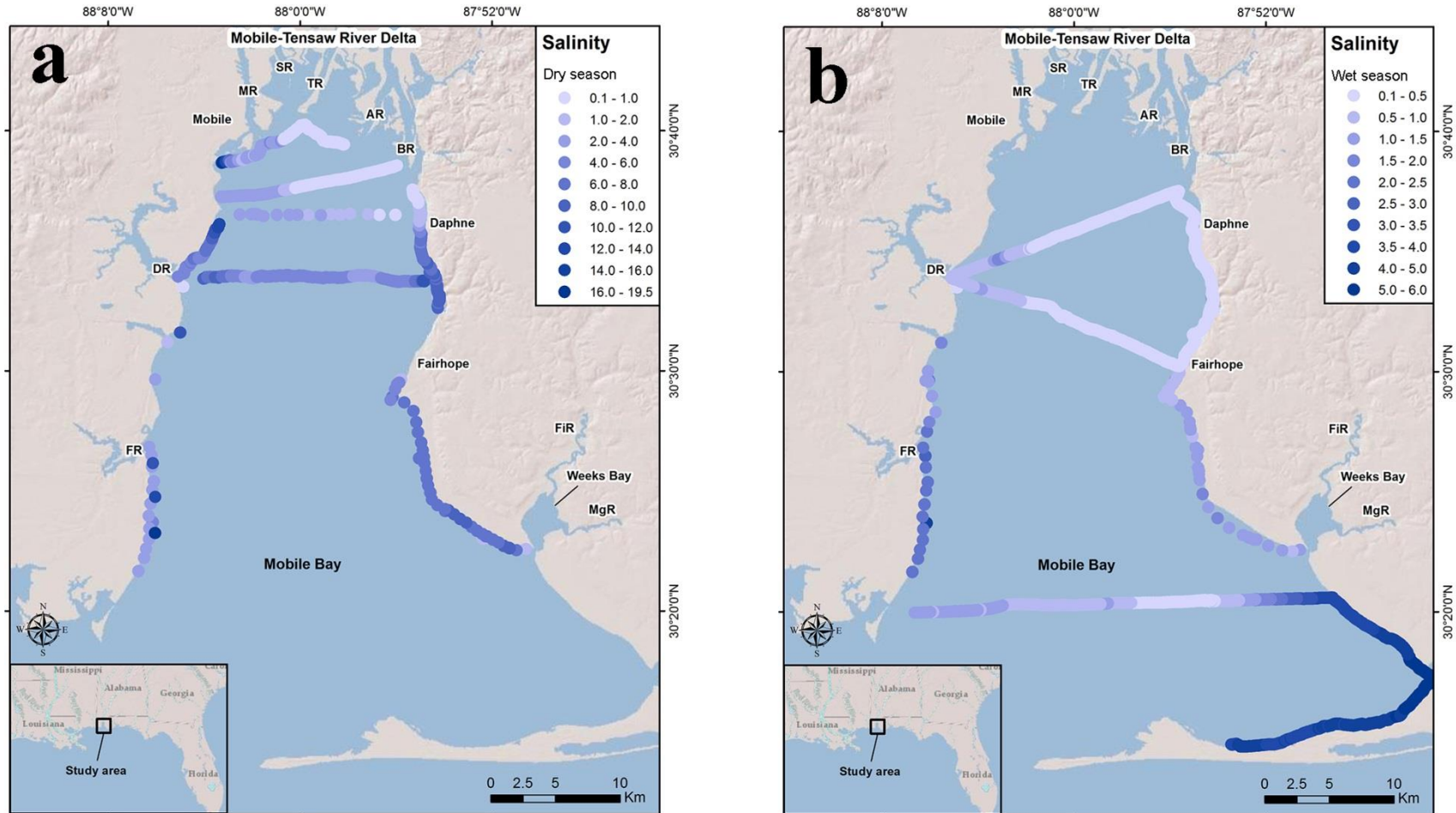


Figure. 2. ^{226}Ra (a), ^{224}Ra (b), and ^{223}Ra (c) concentrations measured in Mobile Bay during all sampling campaigns. The spatial distribution of ^{226}Ra and ^{224}Ra showed a strong correlation with salinity where higher salinity values derived in higher radium concentrations due to desorption from suspended particles. Radium-226 concentrations were highest on the western shore and Bon Secour Bay, whereas ^{224}Ra peaked on the western and southeastern shores. In contrast, ^{223}Ra concentrations were highest on the northern area of the bay and Bon Secour Bay.

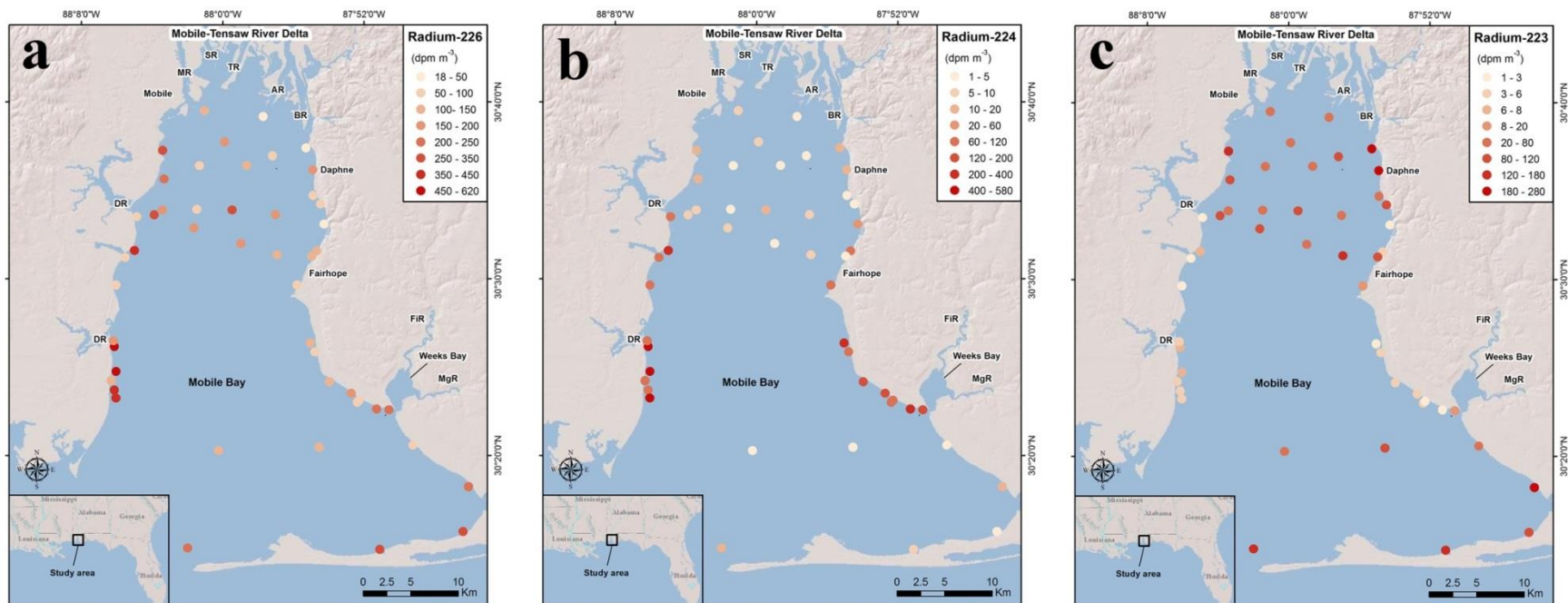
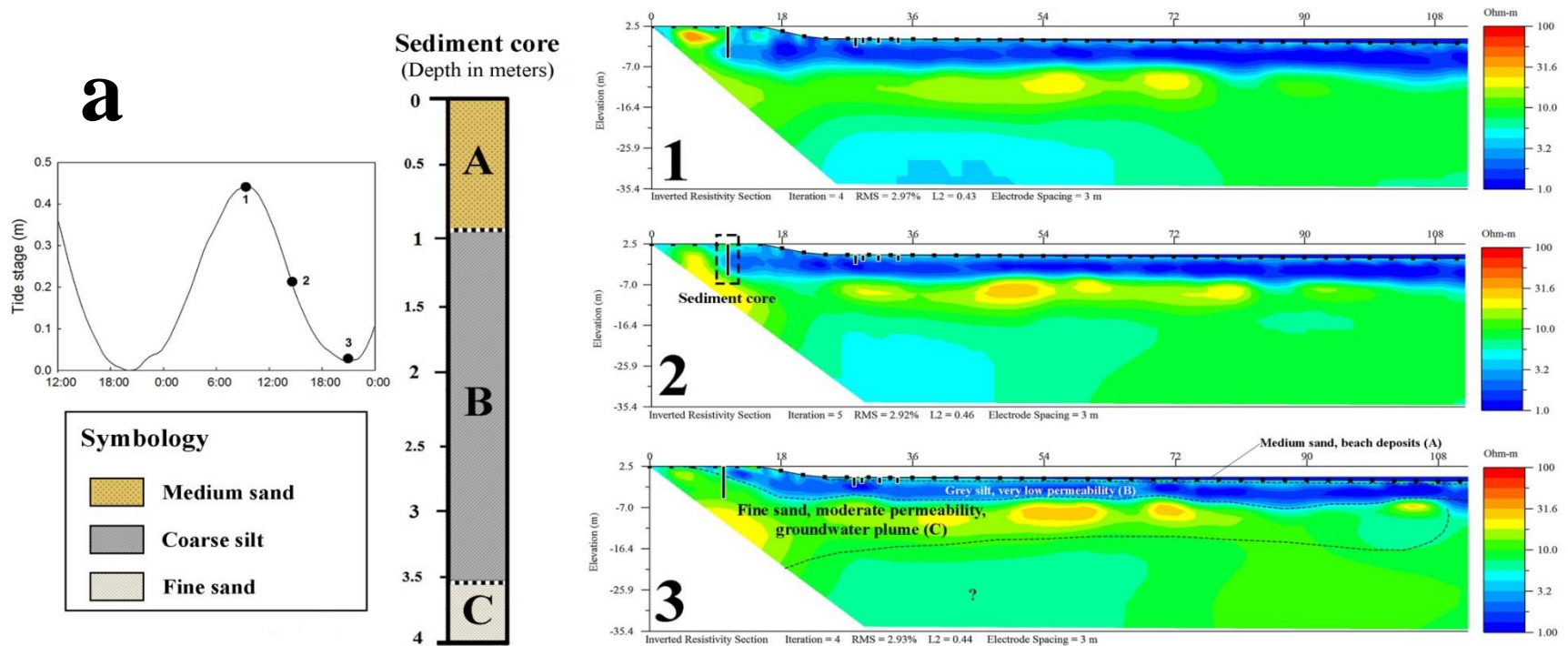
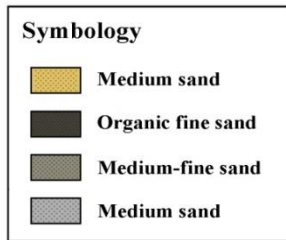
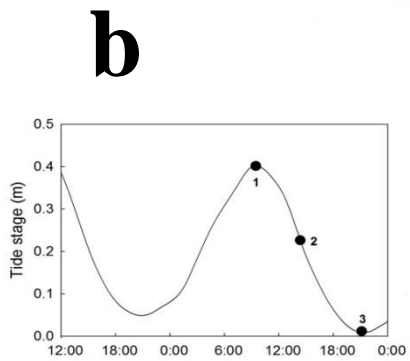
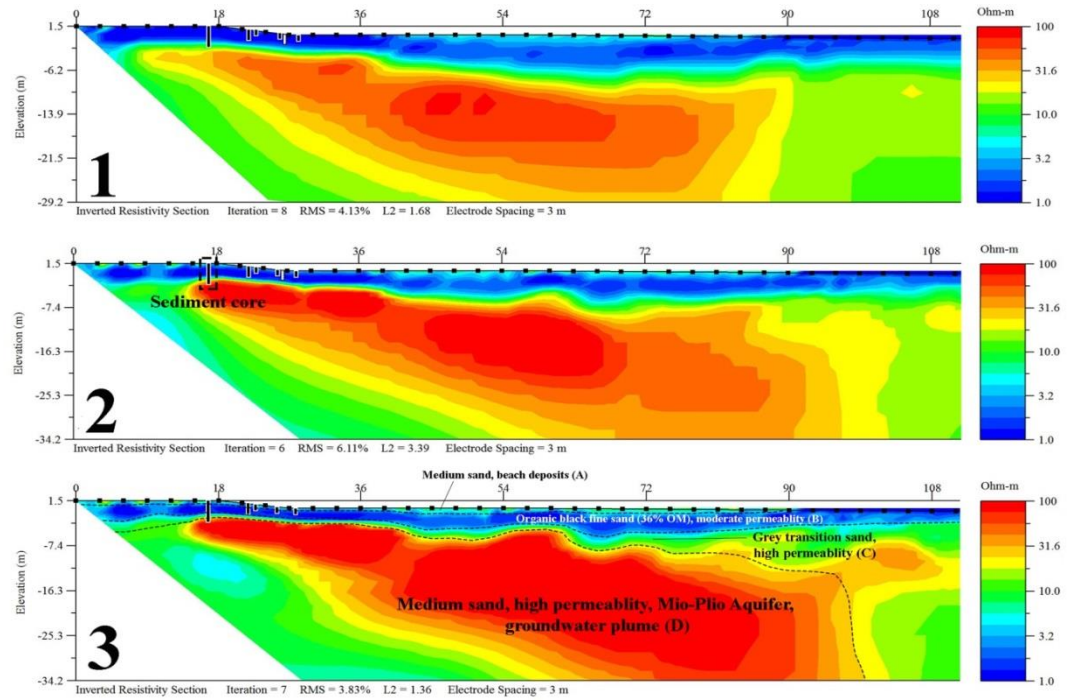
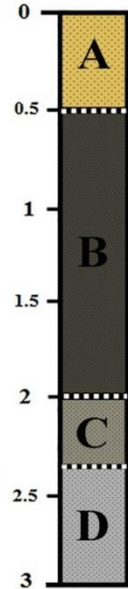


Figure 3. Shore-perpendicular time-lapse ERT performed during falling tide and sediment cores collected at TS-W on the western shore (a), TS-SE on the southeastern shore (b), and TS-NE on the northeastern shore (c). The tide stage and time of each ERT measurement during the time series is shown for each location with numbers (1, 2, and 3) in the left panel, corresponding with the numbers on the ERT images. The sediment cores were retrieved from the installed piezometer Pz-1 at each location and are highlighted with a dashed square in ERT line 2 of each site.





Sediment core
(Depth in meters)



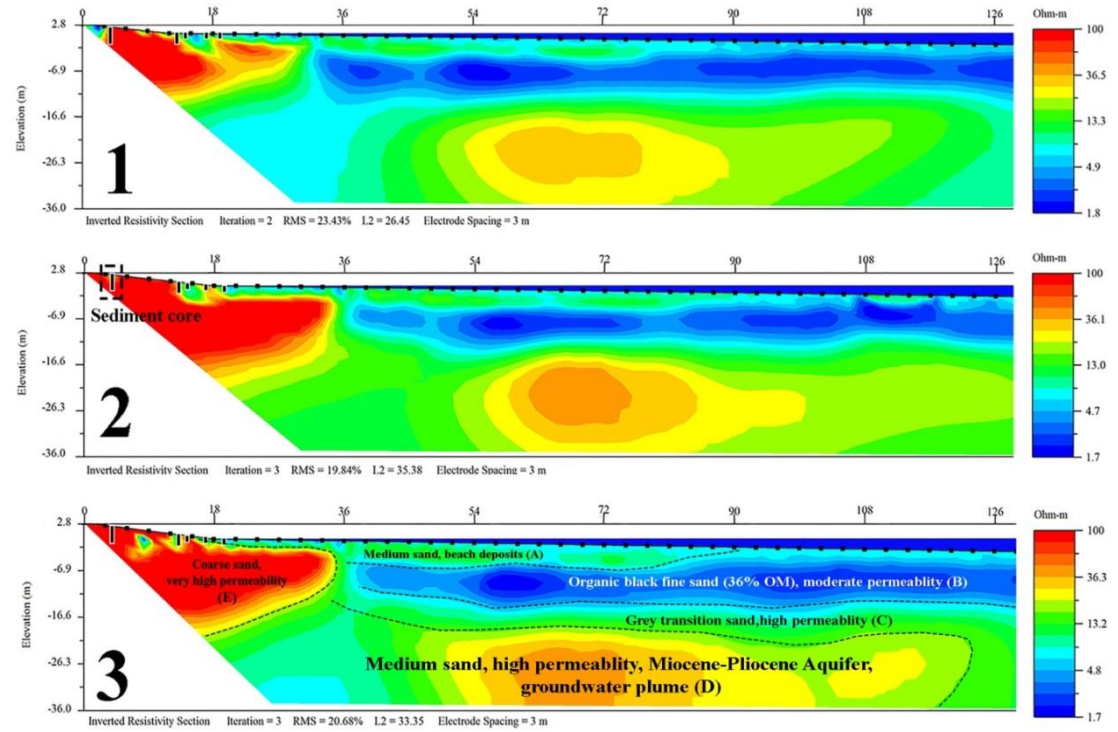
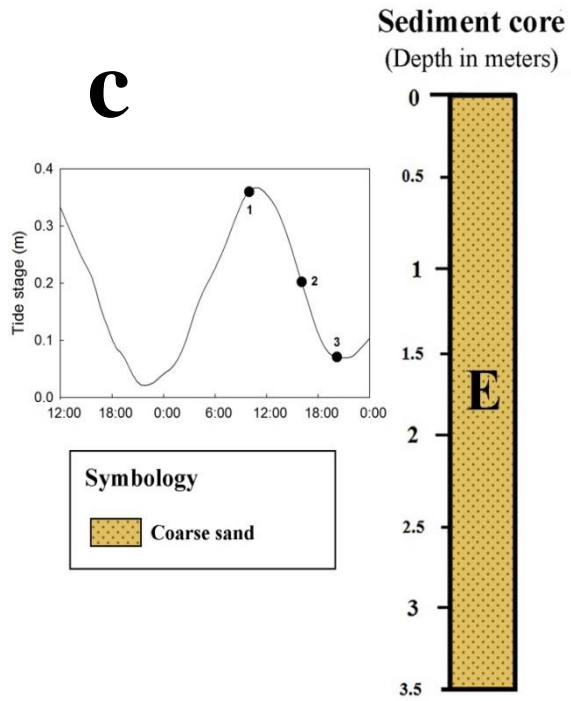


Figure. 4. Scatter plots showing the negative correlation between SGD rates and tide stage on the western shore (study site TS-W) during the high SGD period (a) and base flow SGD period (b) of the 5-day time series measurements conducted during March of 2016. Panel (c) shows the positive correlation between SGD rates and the groundwater elevation during the whole 5-day time series measurements.

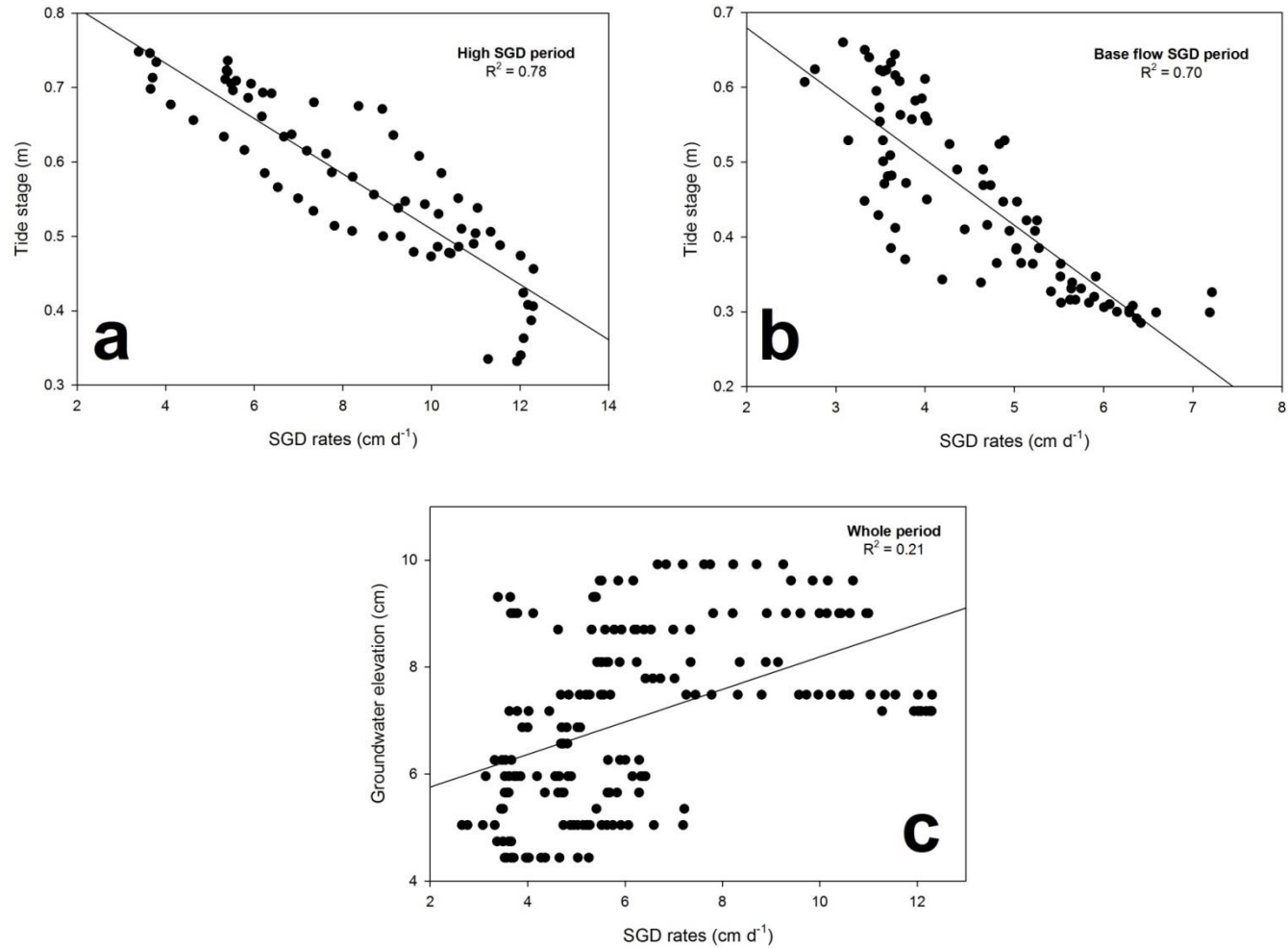


Figure. 5. Scatter plots showing the negative correlation between SGD rates and tide stage on the northeastern shore (study site TS-NE) during the first day of time-series measurements (a) and the positive correlation between SGD rates and groundwater elevation during the remaining 4 days of the time-series (b) of the 5-day time series measurements conducted during March of 2016.

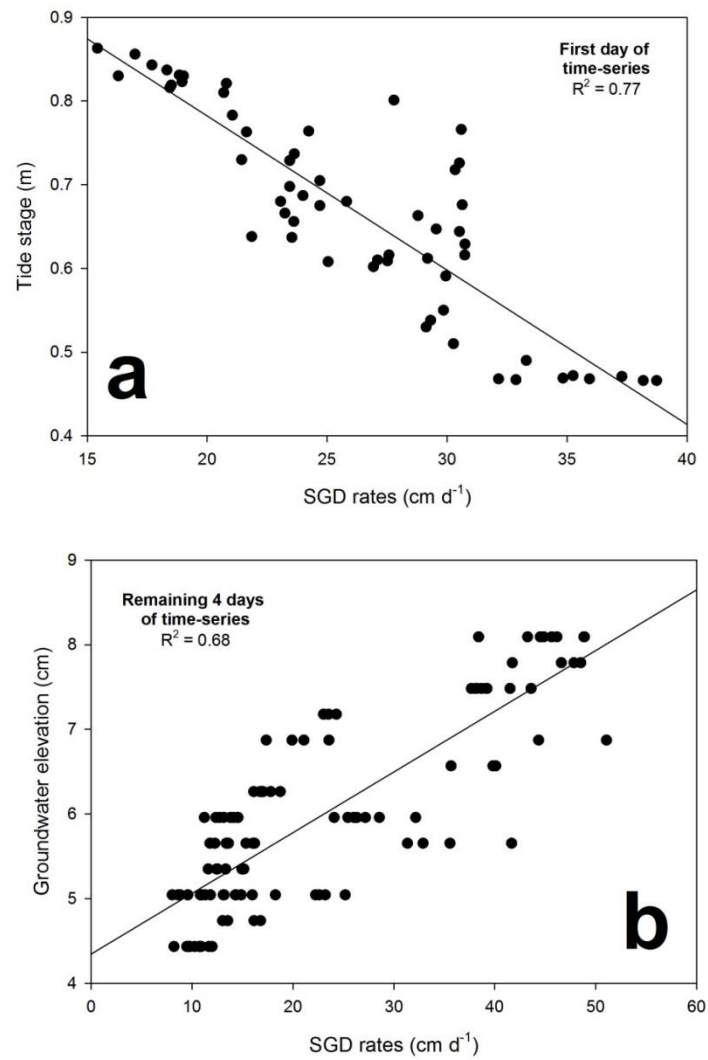
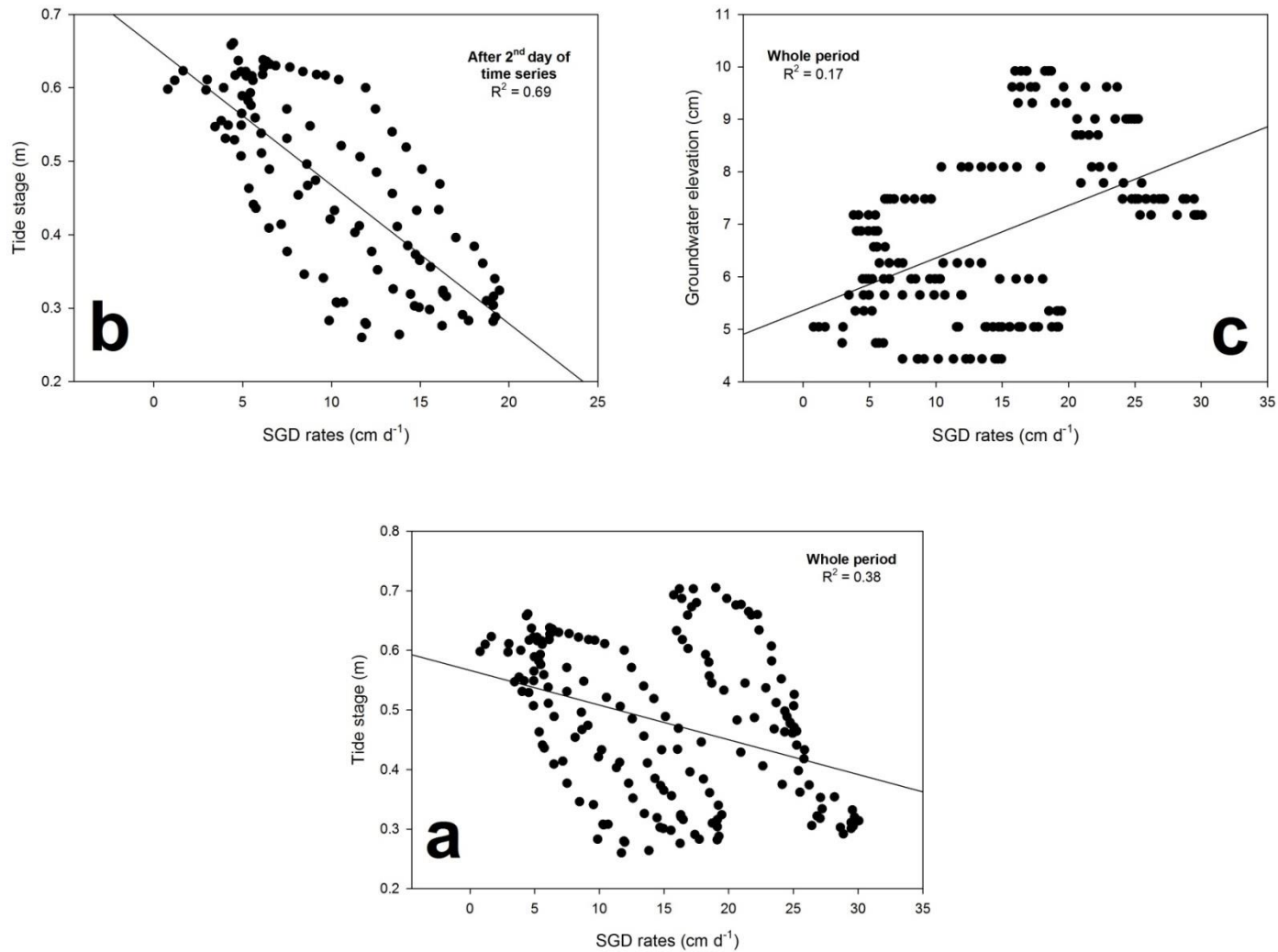


Figure 6. Scatter plots showing the negative correlation between SGD rates and tide stage on the southeastern shore (study site TS-SE) during the whole time series measurements (a) and after the 2nd day of measurements (b) of the 5-day time series measurements conducted during March of 2016. Panel (c) shows the positive correlation between SGD rates and the groundwater elevation during the whole 5-day time series measurements.



CHAPTER 4:

ARE GROUNDWATER-DERIVED NUTRIENT INPUTS IMPORTANT FOR THE JUBILEE EVENTS IN MOBILE BAY, ALABAMA?

4.1 Abstract

In this study I evaluated the importance of submarine groundwater discharge (SGD) for the nutrient (NO_3^- , NH_4^+ , DON and PO_4^{3-}) budget of Mobile Bay and its potential impacts on the estuarine ecosystem from 2015 to 2017. I used a combination of approaches including dissolved oxygen measurements, lithological characterization, radioisotopes (^{210}Pb and ^{137}Cs) dating, stable isotopes (Nitrate $\delta^{15}\text{N}$ - $\delta^{18}\text{O}$ and Sediment $\delta^{13}\text{C}$ - $\delta^{15}\text{N}$), and dissolved organic matter (DOM) composition analyses to identify the main sources of nutrients in Mobile Bay. I found that Mobile Bay receives nearly a quarter of the nutrient budget via anoxic SGD during the dry season, with 56% and 15% of the total NH_4^+ and DON inputs which were delivered to the east shore, where large-scale fish kills locally known as *Jubilees* occur. I provided four lines of evidence to demonstrate that a widespread peat layer, identified on the east shore of the bay, is the main source of SGD-derived nitrogen. Based on this investigation, the peat layer was buried relatively recently (during the 60s) and is mostly comprised of the root system and plant remains of a previously existing marsh area. I demonstrate that the naturally-occurring abundant organic matter mineralization within the peat layer is responsible for the exceptionally high NH_4^+ and DON fluxes delivered by SGD on the east shore of Mobile Bay. This finding is in contradiction with previous studies suggesting that SGD delivered the NO_3^- fertilizers contamination from the coastal aquifer to Mobile Bay. Through this investigation I found no evidence of significant

anthropogenic pollution from fertilizers and sewage waste that could potentially impact Mobile Bay. In contrast, I found that the nitrogen inputs are of natural origin, produced in the sediments and as NH_4^+ and DON. Furthermore, I hypothesize that the anoxic groundwater and NH_4^+ and DON inputs delivered by SGD could be supporting *Jubilee* events and harmful algal blooms (HAB) events observed in Mobile Bay.

4.2 Introduction

Submarine groundwater discharge (SGD) is an important source of natural and anthropogenic dissolved constituents such as nutrients, trace metals, and contaminants in coastal waters (Johannes, 1980; Moore, 1999; Null et al., 2012; Rodellas et al., 2014). The significance of SGD for the water budget of river-dominated systems has been traditionally overlooked because in most cases SGD represents only a small volumetric fraction compared to river discharge (Kohout, 1966; Burnett et al., 2006). However, nutrient concentrations in groundwater are typically orders of magnitude higher than those of surface water, resulting in nutrient fluxes comparable to fluvial inputs (Charette et al., 2003; Santos et al., 2008). Ultimately, excess of SGD-derived nutrient inputs often cause eutrophication (Hwang et al., 2005), hypoxia (McCoy et al., 2011), seagrass beds degradation (Valiela et al., 1990), and harmful algal blooms (HABs) (Garcés et al., 2011; Smith and Swarzenski, 2012).

Dissolved nutrients (e.g. N- and P-) delivered by SGD consist of both inorganic and organic forms (Santos et al., 2008; Garcia-Solsona et al., 2010; Su et al., 2014). In coastal sediments, the two forms undergo unique (yet intertwined) pathways of geochemical transformations resulting in bioavailable forms that can cause the proliferation of specific primary producers (i.e. blooms). Understanding these nutrient transformations is critical in evaluating their ecological effects (Seitzinger et al., 2002; Sadat-Noori et al., 2016).

Estuaries are among the most diverse, productive and economically important ecosystems, yet particularly sensitive to the above mentioned ecological disturbances (Seitzinger et al., 2002; Makings et al., 2014). The ecological implications of the excess of SGD-derived nutrients on estuarine systems have been widely investigated in the last two decades (e.g. Burnett and Dulaiova 2006; Burnett et al., 2007; Null et al., 2012; Xu et al. 2013). In most scenarios, the causes of nutrient enrichment in previous studies were identified as result of anthropogenic activities. However, little attention has been paid to the natural variability in the composition of the shallow aquifers, where SGD occurs in these areas. Coastal sediments at this depth are typically composed of multiple sediment layers of varying composition, organic matter content, and permeability. These hydrogeological conditions combined with daily sea level oscillations due to tidal pumping, set for fast nutrient biogeochemical transformations at the groundwater-surface water wedge (Krantz et al., 2004; Michael et al., 2016; Chapter 3). Because the majority of SGD occurs through the shallow sediments in this near shore zone, the groundwater composition discharging there (and hence of the receiving surface waters) are modulated by both the local hydrodynamics and unique lithological set up of the regional coastal aquifer (Santos et al., 2009; Sadat-Noori et al., 2016; Cerdà-Domènech et al., 2017).

Mobile Bay, located in the Alabama Gulf Coast, is the fourth largest estuary in the USA (Fig. 4.1). Typically, during the summer (or dry season) Mobile Bay experiences massive fish and crustaceans kills locally known as “*Jubilees*” (Loesch, 1960). The economic impact of the *Jubilees* is extensive, affecting recreational and commercial fisheries in Mobile Bay. For example, in 1967 May (1973) estimated that only due to the *Jubilee* events that occurred between 1967 and 1971, 23,000 kg of fish, 18,000 kg of blue crabs, and 2,653,000 oysters died, accounting for a total value of \$595,500 at that time. Recent studies indicate that harmful algal

blooms (HABs) also occur systematically in Mobile Bay during the summer (Liefer et al., 2009; McIntyre et al., 2011; Su et al., 2014). These studies indicate that *Jubilees* and HABs only occur in specific locations of Mobile Bay, often in areas with no direct surface water inputs, and that these events are caused by hypoxia and excess nutrient inputs (Loesch, 1960; May, 1973; Liefer et al., 2009). Although understanding of the effects and direct causes of the fish kill is well established, there is still large uncertainty on the processes triggering and supporting these two phenomena.

In this study, I constructed the nutrient (NO_3^- , NH_4^+ , DON and PO_4^{3-}) budget of Mobile Bay to identify the main forms and sources of nutrients to the fourth largest estuary of the USA. To evaluate the contribution of different water sources and their relative importance for the nutrient budget and ecological impact on these coastal areas, I specifically examined several locations impacted by *Jubilees* and HABs. To elucidate the sources of SGD- and river-derived nutrients I used stable isotopes (Nitrate $\delta^{15}\text{N}$ - $\delta^{18}\text{O}$ and Sediment $\delta^{13}\text{C}$ - $\delta^{15}\text{N}$) and dissolved organic matter (DOM) composition analyses.

4.3 Study area

Mobile Bay is a river-dominated micro-tidal estuary with an area of $1.3 \times 10^9 \text{ m}^2$, an average depth of 3.5 m, and a total volume of approximately $4.6 \times 10^9 \text{ m}^3$. The bay is connected with the Gulf of Mexico through Main Pass between Dauphin Island and the Fort Morgan Peninsula and has a narrow (120 m) and deep (15 m) ship channel extending from the City of Mobile to Main Pass (Greene et al., 2007; Du et al., 2018) (Fig. 4.1).

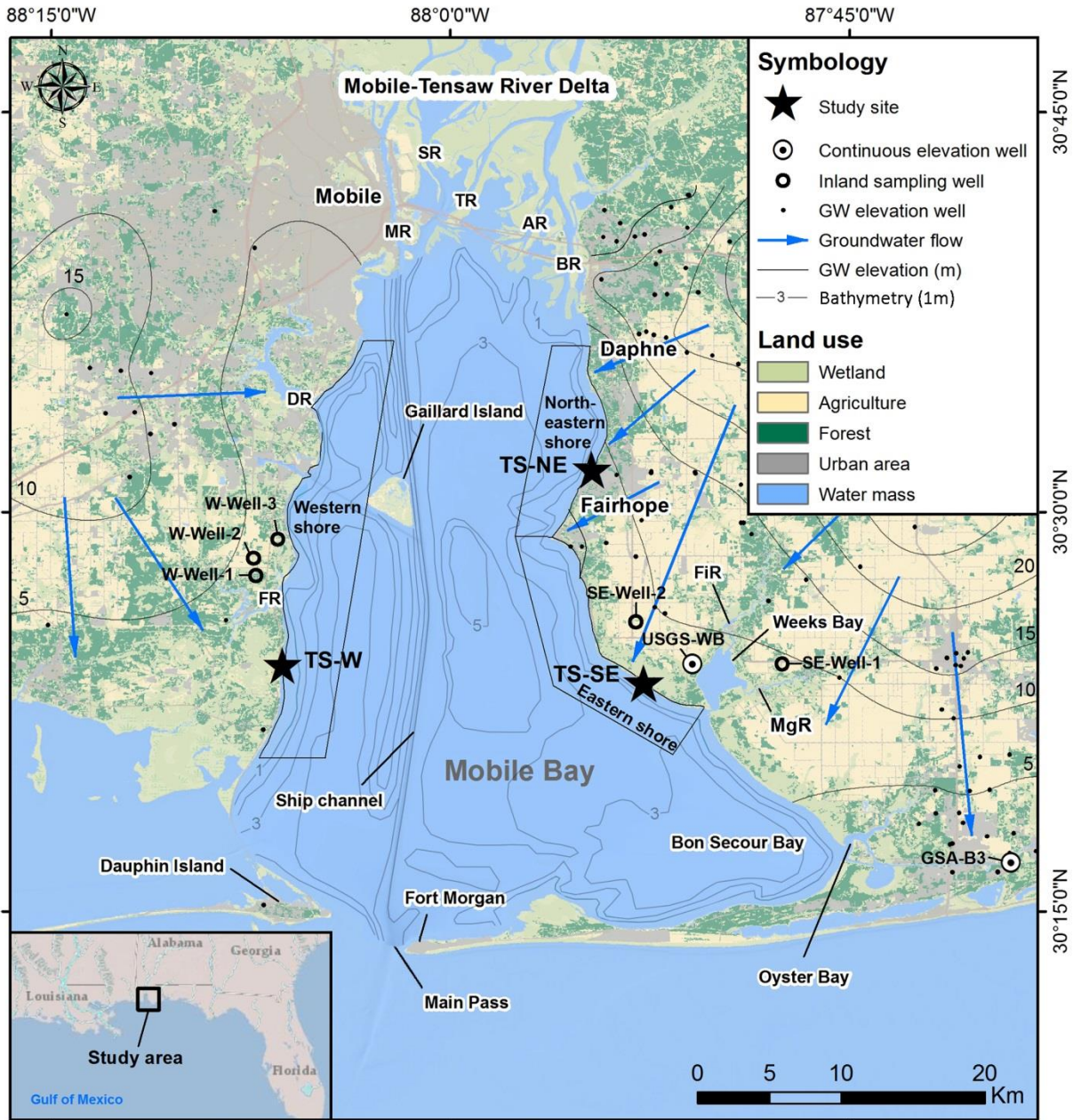


Figure 4.1. Study area location, showing land uses (from Ellis et al., 2011), potentiometric surface of the Miocene-Pliocene Aquifer (Geological Survey of Alabama, 2018), groundwater flow direction, monitoring wells for groundwater elevation, and sampled wells. The study area is divided in three sections: western shore, northeastern shore, and southeastern shore. At each section, the study sites where sediment core collection, intertidal piezometers installation (Pz-1 to Pz-5), SGD assessments, and SGD-derived nutrient fluxes evaluations were conducted, are represented with a star. Inland wells at both western and eastern shores are represented with an open circle. FR, DR, MR, SR, TR, AR, BR, FiR, and MgR represent the location of Fowl River, Dog River, Mobile River, Spanish River, Tensaw River, Apachee River, Blakeley River, Fish River, and Magnolia River.

As in all estuaries along the Alabama Gulf Coast, the tides in Mobile Bay are diurnal with an average tidal range of 0.4 m (Hummel, 1996; Greene et al., 2007; Du et al., 2018). The average annual temperature in Mobile Bay is 21°C, with monthly maximum of 27°C during the summer (June-August) and minimum of 14°C during the winter (December-February). Two maximum rainfall periods exist in the area, one during the spring (February-March) and a second during late summer (July-August), whereas the minimum is usually in June and October, with an annual mean of 1670 mm y⁻¹ (Ward et al., 2005). Mobile Bay receives 95% of its surface water from the Mobile-Tensaw River System, the second largest river system in the Gulf of Mexico after the Mississippi-Atchafalaya River System (Dinnel et al., 1990). The Mobile-Tensaw River System has a daily average discharge of $1500 \times 10^5 \text{ m}^3 \text{ d}^{-1}$ and its flow is controlled mostly by precipitation throughout the year. Thus, the maximum discharge also occurs during March, while the minimum flow typically takes place during the summer months (July - September) when evapotranspiration is highest (Schroeder et al., 1990; Stumpf et al., 1993; Ward et al., 2005).

The drainage area of the Mobile-Tensaw River System is approximately 115,000 km² (Dinnel et al., 1990). The river- and SGD-derived nutrient inputs to Mobile Bay and their source largely depends on the land use and lithology within the Mobile-Tensaw River System watershed. About 75% of the basin is covered by forests and wetlands, whereas 18% is comprised of agricultural land and 2% of urban areas (Ward et al., 2005). The east and west shores of Mobile Bay are located in Baldwin and Mobile counties respectively. On the east shore agricultural activities dominate the land use occupying about 55% of the total area, whereas urban areas represent 5%, and scattered cattle farms 4%. The remaining 36% of this area is naturally preserved as forests (26%) and wetlands (10%). In contrast, on the western shore

natural areas of wetlands and forest dominate the land use with 39% and 22% respectively, while the urbanized area of Mobile City occupy 20% and agriculture 19% (Ellis et al., 2011).

Two main aquifer units comprise the coastal hydrogeology of Mobile Bay: the (1) Watercourse Aquifer and the (2) Miocene-Pliocene Aquifer (Walter and Kidd, 1979; Gillet et al., 2000; Chapter 3). Both units are hydraulically connected to Mobile Bay and are separated by a thin interbedded clay layer. The Watercourse Aquifer is a shallow (10-20 m) unconfined unit comprised of Pleistocene to Holocene sand deposits, present only in the southernmost sector of the western shore and Bon Secour Bay (Fig. 4.1). The Miocene-Pliocene Aquifer is an unconfined to semi-confined formation comprised of sand deposits with a maximum thickness of 50-60 m (Reed, 1971; Chandler et al., 1985; Gillet et al., 2000). The Miocene-Pliocene Aquifer water table elevation as presented by the Geological Survey of Alabama (2018) indicates that SGD should occur uniformly along the whole shoreline of Mobile Bay (Fig. 4.1). However, in Chapter 3 I found that SGD takes place preferentially along the east shore of the bay from the Miocene-Pliocene Aquifer (Fig. 4.1). These preferential pathways were attributed to the lithological heterogeneity of the Miocene-Pliocene Aquifer coastal sediments where SGD takes place. Earlier during this study I found that a continuous silt formation, present uniformly along the western shore of Mobile of very low permeability, restricts SGD in this area (Fig. 4.2a). Conversely, I also found that a peat layer underlain by the Miocene-Pliocene Aquifer is the main conduit for SGD on the east shore of Mobile (Figs. 4.2b and 4.2c) (Chapter 3).

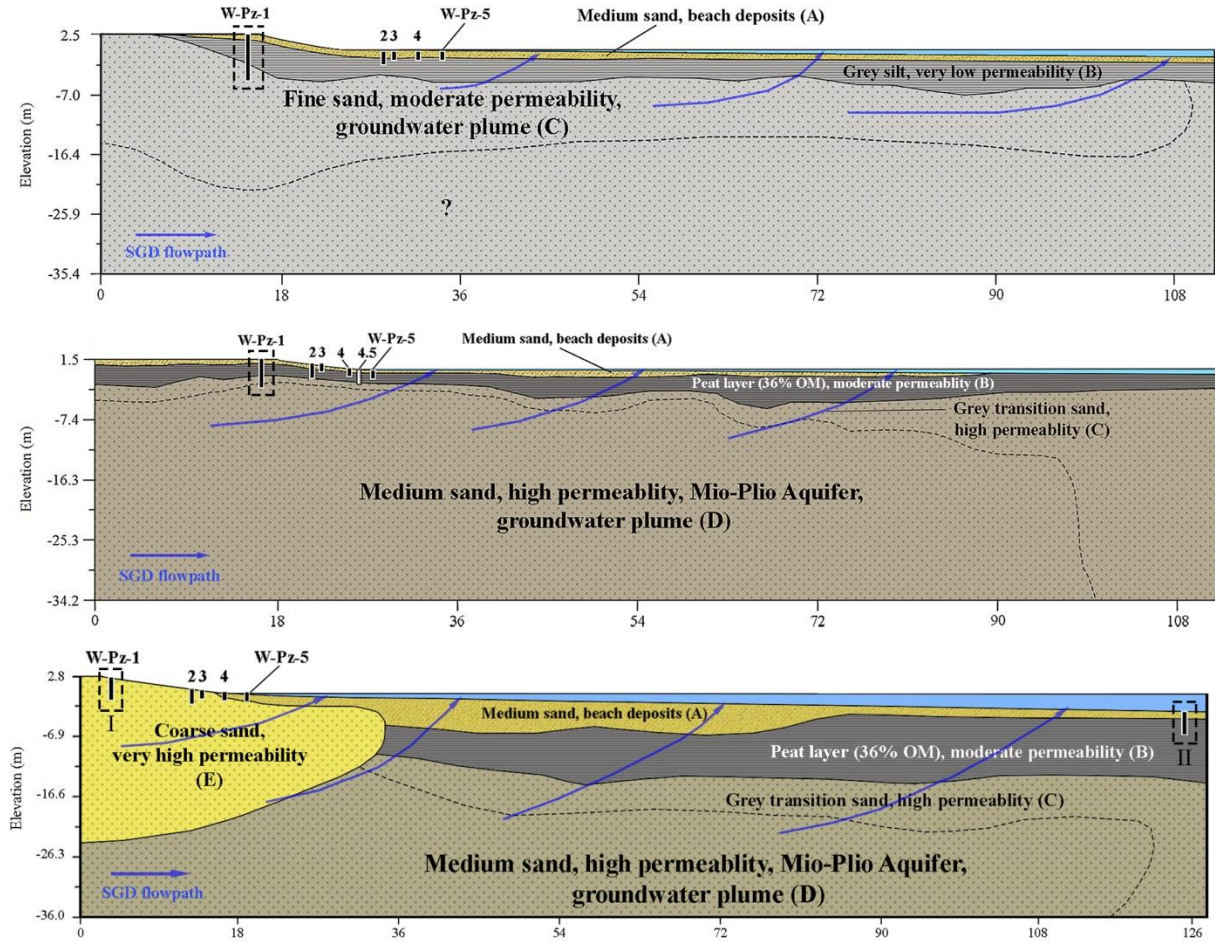


Figure 4.2. Schematic geologic cross sections showing the lithologic characteristics of the shallow coastal sediments at study site TS-W on the western shore (a), TS-SE on the southeastern shore (b), and TS-NE on the northeastern shore (c) as presented in Chapter 3. The locations of all intertidal piezometers (Pz-1 to Pz-5) and sediment cores (highlighted in dashed rectangles) are also shown on each panel. The dashed line represents the SGD plume extent on the western shore at TS-W (80 m), on the southeastern shore at TS-SE (70 m), and the northeastern shore at TS-NE (100 m).

4.4 Methods

4.4.1 Sample collection

To construct the nutrient budget of Mobile Bay, I collected water samples from all input end-members, including groundwater, surface water from the rivers entering the bay, and surface water from Mobile Bay. All water samples were collected following the same protocol.

Surface water samples from Mobile Bay were collected during boat surveys conducted along the shoreline and across Mobile Bay during three wet seasons (March of 2015, March 2016, and July 2017) and two dry seasons (July of 2015 and March 2017). During all surveys GPS positioning of the sampling locations was recorded in 30-sec intervals (Lowrance HDS 5) with an accuracy of ± 1 m. The surface water was collected with a submersible pump from a depth of 0.3 m. Samples for nutrients (NO_3^- , NH_4^+ , DON, and PO_4^{3-}), NO_3^- stable isotopes ($\delta^{15}\text{N}$ and $\delta^{18}\text{O}$), dissolved organic carbon (DOC), and dissolved organic matter (DOM) were filtered in the field with sterile 0.45 μm cellulose acetate filters and collected in acid cleaned 50mL polypropylene vials. Samples were kept in ice until arrival to the laboratory for a maximum of 6 hours and frozen until analysis.

River water samples were collected during all sampling campaigns from the main rivers of the Mobile-Tensaw River Delta, i.e. Mobile, Tensaw, Apalachee, and Blakeley Rivers at their point of discharge to the bay (Fig. 4.1).

Groundwater samples were collected from inland wells and shore-perpendicular transects of piezometers installed at the shore during this study (Fig. 4.2). The shore-perpendicular transects consisted of five piezometers (Pz-1 to Pz-5) installed at different depths as illustrated in Fig. 4.2. Additionally, pore water samples were also collected at TS-SE from a 2-m multi-level piezometer (SE-Pz-4.5). A detailed explanation on the piezometers installation can be found in Chapter 3. Additionally, groundwater was collected from five deeper wells (up to 10 m) farther inland in the western shore (W-Well-1, W-Well-2, W-Well -3) and the east shore (SE-Well-1 and SE-Well-2) of Mobile Bay (Fig. 4.1).

Sediment cores were recovered using a Geoprobe coring system (Model 5410, Geoprobe Systems Inc.) from the deepest piezometer (Pz-1) at each study site (cores TS-W, TS-SE, TS-

NE-I) (Figs. 4.2a, 4.2b, and 4.2c). During July of 2018 a sediment core was collected underwater using a vibracoring system with a built-in tripod at study site TS-NE (TS-NE-II, Fig. 4.2c) to complete the lithologic data set presented in Chapter 3.

4.4.2 Analytical methods

Dissolved oxygen (DO) in surface water and groundwater was measured using a Pro2030 (YSI Inc.) handheld instrument with a Galvanic sensor and a 1.25 mil polyethylene membrane with an accuracy of $\pm 0.2 \text{ mg L}^{-1}$. Before sampling, the DO sensor was calibrated following the YSI calibration procedure.

Nutrient (NO_3^- as $\text{NO}_3^- + \text{NO}_2^-$, NH_4^+ , DON, and PO_4^{3-}) analyses were performed at Dauphin Island Sea Lab (DISL) using a Skalar San⁺⁺ segmented flow autoanalyzer with automatic in-line sample digestion (Skalar Analytical B.V.). The instrument analytical error was $\pm 5\%$ for all nutrients measurements.

Nitrate stable isotopes $\delta^{15}\text{N}$ and $\delta^{18}\text{O}$ were analyzed at the UC Davis Stable Isotope Facility following the bacteria denitrification method (Sigman et al., 2001). Analyses were conducted using a Thermo Finnigan GasBench⁺ PreCon trace gas concentration system (Thermo Scientific Inc.) interfaced to a Thermo Scientific Delta V isotope-ratio mass spectrometer (Thermo Scientific Inc.). Analytical precision for $\delta^{15}\text{N}$ and $\delta^{18}\text{O}$ are 0.4 ‰ and 0.5 ‰ respectively. Values of $\delta^{18}\text{O}$ and $\delta^{15}\text{N}$ were calculated relative to the Vienna Standard Mean Ocean Water (VSMOW) and the atmospheric nitrogen (AIR) standards respectively.

Dissolved organic carbon (DOC) concentrations in water were analyzed using a Shimadzu TOC-V total organic carbon analyzer (Shimadzu Scientific Instruments Inc.) following the method described in Lu et al. (2015), with an accuracy of $\pm 2\%$.

To identify the dissolved organic matter (DOM) origin (e.g., Hernes et al., 2009, Shang et al., 2018), DOM molecular absorbance measurements were performed as described in Lu et al. (2015). Samples were analyzed using a 10-mm path length quartz cuvette on a single beam UV-1800 Shimadzu UV–visible spectrophotometer (Shimadzu Scientific Instruments Inc.) under the scanning wavelength from 190 to 670 nm at an interval of 1 nm. DOM fluorescence properties were evaluated using the excitation-emission matrix (EEM) coupled with parallel factor analysis (PARAFAC) (Yamashita et al. 2008). A three-component EEM-PARAFAC model (C1–C3) was validated by split-half analysis and random initialization. The relative abundance of each of these three fluorescent components (C_i , $i = 1$ to 3) was calculated as:

$$\%F_{C_i} = F_{C_i}/TF \times 100 = F_{C_i}/\sum_{i=1}^3 F_{C_i} \times 100 \quad (4.1)$$

where F_{C_i} represents the fluorescence intensity of each component and TF is the total fluorescence intensity.

The organic matter of the peat layer (B) in core TS-SE (Fig. 4.2b) was analyzed at the Alabama Stable Isotope Laboratory (ASIL) for stable isotopes ($\delta^{13}\text{C}$ and $\delta^{15}\text{N}$), weight percent carbon (C-weight percent), weight percent nitrogen (N-weight percent), and carbon to nitrogen atomic ratios (C/N). The organic matter stable isotopes $\delta^{13}\text{C}$ and $\delta^{15}\text{N}$ were analyzed using an EA-CF-IRMS system consisting of an Elemental Combustion System (ECS 4010) coupled to a Gas Source-IRMS operating in a continuous flow mode and interfaced with a Finnigan MAT Conflo III. Values of $\delta^{13}\text{C}$ were calculated relative to the international Pee Dee Belemnite (PDB) standard (Craig, 1957) with an accuracy of 0.2‰, whereas $\delta^{15}\text{N}$ values were calculated relative to the atmospheric nitrogen (AIR) standard (Mariotti, 1983) with an accuracy of 0.3‰. N-weight percent, C-weight percent, and C/N ratios were measured with the ECS 4010 using a thermal conductivity detector.

A detailed characterization of all sediment cores including density, porosity, grain size, hydraulic conductivity, and organic matter content can be found in Chapter 3.

4.5 Results

4.5.1 Sediment cores

Sediment cores recovered from depths up to 4 m at the intertidal zone of each study site revealed the presence of an organic-rich fine-grained sediment layer (hereafter referred to as peat) with moderate to high permeability on the east shore of Mobile Bay (Figs. 4.2 and 4.3) (Perminova and Hatfield, 2005; Chapter 3). On the western shore this peat layer was absent in sediment core TS-W, which showed a different lithological structure and composition. Core TS-W was comprised of a 0.8 m coarse beach sand (A) with only 2% organic matter, underlain by a 2.5-m thick silt layer (B) with 11% of organic matter, and a 0.5-m fine sand layer (C) with 5% organic matter (Figs. 4.2a and 4.3). Both sediment cores TS-SE and TS-NE-II have on top a coarse beach sand layer (A) of 0.5 m thickness, and 0.2 m thickness and 3% organic matter content. Underlying the beach sand I identified a 1.5-m organic-rich black fine sand (B) with an organic matter content of 36%, which was in contact with the Miocene-Pliocene Aquifer (layers C and D) with an organic matter content of 2-7% (Figs. 4.2b, 4.2c, and 4.3). However, sediment core TS-NE-I collected at the beach face showed no vertical structure, consisting uniquely of coarse sand (E), artificially added to develop beach areas (Fig. 4.3) (Chapter 3).

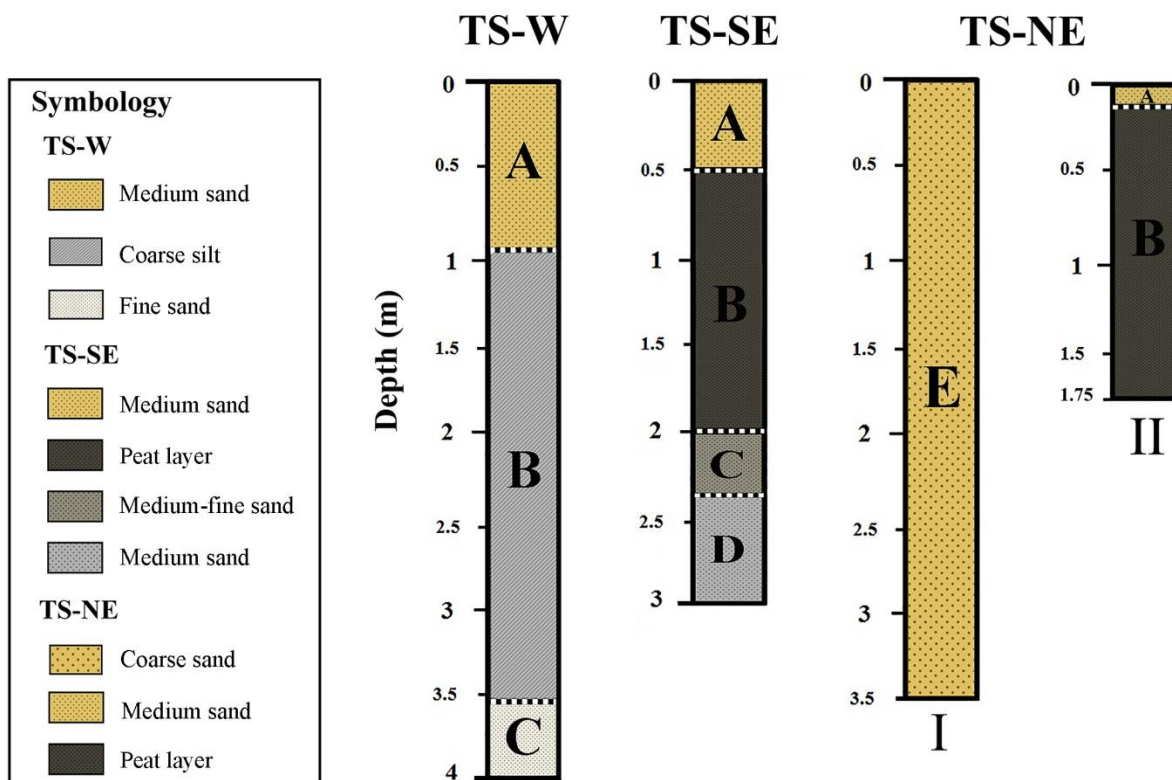


Figure 4.3. Sediment cores collected at study site TS-W on the western shore, TS-SE on the southeastern shore, and TS-NE (TS-NE-I and TS-NE-II) in the northeastern shore from locations indicated in Fig. 4.2. The presence, depth, and thickness of the peat layer (B) in the eastern shore is shown in cores TS-SE and TS-NE-I.

The peat layer (B) analyzed from sediment core TS-SE showed a C-weight percent that ranged between 0.43% at a depth of 90-100 cm and 6.15% at 65 cm, with an average of $3.36 \pm 2.15\%$. The N-weight percent was highest at 45cm with 0.12% and lowest at 70 cm with 0.33%, with an average of $0.25 \pm 0.07\%$ (Table 4.1). The average C/N ratio was 19.0 ± 2.4 , ranging between 16.8 at 55 cm and 24.4 at 45cm. Both $\delta^{13}\text{C}$ and $\delta^{15}\text{N}$ were highest ($\delta^{13}\text{C} = -24\text{-}23\text{‰}$, $\delta^{15}\text{N} = 3\text{-}4\text{‰}$) at a depth of 50-60 cm and were lowest ($\delta^{13}\text{C} = -30\text{-}28\text{‰}$, $\delta^{15}\text{N} = 0\text{-}1\text{‰}$) at 80-90 cm (Fig. 4.4). The $\delta^{13}\text{C}$ values were on average $-25.7 \pm 0.3\text{‰}$, ranging from $-29.4 \pm 0.1\text{‰}$ at 85 cm and $-23.3 \pm 0.3\text{‰}$ at 55 cm. The average $\delta^{15}\text{N}$ in this layer was 2.1 ± 0.2 , with a minimum value of $0.4 \pm 0.2\text{‰}$ at 80 cm and a maximum of $3.8 \pm 0.1\text{‰}$ at 50 cm (Table 4.1).

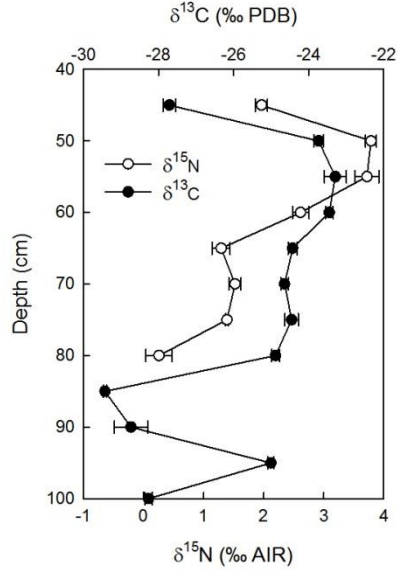


Figure 4.4. Vertical profile of stable isotopes $\delta^{13}\text{C}$ and $\delta^{15}\text{N}$ of the organic matter present in the peat layer (B) analyzed from sediment core TS-SE. Both $\delta^{13}\text{C}$ and $\delta^{15}\text{N}$ were highest ($\delta^{13}\text{C} = -24$ - 23‰ , $\delta^{15}\text{N} = 3$ - 4‰) at a depth of 50-60 cm and were lowest ($\delta^{13}\text{C} = -30$ - 28‰ , $\delta^{15}\text{N} = 0$ - 1‰) at 80-90 cm.

Cores present	Layer ID	Depth (cm)	C-weight percent (%)	$\delta^{13}\text{C}$ (‰ PDB)	N-weight percent (%)	$\delta^{15}\text{N}$ (‰ AIR)	C/N in sediment
TS-SE and TS-NE-II	B	45	2.88	-27.7 ± 0.2	0.12	2.0 ± 0.1	24.4
		50	5.28	-23.7 ± 0.1	0.31	3.8 ± 0.1	17.1
		55	4.97	-23.3 ± 0.3	0.30	3.7 ± 0.2	16.8
		60	4.99	-23.4 ± 0.1	0.29	2.6 ± 0.1	17.1
		65	6.15	-24.4 ± 0.1	0.29	1.3 ± 0.1	21.0
		70	5.98	-24.6 ± 0.1	0.33	1.5 ± 0.1	18.2
		75	4.41	-24.4 ± 0.2	0.24	1.4 ± 0.1	18.0
		80	3.29	-24.9 ± 0.1	0.17	0.4 ± 0.2	19.6
		85	1.03	-29.4 ± 0.1	-	-	-
		90	0.50	-28.7 ± 0.4	-	-	-
		95	0.43	-25.0 ± 0.1	-	-	-
	100	0.43	-28.3 ± 0.1	-	-	-	
Average			3.36	-25.7 ± 0.3	0.26	2.1 ± 0.2	19.0

Table 4.1. Characterization of the organic matter present in the peat layer (B) analyzed from sediment core TS-SE, showing C-weight percent, N-weight percent, C/N ratio, stable isotopes $\delta^{13}\text{C}$ and $\delta^{15}\text{N}$.

4.5.2 Groundwater composition

4.5.2.1 Dissolved oxygen

Dissolved oxygen (DO) in groundwater on the western shore was on average 1.4 ± 0.3 mg L⁻¹ (n = 10) in all inland wells (W-Well-1, W-Well-2, and W-Well-3) and intertidal piezometers (W-Pz-1 to W-Pz-5) during the dry season and 2.3 ± 0.5 mg L⁻¹ during the wet season (n = 7). In the inland wells DO was between 1.3 and 2.3 mg L⁻¹ (n = 3) during dry and wet seasons respectively, whereas in the intertidal piezometers DO was 1.2-2.4 mg L⁻¹ (n = 14) (Fig. 4.5). On the southeastern shore, DO was significantly higher in groundwater collected from the inland wells SE-Well-1 and SE-Well-2, with an average of 5.6 ± 0.7 mg L⁻¹ and values between 4.8 mg L⁻¹ (n = 3) during the dry season and 6.2 mg L⁻¹ (n = 3) during the wet season. In contrast, DO in the intertidal piezometers (SE-Pz-1 to SE-Pz-5) was on average 0.8 ± 0.7 mg L⁻¹ (n = 27), ranging from 0.6 mg L⁻¹ (n = 14) to 0.9 mg L⁻¹ (n = 14) during the dry and wet seasons respectively (Fig. 4.5). In the northeastern shore DO in groundwater was highest in piezometers NE-Pz-4 and NE-Pz-5, located in the tidal mark, with an average concentration of 3.9 ± 1.0 mg L⁻¹ (n = 7). The overall average concentration in all piezometers (NE-Pz-1 to NE-Pz-5) was 2.2 ± 1.0 mg L⁻¹ (n = 19) (Fig. 4.5).

4.5.2.2 Nitrate (NO₃⁻ + NO₂⁻)

On the western shore, NO₃⁻ was on average 96 ± 23 mmol m⁻³ (n = 3) in the inland wells (W-Well-1, W-Well-2, and W-Well-3), which is significantly higher than the average NO₃⁻ concentration measured in the shallow piezometers (W-Pz-1 to W-Pz-5) during the wet season (2.4 ± 0.9 mmol m⁻³ (n = 10)) and during the dry season (6.7 ± 2.1 mmol m⁻³ (n = 4)) (Fig. 4.5). Similarly, on the southeastern shore NO₃⁻ was higher in the inland wells (SE-Well-1 and SE-Well-2) with an average concentration of 110 ± 34 mmol m⁻³ (n = 6) during both the dry and wet

seasons, whereas in the intertidal piezometers (SE-Pz-1 to SE-Pz-5) the average NO_3^- concentration was between $8.0 \pm 3.4 \text{ mmol m}^{-3}$ ($n = 18$) and $20 \pm 8 \text{ mmol m}^{-3}$ ($n = 14$) during the dry and wet seasons. On the northeastern shore, NO_3^- in intertidal piezometers (NE-Pz-1 to NE-Pz-5) was on average $13 \pm 5 \text{ mmol m}^{-3}$ ($n = 12$) during the dry season and $30 \pm 10 \text{ mmol m}^{-3}$ ($n = 7$) during the wet season (Fig. 4.5).

4.5.2.3 Ammonium (NH_4^+)

On the western shore at study site TS-W the average NH_4^+ concentration was similar both groundwater from the inland wells ($2.7 \pm 0.7 \text{ mmol m}^{-3}$) and from the intertidal piezometers ($4.0 \pm 2.0 \text{ mmol m}^{-3}$). The overall average NH_4^+ concentration was $2.0 \pm 1.1 \text{ mmol m}^{-3}$ ($n = 10$) during the wet season and $4.5 \pm 2.0 \text{ mmol m}^{-3}$ ($n = 7$) during the dry season. On the southeastern shore, NH_4^+ was on average between $1.1 \pm 0.4 \text{ mmol m}^{-3}$ ($n = 6$) during the wet season and 7.5 ± 2.2 ($n = 6$) during the dry season in the inland wells. In the intertidal piezometers NH_4^+ was on average between $75 \pm 20 \text{ mmol m}^{-3}$ ($n = 14$) during the wet season and $140 \pm 50 \text{ mmol m}^{-3}$ ($n = 17$) during the dry season. On the northeastern shore intertidal piezometers, NH_4^+ was on average $6.0 \pm 2.5 \text{ mmol m}^{-3}$ ($n = 7$) during the wet season and $8.0 \pm 3.1 \text{ mmol m}^{-3}$ ($n = 12$) during the dry season (Fig. 4.5).

4.5.2.4 Dissolved organic nitrogen (DON)

The DON concentration in groundwater on the western shore during this study was on average $10 \pm 4 \text{ mmol m}^{-3}$ ($n = 3$) in the inland wells and ranged between 20 mmol m^{-3} ($n = 3$) and $28 \pm 10 \text{ mmol m}^{-3}$ ($n = 14$) in the intertidal piezometers during the wet and dry seasons respectively. DON in groundwater in the inland wells on the southeastern shore was on average $50 \pm 30 \text{ mmol m}^{-3}$ ($n = 3$) and $110 \pm 60 \text{ mmol m}^{-3}$ ($n = 3$), while it ranged from $58 \pm 20 \text{ mmol m}^{-3}$ ($n = 13$) to $130 \pm 30 \text{ mmol m}^{-3}$ ($n = 17$) in the intertidal piezometers during the wet and dry

seasons. On the northeastern shore I found that DON in groundwater in the intertidal piezometers was between $16 \pm 6 \text{ mmol m}^{-3}$ and $32 \pm 10 \text{ mmol m}^{-3}$ ($n = 19$) on average (Fig. 4.5).

4.5.2.5 Phosphorous (PO_4^{3-})

In general, PO_4^{3-} in groundwater was low throughout the research area and during all sampling events. On the western shore the average PO_4^{3-} concentration was similar in the inland wells ($0.1 \pm 0.02 \text{ mmol m}^{-3}$) and in the intertidal piezometers ($0.2 \pm 0.04 \text{ mmol m}^{-3}$) with an overall average concentration of $0.1 \pm 0.03 \text{ mmol m}^{-3}$ and $0.2 \pm 0.05 \text{ mmol m}^{-3}$ during the dry ($n = 10$) and wet ($n = 7$) seasons. On the southeastern shore, PO_4^{3-} in groundwater during this study was on average $0.1 \pm 0.01 \text{ mmol m}^{-3}$ ($n = 6$) in the inland wells during both the dry and wet seasons, whereas in the intertidal piezometers it was $0.5 \pm 0.2 \text{ mmol m}^{-3}$ ($n = 17$) during the dry season and $0.9 \pm 0.4 \text{ mmol m}^{-3}$ ($n = 14$) during the wet season. The average PO_4^{3-} concentration in groundwater from the intertidal piezometers installed on the northeastern shore of Mobile Bay was between $0.2 \pm 0.1 \text{ mmol m}^{-3}$ ($n = 7$) and $0.5 \pm 0.2 \text{ mmol m}^{-3}$ ($n = 12$) during the wet and dry seasons respectively (Fig. 4.5).

4.5.2.6 N/P ratios ($\text{NO}_3^- + \text{NH}_4^+ / \text{PO}_4^{3-}$)

The N/P ratios were significantly higher in the inland wells compared to the intertidal piezometers on all study sites (Fig. 4.5). In the inland wells located on the western and southeastern shores N/P was on average 870 ± 220 ($n = 3$) and 1200 ± 490 ($n = 6$) respectively. In the intertidal piezometers of the western, southeastern, and northeastern shores the average N/P ratios were 79 ± 23 ($n = 14$), 250 ± 120 ($n = 31$), and 66 ± 29 ($n = 19$) (Fig. 4.5).

4.5.2.7 Stable isotopes of NO_3^- ($\delta^{15}\text{N}$ and $\delta^{18}\text{O}$)

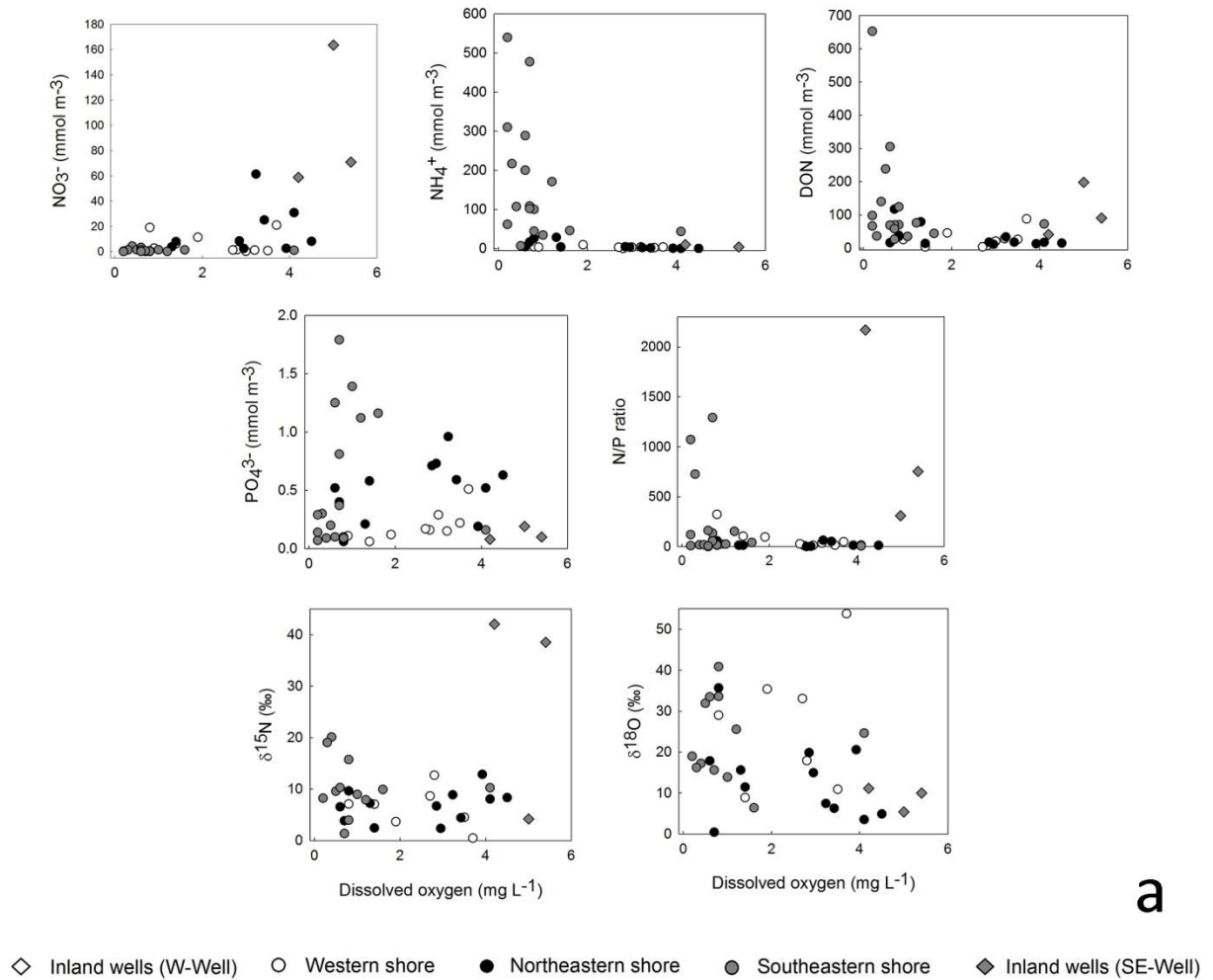
On the western shore $\delta^{15}\text{N}$ values were similar in inland wells and intertidal piezometers with an overall average of $8 \pm 3\text{‰}$ ($n = 7$) and $6 \pm 2\text{‰}$ ($n = 7$) during the dry and wet seasons.

On the southeastern shore the overall $\delta^{15}\text{N}$ average in the inland wells was between $3 \pm 1\text{‰}$ ($n = 3$) and $28 \pm 15\text{‰}$ ($n = 3$) during the wet and dry seasons, whereas in the intertidal piezometers $\delta^{15}\text{N}$ was nearly identical during the dry ($10 \pm 4\text{‰}$) and wet ($11 \pm 2\text{‰}$) seasons. On the northeastern shore the average $\delta^{15}\text{N}$ in the intertidal piezometers was on average $7 \pm 2\text{‰}$ ($n = 19$) during both seasons (Fig. 4.5). The $\delta^{18}\text{O}$ values were generally lower in the inland wells of the western shore with an average of $9 \pm 3\text{‰}$ ($n = 3$) compared to the intertidal piezometers where $\delta^{18}\text{O}$ ranged from $19 \pm 6\text{‰}$ ($n = 4$) to $27 \pm 10\text{‰}$ ($n = 7$). In the inland wells of the southeastern shore the average $\delta^{18}\text{O}$ was $6 \pm 1\text{‰}$ ($n = 3$) during the wet season and $9 \pm 2\text{‰}$ ($n = 3$) during the dry season. In the intertidal piezometers of the southeastern shore $\delta^{18}\text{O}$ was $14 \pm 4\text{‰}$ ($n = 14$) during the wet season and $23 \pm 8\text{‰}$ ($n = 14$) during the dry season. On the northeastern shore the average $\delta^{18}\text{O}$ in the intertidal piezometers was on average between $10 \pm 3\text{‰}$ ($n = 7$) during the wet season and $13 \pm 5\text{‰}$ ($n = 12$) during the dry season (Fig. 4.5).

4.5.2.8 Dissolved organic carbon (DOC) and dissolved organic matter (DOM) characterization

The average DOC concentration in the intertidal piezometers of the western shore was $1.9 \pm 0.8 \text{ mg L}^{-1}$ ($n = 4$). On the southeastern shore the average groundwater DOC concentration in the intertidal piezometers was $10 \pm 5 \text{ mg L}^{-1}$ ($n = 14$), whereas in the northeastern shore was $1.4 \pm 0.8 \text{ mg L}^{-1}$ ($n = 5$) (Appendix III Table 1). Three molecular components (C1-C3) were identified in DOM analyses conducted in all groundwater samples at excitation-emission maximum ranges of 255-456 nm (C1), 310-386 nm (C2), and 280-320 nm (C3) (Appendix III Table 1). Components 1 and 2 correspond to humic-like degradation products of allochthonous and autochthonous organic compounds. Component 3, in contrast, represents a protein-like (tyrosine) DOM composition. On the western shore, C3 was the major DOM component with an average of $89 \pm 1\%$, while the remaining $11 \pm 1\%$ corresponded with component 1. On the

southeastern shore, C3 was also the major DOM component with an average of $89 \pm 2\%$ in piezometers SE-Pz-1-5, being component 1 an average of $9 \pm 1\%$. However, in the multi-level piezometer SE-Pz-4.5 installed in the peat layer on the southeastern shore, C2 was the major component with an average of $43 \pm 4\%$, while C1 and C3 represented $29 \pm 10\%$ and $28 \pm 12\%$ respectively. On the northeastern shore, C3 was the major DOM component with an average of $89 \pm 1\%$ and $10 \pm 1\%$ corresponded with component 1.



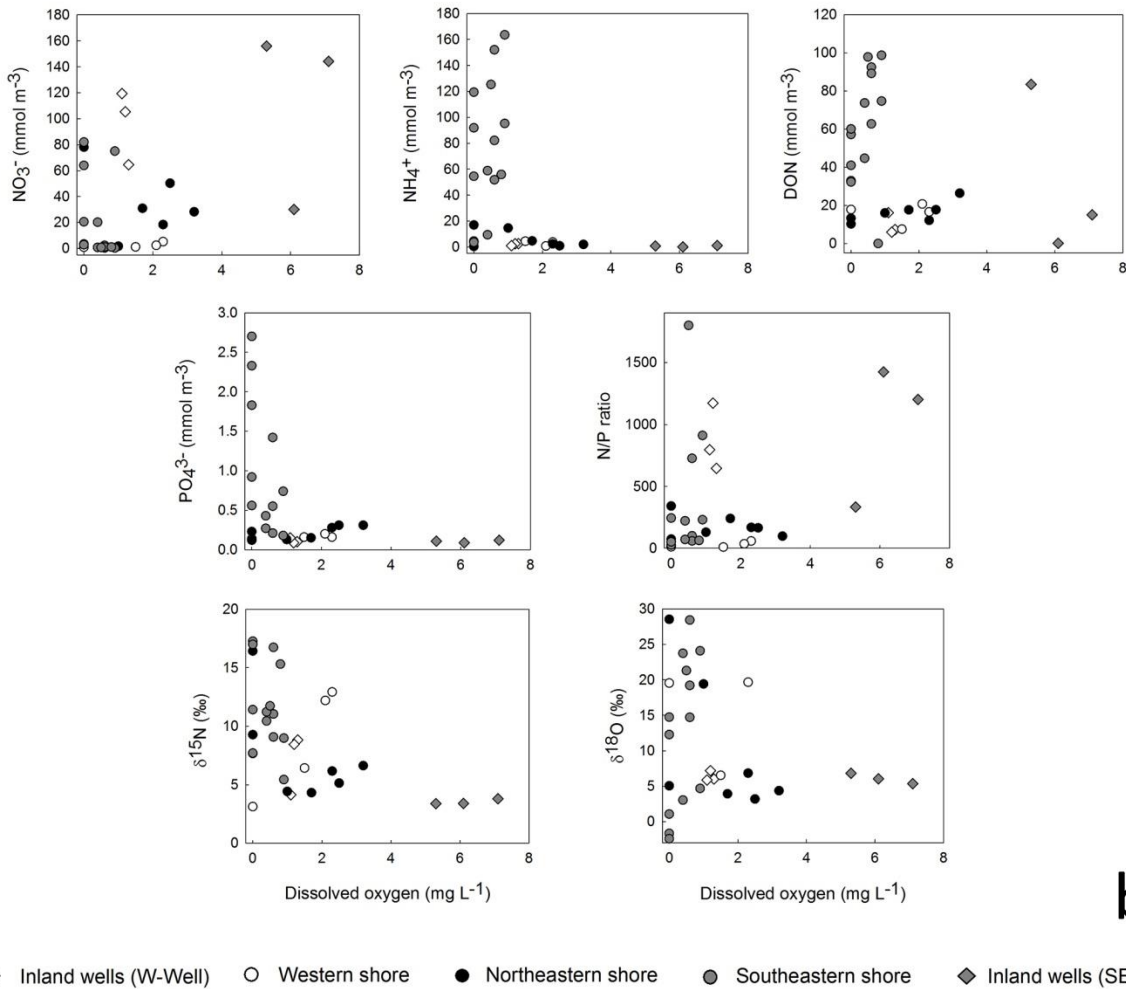


Figure 4.5. Groundwater dissolved oxygen (DO), NO_3^- , NH_4^+ , DON, and PO_4^{3-} concentrations, N/P molar ratio, and nitrate stable isotopes ($\delta^{15}\text{N}$ and $\delta^{18}\text{O}$) values in the inland wells and the intertidal piezometers during the dry (a) and wet (b) seasons.

4.5.3 Surface water composition

Surface water DO, nutrient (NO_3^- , NH_4^+ , DON, and PO_4^{3-}), NO_3^- - $\delta^{15}\text{N}$ - $\delta^{18}\text{O}$, DOC concentrations, and DOM compositions did not vary significantly during the dry and wet seasons at either shore of Mobile Bay (Appendix III Table 1). However, significant spatial variations were found in Mobile Bay.

4.5.3.1 Dissolved oxygen

As to be expected, the highest DO values in surface waters of Mobile Bay were measured near the river delta and Main Pass with concentrations of 6-8 mg L⁻¹. However, during this study, DO in Mobile Bay water along the east shore was always below 2 mg L⁻¹. Considering the whole bay, the overall average DO concentration during all sampling campaigns was 4.1 ± 1.4 mg L⁻¹ (n = 88) (Appendix III Fig. 1).

4.5.3.2 Nitrate (NO₃⁻ + NO₂⁻)

The average NO₃⁻ concentration in Mobile Bay during all sampling campaigns was 3.6 ± 1.4 mmol m⁻³ (n = 77). NO₃⁻ was highest along the northeastern shore and the northern sector of the bay near the river delta with concentrations of 6.0-22 mmol m⁻³ and was lowest in Bon Secour Bay 0.7-0.9 mmol m⁻³ (Appendix III Fig. 2a).

4.5.3.3 Ammonium (NH₄⁺)

In comparison, the NH₄⁺ concentration in Mobile Bay during all boat surveys was on average 2.2 ± 1.0 mmol m⁻³ (n = 77). NH₄⁺ was highest on the southeastern shore with concentrations of 8.0-11 mmol m⁻³ and was lowest in Bon Secour Bay and near the river delta with concentrations of 0.3-0.7 mmol m⁻³ (Appendix III Fig. 2b).

4.5.3.4 Dissolved organic nitrogen (DON)

The average dissolved organic nitrogen (DON) in Mobile Bay during this study was 28 ± 6.9 mmol m⁻³ (n = 77). The highest DON concentrations were found in the northeastern shore and Bon Secour Bay with values of 30-51 mmol m⁻³ and were lowest along the western shore with concentrations of 0.1-20 mmol m⁻³ (Appendix III Fig. 2c).

4.5.3.5 Phosphorous (PO₄³⁻)

The average PO₄³⁻ concentration in Mobile Bay during all sampling campaigns was 0.4 ± 0.1 mmol m⁻³ (n = 77). The highest PO₄³⁻ concentrations were found on the northeastern shore

and as to be expected near the river delta with values of 0.5-1.4 mmol m⁻³, and were lowest along the western shore and Bon Secour Bay with concentrations of 0.1-0.3 mmol m⁻³ (Appendix III Fig. 2d).

4.5.3.6 N/P ratios (NO₃⁻ + NH₄⁺ / PO₄³⁻)

The highest N/P ratios in Mobile Bay were found along the western and southeastern shores with average values of 30-350, whereas the minimum values were found in Bon Secour Bay with 2-6. The overall average N/P ratio in Mobile Bay during this study was 16 ± 5 (Appendix III Fig. 2e).

4.5.3.7 Stable isotopes of NO₃⁻ (δ¹⁵N and δ¹⁸O)

Mobile Bay water δ¹⁵N and δ¹⁸O were on average 13 ± 3‰ and 21 ± 3‰ (n = 54) during all sampling campaigns. Both isotopes were the highest in the southern sector of the bay, specifically in Bon Secour Bay, with values of 16-27‰ and were lower near the river delta with values of 6-10‰ and 4-11‰ respectively (Appendix III Figs. 3a and 3b).

4.5.3.8 Dissolved organic carbon (DOC) and dissolved organic matter (DOM) characterization

DOC concentrations in Mobile Bay during all sampling campaigns were on average 6.2 ± 3.8 mg L⁻¹ (n = 30). The highest DOC concentrations were measured along the east shore of the bay in the southern sector of the bay including Bon Secour Bay with values of 6.5-15 mg L⁻¹, whereas the lowest concentrations were measured near the river delta and the western shore with values of 2.8-4.5 mg L⁻¹ (Appendix III Fig. 4). The three DOM components (C1, C2, and C3) were similarly present in Mobile Bay during all sampling campaigns with average percentages of 28 ± 6% (C1), 34 ± 7% (C2), and 38 ± 12% (C3) (n = 31). The percentage of components 1 and 2 were higher near the river delta and in Bon Secour Bay with values of 26-46% and were lowest in the mid-bay area (6-30%) and on the southeastern shore (6-8%) (Appendix III Figs. 5a and

5b). The spatial distribution of component 3 showed nearly the opposite trend, being highest in the mid-bay area and on the southeastern shore (35-65%) and lower near the river delta and in Bon Secour Bay (20-25%) (Appendix III Fig. 5c).

In the Mobile-Tensaw River System DO was on average $7.0 \pm 1.8 \text{ mg L}^{-1}$ ($n = 18$) during all sampling campaigns, ranging between 5.4 mg L^{-1} and 10 mg L^{-1} (Appendix III Table 1).

Nutrient (NO_3^- , NH_4^+ , DON, and PO_4^{3-}) concentrations were on average $8.4 \pm 2.0 \text{ mmol m}^{-3}$, $5.1 \pm 1.3 \text{ mmol m}^{-3}$, $31 \pm 8.1 \text{ mmol m}^{-3}$, and $0.8 \pm 0.2 \text{ mmol m}^{-3}$ ($n = 20$) respectively. The river N/P ratio was on average 21 ± 9 (Appendix III Table 1). The nitrate stable isotopes ($\delta^{15}\text{N}$ and $\delta^{18}\text{O}$) were on average $5 \pm 1\%$ and $6 \pm 1\%$ ($n = 16$) respectively. The average DOC concentration was $6.9 \pm 1.0 \text{ mg L}^{-1}$ ($n = 5$). The predominant DOM component was C2 with $41 \pm 3\%$, whereas C1 and C3 were on average $26 \pm 4\%$ and $33 \pm 6\%$ respectively (Appendix III Table 1).

4.5.4 Nutrient fluxes via SGD and river discharge

Using the SGD rates presented in Chapter 3 obtained during dry and wet seasons, I calculated the SGD-derived nutrient fluxes on the three sections of Mobile Bay.

On the western shore SGD was $1.8 \pm 0.6 \times 10^5 \text{ m}^3 \text{ d}^{-1}$ during the dry season, and $2.4 \pm 0.7 \times 10^5 \text{ m}^3 \text{ d}^{-1}$ during the wet season (Chapter 3). The average groundwater NO_3^- concentration during the dry season was $6.7 \pm 2.1 \text{ mmol m}^{-3}$ in piezometers W-Pz-1-5 and $2.4 \pm 0.9 \text{ mmol m}^{-3}$ during the wet season. Multiplying the dry and wet seasons SGD rates by the corresponding groundwater NO_3^- concentration, I obtained a SGD- NO_3^- flux of $5.8 \times 10^5 \text{ mmol d}^{-1}$ during the wet season and $12 \times 10^5 \text{ mmol d}^{-1}$ during the dry season (Table 4.2).

	Discharge (dry – wet) ($\times 10^5 \text{ m}^3 \text{ d}^{-1}$)	NO ₃ ⁻	NH ₄ ⁺	DON	PO ₄ ³⁻	Nutrient fluxes (dry – wet) ($\times 10^5 \text{ mmol d}^{-1}$ ($\times 10^6 \text{ mol y}^{-1}$))				Mobile Bay nutrient budget (%)
						NO ₃ ⁻	NH ₄ ⁺	DON	PO ₄ ³⁻	
		Average concentration (dry – wet) (mmol m^{-3})								
Western shore SGD	1.8 – 2.4	6.7	4.5	28	0.2	12 (0.4)	8.1 (0.3)	50 (0.2)	0.4 (0.01)	NO ₃ ⁻ = 1.7 – 0.1
		–	–	–	–	–	–	–	–	NH ₄ ⁺ = 1.3 – 0.1
		2.4	2.0	20	0.1	5.8 (0.2)	4.8 (0.2)	48 (0.2)	0.2 (0.01)	DON = 1.9 – 0.1 PO ₄ ³⁻ = 0.4 – 0.1
Southeastern shore SGD	2.3 – 3.8	8.0	140	130	0.5	18 (0.7)	320 (12)	300 (11)	1.1 (0.04)	NO ₃ ⁻ = 2.6 – 0.6
		–	–	–	–	–	–	–	–	NH ₄ ⁺ = 50 – 2.3
		20	75	60	0.9	74 (2.7)	290 (10)	220 (8.0)	3.4 (0.03)	DON = 12 – 0.4 PO ₄ ³⁻ = 1.4 – 0.6
Northeastern shore SGD	3.9 – 5.7	13	8.0	32	0.5	50 (1.8)	31 (1.1)	120 (1.1)	1.9 (0.7)	NO ₃ ⁻ = 7.1 – 1.3
		–	–	–	–	–	–	–	–	NH ₄ ⁺ = 4.9 – 0.3
		30	6.0	16	0.2	170 (6.3)	34 (1.2)	90 (0.8)	1.1 (0.4)	DON = 4.7 – 0.2 PO ₄ ³⁻ = 2.3 – 0.2
Total SGD	8.0 – 12	N/A	N/A	N/A	N/A	80 (2.9)	360 (13)	470 (17)	3.5 (1.2)	NO ₃ ⁻ = 12 – 2.0
						250 (9.2)	320 (12)	360 (13)	4.8 (1.7)	NH ₄ ⁺ = 56 – 2.7 DON = 18 – 0.7 PO ₄ ³⁻ = 4.1 – 0.8
Rivers	70 – 1,700	8.9	4.0	31	1.0	620 (230)	280 (100)	2,200 (790)	70 (26)	NO ₃ ⁻ = 88 – 98
		–	–	–	–	–	–	–	–	NH ₄ ⁺ = 44 – 97
		7.4	7.0	29	0.3	13,000 (4,600)	12,000 (4,300)	49,000 (18,000)	510 (190)	DON = 82 – 99 PO ₄ ³⁻ = 96 – 99
Total in Mobile Bay	88 – 1,712	N/A	N/A	N/A	N/A	700 (233)	640 (293)	2,670 (807)	73 (27)	
						–	–	–	–	100
						13,250 (4,609)	12,320 (4,312)	49,360 (18,013)	515 (190)	

Table 4.2. All values utilized to evaluate the river- and SGD-derived nutrient (NO₃⁻, NH₄⁺, DON and PO₄³⁻) fluxes on the western, southeastern, and northeastern shores in Mobile Bay. The table includes values of SGD fluxes at each study site (from Chapter 3) and river discharge during the dry and wet seasons, nutrient concentrations, nutrient fluxes, and the relative importance of each nutrient to the total nutrient budget of Mobile Bay considering both river- and SGD-derived inputs.

Following the same strategy, I estimated a SGD-NH₄⁺ flux of 4.8-8.1 × 10⁵ mmol d⁻¹ (dry-wet seasons), a SGD-DON flux of 48-50 × 10⁵ mmol d⁻¹ (wet-dry seasons), and a SGD-PO₄³⁻ flux of 0.2-0.4 × 10⁵ mmol d⁻¹ (wet-dry seasons) (Figs. 4.6a and 4.6b, Table 4.2).

On the southeastern shore SGD was 2.3 ± 1.0 × 10⁵ m³ d⁻¹ during the dry season and 3.8 ± 1.3 × 10⁵ m³ d⁻¹ during the wet season (Chapter 3). Multiplying the dry and wet seasons SGD rates by the groundwater NO₃⁻, NH₄⁺, DON, and PO₄³⁻ concentrations during the dry and wet seasons, I obtained a SGD-NO₃⁻ flux of 18-74 × 10⁵ mmol d⁻¹ (dry-wet seasons), a SGD-NH₄⁺ flux of 290-320 × 10⁵ mmol d⁻¹ (wet-dry seasons), a SGD-DON flux of 220-300 mmol d⁻¹ (wet-dry seasons), and a SGD-PO₄³⁻ flux of 1.1-3.4 mmol d⁻¹ (dry-wet seasons) (Figs. 4.6a and 4.6b, Table 4.2).

On the northeastern shore SGD was 3.9 ± 1.7 × 10⁵ m³ d⁻¹ during the dry season and 5.7 ± 2.1 × 10⁵ m³ d⁻¹ during the wet season (Chapter 3). Multiplying these dry-wet SGD rates by the groundwater NO₃⁻, NH₄⁺, DON, and PO₄³⁻ concentrations, I obtained a SGD-NO₃⁻ flux of 50-170 × 10⁵ mmol d⁻¹ (dry-wet seasons), a SGD-NH₄⁺ flux of 31-34 × 10⁵ mmol d⁻¹ (dry-wet seasons), a SGD-DON flux of 90-120 × 10⁵ mmol d⁻¹ (wet-dry seasons), and a SGD-PO₄³⁻ flux of 1.1-1.9 × 10⁵ mmol d⁻¹ (wet-dry seasons) (Figs. 4.6a and 4.6b, Table 4.2).

Combining all SGD-derived nitrogen inputs in Mobile Bay, I found that during the wet season the total SGD-NO₃⁻, SGD-NH₄⁺, SGD-DON, and SGD-PO₄³⁻ inputs in Mobile Bay were 250 × 10⁵ mmol d⁻¹, 320 × 10⁵ mmol d⁻¹, 360 × 10⁵ mmol d⁻¹, and 4.8 × 10⁵ mmol d⁻¹ respectively. In contrast, during the dry season SGD-NO₃⁻, SGD-NH₄⁺, SGD-DON, and SGD-PO₄³⁻ were 80 × 10⁵ mmol d⁻¹, 360 × 10⁵ mmol d⁻¹, 470 × 10⁵ mmol d⁻¹, and 3.5 × 10⁵ mmol d⁻¹ (Table 4.2).

During this study, the Mobile-Tensaw River System discharge ranged between 70×10^5 $\text{m}^3 \text{d}^{-1}$ and $1700 \times 10^5 \text{m}^3 \text{d}^{-1}$ during dry and wet seasons respectively (<https://waterwatch.usgs.gov>). The combined average NO_3^- , NH_4^+ , DON, and PO_4^{3-} concentrations from all rivers that I sampled during the dry season were $8.9 \pm 2.4 \text{mmol m}^{-3}$, $4.0 \pm 1.3 \text{mmol m}^{-3}$, 31 ± 10 , and $1.0 \pm 0.3 \text{mmol m}^{-3}$ respectively. During the wet season, average river NO_3^- , NH_4^+ , DON, and PO_4^{3-} concentrations were $7.4 \pm 1.7 \text{mmol m}^{-3}$, $7.0 \pm 1.1 \text{mmol m}^{-3}$, 29 ± 8.5 , and $0.3 \pm 0.1 \text{mmol m}^{-3}$ respectively. Multiplying the dry-wet seasons river discharge by the corresponding NO_3^- , NH_4^+ , DON, and PO_4^{3-} concentrations, I obtained a NO_3^- flux of 620-13,000 mmol d^{-1} , a NH_4^+ flux of 280-12,000 mmol d^{-1} , a DON flux of 2,200-49,000 mmol d^{-1} , and a PO_4^{3-} flux of 70-510 mmol d^{-1} (Figs. 4.6a and 4.6b, Table 4.2).

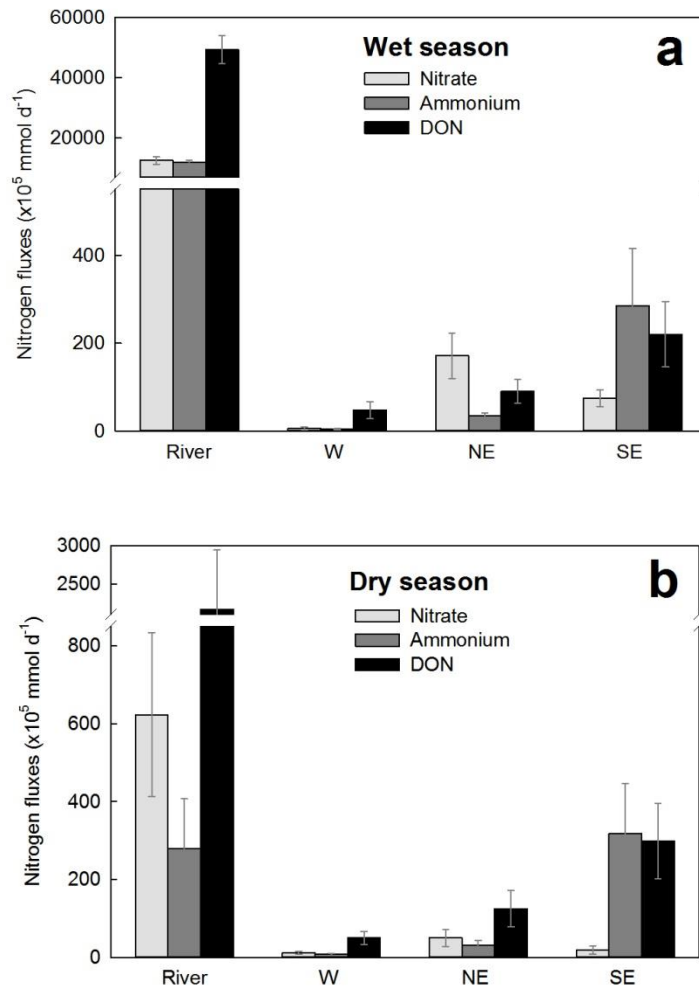


Figure 4.6. River-derived and SGD-derived nitrogen fluxes (NO_3^- , NH_4^+ , and DON) to Mobile Bay on the western, northeastern, and southeastern shores during the wet (a) and dry (b) seasons. Most of the SGD-derived nitrogen inputs to Mobile Bay occurred on the southeastern and northeastern shores, representing an average of 93% of the total SGD-N in the bay.

4.6 Discussion

4.6.1 Evaluating nutrients loading to Mobile Bay

4.6.1.1 Spatial variability of SGD-derived nutrient fluxes

During this study, I found that SGD-derived nutrient fluxes occurred preferentially on the east shore of Mobile Bay. The preferential delivery of nutrients to the east shore via SGD is, in part, result of the higher SGD rates found on the northeastern ($4.8 \times 10^5 \text{ m}^3 \text{ d}^{-1}$) and southeastern

shores ($3.1 \times 10^5 \text{ m}^3 \text{ d}^{-1}$), which represented ~80% of the total SGD to Mobile Bay (Chapter 3). Specifically, during this study I found that 93% of the total SGD-derived nitrogen inputs to the bay ($920 \times 10^5 \text{ mmol d}^{-1}$) occurred on the east shore, with two thirds occurring on the southeastern shore ($610 \times 10^5 \text{ mmol d}^{-1}$) and one third on the northeastern shore ($250 \times 10^5 \text{ mmol d}^{-1}$). In contrast, only 7% (i.e. $65 \times 10^5 \text{ mmol d}^{-1}$) of the total SGD-derived nitrogen fluxes to Mobile Bay were delivered to the western shore (Table 4.2). Furthermore, I found that most of the total nitrogen delivered via SGD to Mobile Bay occurred in the form of DON (45%) and NH_4^+ (37%). In comparison, nitrate only accounted for less than 20% of the total SGD-N flux (Fig. 4.6).

Additionally to this spatial variability of SGD-N fluxes across the bay I also found significant differences in the distribution of each nitrogen species (NO_3^- , NH_4^+ , and DON) (Fig. 4.6). For instance, the southeastern section (at study site TS-SE) receives close to 90% of all the SGD-derived NH_4^+ , and two thirds of the DON (62%) (Table 4.2). These distributions are a strong indication of consistent anoxic conditions in the southeastern shore. Indeed, during this 3-year study, DO concentrations in groundwater were on average 0.8 mg L^{-1} and were nearly hypoxic with 2.7 mg L^{-1} in the adjacent surface water of Mobile Bay during all sampling campaigns (Fig. 4.5, Appendix III Fig. 1). Consequently under these conditions, the nitrate fluxes to the eastern shore accounted for only 28% of the total SGD-derived NO_3^- flux to Mobile Bay (Table 4.2).

The nitrogen speciation on the northeastern shore of the bay (study site TS-NE), showed the opposite pattern with two thirds of all SGD-derived NO_3^- fluxes ($110 \times 10^5 \text{ mmol d}^{-1}$) occurring in this section, only 10% ($33 \times 10^5 \text{ mmol d}^{-1}$) of the NH_4^+ , and one fifth ($110 \times 10^5 \text{ mmol d}^{-1}$) of the SGD-derived DON fluxes (Fig. 4.6, Table 4.2). This distribution is consistent

with the field observations as groundwater DO was always higher at this study site with an average concentration up to $3.9 \pm 1.0 \text{ mg L}^{-1}$. The observed oxic conditions are result of a much higher hydraulic conductivity (58 m d^{-1}) and higher infiltration rates in the shallow coarse sand layer (depth up to 3.5 m) where I installed the intertidal piezometers (Fig. 4.2c). However, I would like to emphasize that the nutrient fluxes measured on the northeastern shore might be higher than reported here. My calculations are based on groundwater nutrients end-members measured in piezometers that were installed during the early stages of this study at site TS-NE. These piezometers did not capture the nutrient concentrations of SGD percolating through the peat layer. Later during this study, I found through detailed sediment core collection and electrical resistivity tomography (ERT) measurements, that the peat layer is also present along the northeastern shore of Mobile Bay, but 20-30 m offshore (Fig. 4.2c). I have evidence that groundwater seepage takes place partially through the organic sand layer along ~80 m from the shore (Fig. 4.2c) (Chapter 3). I theorize that NH_4^+ and DON concentrations in part of the SGD plume may have been higher than measured in piezometers NE-Pz-1-5. Therefore, the SGD-derived nutrient inputs in the northeastern shore represent a conservative estimation.

In comparison, I found very small SGD-derived nitrogen fluxes (1% of the total) on the western shore of Mobile Bay (Fig. 4.6, Table 4.2). As discussed in Chapter 3, SGD in the western section is impeded by a silt layer, which presence was confirmed both by ERT measurements and multiple sediment cores collected in the northern and southern ends of its shoreline.

The SGD-derived PO_4^{3-} fluxes to Mobile Bay were one order of magnitude lower than the nitrogen fluxes. Phosphate is particle reactive and efficiently immobilized in natural environments at normal pH values (Weiskel and Howes, 1992; Slomp and Van Cappellen, 2004)

and thus, these findings are consistent with other studies in a variety of coastal environments (e.g. Lee et al., 2009; Santos et al., 2009; Rodellas et al., 2014). The spatial distribution of SGD-derived PO_4^{3-} inputs to Mobile Bay was similar to the nitrogen fluxes pattern, also occurring primarily in the east shore. The vast majority (up to 93%) of the total SGD- PO_4^{3-} (4.1×10^5 mmol d^{-1}) was detected on the east shore of the Bay, with two thirds on the southeastern section (2.3×10^5 mmol d^{-1}) and the rest on the northeastern shore with 1.5×10^5 mmol d^{-1} (Table 4.2).

4.6.1.2 Temporal variability of nutrient fluxes

The total SGD-derived nutrient inputs to Mobile Bay were fairly constant throughout the year with a seasonal variability of less than 5% for nitrogen (913 vs 940×10^5 mmol d^{-1} during the dry and wet seasons) and 25% for phosphate (3.5 vs 4.8×10^5 mmol d^{-1} during the dry and wet seasons). In contrast, river-derived nutrient inputs varied significantly seasonally due to temporally constant nutrient concentrations but highly variable river discharge between the dry and wet seasons (Fig. 4.7). River-derived nitrogen fluxes ($3,100$ vs $74,000 \times 10^5$ mmol d^{-1} during the dry and wet seasons) varied by more than an order of magnitude. Similarly, the river-derived phosphate fluxes were more than 7 times higher during the wet season (70 vs 510×10^5 mmol d^{-1} during the dry and wet seasons) (Fig. 4.7). The combination of a significantly higher nutrient concentration in groundwater during the dry season (Fig. 4.5) with the relatively constant SGD rates (Chapter 3) derives in temporally uniform SGD nutrient fluxes. However, the temporal variability of SGD-derived nutrient fluxes was different for each nutrient at all sections of Mobile Bay (Table 4.2). Particularly, in the east shore (southeastern and northeastern shore) the SGD- NO_3 fluxes increased by 75% during the wet season. However, SGD-DON experienced a decrease of 36% during the wet season compared to the dry season (Table 4.2). In comparison, the SGD-derived phosphate fluxes showed a different behavior in all sections. On both the

northeastern and the western shores SGD- PO_4^{3-} was 71% and 50% lower during the wet season, whereas on the southeastern shore I observed a decrease of 66%.

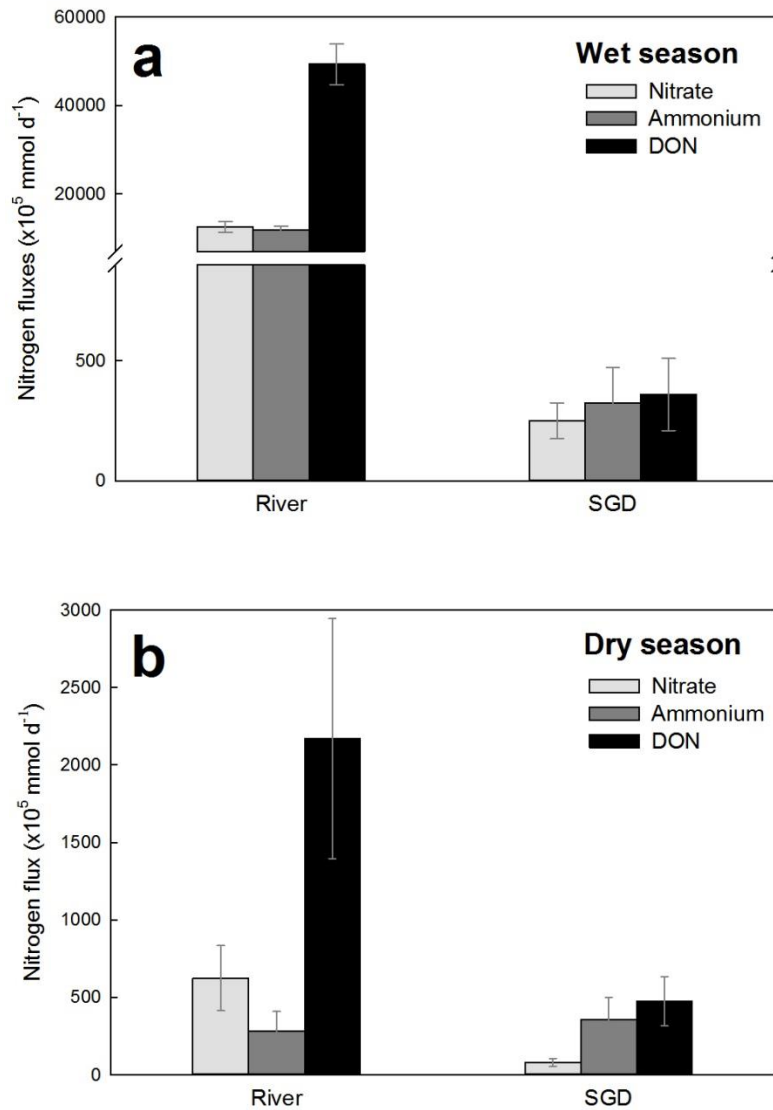


Figure 4.7. River-derived and total SGD-derived nitrogen fluxes (NO_3^- , NH_4^+ , and DON) to Mobile Bay from all sections during the wet (a) and dry seasons (b). Ammonium and DON were the main forms of nitrogen delivered to Mobile Bay via SGD during both the dry and wet seasons, being relatively more important to the nitrogen budget of Mobile Bay during the dry season (56% and 18% of the total respectively).

Nutrient	Inland zone of the Miocene-Pliocene Aquifer						Intertidal zone of the Miocene-Pliocene Aquifer (SGD)						Net flux		
	Dry	Wet	Dry	Wet	Dry	Wet	Dry	Wet	Dry	Wet	Dry	Wet	Dry	Wet	
	Average concentration (mmol m ⁻³)		Groundwater flow velocity (m d ⁻¹)		Specific nutrient flux mmol m ⁻² d ⁻¹ (mmol m ⁻² y ⁻¹)			Average concentration (mmol m ⁻³)		Groundwater flow velocity (m d ⁻¹)		Specific nutrient flux mmol m ⁻² d ⁻¹ (mmol m ⁻² y ⁻¹)		Net specific nutrient flux mmol m ⁻² d ⁻¹ (mmol m ⁻² y ⁻¹)	
East shore	NO ₃ ⁻	110	110	0.02	0.18	2.2 (790)	20 (7,200)	8.0	20	0.17	0.23	1.4 (500)	4.5 (1,600)	-0.8 (-300)	-15 (-5,600)
	NH ₄ ⁺	7.5	1.1	0.02	0.18	0.2 (55)	0.2 (72)	140	75	0.17	0.23	24 (8,600)	17 (6,300)	23 (8,500)	17 (6,200)
	DON	110	50	0.02	0.18	2.2 (800)	9.0 (3,300)	130	58	0.17	0.23	22 (8,100)	13 (4,900)	20 (7,300)	4.3 (1,600)
	PO ₄ ³⁻	0.2	0.1	0.02	0.18	0.004 (1.1)	0.01 (1.3)	0.5	0.9	0.17	0.23	0.1 (36)	0.2 (76)	0.08 (30)	0.2 (72)
West shore	NO ₃ ⁻	64	120	0.02	0.10	1.3 (470)	12 (4,400)	6.7	2.4	0.05	0.06	0.3 (120)	0.2 (55)	-0.9 (-340)	-12 (-4,300)
	NH ₄ ⁺	2.6	1	0.02	0.10	0.1 (19)	0.1 (32)	4.5	2	0.05	0.06	0.2 (84)	0.1 (46)	0.2 (65)	0.02 (9.2)
	DON	16	6	0.02	0.10	0.3 (120)	0.6 (220)	28	20	0.05	0.06	1.4 (520)	1.3 (460)	1.1 (400)	0.7 (240)
	PO ₄ ³⁻	0.1	0.1	0.02	0.10	0.003 (1.0)	0.01 (2.6)	0.2	0.1	0.05	0.06	0.01 (3.7)	0.01 (2.3)	0.01 (2.7)	-0.001 (-0.3)

Table 4.3. Groundwater specific nutrient fluxes from the Inland zone of the Miocene-Pliocene Aquifer to the intertidal zone of the aquifer, fluxes from the intertidal zone to Mobile Bay as SGD, and net fluxes after groundwater flows through the intertidal zone. Values of groundwater nutrient concentrations, groundwater flow velocity at each study site during the dry and wet seasons are also included in this table.

Comparing the total SGD-derived and river-derived nutrient fluxes to Mobile Bay during the wet season, SGD only represented a small portion (less than 3%) of the nutrient (NO_3^- , NH_4^+ , DON, and PO_4^{3-}) budgets of Mobile Bay (Fig. 4.7a). However, during the dry season when the river discharge is considerably lower, I found that SGD accounted for 12% of the NO_3^- , 56% of the NH_4^+ , 17% of the DON, and 5% of the PO_4^{3-} budgets (Fig. 4.7b). Considering the total nitrogen (inorganic and organic) inputs to the bay ($4,000\text{-}7,500 \times 10^5 \text{ mmol d}^{-1}$), SGD accounted for a maximum of 23% ($910 \times 10^5 \text{ mmol d}^{-1}$) during the dry season (Table 4.2). The relatively constant inputs of nutrients via SGD in Mobile Bay throughout the year compared to the highly fluctuating river discharge, makes the importance of SGD to be highest during the dry season.

In order to compare these nutrient fluxes with other estuaries I normalized the fluxes by the SGD seepage area and extrapolated the daily SGD-derived nutrient fluxes to obtain the annual nutrient delivery in the bay. In Mobile Bay SGD provides $34 \times 10^6 \text{ mol y}^{-1}$ of nitrogen and $0.2 \times 10^6 \text{ mol y}^{-1}$ of phosphate to the nutrients budget (Table 4.2). For instance, Charette et al. (2001) found that SGD accounted for a total nitrogen input of $0.8 \times 10^6 \text{ mol y}^{-1}$ in the Waquoit Bay estuary (Massachusetts, USA), almost two orders of magnitude lower ($0.2 \text{ mol m}^{-2} \text{ y}^{-1}$) compared to Mobile Bay ($15 \text{ mol m}^{-2} \text{ y}^{-1}$) when normalized by the seepage area (Table 4.3). Similarly, in Tampa Bay (Florida, USA) Kroeger et al. (2007) found a total nitrogen flux of $6.9 \times 10^6 \text{ mol y}^{-1}$ via SGD, also significantly lower ($4.7 \text{ mol m}^{-2} \text{ y}^{-1}$) than Mobile Bay ($15 \text{ mol m}^{-2} \text{ y}^{-1}$). The shallow sediments of both Waquoit Bay and Tampa Bay are comprised of sand and gravel with low organic matter content (Charette et al., 2001; Slomp and Van Cappellen, 2004; Kroeger et al., 2007). In contrast, in the Neuse River Estuary (North Carolina, USA) Null et al. (2011) showed that NH_4^+ was also the dominant form of nitrogen in SGD, providing alone about the same nitrogen inputs ($15 \text{ mol m}^{-2} \text{ y}^{-1}$) as in Mobile Bay (Table 4.3). The authors attributed the

high NH_4^+ fluxes via SGD to a slow groundwater flow and a high organic matter degradation in the coastal sediments (Null et al., 2011; Spiteri et al., 2008).

4.6.2 Groundwater biogeochemical transformations and N- and P-fluxes to Mobile Bay

During this study I found that lithological heterogeneities in the shallow coastal sediments of the intertidal zone of the Miocene-Pliocene Aquifer were critical for the nutrient (N and P) biogeochemical transformations as groundwater percolated through the intertidal zone of the aquifer from the inland zone to Mobile Bay. To better understand the observed differences in groundwater quality in the coastal aquifer along the Mobile Bay shoreline, I constructed a conceptual N- and P- specific flux models that illustrate the east and west shores of Mobile Bay (Fig. 4.8). Using the results from this models, I evaluated the nature of the biogeochemical transformations that might have occurred as groundwater flows through the coastal sediments of the Miocene-Pliocene Aquifer to Mobile Bay.

On each shore, the boundaries of this box-models were defined by the distances between the farthest inland groundwater wells sampled during this study, and the sets of intertidal piezometers installed at the SGD zone (Figs. 4.1 and 4.8). On the east shore this distance was 3.1 km and was 1.7 km on the west shore (Fig. 4.1). The groundwater flow velocities at the inland zone of these shore-perpendicular mass balances were $0.02\text{-}0.18\text{ m d}^{-1}$ on the east shore and $0.02\text{-}0.10\text{ m d}^{-1}$ on the west shore, based on evaluations conducted by Gillet et al. (2000), Dowling et al. (2004), and Ellis et al. (2013) (Table 4.3). All specific nutrient fluxes between the inland wells and the intertidal piezometers (Pz-1 to Pz-5) were calculated using nutrient concentrations obtained during this study at the inland wells and thus, I can confidently compare these estimates to the intertidal SGD fluxes.

SGD groundwater flow velocities were obtained from Chapter 3, which are based on site- and season-specific radon mass balance models using data collected from each of the intertidal piezometers nests and seepage meters deployments. In all scenarios specific nutrient fluxes ($\text{mmol m}^{-2} \text{d}^{-1}$) were calculated by multiplying average nutrient concentrations (mmol m^{-3}) in groundwater collected during wet or dry seasons by the groundwater flow velocities (m d^{-1}) assessed for this particular season.

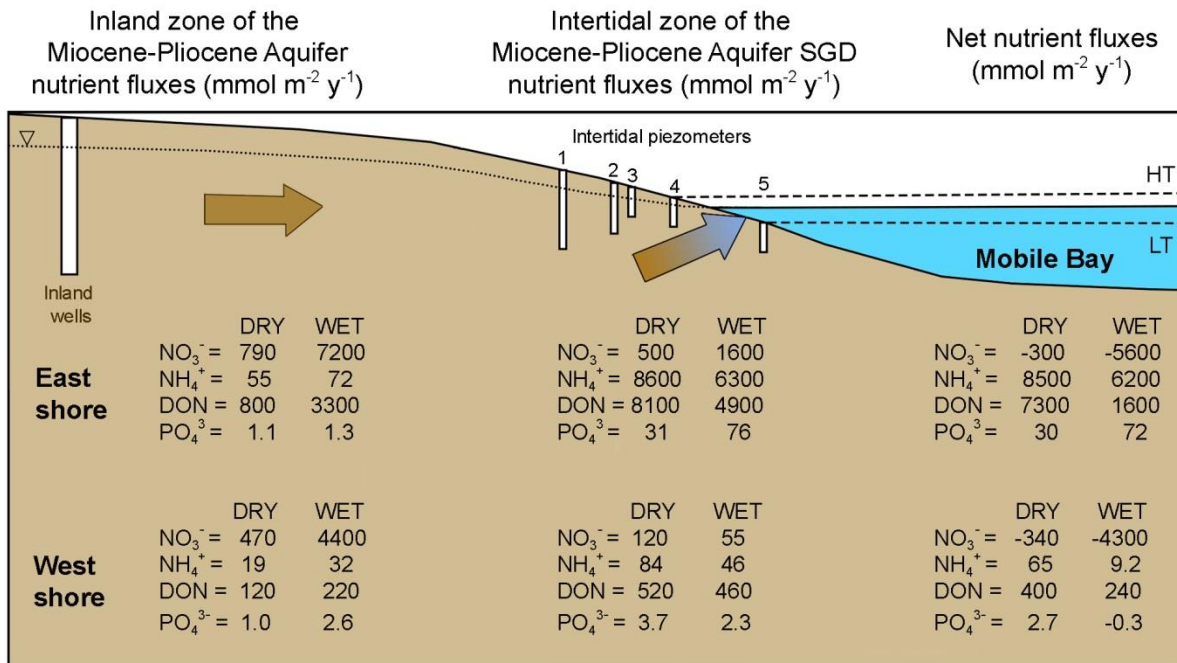


Figure 4.8. Schematic profile showing the annual groundwater specific nutrient fluxes from the inland zone of the Miocene-Pliocene Aquifer to the intertidal zone of the aquifer, fluxes from the intertidal zone to Mobile Bay as SGD, and net fluxes after groundwater flows through the coastal sediments. The coastal sediments at the intertidal zone generated negative net fluxes of NO_3^- and positive net fluxes of NH_4^+ , DON, and PO_4^{3-} . The sketch is not drawn to scale vertically or horizontally for an easier comparison.

4.6.2.1 N- and P-fluxes on the east shore of Mobile Bay

On the east shore of Mobile Bay the shallow Miocene-Pliocene Aquifer in the inland zone consists of quartzitic sand deposits with undetectable organic matter content and a hydraulic

conductivity of 10-20 m d^{-1} (Fig. 4.1) (Chandler et al., 1985; Gillet et al., 2000; Dowling et al., 2004). Based on previous studies conducted by Murgulet and Tick (2009; 2013), NO_3^- was the main form of nitrogen in the inland zone of the Miocene-Pliocene Aquifer, with groundwater concentrations as high as $1,600 \text{ mmol m}^{-3}$. Although during this study I did not find such high levels of nitrate in the same wells, average NO_3^- concentrations in the inland wells (SE-Well-1 and SE-Well-2), installed at a depth of 7-10 m, were always much higher (110 mmol m^{-3}) compared to the intertidal piezometers (14 mmol m^{-3}) (Table 4.3). In comparison, NH_4^+ (3 mmol m^{-3}) and DON (80 mmol m^{-3}) were relatively low. Oxidic conditions in this part of the aquifer were also confirmed from DO measurements; throughout the year DO was on average 5.6 mg L^{-1} .

When calculating the total N-fluxes for this inland zone of the Miocene-Pliocene Aquifer, I obtained an average annual flux of about $6,100 \text{ mmol m}^{-2} \text{ y}^{-1}$. This flux was mainly distributed between NO_3^- ($4,000 \text{ mmol m}^{-2} \text{ y}^{-1}$) and DON ($2,000 \text{ mmol m}^{-2} \text{ y}^{-1}$) with large seasonal variations; both fluxes were one order of magnitude higher during the wet season compared to the dry season. Contrastingly, the annual NH_4^+ flux in the inland section was two orders of magnitude lower ($64 \text{ mmol m}^{-2} \text{ y}^{-1}$), being constant throughout the year (Table 4.3, Fig 4.8). The total inorganic P-fluxes were much lower ($2.2 \text{ mmol m}^{-2} \text{ y}^{-1}$) compared to the N-fluxes, also showing no seasonal variability (Fig. 4.8). I suggest that these low P-fluxes are produced by the observed oxidic conditions, which can rapidly induce the removal of PO_4^{3-} from groundwater through sorption onto minerals and co-precipitation (Robertson, 1995, Weiskel and Howes, 1992, Zanini et al., 1998). On the other hand, I attribute the large fluxes of NO_3^- and DON in this section during the wet season ($7,200 \text{ mmol m}^{-2} \text{ y}^{-1}$) to the seasonal fertilization on the overlying agricultural lands (Fig. 4.1). The main agricultural crops in southern Alabama are cotton and

corn, which require intensive fertilization. Fertilization occurs twice a year in these areas, once in the spring (March-April) and once in the fall (October) using inorganic fertilizers and organic material (<https://www.nass.usda.gov/Surveys>). This can explain the high fluxes of NO_3^- and DON observed in this area. Since the organic content in the Miocene-Pliocene Aquifer sands in the inland zone is very low, I suggest that the high DON concentration are most likely generated by the use of organic fertilizers in combination with NO_3^- - and NH_4^+ -based fertilizers.

When applying the same mass-balance flux approach to the intertidal zone of the east shore and using SGD calculated fluxes in Chapter 3, I found that the average annual total N-flux delivered by SGD to Mobile Bay was $15,000 \text{ mmol m}^{-2} \text{ y}^{-1}$, producing a net total nitrogen surplus of $8,8000 \text{ mmol m}^{-2} \text{ y}^{-1}$. However, unlike the inland zone, the largest portion of the N-fluxes in the intertidal zone of the Miocene-Pliocene Aquifer occurred in the form of NH_4^+ ($7,400 \text{ mmol m}^{-2} \text{ y}^{-1}$) and DON ($6,500 \text{ mmol m}^{-2} \text{ y}^{-1}$) with a smaller seasonal variability (Fig. 4.8). For comparison, the average annual NO_3^- fluxes in the intertidal zone were only $1,100 \text{ mmol m}^{-2} \text{ y}^{-1}$, resulting in a net negative balance of $-2,900 \text{ mmol m}^{-2} \text{ y}^{-1}$. These SGD- NO_3^- fluxes showed the largest seasonal variability with an annual average flux three times larger during the wet season (Fig. 8). Although still lower than N-loadings, the total P-fluxes to Mobile Bay via SGD was more than one order of magnitude higher compared to the inland zone ($51 \text{ mmol m}^{-2} \text{ y}^{-1}$). This effect could be caused by a higher PO_4^{3-} solubility promoted by desorption as groundwater flows through the coastal sediments under anoxic conditions (Fig. 4.5) (Weiskel and Howes, 1992; Slomp and Van Cappellen, 2004).

4.6.2.2 N- and P- fluxes on the west shore of Mobile Bay

When using the same mass-balance calculations and boundary conditions on the west shore of Mobile Bay, I found significantly different fluxes. The inland annual N-fluxes were

three times lower than on the east shore with about $2,600 \text{ mmol m}^{-2} \text{ y}^{-1}$, whereas the P-flux was almost the same with about $1.8 \text{ mmol m}^{-2} \text{ y}^{-1}$ (Table 4.3). A pronounced seasonal pattern (90% increase during the wet season) was observed in the NO_3^- fluxes compared to the rest of nutrients. Since this area is dominated by forests and wetlands (61%) I attribute the higher N-fluxes mostly to the groundwater flow velocity seasonal variability. In the intertidal zone of the Miocene-Pliocene Aquifer, the annual SGD-delivered nitrogen fluxes were almost five times lower ($640 \text{ mmol m}^{-2} \text{ y}^{-1}$) compared to the inland fluxes, with insignificant seasonal variability (Fig. 4.8). When calculating the net nutrient fluxes, I found that the largest contribution to the deficit observed from the inland zone to the SGD zone is generated by NO_3^- ($-2,300 \text{ mmol m}^{-2} \text{ y}^{-1}$), similar to the negative fluxes found on the east shore ($-2,900 \text{ mmol m}^{-2} \text{ y}^{-1}$). The P-fluxes did not vary between seasons and were higher than in the inland zone of the aquifer, following the same trend observed on the east shore of Mobile Bay.

Based on the calculated annual groundwater fluxes in the coastal Miocene-Pliocene Aquifer I conclude that the coastal sediments in Mobile Bay serve as a sink of the high NO_3^- loading observed in the inland groundwater, transforming NO_3^- into NH_4^+ and DON. I observed this process in both the east and the west shores of Mobile Bay. However, I found that apart from this N transformation, there is a significant net production of nitrogen as NH_4^+ and DON ($8,800 \text{ mmol m}^{-2} \text{ y}^{-1}$) on the east shore, resulting in a total nitrogen export via SGD of $15,000 \text{ mmol m}^{-2} \text{ y}^{-1}$ to the bay. These large N-fluxes were accompanied by a net production of about $51 \text{ mmol m}^{-2} \text{ y}^{-1}$ of PO_4^{3-} on the east shore of Mobile Bay.

I argue that the net production of nitrogen observed on the east shore of Mobile Bay is generated by the peat layer that is only present on this shore, explaining the difference with the west shore. Additionally, I hypothesize that the occurrence of SGD-derived nutrient fluxes

concentrated in a relatively small portion of the bay, must have significant effects on the nutrient balance and the ecological health of these areas. The water column stratification common during the summer in combination with large N-fluxes in reduced forms (as NH_4^+ and DON) can have a significant impact on *Jubilee* events in Mobile Bay. The delivery of NH_4^+ and DON can enhance the persistent hypoxia in the bottom waters of the east shore, where *Jubilees* occur in Mobile Bay. In fact, the areas of excess of N-reducing SGD fluxes coincide exactly with the areas where the *Jubilees* occur (Loesch, 1960; May, 1973; Turner et al., 1987; Schroeder and Wiseman, 1988).

4.6.3 Nitrogen sources in Mobile Bay

I strongly suggest that the quality of SGD to Mobile Bay and thus its effect on the surface water of the bay is mostly result of the natural lithological composition and biogeochemical transformations in the intertidal zone of the Miocene-Pliocene Aquifer, which is the principal surficial aquifer in the estuary. Although the Mobile Bay area is well developed, I did not find evidence of anthropogenic influence on the quality of SGD to the bay. Pieces of evidence for this major conclusion are found across a wide spectrum of approaches used during this three-year study.

4.6.3.1 Lithological evidence

Sediment cores recovered during this study from both the northeastern and southeastern shores of Mobile Bay showed the presence of an organic-rich (up to 36%) peat layer along the entire east shore. Detailed shallow geophysical exploration (both ERT and CRP surveys) revealed that this layer extends at least 200 m offshore in some parts of the bay (Chapter 3 Figs. 3.2b, 3.5b and 3.5c). Combined ERT time-series measurements of the subsurface during falling tide and sediment properties analyses of the cores confirmed that the peat layer has relatively

high hydraulic conductivity (8.2 m d^{-1}) and serves as a conduit for SGD (Chapter 3 Table 3.1 and Appendix III Fig. 3). Furthermore, I found that the peat layer creates anoxic conditions in groundwater at the intertidal zone along the east shore and very high net fluxes of NH_4^+ and DON (see section 4.6.2). However, I found that the conditions observed on the east shore are not ubiquitous in Mobile Bay. Parallel geophysical and lithological investigations of the shallow aquifer structure and composition on the west shore did not reveal the same conditions. The ERT and CRP surveys as well as sedimentological characterization showed a spatially uniform fine-grained lithology, which was confirmed to be a silt layer with very low permeability based on the recovered cores (Chapter 3 Figs. 3.2b, 3.5b and 3.5c). In addition, I found that the organic content of the silt layer on the west shore was low (only 11%), i.e. I did not identify the distinct peat layer found on the east shore (Table 3.1). In turn, although anoxic conditions were present, I found negative net N-fluxes through the coastal aquifer on this shore and thus, I am confident that the coastal sediments on the west serve only as a sink of nutrients. Therefore, I conclude that the peat layer on the east shore is a natural source of nitrogen to Mobile Bay. The important net production of nitrogen only observed on the east shore indicated that the organic matter mineralization in the peat layer must be responsible for the additional nitrogen fluxes as NH_4^+ and DON (Fig. 4.9). Additionally, the net loss of NO_3^- on both the west and east shores of the bay indicate that denitrification and dissimilatory nitrate reduction to ammonium (DNRA) are occurring in the coastal sediments (Fig. 4.9). Bernard et al. (2015) demonstrated in a coastal lagoon near Mobile Bay (Little Lagoon) that DNRA and denitrification occur during both wet and dry seasons in this area. Furthermore, Bernard et al. (2015) found that during the dry season, when *Jubilees* and HABs occur, DNRA is the dominant NO_3^- reduction pathway.

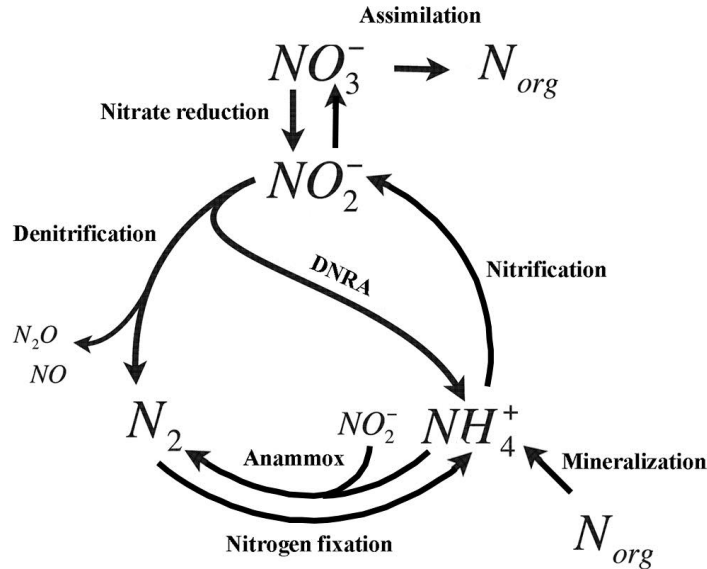


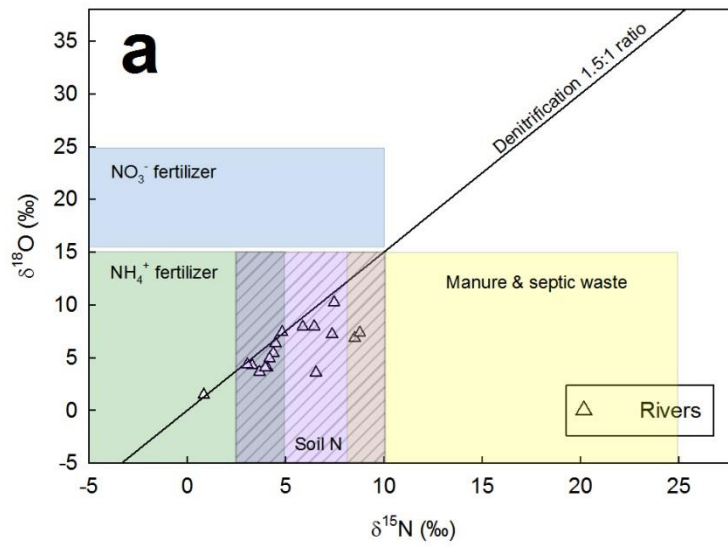
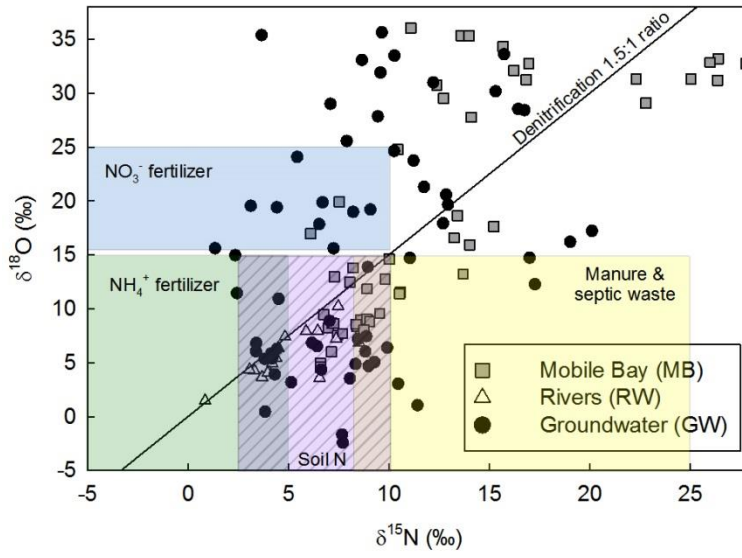
Figure 4.9. Schematic illustrating the nitrogen cycle. The dissimilatory nitrate reduction to ammonium is indicated as DNRA. This figure was modified from Chen and Wang (2015).

4.6.3.2 Stable isotopes evidence

To identify the sources of nitrogen in Mobile Bay I utilized the $\delta^{15}N$ and $\delta^{18}O$ isotopic signatures measured in the two main water end-members entering the bay (e.g. groundwater and surface water from the main rivers) and bay waters. The principle of this widely accepted approach is that different sources of nitrogen are associated with specific ranges of NO_3^- $\delta^{15}N$ and $\delta^{18}O$ values (Amberger and Schmidt, 1987; Kendall, 1998; Kendall et al., 2007; Xue et al., 2009). While $\delta^{15}N$ and $\delta^{18}O$ data alone sometimes can be inconclusive and discussion about its applications still exist among scientists, when combined with lithological composition and changes in N-species fluxes across scales, it has proven to be a very powerful tool.

Using this approach I was able (1) to identify possible sources of nitrogen and (2) to predict the geochemical pathways of nitrogen-transformations in the shallow coastal aquifer. I found isotopic signatures that suggest the influence of three main sources of NO_3^- in the Mobile Bay system; including inorganic fertilizers (both NO_3^- and NH_4^+ -based), organic fertilizers (e.g.

manure), and organic soil mineralization. I found that each of these sources had different contributions to the overall water quality of Mobile Bay. Based on these data, the main source of nitrogen to the bay is the organic soil mineralization (Fig 4.10). Additionally, I was able to identify an overall trend of denitrification both on land in in surface water that is supported by the 1.5:1 ratio of this large data set (n= 137). This trend and thus denitrification are much easier identified in water samples collected from the Mobile-Tensaw River System (Fig 4.10a) and within Mobile Bay (Fig 4.10b). The maximum isotopic values measured in Bon Secour Bay (~16-27‰) and the values distribution in the bay indicate that nitrate $\delta^{15}\text{N}$ and $\delta^{18}\text{O}$ experienced isotopic fractionation from denitrification in the water column (Fig 4.10b) (Kendall et al., 2007). Furthermore, most of the NO_3^- inputs to the bay occurred via riverine discharge, with 88-98% of the total NO_3^- budget. After entering the bay, NO_3^- concentrations gradually decreased from the river delta (9-26 mmol m^{-3}) to Bon Secour Bay (0.1-1.2 mmol m^{-3}). Nearly the opposite spatial distribution was found for NH_4^+ and DON, where the highest values were found in the southeastern shore, the southern sector of the western shore, and Bon Secour Bay (Appendix III Figs. 2a, 2b, and 2c). These spatial distributions strongly support the consumption of NO_3^- by primary producers and via microbial denitrification in Mobile Bay waters (Fig. 4. 9).



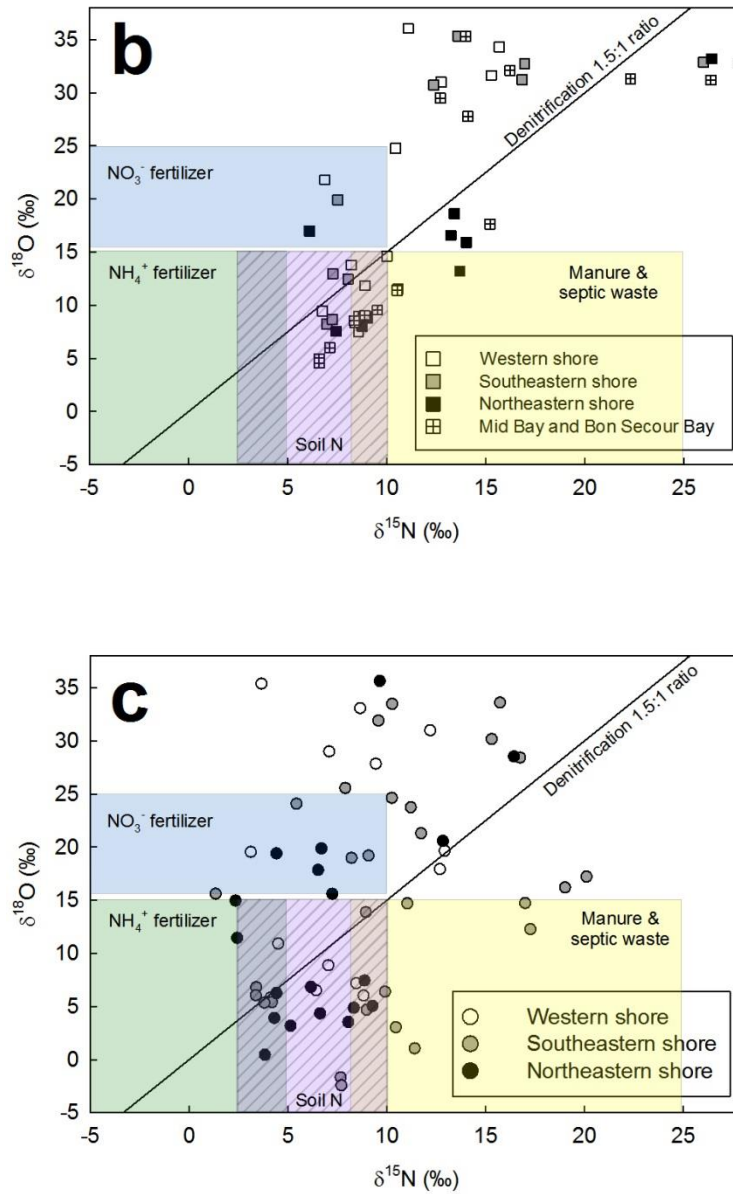


Figure 4.10. Cross plot showing the nitrate stable isotopes $\delta^{15}\text{N}$ and $\delta^{18}\text{O}$ values measured in all samples, rivers (a), Mobile Bay (b), and in groundwater (c). Samples collected on the western, southeastern, and northeastern shores are represented as white, grey, and black circles respectively. Theoretical values for anthropogenic (NO_3^- and NH_4^+ fertilizers, manure and septic waste) and natural (organic nitrogen in the sediments or soil) sources of nitrate $\delta^{15}\text{N}$ and $\delta^{18}\text{O}$ signatures are shown in all panels (Amberger and Schmidt, 1987; Kendall, 1998; Kendall et al., 2007; Xue et al., 2009). The theoretical denitrification line of $\delta^{18}\text{O}:\delta^{15}\text{N}$ as 1.5:1 is shown in all panels based on Kendall et al. (2007) and Murgulet and Tick (2013).

However, when plotting the stable isotope groundwater data alone (Fig. 4.10c), I was able to recognize a few facts that support my hypothesis for the large scale denitrification that occurs at the intertidal zones on both sides of the bay. For example, all of the groundwater NO_3^- $\delta^{15}\text{N}$ and $\delta^{18}\text{O}$ values in the inland wells, both on the east and west shore, suggest an organic soil mineralization source, experiencing denitrification as it flows through the intertidal sediments (Fig. 4.10c). Beebe and Lowery (2018) also observed on the western shore that the main source of nitrogen in groundwater was the soil organic matter mineralization, compared to nearly absent anthropogenic nitrogen inputs. In the inland wells I observed regularly elevated NO_3^- concentrations, which I associated with fertilization occurring on a larger scale on the highly agricultural east shore (Fig. 4.8, Table 4.3). However, at the intertidal zone groundwater showed significantly higher values of $\delta^{15}\text{N}$ and $\delta^{18}\text{O}$ (Fig. 4.10c). Because most of the data were either aligned along the theoretical denitrification line or/and above this line, I conclude that although DNRA is most likely occurring simultaneously, denitrification is the main NO_3^- reduction pathway in the groundwater transition from the inland zone to the intertidal zone (Fig. 4.9). However, the observed net production of total nitrogen in the form of NH_4^+ and DON at the intertidal zone of the east shore indicates that as SGD occurs to the bay, abundant organic matter mineralization of the peat layer is the dominant biogeochemical transformation of nitrogen (Figs. 4.8 and 4.9).

4.6.3.3 Evidence from DOM quality and organic matter characterization

I analyzed the DOM composition entering to Mobil Bay via river and groundwater to further confirm the hypothesis of a natural origin of nitrogen to the system. In this work, I followed the nomenclature established in the environmental organic geochemistry field. I refer to C1 and C2 (components 1 and 2) a mixture of humic-like organic compounds, whereas C3 is a

group of compounds with a protein-like structure. Components 1 and 2 are associated with the presence of humic acids degradation products from plant material naturally present in the soil, whereas protein-like compounds (C3) indicate the degradation of planktonic and bacterial remains (Lu et al., 2015). In Mobile Bay surface water, humic-like degradation components C1 and C2 were detected in almost equal percentage (28% and 34%), whereas protein-like component C3 was 38%. Following the counter-clock wise water circulation of Mobile Bay (Chapter 3), I suggest that components 1 and 2 were degraded in the bay from the river delta in the north (26-46%) to Bon Secour Bay (6-30%) in the south (Appendix III Figs. 5a, 5b, and 5c). Similarly, the lowest isotopic values ($\delta^{15}\text{N}$ and $\delta^{18}\text{O}$) measured near the delta ($\sim 8\text{-}7\text{‰}$) are indicative of the massive riverine nitrogen inputs from natural soil organic nitrogen and NH_4^+ -fertilizers (Fig 4.10a).

In groundwater collected from a multi-level piezometer (SE-Pz-4.5) on the east shore of Mobile Bay, where the peat layer is located, DOM was primarily composed of humic-like components C2 (43%) and C1 (29%) (Fig 4.11a). This is a clear indication that SGD is transporting the degradation products of terrestrial organic matter to Mobile Bay waters. I theorize that the presence of components 1 and 2 in the peat layer can result from decomposing C3 and C4 salt marsh plants such as *Juncus roemerianus*, *Spartina alterniflora* and freshwater marsh *Typha* and *Schoenoplectus* (undifferentiated) common in the Mobile Bay area (Cory and McKnight, 2005; Fellman et al., 2010; Lu et al., 2015; Smith and Osterman, 2014; Wheeler et al., 2017).

To confirm the origin of the peat layer on the east shore of Mobile Bay and the origin of the degradation products released by SGD, I also conducted stable isotope analyzes of the organic matter present in sediment core TS-SE recovered at the southeastern shore (Fig. 4.3). I

identified the grain size of the peat layer as fine and found an average C-weight percent of 3.3% and a N-weight percent of 0.3%. The average C/N atomic ratios of 19 of this layer (Fig. 4.4, Table 4.1) are similar to other peat sediments (fine-grained organic-rich) sediments identified elsewhere (e.g. Stanek and Silc, 1977; Schnurrenberger et al., 2003; Lambert et al., 2008). When comparing the C/N ratios with the $\delta^{13}\text{C}$ isotopic composition along the core profile and using reference values reported by Meyers (1997) and Lamb et al. (2006), I identified two organic matter sources: (1) terrestrial C3 plants litter (e.g. pine and oak tree debris) and (2) remains of C3 plants of marsh environments (Fig. 4.11b). The C/N values of all samples, except for the shallowest sample (45 cm), are closely clustered in the range between 17 and 21 with a narrow $\delta^{13}\text{C}$ isotopic signatures of 23-28‰ (Fig. 4.11b), confirming that marsh C3 plants are the main source of organic matter in the peat layer (Guerra et al., 2015). Furthermore, based on the Mobile Bay end-members as presented by Smith and Osterman (2014), the plant remains conforming the peat layer most likely correspond to marsh species *Spartina alterniflor* and *Juncus roemarianus* (Fig. 4.11b) .

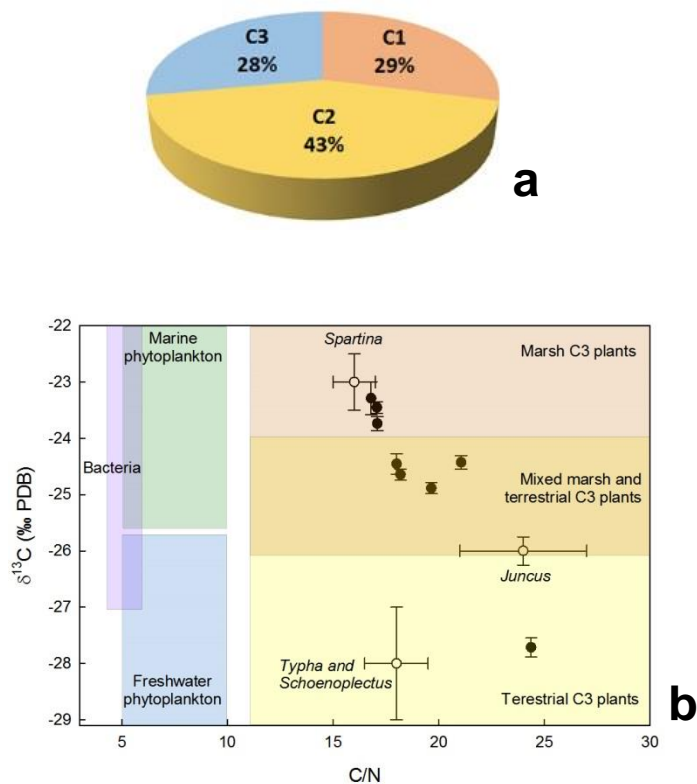


Figure 4.11. (a) Percentage presence of components 1, 2, and 3 (C1, C2, and C3) of dissolved organic matter (DOM) measured in pore water of the peat layer (B) at piezometer SE-Pz-4.5. DOM was primarily composed of humic-like components 2 (43%) and 1 (29%), compared to the protein-like component 3 (28%). (b) Cross plot showing the relationship between $\delta^{13}\text{C}$ and C/N of the organic matter present in the peat layer from sediment core TS-SE (black circles). Ranges of all possible theoretical origins of organic matter (bacteria, marine and freshwater phytoplankton, marsh and terrestrial C3 plants) are represented as defined by Lamb et al. (2006) and Guerra et al. (2015). Three specific regional end-member values measured in Mobile Bay are also shown (white circles) for marsh plant species *Spartina alterniflora* (*Spartina*), *Typha* and *Schoenoplectus* undifferentiated (*Typha* and *Schoenoplectus*), and *Juncus roemarianus* (*Juncus*) as presented by Smith and Osterman (2014). These data highlight the importance of terrestrial organic matter to Mobile Bay. All samples fall in the marsh and terrestrial C3 plants value range and regional *Spartina alterniflora* and *Juncus roemarianus* end-members.

4.6.3.4 Evidence from sediment depositional ages

To explore even further the nature and age of this layer I performed ^{210}Pb and ^{137}Cs analyses (Fig. 4.12) and found that the peat layer is very young in age. Based on the peak of

^{137}Cs the peat layer was most likely buried in the late 60s. Similarly, Smith and Osterman (2013) also found a peak of ^{210}Pb and ^{137}Cs only in a sediment layer underling a sand lens in Bon Secour Bay (east shore), whereas on the west shore and mid-bay areas these peaks were not present. Although profiles of ^{210}Pb and ^{137}Cs in shallow sediments of the east shore of Mobile Bay do not exist in the literature, these results further support the presence of the peat layer only on the east shore of the bay and its recent age (Smith and Osterman, 2013; Osterman and Smith, 2012). To verify the geologic age of the peat layer I also looked at historical aerial photos (Google Earth) and found that the east shore of Mobile Bay was developed during the second half of the 20th century, followed by a rapid population increase (up to 3 times) in Baldwin County, Alabama (United States Census Bureau). Indeed, the rapid development of private houses along the shorelines of the east shore of Mobile Bay that started in the early 60s. After the development of the area the previously abundant marsh on the east shore were destroyed; however, the root system and plant detritus were buried, starting the decomposition process and formation of the peat layer (Ellis et al., 2011).

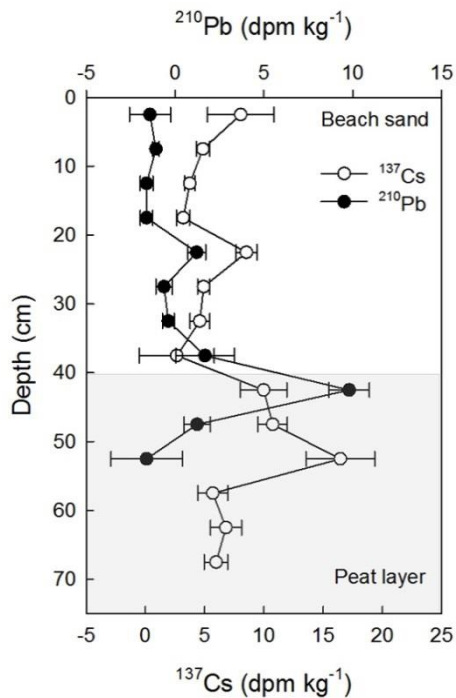


Figure 4.12. Vertical profile of (a) ^{210}Pb and (b) ^{137}Cs analyzes conducted on sediment core TS-SE. A peak of both isotopes can be observed from a depth of 40 cm, coinciding with the beginning of the peat layer. The depth of the peat layer is highlighted in grey.

Based on all the discussed independent lines of evidence, I am confident that the peat layer present on the east shore of Mobile Bay is comprised of the root system and plant remains of previously existing marsh areas. Infiltration of SGD through this layer and degradation products released at the beach face is the primary factor affecting the water quality of the east shore of Mobile Bay. During this three-year study I did not find evidence of pollution or direct impact from anthropogenic fertilizers and sewage waste inputs.

4.7 Ecological implications of SGD

Loesch (1960) showed that *Jubilee* events are linked to water hypoxia and May (1973) further demonstrated that *Jubilees* are triggered by a synergetic combination of physical forces and geochemical reactions that only coincide during the summer months (dry season). The small area of the east shore where the important SGD-derived NH_4^+ and DON inputs occur, coincide

very well with the areas affected by *Jubilees*. The delivery of these reduced forms of nitrogen to the water column can increase the chemical oxygen demand, enhancing hypoxia in the deeper water layer and potentially affecting *Jubilees*. Further evidence for the effect of SGD on *Jubilees* can be found on the physical and climatic conditions during these events. SGD is a fairly uniform process throughout the year; therefore during climatic and physical settings suitable for *Jubilees*, SGD can generate the necessary water hypoxia. This hypothesis is indirectly validated by the absence of *Jubilees* on the western shore of Mobile Bay. May (1973) showed that hypoxia also occurred along the western shore when an extensive *Jubilee* only took place on the eastern shore, triggered by the easterly winds. During the summer months slight southwest to westerly winds are common in Mobile Bay; however, *Jubilees* have never occurred in the western shore. As discussed in Loesch (1960), the lack of a topographic protection against winds near the shore may restrict the occurrence of *Jubilees* on the western shore. Nevertheless, it is plausible that the absence of an organic sediment layer combined with the insignificant SGD inputs found in this area, could be limiting *Jubilee* event on the western shore. SGD-derived nutrient inputs on the western shore always represented $< 2\%$ of the total inputs in Mobile Bay for all nutrients, restricting the potential effect of SGD on *Jubilees*.

Although HABs have never been studied in the northern half of the bay, I theorize that the SGD-derived nutrient inputs evaluated in this study could also be affecting HABs. N/P ratios in SGD significantly different from the receiving coastal waters, and thus could potentially result in the ecological disequilibrium that directly affects phytoplankton growth (Kim and Swarzenski, 2010). The optimum nutrient uptake by primary producers in typical marine environments occurs at the N/P Redfield ratio of 16:1 during cellular growth. As a result, coastal waters where degradation of this planktonic material occurs would follow relatively closely this N/P ratio.

However, SGD-delivered excess nitrogen (i.e. high N/P ratios) to the coastal areas often triggers HABs among other ecological impacts (e.g. Yamaguchi et al., 2001; Garcés et al., 2011; Smith and Swarzenski, 2012).

During this study I found that the average N/P ratio of Mobile Bay waters was exactly 16:1, indication that Mobile Bay is nutrient unlimited. However, the bay's surface waters on the southeastern shore and the southern sector of the western shore showed significant excess of nitrogen with N/P values, always above 30 and up to 350 (Fig. 4.13a, Appendix III Fig. 2e). Previous studies by Liefer et al. (2009) and McIntyre et al. (2011) have shown that these two areas are largely impacted by toxic blooms of diatoms. During this study I found that N/P ratio in the Mobile-Tensaw River System was relatively constant and only slightly higher than the Redfield ratio with an average of 21:1 (Fig. 4.13b). Thus, the excess nitrogen observed in the areas impacted by HABs must be affected by the NH_4^+ inputs via SGD. I found that the N/P ratios measured in groundwater samples in the intertidal zone of the western (79) and southeastern shores (250) were very high (Fig. 4.13c), coinciding with the areas of highest N/P ratios in Mobile Bay where HABs occur.

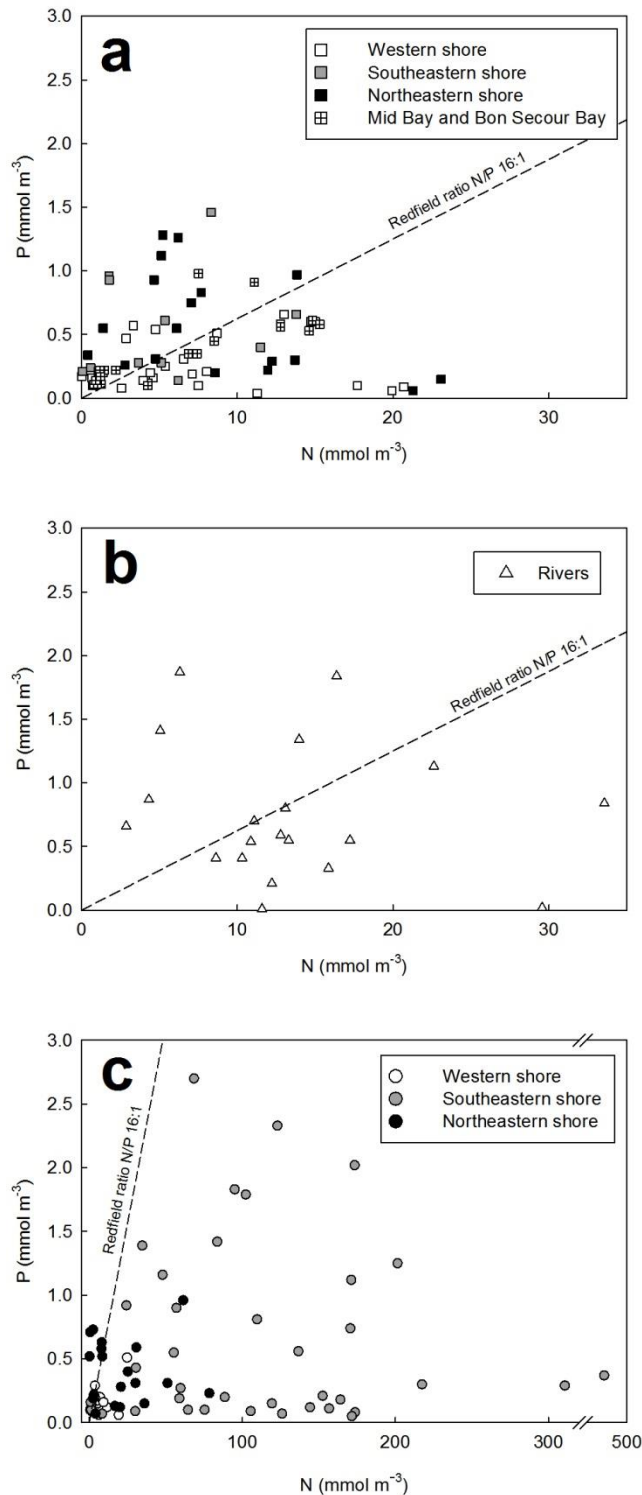


Figure 4.13. Cross plot showing the nitrogen and phosphorous concentrations measure in Mobile Bay (a), rivers (b), and groundwater (c). The Redfield molar N/P ratio of 16:1 is shown in all panels for reference. The average N/P ratio in Mobile Bay waters was 16 (Redfield ratio), while in rivers and groundwater the N/P ratios were 21 ± 9 and 270 ± 130 respectively.

4.8 Conclusions

Although dominated by river inputs, Mobile Bay receives nearly a quarter of the nutrient budgets via SGD during the dry season, when river discharge is lowest. During low river flow conditions 92-94% of these SGD nutrients fluxes occur on the eastern shore, coinciding exactly with the time of the year and area where *Jubilees* take place (Loesch, 1960). I hypothesize that the *Jubilee* events are supported by SGD-derived nutrients inputs during optimum climatic and physical conditions. I found that during the dry season (when *Jubilees* occur) 56% and 15% of the total NH_4^+ and DON budgets of Mobile Bay are delivered to the eastern shore (where *Jubilees* occur) via SGD (Table 4.2). I suggest that NO_3^- reduction via DNRA and denitrification combined with the abundant organic matter mineralization within the peat layer are responsible for these exceptionally high SGD-derived NH_4^+ and DON fluxes compared to the NO_3^- inputs. Based on all evidences presented in this study, the peat layer identified on the east shore of Mobile Bay is composed of the remains of previously existing marsh areas. Thus, SGD-derived nutrient inputs have a natural origin in the coastal sediments, where no evidence of anthropogenic fertilizers or sewage waste was observed.

Based on the results obtained during this study, I additionally theorize that the HAB events observed in Mobile Bay can be triggered by these important SGD-derived NH_4^+ and DON inputs during the summer. Furthermore, previous studies assumed that SGD could affect HABs by delivering the NO_3^- contamination of the Miocene-Pliocene Aquifer from nearby agricultural fertilizers to Mobile Bay (Liefer et al., 2009; Murgulet and Tick, 2009; McIntyre et al., 2011; Liefer et al., 2014). However, I demonstrated here that in the case that HABs are indeed impacted by SGD, the nitrogen inputs are of natural origin produced in the sediments and in the form of NH_4^+ and DON.

4.9 References

- Amberger, A. and H. L. Schmidt. 1987. Natürliche isotopengehalte von Nitrat als Indikatoren für dessen Herkunft. *Geochimica et Cosmochimica Acta* 51: 2699-2705.
- Bernard, R. J., B. Mortazavi and A. A. Kleinhuizen. 2015. Dissimilatory nitrate reduction to ammonium (DNRA) seasonally dominates NO_3^- reduction pathways in an anthropogenically impacted sub-tropical coastal lagoon. *Biogeochemistry* 125: 47-64.
- Burnett, W. C. and H. Dulaiova. 2006. Radon as a tracer of submarine groundwater discharge into a boat basin in Donnalucata, Sicily. *Continental Shelf Research*, 26: 862-873.
- Burnett, W. C., I. R. Santos, Y. Weinstein, P. W. Swarzenski and B. Herut. 2007. Remaining uncertainties in the use of Rn-222 as a quantitative tracer of submarine groundwater discharge. A New Focus on Groundwater–Seawater Interactions (Proceedings of Symposium HS1001 at IUGG2007, Perugia, July 2007. IAHS publication 312: 109.
- Cerdà-Domènech, M., V. Rodellas, A. Folch and J. Garcia-Orellana. 2017. Constraining the temporal variations of Ra isotopes and Rn in the groundwater end-member: Implications for derived SGD estimates. *Science of the total environment* 595: 849-857.
- Chandler RV, J.D. Moorea and B. Gillett. 1985. Ground-water chemistry and salt-water encroachment, southern Baldwin County, Alabama. Geological Survey of Alabama Bulletin 126, 70 pp.
- Charette, M. A., K. O. Buesseler and J. E. Andrews. 2001. Utility of radium isotopes for evaluating the input and transport of groundwater-derived nitrogen to a Cape Cod estuary. *Limnology and Oceanography* 46: 465-470.
- Charette, M. A., R. Splivallo, C. Herbold, M. S. Bollinger and W. S. Moore. 2003. Salt marsh submarine groundwater discharge as traced by radium isotopes. *Marine Chemistry* 84: 113-121.
- Chen, Y. and F. Wang. 2015. Insights on nitrate respiration by *Shewanella*. *Frontiers in Marine Science* 1: 80.
- Cory, R. M., and D. M. McKnight. 2005. Fluorescence spectroscopy reveals ubiquitous presence of oxidized and reduced quinones in dissolved organic matter. *Environmental science & technology* 39: 8142-8149.
- Craig, H. 1957. Isotopic standards for carbon and oxygen and correction factors for mass-spectrometric analysis of carbon dioxide. *Geochimica et cosmochimica acta* 12: 133-149.
- Dinnel, S. P., W. W. Schroeder and W. J. Wiseman Jr. 1990. Estuarine-shelf exchange using Landsat images of discharge plumes. *Journal of Coastal Research* 789-799.

- Dowling, C. B., R. J. Poreda, A. G. Hunt and A. E. Carey. 2004. Ground water discharge and nitrate flux to the Gulf of Mexico. *Groundwater* 42: 401-417.
- Du, J., K. Park, J. Shen, B. Dzwonkowski, X. Yu and B. I. Yoon. 2018. Role of baroclinic processes on flushing characteristics in a highly stratified estuarine system, Mobile Bay, Alabama. *Journal of Geophysical Research: Oceans* 123.
- Dulaiova, H., W. Burnett, G. Wattayakorn and P. Sojisuorn. 2006. Are groundwater inputs into river-dominated areas important? The Chao Phraya River—Gulf of Thailand. *Limnology and Oceanography* 51: 2232-2247.
- Ellis, J. 2013. Evaluation of submarine groundwater discharge and groundwater quality using a novel coupled approach: isotopic tracer techniques and numerical modeling. Master's thesis, University of Alabama, 67 pp.
- Ellis, J. T., J. P. Spruce, R. A. Swann, J. C. Smoot and K. W. Hilbert. 2011. An assessment of coastal land-use and land-cover change from 1974–2008 in the vicinity of Mobile Bay, Alabama. *Journal of Coastal Conservation*, 15: 139-149.
- Fellman, J. B., R. G. M. Spencer, P. J. Hernes, R. T. Edwards, D. V. D'Amore, and E. Hood. 2010. The impact of glacier runoff on the biodegradability and biochemical composition of terrigenous dissolved organic matter in near-shore marine ecosystems. *Marine Chemistry* 121: 112-122.
- Garcés, E., G. Basterretxea and A. Tovar-Sánchez. 2011. Changes in microbial communities in response to submarine groundwater input. *Marine Ecology Progress Series* 438: 47-58.
- Garcia-Solsona, E., J. Garcia-Orellana, P. Masqué, V. Rodellas, M. Mejías, B. Ballesteros and J. Domínguez. 2010. Groundwater and nutrient discharge through karstic coastal springs (Castelló, Spain). *Biogeosciences* 7: 2625-2638.
- Gillett, B., D. Raymond, J. Moore and B. Tew. 2000. Hydrogeology and vulnerability to contamination of major aquifers in Alabama: Area 13. Geological Survey of Alabama Circular 199A, 68 pp.
- Greene Jr, D. L., A. B. Rodriguez and J. B. Anderson. 2007. Seaward-branching coastal-plain and piedmont incised-valley systems through multiple sea-level cycles: Late Quaternary examples from Mobile Bay and Mississippi Sound, USA. *Journal of Sedimentary Research* 77: 139-158.
- Guerra, R., et al. (2015). Modern accumulation rates and sources of organic carbon in the NE Gulf of Cadiz (SW Iberian Peninsula). *Journal of Radioanalytical and Nuclear Chemistry* 305: 429-437.

- Hernes, P. J., B. A. Bergamaschi, R. S. Eckard and R. G. Spencer. 2009. Fluorescence-based proxies for lignin in freshwater dissolved organic matter. *Journal of Geophysical Research: Biogeosciences* 114.
- Hummel, R.L. 1996. Holocene Geologic History of the West Alabama Inner Continental Shelf, Alabama. Geological Survey of Alabama Bulletin 189, 131 p.
- Hwang, D. W., G. Kim, Y. W. Lee and H. S. Yang. 2005. Estimating submarine inputs of groundwater and nutrients to a coastal bay using radium isotopes. *Marine Chemistry* 96: 61-71.
- Johannes, R. E. 1980. The ecological significance of the submarine discharge of groundwater. *Marine Ecology Progress Series* 365-373.
- Kendall, C. (1998). Tracing nitrogen sources and cycling in catchments. In *Isotope tracers in catchment hydrology*, eds Kendall C., McDonnell J.J. 519-576.
- Kendall, C., E. M. Elliott and S. D. Wankel. 2007. Tracing anthropogenic inputs of nitrogen to ecosystems. *Stable isotopes in ecology and environmental science*, 375-449.
- Kim, G., and P. W. Swarzenski. 2010. Submarine groundwater discharge (SGD) and associated nutrient fluxes to the coastal ocean. In *Carbon and nutrient fluxes in continental margins*, EDS. Liu K., Atkinson L., Quiñones R., Talaue-McManus L. 529-538.
- Kohout F. A. 1966. Submarine springs: A neglected phenomenon of coastal hydrology. *Hydrology* 26: 391-413.
- Krantz, D. E., F. T. Manheim, J. F. Bratton and D. J. Phelan. 2004. Hydrogeologic setting and ground water flow beneath a section of Indian River Bay, Delaware. *Groundwater* 42: 1035-1051.
- Kroeger, K. D., P. W. Swarzenski, W. J. Greenwood and C. Reich. 2007. Submarine groundwater discharge to Tampa Bay: Nutrient fluxes and biogeochemistry of the coastal aquifer. *Marine Chemistry* 104: 85-97.
- Lamb, A. L., G. P. Wilson and M. J. Leng. 2006. A review of coastal palaeoclimate and relative sea-level reconstructions using $\delta^{13}\text{C}$ and C/N ratios in organic material. *Earth-Science Reviews* 75: 29-57.
- Lambert, W. J., P. Aharon and A. B. Rodriguez. 2008. Catastrophic hurricane history revealed by organic geochemical proxies in coastal lake sediments: a case study of Lake Shelby, Alabama (USA). *Journal of Paleolimnology* 39: 117-131.
- Lee, Y. W., D. W. Hwang, G. Kim, W. C. Lee and H. T. Oh. 2009. Nutrient inputs from submarine groundwater discharge (SGD) in Masan Bay, an embayment surrounded by heavily industrialized cities, Korea. *Science of the Total Environment* 407: 3181-3188.

- Liefer, J. D., H. L. MacIntyre, L. Novoveska, W. L. Smith and C. P. Dorsey. 2009. Temporal and spatial variability in *Pseudo-nitzschia* spp. in Alabama coastal waters: a hot spot linked to submarine groundwater discharge? *Harmful algae* 8: 706-714.
- Loesch, H. 1960. Sporadic mass shoreward migrations of demersal fish and crustaceans in Mobile Bay, Alabama. *Ecology* 41: 292-298.
- Lu, Y. H., J. W. Edmonds, Y. Yamashita, B. Zhou, A. Jaegge, and M. Baxley. 2015. Spatial variation in the origin and reactivity of dissolved organic matter in Oregon-Washington coastal waters. *Ocean Dynamics* 65:17-32.
- Macintyre, H. L., A. L. Stutes, W. L. Smith, C. P. Dorsey, A. Abraham and R. W. Dickey. 2011. Environmental correlates of community composition and toxicity during a bloom of *Pseudo-nitzschia* spp. in the northern Gulf of Mexico. *Journal of Plankton Research* 33: 273-295.
- Makings, U., I. R. Santos, D. T. Maher, L. Golsby-Smith and B. D. Eyre. 2014. Importance of budgets for estimating the input of groundwater-derived nutrients to an eutrophic tidal river and estuary. *Estuarine, Coastal and Shelf Science* 143: 65-76.
- Mariotti, A. (1983). Atmospheric nitrogen is a reliable standard for natural ¹⁵N abundance measurements. *Nature* 303: 685.
- May, E. B. 1973. Extensive oxygen depletion in Mobile Bay, Alabama. *Limnology and Oceanography* 18: 353-366.
- McCoy, C., R. Viso, R. N. Peterson, S. Libes, B. Lewis, J. Ledoux, G. Voulgaris, E. Smith and D. Sanger. 2011. Radon as an indicator of limited cross-shelf mixing of submarine groundwater discharge along an open ocean beach in the South Atlantic Bight during observed hypoxia. *Continental Shelf Research* 31: 1306-1317.
- Meyers, P. A. (1997). Organic geochemical proxies of paleoceanographic, paleolimnologic, and paleoclimatic processes. *Organic geochemistry* 27: 213-250.
- Michael, H. A., K. C. Scott, M. Koneshloo, X. Yu, M. R. Khan and K. Li. 2016. Geologic influence on groundwater salinity drives large seawater circulation through the continental shelf. *Geophysical Research Letters* 43.
- Moore, W. S. 1999. The subterranean estuary: a reaction zone of ground water and sea water. *Marine Chemistry*, 65: 111-125.
- Murgulet, D., and G. R. Tick. 2009. Assessing the extent and sources of nitrate contamination in the aquifer system of southern Baldwin County, Alabama. *Environmental Geology* 58: 1051-1065.

- Murgulet, D., and G. R. Tick. 2013. Understanding the sources and fate of nitrate in a highly developed aquifer system. *Journal of contaminant hydrology* 155: 69-81.
- Null, K. A., D. R. Corbett, D. J. DeMaster, J. M. Burkholder, C. J. Thomas and R. E. Reed. 2011. Porewater advection of ammonium into the Neuse river estuary, North Carolina, USA. *Estuarine, Coastal and Shelf Science* 95: 314-325.
- Null, K. A., N. T. Dimova, K. L. Knee, B. K. Esser, P. W. Swarzenski, M. J. Singleton, M. Stacey and A. Paytan. 2012. Submarine groundwater discharge-derived nutrient loads to San Francisco Bay: implications to future ecosystem changes. *Estuaries and Coasts* 35: 1299-1315.
- Perminova, I. V. and K. Hatfield. 2005. Remediation chemistry of humic substances: theory and implications for technology. In Use of humic substances to remediate polluted environments: from theory to practice, eds. Perminova, I. V., Hatfield K., Hertkorn N. 3-36.
- Reed P. C. 1971. Geologic map of Baldwin County, Alabama. Geological Survey of Alabama Special Map 94, p 55.
- Robertson, W. D. (1995). Development of steady-state phosphate concentrations in septic system plumes. *Journal of Contaminant Hydrology* 19: 289-305.
- Rodellas, V., J. García-Orellana, A. Tovar-Sánchez, G. Basterretxea, J. M. López-García, D. Sánchez-Quiles, E. García-Solsona and P. Masqué. 2014. Submarine groundwater discharge as a source of nutrients and trace metals in a Mediterranean bay (Palma Beach, Balearic Islands). *Marine Chemistry* 160: 56-66.
- Sadat-Noori, M., I. R. Santos, D. R. Tait and D. T. Maher. 2016. Fresh meteoric versus recirculated saline groundwater nutrient inputs into a subtropical estuary. *Science of the Total Environment* 566: 1440-1453.
- Santos, I. R. S., W. C. Burnett, J. Chanton, B. Mwashote, I. G. Suryaputra and T. Dittmar. 2008. Nutrient biogeochemistry in a Gulf of Mexico subterranean estuary and groundwater-derived fluxes to the coastal ocean. *Limnology and Oceanography* 53: 705-718.
- Santos, I. R., W. C. Burnett, J. Chanton, N. Dimova and R. N. Peterson. 2009. Land or ocean?: Assessing the driving forces of submarine groundwater discharge at a coastal site in the Gulf of Mexico. *Journal of Geophysical Research: Oceans* 114: 1-11.
- Schnurrenberger, D., J. Russell and K. Kelts 2003. Classification of lacustrine sediments based on sedimentary components. *Journal of Paleolimnology* 29: 141-154.
- Schroeder, W. W. and W. J. Wiseman Jr. 1988. The Mobile Bay estuary: Stratification, oxygen depletion, and jubilees. *Hydrodynamics of Estuaries. Vol II. Estuarine Case Studies*, 41-52.

- Schroeder, W. W., S. P. Dinnel and W. J. Wiseman. 1990. Salinity stratification in a river-dominated estuary. *Estuaries* 13: 145-154.
- Seitzinger, S. P., C. Kroeze, A. F. Bouwman, N. Caraco, F. Dentener and R. V. Styles. 2002. Global patterns of dissolved inorganic and particulate nitrogen inputs to coastal systems: Recent conditions and future projections. *Estuaries* 25: 640-655.
- Shang, P., Y. Lu, Y. Du, R. Jaffé, R. H. Findlay and A. Wynn. 2018. Climatic and watershed controls of dissolved organic matter variation in streams across a gradient of agricultural land use. *Science of The Total Environment* 612: 1442-1453.
- Slomp, C. P., and P. Van Cappellen. 2004. Nutrient inputs to the coastal ocean through submarine groundwater discharge: controls and potential impact. *Journal of Hydrology* 295: 64-86.
- Smith, C. G. and P. W. Swarzenski. 2012. An investigation of submarine groundwater-borne nutrient fluxes to the west Florida shelf and recurrent harmful algal blooms. *Limnology and oceanography* 57: 471-485.
- Osterman, L. E. and C. G. Smith. 2012. Over 100 years of environmental change recorded by foraminifers and sediments in Mobile Bay, Alabama, Gulf of Mexico, USA. *Estuarine, Coastal and Shelf Science* 115: 345-358.
- Smith, C. G., L. E. Osterman and R. Z. Poore. 2013. An examination of historical inorganic sedimentation and organic matter accumulation in several marsh types within the Mobile Bay and Mobile—Tensaw River Delta region. *Journal of Coastal Research* 63: 68-83.
- Smith, C. G. and L. E. Osterman. 2014. An evaluation of temporal changes in sediment accumulation and impacts on carbon burial in Mobile Bay, Alabama, USA. *Estuaries and coasts* 37: 1092-1106.
- Spiteri, C., C. P. Slomp, M. A. Charette, K. Tuncay and C. Meile. 2008. Flow and nutrient dynamics in a subterranean estuary (Waquoit Bay, MA, USA): field data and reactive transport modeling. *Geochimica et Cosmochimica Acta* 72: 3398-3412.
- Stanek, W. T. and Silc. 1977. Comparisons of four methods for determination of degree of peat humification (decomposition) with emphasis on the von Post method. *Canadian Journal of Soil Science* 57: 109-117.
- Stumpf, R. P., G. Gelfenbaum and J. R. Pennock. 1993. Wind and tidal forcing of a buoyant plume, Mobile Bay, Alabama. *Continental Shelf Research* 13: 1281-1301.
- Su, N., W. C. Burnett, H. L. MacIntyre, J. D. Liefer, R. N. Peterson and R. Viso. 2014. Natural radon and radium isotopes for assessing groundwater discharge into Little Lagoon, AL: Implications for harmful algal blooms. *Estuaries and Coasts* 37: 893-910.

- Turner, R., W. Schroeder and W. J. Wiseman. 1987. The role of stratification in the deoxygenation of Mobile Bay and adjacent shelf bottom waters. *Estuaries* 10: 13-19.
- Valiela, I., J. Costa, K. Foreman, J. M. Teal, B. Howes and D. Aubrey. 1990. Transport of groundwater-borne nutrients from watersheds and their effects on coastal waters. *Biogeochemistry* 10: 177-197.
- Walter G.R. and R. E. Kidd. 1979. Ground-water management techniques for the control of salt-water encroachment in Gulf Coast aquifers, a summary report. Geological Survey of Alabama Open-file Report, p 84.
- Ward, G. M., P. M. Harris and A. K. Ward. 2005. Gulf Coast rivers of the southeastern United States. *Rivers of North America*: 125-178.
- Weiskel, P. K., and B. L. Howes. 1992. Differential transport of sewage-derived nitrogen and phosphorus through a coastal watershed. *Environmental science & technology* 26: 352-360.
- Wheeler, K. I., D. F. Levia, and J. E. Hudson. 2017. Tracking senescence-induced patterns in leaf litter leachate using parallel factor analysis (PARAFAC) modeling and self-organizing maps. *Journal of Geophysical Research-Biogeosciences* 122: 2233-2250.
- Xu, B., W. Burnett, N. Dimova, S. Diao, T. Mi, X. Jiang and Z. Yu. 2013. Hydrodynamics in the Yellow River Estuary via radium isotopes: Ecological perspectives. *Continental Shelf Research* 66: 19-28.
- Xue, D., J. Botte, B. De Baets, F. Accoe, A. Nestler, P. Taylor, O. Van Cleemput, M. Berglund and P. Boeckx. 2009. Present limitations and future prospects of stable isotope methods for nitrate source identification in surface-and groundwater. *Water research* 43: 1159-1170.
- Yamaguchi, M., S. Itakura and T. Uchida. 2001. Nutrition and growth kinetics in nitrogen-or phosphorus-limited cultures of the 'novel red tide' dinoflagellate *Heterocapsa circularisquama* (Dinophyceae). *Phycologia* 40: 313-318.
- Yamashita, Y., R. Jaffé, N. Maie and E. Tanoue. 2008. Assessing the dynamics of dissolved organic matter (DOM) in coastal environments by excitation emission matrix fluorescence and parallel factor analysis (EEM-PARAFAC). *Limnology and Oceanography* 53: 1900-1908.
- Zanini, L., W. D. Robertson, C. J. Ptacek, S. L. Schiff and T. Mayer. 1998. Phosphorus characterization in sediments impacted by septic effluent at four sites in central Canada. *Journal of Contaminant Hydrology* 33: 405-429.

4.10 Appendix III

Table 1. Dissolved oxygen (DO), nitrate stable isotopes $\delta^{15}\text{N}$ - $\delta^{18}\text{O}$, nitrate (NO_3^-), ammonium (NH_4^+), dissolved organic nitrogen (DON), phosphate (PO_4^{3-}), N/P molar ratio, dissolved organic carbon (DOC), dissolved organic matter (DOM) component 1 (DOM-C1), component 2 (DOM-C2), and (DOM-C3) measured in Mobile Bay, Mobile-Tensaw River System, groundwater wells and piezometers during all sampling campaigns.

Date	Sample ID	Longitude	Latitude	DO (mg L^{-1})	$\delta^{15}\text{N}$ (AIR‰)	$\delta^{18}\text{O}$ (VSMOW‰)	NO_3^-	NH_4^+ (mmol m^{-3})	DON	PO_4^{3-}	N/P	DOC (g m^{-3})	DOM- C1	DOM- C2 (%)	DOM- C3
March 2015	S-1	-87.84328	30.37614	3.5	7.3	13.0	2.8	4.2	-	0.8	9	-	-	-	-
	S-2	-87.87306	30.38349	3.8	-	-	0.1	2.8	-	0.3	11	-	-	-	-
	S-3	-87.91313	30.43098	2.1	-	-	1.1	4.1	-	1.3	4	-	-	-	-
	S-4	-87.93006	30.49403	2.4	13.2	16.6	3.1	2.9	-	0.1	44	-	-	-	-
	S-5	-87.90449	30.55144	3.1	13.4	18.6	2.2	2.7	-	0.3	18	-	-	-	-
	S-6	-88.08128	30.55829	5.5	9.8	12.8	5.3	3.1	-	0.5	17	-	-	-	-
	S-7	-88.09216	30.51984	5.1	-	-	0.4	2.1	-	0.1	32	-	-	-	-
	S-8	-88.10060	30.49407	5.3	-	-	-	-	-	-	-	-	-	-	-
	S-9	-88.10475	30.44645	4.7	-	-	0.8	2.4	-	0.6	6	-	-	-	-
	S-10	-88.10332	30.44149	5.1	-	-	-	-	-	-	-	-	-	-	-
	S-11	-88.10099	30.42176	5.7	-	-	0.4	4.3	-	0.5	9	-	-	-	-
	S-12	-88.10169	30.40087	5.4	-	-	-	-	-	-	-	-	-	-	-
	S-13	-88.10223	30.39501	5.8	-	-	1.1	3.4	-	0.2	29	-	-	-	-
	TS-SE-R3	-87.87887	30.39188	1.7	-	-	0.2	21	-	0.1	350	-	-	-	-
	TS-W-R3	-88.10527	30.40376	4.8	-	-	0.7	11	-	0.1	280	-	-	-	-
	MR	-88.01071	30.68467	-	-	-	1.1	10	-	0.1	1100	-	-	-	-
	TR	-88.00559	30.68133	-	-	-	0.3	29	-	0.1	1500	-	-	-	-
July 2015	S-14	-88.10082	30.38729	3.1	-	-	0.5	17	26	0.1	180	-	-	-	-
	S-15	-88.10063	30.41235	3.5	-	-	0.5	7.5	26	0.2	38	-	-	-	-
	S-16	-88.10221	30.43576	3.7	15.7	34.3	0.5	20	14	0.1	230	-	-	-	-

	S-17	-88.10332	30.44149	3.4	11.1	36.1	0.7	6.8	68	0.1	75	-	-	-	-
	S-18	-88.08348	30.52646	4.1	-	-	0.4	5.0	27	0.3	22	-	-	-	-
	S-19	-87.85488	30.37703	1.7	13.6	35.3	1.0	3.8	28	0.3	15	-	-	-	-
	S-20	-87.87132	30.38527	1.5	-	-	0.3	5.8	24	0.6	11	-	-	-	-
	S-21	-87.89934	30.40281	1.9	17.0	32.7	1.1	11	26	0.3	42	-	-	-	-
	S-22	-87.91749	30.43925	1.1	-	-	0.1	14	14	0.3	46	-	-	-	-
	S-23	-87.93801	30.48410	1.2	-	-	0.4	4.3	38	0.9	5	-	-	-	-
	MR	-88.01071	30.68467	5.7	4.5	6.4	10	23	18	0.8	40	-	-	-	-
	TR	-88.00559	30.68133	6.8	4.4	5.4	13	3.1	56	0.3	48	-	-	-	-
	AR	-87.95435	30.67318	5.4	3.3	4.3	7.7	15	66	1.1	20	-	-	-	-
	SE-Well-1	-87.79257	30.40586	5.3	42.0	11.1	160	10	41	0.1	2200	-	-	-	-
	SE-Well-2	-87.88392	30.43140	6.1	38.5	10.0	71	4.2	91	0.1	750	-	-	-	-
March 2016	S-24	-88.10502	30.38330	5.1	8.9	11.8	3.6	0.5	5.2	0.1	35	-	-	-	-
	S-25	-88.10226	30.42125	4.2	8.2	13.8	3.7	0.6	9.1	0.1	28	-	-	-	-
	S-26	-88.09991	30.46609	4.7	10.0	14.6	4.1	4.0	18	0.2	22	-	-	-	-
	S-27	-88.10152	30.49469	5.4	6.8	9.5	6.9	2.3	17	0.2	37	-	-	-	-
	S-28	-87.87852	30.38507	3.2	7.0	8.2	22	1.5	6.0	0.2	150	-	-	-	-
	S-29	-87.91357	30.42801	4.1	8.1	12.5	8.3	1.9	24	0.2	43	-	-	-	-
	S-30	-87.91951	30.46050	4.2	7.1	8.7	-	-	-	-	-	-	-	-	-
	TS-SE-R3	-87.87887	30.39188	1.3	7.3	8.6	21	1.3	20	0.1	210	-	-	-	-
	TS-SE-R3	-87.91136	30.52604	2.4	7.5	7.5	13	3.3	24	0.7	21	-	-	-	-
	TS-W-R3	-88.10527	30.40376	4.1	-	-	20	9.0	28	0.1	330	-	-	-	-
	MR	-88.01071	30.68467	7.5	6.5	8.0	-	-	-	-	-	-	-	-	-
	TR	-88.00559	30.68133	8.6	5.9	7.9	12	3.8	30	0.2	58	-	-	-	-
	AR	-87.95435	30.67318	6.5	-	-	10	2.3	21	0.4	25	-	-	-	-
	SE-Well-1	-87.79257	30.40586	4.2	3.4	6.8	140	1.2	15	0.1	1200	-	-	-	-
	SE-Well-2	-87.88392	30.43140	5.4	3.4	6.1	30	0.1	0.2	0.1	330	-	-	-	-
	W-Well-1	-88.12211	30.46031	1.3	8.8	6.0	64	2.6	7.3	0.1	640	-	-	-	-

	W-Well-2	-88.12330	30.47109	1.2	8.5	7.2	100	2.5	6.0	0.1	1200	-	-	-	-
	W-Well-3	-88.10803	30.48300	1.1	4.1	5.8	120	1.1	16.2	0.2	800	-	-	-	-
April 2016	NE-Pz-1	-87.90843	30.53010	2.9	7.2	16	2.7	29	79	0.2	14	-	-	-	-
	NE-Pz-2	-87.90854	30.53015	2.8	3.8	0.4	25	16	120	0.4	63	-	-	-	-
	NE-Pz-3	-87.90855	30.53013	3.4	4.4	6.3	31	1.4	18	0.6	52	-	-	-	-
	NE-Pz-4	-87.90860	30.53016	3.2	8.9	7.4	61	2.2	33	1.0	64	-	-	-	-
	NE-Pz-5	87.90863	30.53017	3.9	12.8	21	2.5	0.6	13	0.2	13	-	-	-	-
June 2016	SE-Pz-1a	-87.87815	30.39243	0.6	4.0	41	1.3	540	650	0.1	10	-	-	-	-
	SE-Pz-1b	-87.87815	30.39243	0.7	9.6	32	0.6	290	300	0.1	6	-	-	-	-
	SE-Pz-2a	-87.87819	30.39237	0.7	20.1	17	1.4	100	120	0.1	17	-	-	-	-
	SE-Pz-2b	-87.87819	30.39237	0.8	19.0	16	3.2	7.0	240	0.2	18	-	-	-	-
	SE-Pz-3a	-87.87818	30.39236	0.2	-	-	4.3	62	98	0.1	120	-	-	-	-
	SE-Pz-3b	-87.87818	30.39236	0.4	8.9	14	1.3	110	140	0.1	18	-	-	-	-
	SE-Pz-4	-87.87823	30.39231	0.8	15.7	34	1.3	44	70	0.1	13	-	-	-	-
	SE-Pz-5	-87.87827	30.39228	4.1	10.3	25	0.9	44	73	0.2	6	-	-	-	-
	TS-SE-R1	-87.87841	30.39241	0.7	16.8	31	0.8	0.1	20	0.1	7	-	-	-	-
	TS-SE-R2	-87.87858	30.39221	0.9	12.4	31	0.4	0.1	30	0.3	1	-	-	-	-
	TS-SE-R3	-87.87887	30.39188	1.4	-	-	12	1.8	23	0.2	54	-	-	-	-
	W-Pz-1	-88.10646	30.40353	0.9	8.7	33.1	2.7	3.6	25	0.1	25	-	-	-	-
	W-Pz-2	-88.10632	30.40352	1.9	12.7	17.9	11	9.6	46	0.1	96	-	-	-	-
	W-Pz-3	-88.10632	30.40352	0.8	0.5	53.8	19	4.7	38	0.1	320	-	-	-	-
	W-Pz-4	-88.10629	30.40351	1.4	7.0	8.9	6.1	4.2	3.5	0.1	100	-	-	-	-
	W-Pz-5	-88.10625	30.40350	2.7	9.4	27.8	-	-	-	-	-	-	-	-	-
	TS-W-R1	-88.10606	30.40380	4.0	6.9	21.8	0.7	0.1	17	0.2	4	-	-	-	-
	TS-W-R2	-88.10573	30.40377	6.1	12.7	31.0	0.7	0.1	23	0.1	7	-	-	-	-
	TS-W-R3	-88.10527	30.40375	8.7	15.3	31.6	0.1	0.1	21	0.2	0.5	-	-	-	-
	MR	-88.01071	30.68467	6.8	4.8	7.4	4.7	0.1	30	1.9	3.0	-	-	-	-

	TR	-88.00559	30.68133	10.3	7.4	7.2	10	1.1	13	1.3	10	-	-	-	-
	AR	-87.95435	30.67318	8.1	-	-	8.0	0.4	27	0.8	16	-	-	-	-
	SE-Well-1	-87.79257	30.40586	7.1	-	-	82	3.3	22	0.2	440	-	-	-	-
	SE-Well-2	-87.88392	30.43140	5.4	-	-	160	5.6	21	0.1	3400	-	-	-	-
	NE-Pz-1a	-87.90843	30.53010	1.3	9.6	35.6	3.8	26	35	0.1	59	-	-	-	-
	NE-Pz-1b	-87.90843	30.53010	1.4	2.4	11.4	7.9	3.9	14	0.6	14	-	-	-	-
	NE-Pz-2	-87.90854	30.53015	0.7	2.3	15.0	2.5	3.2	11	0.7	4	-	-	-	-
	NE-Pz-3a	-87.90855	30.53013	0.6	6.5	17.8	0.3	4.7	16	0.5	1	-	-	-	-
	NE-Pz-3b	-87.90855	30.53013	0.8	6.7	19.9	0.6	4.7	18	0.7	1	-	-	-	-
	NE-Pz-4	-87.90860	30.53016	4.1	8.1	3.5	8.4	0.2	17	0.5	16	-	-	-	-
	NE-Pz-5	-87.90863	30.53017	4.5	8.3	4.9	8.1	0.1	15	0.6	13	-	-	-	-
	TS-NE-R1	-87.91106	30.52579	0.5	-	-	0.6	0.1	23	0.2	2	-	-	-	-
	TS-NE-R3	-87.91136	30.52604	0.6	-	-	0.1	0.1	20	0.2	0.5	-	-	-	-
	TR	-88.00559	30.68133	7.8	4.2	4.9	16	4.1	21	0.6	31	-	-	-	-
	AR	-87.95435	30.67318	7.6	0.8	1.5	12	1.7	16	0.6	22	-	-	-	-
December 2016	SE-Pz-1a	-87.87815	30.39243	0.2	10.3	33.5	0.1	480	26	0.4	1300	-	-	-	-
	SE-Pz-1b	-87.87815	30.39243	0.4	-	-	0.1	310	66	0.3	1000	-	-	-	-
	SE-Pz-2a	-87.87819	30.39237	0.5	1.3	15.6	0.6	200	69	1.3	160	-	-	-	-
	SE-Pz-2b	-87.87819	30.39237	0.6	-	-	0.3	100	58	1.8	57	-	-	-	-
	SE-Pz-3a	-87.87818	30.39236	0.3	8.2	19.0	0.1	220	36	0.3	720	-	-	-	-
	SE-Pz-3b	-87.87818	30.39236	0.4	-	-	0.3	110	69	0.8	130	-	-	-	-
	SE-Pz-4a	-87.87823	30.39231	1.6	9.9	6.4	1.4	46	44	1.2	41	-	-	-	-
	SE-Pz-4b	-87.87823	30.39231	1.0	-	-	0.1	34	35	1.4	25	-	-	-	-
	SE-Pz-5a	-87.87823	30.39231	1.2	7.9	25.6	0.1	170	76	1.1	150	-	-	-	-
	SE-Pz-5b	-87.87827	30.39228	1.3	-	-	0.1	170	58	2.0	86	-	-	-	-
	TS-E-Sea	-87.87827	30.39226	7.7	7.5	19.9	0.1	7.5	21	0.8	9	-	-	-	-
	SE-Well-2	-87.88392	30.43140	7.1	4.2	5.4	59	0.0	200	0.2	310	-	-	-	-
	W-Pz-1a	-88.10646	30.40353	3.0	3.7	35.4	0.3	3.4	21	0.3	13	-	-	-	-

	W-Pz-1b	-88.10646	30.40353	3.2	-	-	1.1	4.1	28	0.2	36	-	-	-	-
	W-Pz-2a	-88.10631	30.40352	3.0	-	-	-	-	-	-	-	-	-	-	-
	W-Pz-2b	-88.10631	30.40352	3.2	-	-	-	-	-	-	-	-	-	-	-
	W-Pz-3a	-88.10629	30.40351	2.8	7.1	29.0	1.4	0.1	7.0	0.2	10	-	-	-	-
	W-Pz-3b	-88.10629	30.40351	2.7	-	-	1.3	3.2	3.7	0.2	28	-	-	-	-
	W-Pz-4a	-88.10625	30.40351	3.5	4.5	10.9	0.7	2.4	26	0.2	14	-	-	-	-
	W-Pz-4b	-88.10625	30.40351	3.7	-	-	21	3.8	88	0.5	49	-	-	-	-
	W-Pz-5a	-88.10623	30.40351	3.9	-	-	-	-	-	-	-	-	-	-	-
	W-Pz-5b	-88.10623	30.40351	2.8	-	-	-	-	-	-	-	-	-	-	-
	TS-W-Sea	-88.10619	30.40350	8.0	10.4	24.8	0.2	2.6	7.5	0.5	6	-	-	-	-
	MR	-88.01071	30.68467	5.9	3.1	4.3	2.7	0.1	33	0.7	4	-	-	-	-
	TR	-88.00559	30.68133	7.1	3.7	3.7	5.0	0.1	43	1.4	4	-	-	-	-
	AR	-87.95435	30.67318	7.7	7.5	10.2	0.8	3.1	26	0.9	5	-	-	-	-
March 2017	S-31	-88.05538	30.59405	5.4	10.6	11.5	5.3	1.1	21	0.3	21	4.2	30	44	26
	S-32	-88.05687	30.62115	5.8	8.6	7.5	8.6	3.9	20	0.6	22	3.4	34	35	31
	S-33	-88.01750	30.65843	6.5	8.6	8.9	6.2	1.2	20	1.0	8	4.5	28	23	49
	S-34	-87.96182	30.65287	7.1	8.4	8.4	11	0.4	24	0.9	12	4.5	36	42	22
	S-35	-88.05711	30.56466	6.2	9.0	8.9	13	2.1	26	0.6	25	2.8	15	24	61
	S-36	-88.02453	30.56527	5.7	7.7	7.7	10	2.2	0.1	0.7	20	-	-	-	-
	S-37	-87.99126	30.56479	5.4	8.9	9.0	13	1.3	25	0.5	28	4.6	35	46	18
	S-38	-87.95009	30.56048	6.7	9.5	9.6	7.1	0.1	20	0.4	21	3.6	12	18	69
	S-39	-87.95414	30.56881	5.1	10.5	11.4	6.6	0.1	23	0.4	20	4.0	26	35	39
	S-40	-88.02212	30.60659	4.7	8.4	8.6	7.2	1.1	30	0.5	19	3.9	34	45	21
	S-41	-88.05722	30.24987	7.4	22.8	29.1	3.5	0.1	23	0.3	11	-	-	-	-
	S-42	-88.03319	30.24594	8.1	25.0	31.3	0.9	0.8	21	0.3	6	3.7	30	40	30
	S-43	-87.91487	30.57848	5.4	14.0	15.9	3.4	0.1	24	0.3	13	3.5	29	41	30
	S-44	-87.91509	30.60275	6.9	9.0	8.8	11	0.6	28	0.4	29	5.2	33	43	24
	S-45	-87.92152	30.62343	5.3	8.8	8.0	14	0.3	32	0.6	25	5.5	37	41	23

S-46	-87.99826	30.62905	5.7	-	-	-	-	-	-	-	-	-	-	-	-
S-47	-87.94899	30.52249	6.5	-	-	-	-	-	-	-	-	-	-	-	-
S-48	-87.98315	30.53314	6.0	-	-	-	-	-	-	-	-	-	-	-	-
S-49	-88.02727	30.54792	7.1	-	-	-	-	-	-	-	-	-	-	-	-
S-50	-88.06469	30.56019	6.2	-	-	-	-	-	-	-	-	-	-	-	-
NE-Pz-1	-87.90843	30.53010	1.0	4.4	19.4	1.7	15	16	0.1	130	0.5	10	2	88	
NE-Pz-2	-87.90854	30.53015	1.7	4.3	3.9	31	4.6	18	0.2	240	1.3	10	2	88	
NE-Pz-3	-87.90855	30.53013	2.5	5.1	3.2	50	0.9	18	0.3	160	0.8	11	0	89	
NE-Pz-4	-87.90860	30.53016	3.2	6.6	4.3	28	1.9	26	0.3	97	3.4	11	0	89	
NE-Pz-5	87.90863	30.53017	2.3	6.2	6.8	18	2.4	12	0.3	74	1.1	10	0	90	
SE-Pz-1	-87.87815	30.39243	0.8	15.3	30.2	1.0	56	0.0	0.9	63	1.8	10	0	90	
SE-Pz-2	-87.87819	30.39237	0.9	5.4	24.1	0.3	160	75	0.2	910	10.8	10	0	90	
SE-Pz-3	-87.87818	30.39236	0.6	9.1	19.2	0.3	150	89	0.2	730	14.6	10	0	90	
SE-Pz-4	-87.87823	30.39231	0.6	11.2	23.7	0.7	59	74	0.3	220	23.4	11	1	88	
SE-Pz-5	-87.87827	30.39228	0.9	9.0	4.7	75	95	99	0.7	230	10.3	11	1	88	
W-Pz-1	-88.10646	30.40353	1.5	6.4	6.5	1.1	0.4	7.5	0.2	10	2.3	11	0	89	
W-Pz-3	-88.10625	30.40351	2.1	12.2	31.0	2.4	4.4	21	0.2	35	1.5	11	0	89	
W-Pz-5	-88.10623	30.40351	4.1	12.9	19.7	5.2	3.8	17	0.2	58	1.0	11	0	89	
MR	-88.01071	30.68467	5.6	8.5	6.9	15	1.4	31	1.8	9	6.1	28	43	29	
BR	-87.92734	30.66650	6.2	8.8	7.4	10	0.4	30	0.7	16	5.3	28	45	27	
July 2017															
S-51	-87.85198	30.24455	3.6	-	-	0.9	0.5	41	0.2	7	6.6	30	44	26	
S-52	-87.79181	30.25622	3.8	-	-	0.7	0.1	32	0.1	7	-	-	-	-	
S-53	-87.75262	30.28377	4.6	-	-	0.7	0.2	31	0.1	7	6.2	35	36	30	
S-54	-87.77329	30.26144	3.2	14.1	27.8	0.7	0.3	26	0.2	5	5.9	32	43	26	
S-55	-87.76827	30.30386	3.3	16.2	32.1	0.8	0.7	36	0.2	7	-	42	42	16	
S-56	-87.80235	30.32724	3.8	14.0	35.3	0.8	0.3	42	0.2	5	6.0	37	44	20	
S-57	-87.82057	30.34272	5.1	12.7	29.5	0.8	0.4	39	0.2	7	-	-	-	-	
S-58	-87.87329	30.34164	3.1	26.4	31.2	0.6	0.6	29	0.1	11	-	-	-	-	

S-59	-87.90930	30.34115	2.7	22.3	31.3	1.8	0.3	33	0.2	10	4.8	30	39	30
S-60	-88.00410	30.33785	4.5	15.2	17.6	3.5	0.5	29	0.1	43	7.2	31	41	28
S-61	-88.01090	30.59418	4.7	7.1	6.0	12	0.9	31	0.6	23	7.1	32	41	28
S-62	-87.95299	30.61587	3.1	6.6	4.9	13	1.2	30	0.6	24	6.1	31	43	27
S-63	-87.92827	30.62521	3.8	6.6	4.6	14	1.3	29	0.6	26	5.7	35	43	22
S-64	-87.91608	30.59560	3.5	26.4	33.2	1.5	0.2	34	1.0	2	6.1	30	39	31
S-65	-87.90781	30.57037	2.1	13.7	13.2	4.8	0.3	32	0.6	9	6.7	39	46	15
S-66	-87.99113	30.53048	3.4	27.8	32.8	1.4	0.3	34	0.9	2	6.6	38	41	22
TS-SE-R1	-87.87841	30.39241	1.7	-	-	13	0.5	25	1.0	14	5.4	8	0	92
TS-SE-R2	-87.87858	30.39221	1.5	-	-	5.2	0.9	31	1.3	5	6.9	8	0	91
TS-SE-R3	-87.87887	30.39188	3.1	-	-	4.1	0.9	25	1.1	5	5.9	7	0	93
TS-SE-Sea	-87.87827	30.39226	4.5	26.0	32.9	0.6	0.8	36	0.6	3	7.0	7	0	93
TS-NE-R1	-87.91106	30.52579	3.5	6.1	17.0	6.2	2.0	51	1.5	6	31.2	20	35	44
TS-NE-R2	-87.91120	30.52587	2.9	-	-	-	-	-	-	-	-	-	-	-
TS-NE-R3	-87.91136	30.52604	3.1	-	-	-	-	-	-	-	-	-	-	-
SE-Pz-1	-87.87815	30.39243	0.7	11.7	21.3	0.7	120	98	0.1	1800	0.8	8	0	92
SE-Pz-2	-87.87819	30.39237	0.8	10.5	3.0	20	9.4	45	0.4	71	9.8	6	10	84
SE-Pz-3	-87.87818	30.39236	0.7	16.7	28.4	1.1	82	63	1.4	59	19.1	8	0	92
SE-Pz-4.5-a	-87.87825	30.39229	0.6	7.7	-1.7	82	54	33	0.6	240	6.2	36	45	20
SE-Pz-4.5-b	-87.87825	30.39229	-	7.7	-2.4	64	4.5	32	2.7	25	6.7	32	47	21
SE-Pz-4.5-c	-87.87825	30.39229	-	11.4	1.1	20	3.5	41	0.9	26	7.5	39	47	14
SE-Pz-4.5-d	-87.87825	30.39229	-	17.3	12.3	3.3	120	57	2.3	53	10.9	38	45	16
SE-Pz-4.5-e	-87.87825	30.39229	-	17.0	14.7	2.8	92	60	1.8	52	10.6	10	38	52
SE-Pz-4.5-f	-87.87825	30.39229	-	11.0	14.7	2.3	52	92	0.6	100	14.2	20	36	44
SE-Well-2	-87.88392	30.43140	-	3.8	5.4	156	0.8	83	0.1	1400	-	-	-	-
W-Pz-1	-88.10646	30.40353	-	3.1	19.5	0.9	0.7	18	0.1	12	2.7	11	0	89
NE-Pz-1	-87.90843	30.53010	-	9.3	5.0	78	0.5	10	0.2	340	-	-	-	-
NE-Pz-5	87.90863	30.53017	-	16.4	28.5	3.1	17	13	0.1	170	-	-	-	-
MR	-88.01071	30.68467	5.7	4.1	4.1	9.3	1.2	33	0.5	20	8.0	22	39	39

TR	-88.00559	30.68133	7.8	4.0	4.1	11	1.5	32	0.6	24	7.2	22	38	40
BR	-87.92734	30.66650	6.1	6.5	3.6	7.6	0.8	30	0.4	21	7.8	32	38	30

Figure 1. Spatial distribution of dissolved oxygen (DO) measured in Mobile Bay showing values from all surveys conducted during the dry season and wet seasons. The average DO concentration in Mobile Bay was $4.1 \pm 1.4 \text{ mg L}^{-1}$. The highest DO values in Mobile Bay were measured near the river delta and Main Pass with concentrations of $6\text{--}8 \text{ mg L}^{-1}$, whereas along the eastern shore DO was always below 2 mg L^{-1} .

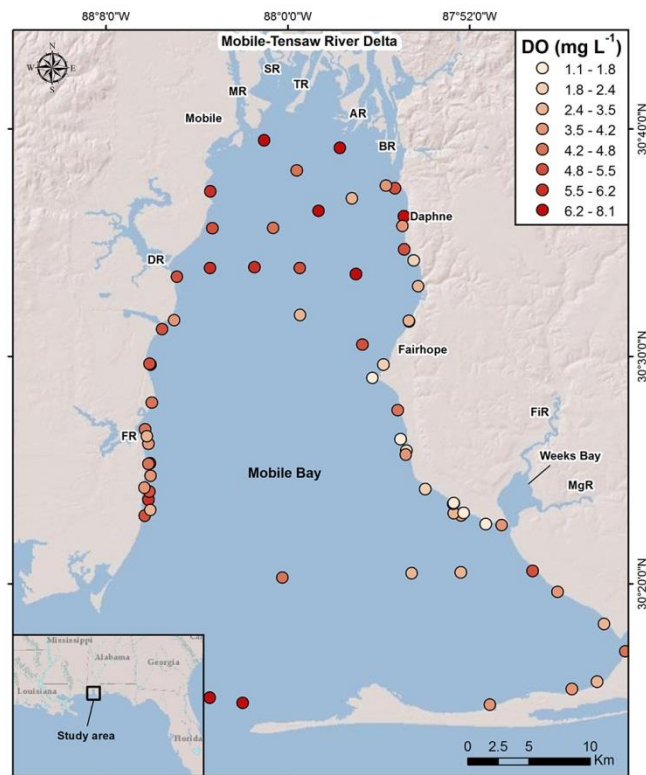
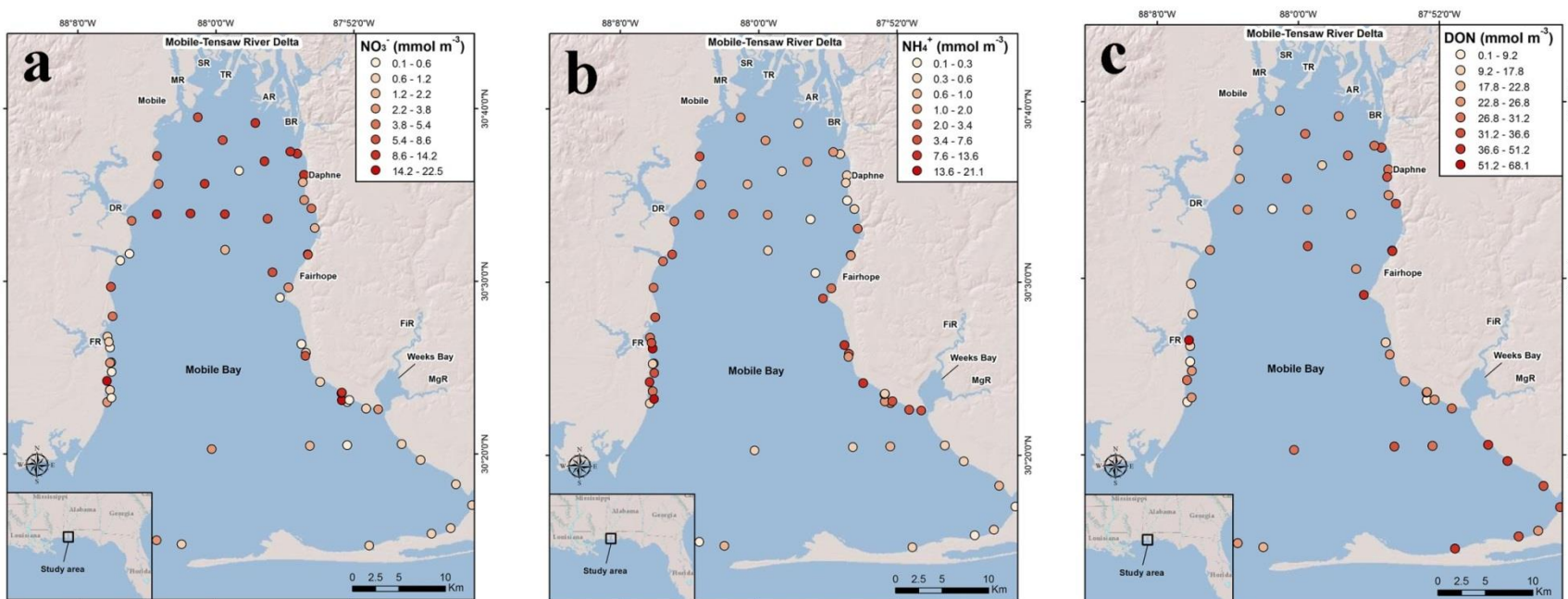


Figure 2. NO_3^- (a), NH_4^+ (b), DON (c), PO_4^{3-} (d) concentrations, and N/P molar ratio (e) measured in Mobile Bay during all sampling campaigns. NO_3^- , DON, and PO_4^{3-} concentrations in Mobile Bay were highest along the northeastern shore and near the river delta, while NH_4^+ was highest in the southeastern shore. The highest N/P ratios in Mobile Bay were found along the western and southeastern shores.



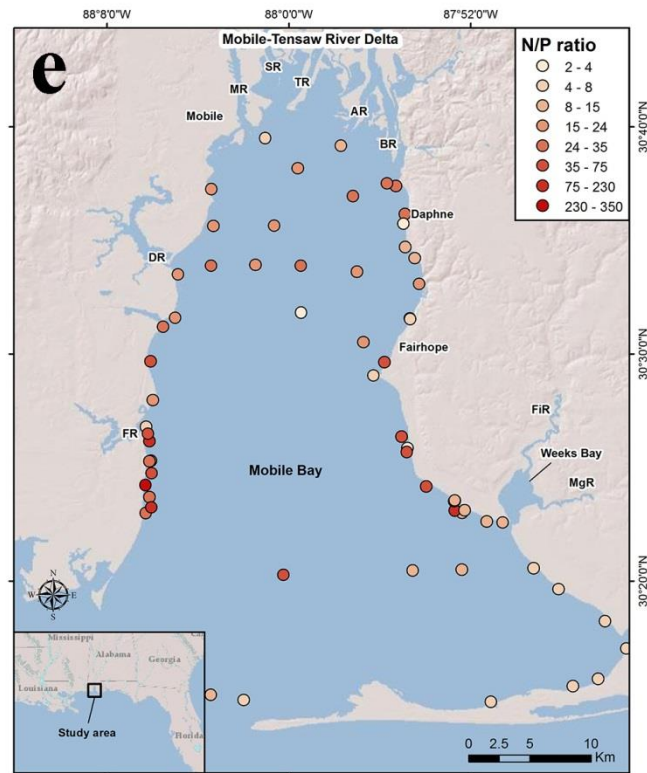
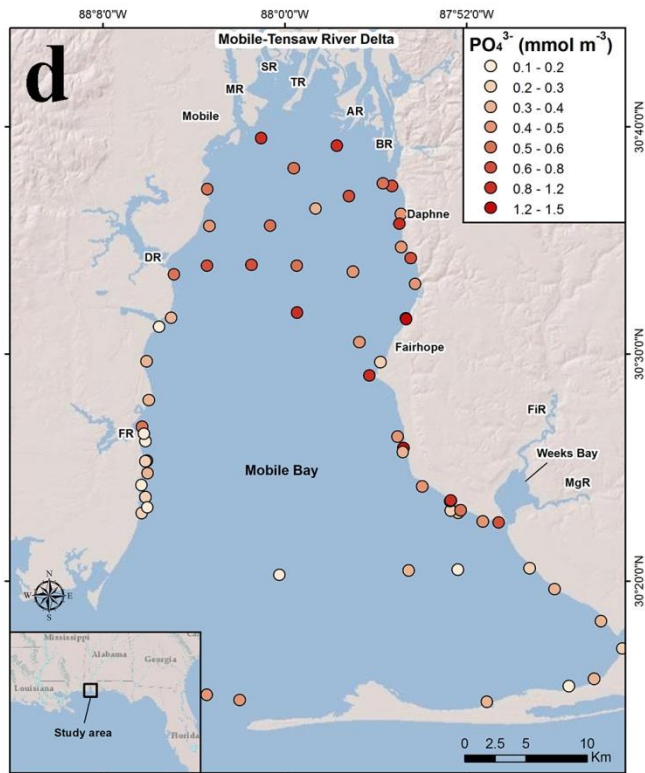


Figure 3. Nitrate stable isotopes $\delta^{15}\text{N}$ (a) and $\delta^{18}\text{O}$ (b) values measured in Mobile Bay during all sampling campaigns. Both isotopes were the highest in the southern sector of the bay in Bon Secour Bay (16-27‰) and were lower near the river delta (4-11‰).

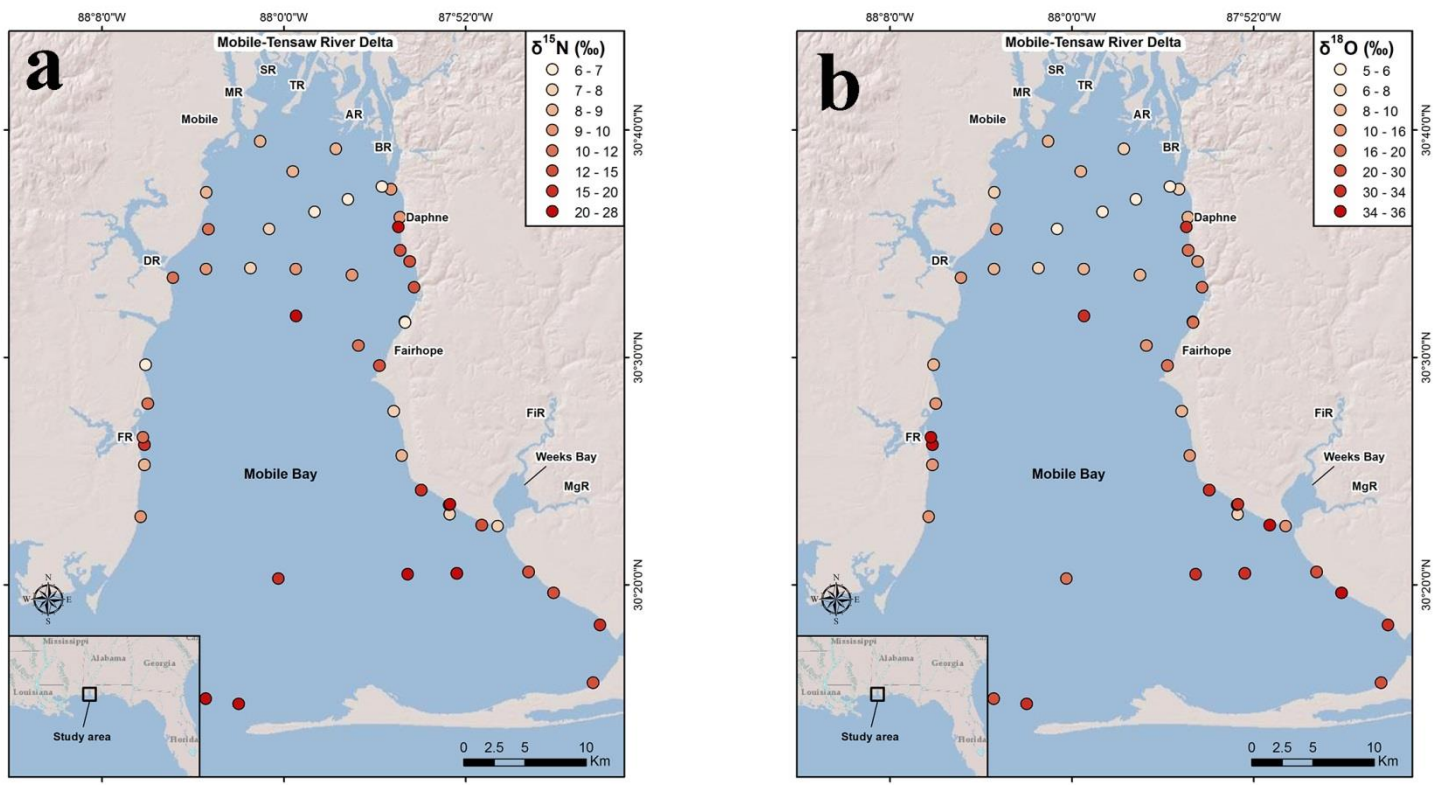


Figure 4. Dissolved organic carbon (DOC) concentration in Mobile Bay measured during the 2017 sampling campaigns. DOC was on average $6.2 \pm 3.8 \text{ mg L}^{-1}$, being highest along the eastern shore and Bon Secour Bay ($6.5\text{-}15 \text{ mg L}^{-1}$).

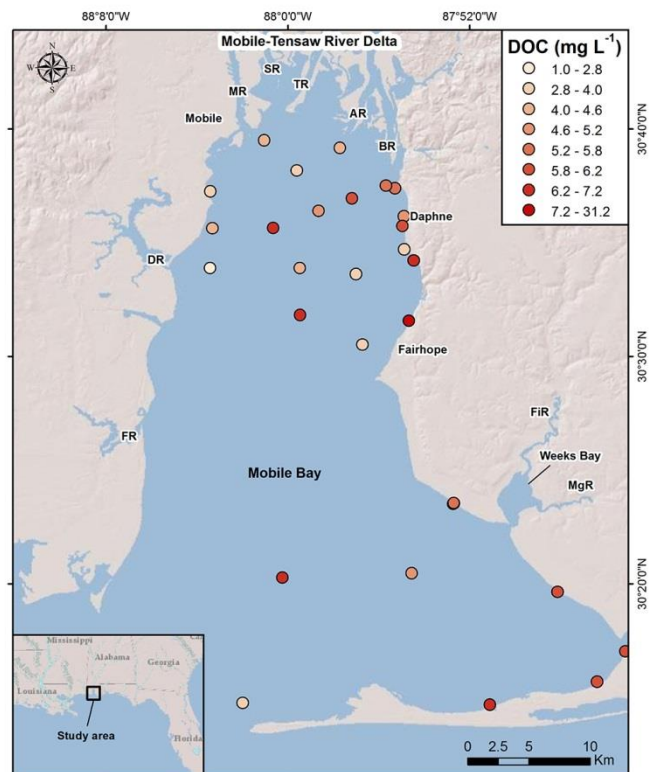
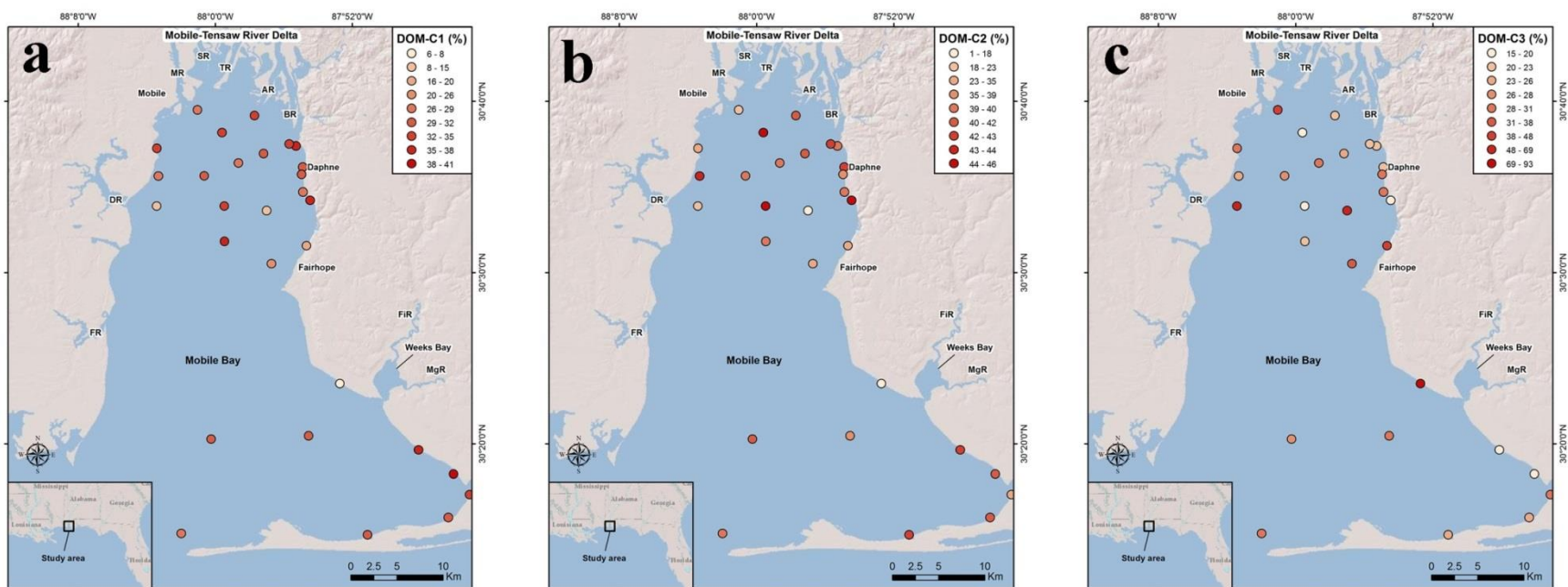


Figure 5. DOM components 1 (a), 2 (b), and 3 (c) were similarly present in Mobile Bay during all sampling campaigns ($28 \pm 6\%$ (C1), $34 \pm 7\%$ (C2), and $38 \pm 12\%$ (C3)). Components 1 and 2 were higher near the river delta and in Bon Secour Bay (26-46%), while component 3 was highest in the mid-bay area and on the southeastern shore (35-65%).



CHAPTER 5: CONCLUSIONS

In this dissertation, I used a wide variety of techniques to investigate SGD and the associated nutrient inputs in two study areas with contrasting hydrogeological settings, an estuary overlain by a sandy coastal aquifer (Mobile Bay, Alabama), and a karst coastal system (Maro-Cerro Gordo in southern Spain). I demonstrated that SGD was an essential part of the water budget of Maro-Cerro Gordo, where the SGD-delivered nutrient inputs could be causing significant damage to the protected marine ecosystem. In Mobile Bay, I demonstrated that although SGD is not significant for the water budget of the bay, delivered nutrients are a significant portion of the nutrient budget, specifically in areas impacted by *Jubilees* and harmful algal blooms (Loesch, 1960; May, 1973; Turner et al., 1987; Schroeder and Wiseman, 1988; Liefer et al., 2009; McIntyre et al., 2011).

In Chapter 2, I showed how the assessment of groundwater discharge to the sea in coastal karst aquifers is highly complicated, using the example of Sierra Almirajara-Alberquillas Aquifer in the Maro-Cerro Gordo coastal area. Groundwater discharge occurred in four different forms as subaerial groundwater-fed creeks, coastal springs, via submerged groundwater seepage through the seabed sediments, and submarine springs. I demonstrated that only a specific set of methods targeting each form of discharge should be applied to assess adequately and inclusively the total groundwater discharge to the sea. Radon-222 surveys and time-series deployments best detected diffuse groundwater seepage through seabed sediments along the shoreline. In contrast, submarine springs discharge was reliably detected by salinity anomalies along the coastline and

confirmed by ^{224}Ra measurements and direct observations via SCUBA diving. Subaerial coastal springs and groundwater-fed creeks were successfully identified using salinity and ^{224}Ra anomalies in coastal waters and quantified using flowmeter measurements. The complexity of the Sierra Almirajara-Alberquillas coastal karst aquifer was such that understanding the water origin at each point of groundwater discharge required the use of hydrochemistry (SO_4^{2-} and NO_3^-) and water stable isotopes ($\delta^2\text{H}$ and $\delta^{18}\text{O}$). Similarly to the Maro-Cerro Gordo coastal area, all these forms of groundwater discharge are expected to be present in other coastal aquifers with similar characteristics (e.g. karst and even volcanic aquifers) worldwide (e.g., Fleury et al., 2007; Katz et al., 2009; García-Solsona et al., 2010; Knee et al., 2010; Tovar-Sánchez et al., 2014). Thus, I conclude that the multi-method approach presented in this dissertation chapter can be applied in the numerous coastal karst areas worldwide to assess the groundwater discharge to the sea and associated nutrients fluxes (e.g. Fleury et al., 2007; Burnett et al., 2008; Dimova et al., 2012; Gonneea et al., 2014; Null et al., 2014).

In Chapter 3, I demonstrated that hydrogeological heterogeneities in the shallow sediments, typical in estuaries, largely controlled the permeability and residence time of groundwater in the coastal aquifer and was thus, the main control of SGD and SGD-delivered nutrient fluxes to Mobile Bay. In this study I showed that SGD accounts for only 0.2% of the water budget during the wet season, but is up to 5% during the dry season (Fig. 3.7). The magnitude of SGD did not vary significantly throughout the year; it was 36% higher during the wet season. In contrast, the discharge from the Mobile-Tensaw River System varied significantly and it was two orders of magnitude higher during the wet season compared to the dry season. Coincidentally, I found that SGD has larger contribution to the nutrient budget of the bay during the time when *Jubilees* and HABs occur. Furthermore, I observed that up to 80% of the total

SGD takes place preferentially on the east shore of Mobile Bay, again coinciding precisely with the most frequent areas of *Jubilee* events (Fig 3.2). The combination of a high hydraulic gradient in the Miocene-Pliocene Aquifer and the presence of permeable sand deposits in the intertidal zone of the east shore facilitated the maximum SGD inputs measured in the bay (Fig. 3.1 and Fig. 3.5b and 3.5c). However, a silt layer with very low permeability in the intertidal zone of the western shore and a much lower hydraulic gradient, derived in the lowest SGD rates of Mobile Bay (Fig. 3.1 and Fig. 3.5a). I determined that SGD was mainly driven by marine forcing, i.e., tidal pumping, during base-flow conditions in all areas of Mobile Bay. In comparison, during high flow conditions tidal pumping also controlled SGD on the western shore, while the terrestrially-driven hydraulic gradient of the coastal aquifer was the primary control driver of SGD on the east shore (Fig. 3.6).

In Chapter 4, I showed how the shallow coastal sediments are the primary source of nutrients to Mobile Bay via SGD. The dominant forms of nitrogen delivered by SGD were NH_4^+ and DON, which I found to be a product of organic matter mineralization of a naturally existing peat layer in the shallow aquifer. After constructing the nutrient (NO_3^- , NH_4^+ , DON, and PO_4^{3-}) budgets of Mobile Bay, I found that similarly to the water budget, SGD only represented a small portion (less than 3%) of the nutrient budgets during the wet season (Table 4.2). However, during the dry season, when *Jubilees* and HABs occur, SGD supplied as much as 56% and 17% of the total NH_4^+ and DON inputs in the bay respectively. Considering the total nutrient budgets, SGD accounted for 23% of the total nitrogen delivery and 5% of the phosphate budget. The majority (93%) of these nutrient inputs occur on the east shore of the bay, also coinciding with the area impacted by *Jubilees* (Table 4.2). The total nitrogen budget of nitrogen revealed that the coastal sediments of Mobile Bay are a sink for the high NO_3^- loading as groundwater flowed

through the intertidal zone, transforming NO_3^- into NH_4^+ and DON, and producing additional nitrogen only on the east shore ($21 \text{ mmol m}^{-2} \text{ d}^{-1}$) (Fig 4.8). This net production of nitrogen is generated by the peat layer that was identified during this study only on the east shore, explaining the difference with the western shore (Figs. 4.2 and 4.3). The observed inputs of reduced forms of nitrogen (NH_4^+ and DON) to the water column on the east shore can have a significant effect on the hypoxia that causes *Jubilees* events on this shore during the dry season (Loesch, 1960; May, 1973; Turner et al., 1987; Schroeder and Wiseman, 1988). Furthermore, I suggest that SGD might also be responsible for the nitrogen/phosphorous disequilibrium observed in areas affected by HABs, probably affecting their occurrence (Liefer et al., 2009; McIntyre et al., 2011; Liefer et al., 2014).

In Chapters 3 and 4 I demonstrated that the lithological heterogeneities of the shallow unconsolidated sedimentary coastal aquifer played a critical role for the importance of SGD for the water and nutrient budgets of Mobile Bay. Similar lithological settings should be expected in other large estuaries worldwide, especially in the Northern Gulf of Mexico. However, the shallow sediment heterogeneities are often overlooked.

Comparing the magnitude and spatial distribution of SGD in the coastal karst system of Maro-Cerro Gordo with the Mobile Bay Estuary, major differences in their driving mechanisms can be identified. In Maro-Cerro Gordo, SGD was primarily driven by the terrestrial force of a hydraulic gradient in the karst aquifer as high as 6% (Fig. 2.1). In Mobile Bay the spatial variation of SGD rates was controlled primarily by the marine-driven tidal pumping and, to a lower extent, by a terrestrially-driven hydraulic gradient of 0.2% on the east shore (Fig. 3.1). At the beach face of Cantarrijan Beach (Maro-Cerro Gordo) I also observed seawater recirculation;

however, was much less pronounced and driven mostly by the annual sea level fluctuation (Fig. 2.2).

The most significant difference between Maro-Cerro Gordo and Mobile Bay was in the magnitude and form of SGD-derived nutrient fluxes at each location. The fast and turbulent groundwater flow in the karst system results in highly oxic conditions, where the primary form of nitrogen was NO_3^- . In the SGD area of Maro Cliff I found the highest fluxes of NO_3^- via SGD as a point-source discharge ($44\text{-}61 \text{ mmol m}^{-2} \text{ d}^{-1}$) originated from agricultural activities located (Fig. 2.2, Table 2.4). In contrast, in the intertidal zone of Mobile Bay, organic matter degradation resulted in groundwater anoxic conditions, important nutrient biogeochemical transformations, and a relatively slower groundwater flow compared to Maro-Cerro Gordo. The anoxic conditions at the intertidal zone are the main reason for the high NH_4^+ and DON concentrations in SGD, where the SGD-derived nitrogen fluxes were $21 \text{ mmol m}^{-2} \text{ d}^{-1}$ (Fig. 8). However, although these specific nitrogen fluxes are relatively lower than in Maro-Cerro Gordo, they occurred along a much greater area, resulting in higher nitrogen fluxes in Mobile Bay (Figs. 2.1 and 4.1). In comparison, in Mobile Bay, a river-dominated estuary, about 75% of the nitrogen inputs are delivered by the Mobile-Tensaw River System; whereas in Maro-Cerro Gordo, a coastal karst area with nearly null runoff, 99% of the nitrogen inputs to the sea were derived from groundwater discharge (Tables 2.4 and 4.2).

References

- Burnett, W. C., R. Peterson, W. S. Moore and J. de Oliveira. 2008. Radon and radium isotopes as tracers of submarine groundwater discharge—results from the Ubatuba, Brazil SGD assessment intercomparison. *Estuarine, Coastal and Shelf Science* 76: 501-511.
- Dimova, N. T., P. W. Swarzenski, H. Dulaiova and C. R. Glenn. 2012. Utilizing multichannel electrical resistivity methods to examine the dynamics of the fresh water–seawater interface in two Hawaiian groundwater systems. *Journal of Geophysical Research: Oceans* 117: 1-12.
- Fleury, P., M. Bakalowicz and G. de Marsily. 2007. Submarine springs and coastal karst aquifers: a review. *Journal of Hydrology* 339: 79-92.
- García-Solsona, E., J. García-Orellana, P. Masqué, V. Rodellas, M. Mejías, B. Ballesteros and J. A. Domínguez. 2010. Groundwater and nutrient discharge through karstic coastal springs (Castelló, Spain). *Biogeosciences* 7: 2625-2638.
- Gonnee, M. E., M. A. Charette, Q. Liu, J. A. Herrera-Silveira and S. M. Morales-Ojeda. 2014. Trace element geochemistry of groundwater in a karst subterranean estuary (Yucatan Peninsula, Mexico). *Geochimica et Cosmochimica Acta* 132: 31-49.
- Katz, B. G., D. W. Griffin and J. H. Davis. 2009. Groundwater quality impacts from the land application of treated municipal wastewater in a large karstic spring basin: chemical and microbiological indicators. *Science of the Total Environment* 407: 2872-2886.
- Knee, K. L., J. H. Street, E. E. Grossman, A. B. Boehm and A. Paytan. 2010. Nutrient inputs to the coastal ocean from submarine groundwater discharge in a groundwater-dominated system: relation to land use (Kona coast, Hawai'i, USA). *Limnology and Oceanography* 55: 1105-1122.
- Liefer, J. D., H. L. MacIntyre, L. Novoveska, W. L. Smith and C. P. Dorsey. 2009. Temporal and spatial variability in *Pseudo-nitzschia* spp. in Alabama coastal waters: a hot spot linked to submarine groundwater discharge? *Harmful algae* 8: 706-714.
- Liefer, J. D., H. L. MacIntyre, N. Su and W. C. Burnett 2014. Seasonal alternation between groundwater discharge and benthic coupling as nutrient sources in a shallow coastal lagoon. *Estuaries and coasts* 37: 925-940.
- Loesch, H. 1960. Sporadic mass shoreward migrations of demersal fish and crustaceans in Mobile Bay, Alabama. *Ecology* 41: 292-298.
- Macintyre, H. L., A. L. Stutes, W. L. Smith, C. P. Dorsey, A. Abraham and R. W. Dickey. 2011. Environmental correlates of community composition and toxicity during a bloom of *Pseudo-nitzschia* spp. in the northern Gulf of Mexico. *Journal of Plankton Research* 33: 273-295.

- May, E. B. 1973. Extensive oxygen depletion in Mobile Bay, Alabama. *Limnology and Oceanography* 18: 353-366.
- Null, K. A., K. L. Knee, E. D. Crook, N. R. de Sieyes, M. Rebolledo-Vieyra, L. Hernández-Terrones and A. Paytan. 2014. Composition and fluxes of submarine groundwater along the Caribbean coast of the Yucatan Peninsula. *Continental Shelf Research* 77: 38-50.
- Schroeder, W. W. and W. J. Wiseman. 1988. The Mobile Bay estuary: Stratification, oxygen depletion, and jubilees. *Hydrodynamics of Estuaries. Vol II. Estuarine Case Studies*, 41-52.
- Tovar-Sánchez, A., G. Basterretxea, V. Rodellas, D. Sánchez-Quiles, J. García-Orellana, P. Masqué and E. García-Solsona. 2014. Contribution of groundwater discharge to the coastal dissolved nutrients and trace metal concentrations in Majorca Island: karstic vs detrital systems. *Environmental Science Technology* 48: 11819-11827.
- Turner, R., W. Schroeder and W. J. Wiseman. 1987. The role of stratification in the deoxygenation of Mobile Bay and adjacent shelf bottom waters. *Estuaries* 10: 13-19.